THE UNIVERSITY of ADELAIDE

Metal-Organic Framework Nanosheets for Electrocatalysis

By Dongdong Zhu

School of Chemical Engineering

Faculty of Engineering, Computer and Mathematical Science

A thesis submitted for the degree of Doctor of Philosophy

The University of Adelaide

January 2019

Table of Contents

Abstract

Metal-organic frameworks (MOFs) have aroused great interest in many fields due to their appearing properties such as tailorable structure and function, high specific surface area and porosity. Electrocatalysis is attractive and significant for the academia and industry because it underpins various clean and renewable technologies like water splitting, fuel cell, metal-air batteries, etc. In recent years, MOFs-derived materials prepared through post high-temperature calcination have been widely investigated for electrocatalysis. However, the pyrolysis process always destroys the structure of the MOFs, resulting in the agglomeration of metal nodes and loss of organic ligands, which are not favourable for electrocatalysis. Meanwhile, only very limited number of works directly used pristine MOFs as electrocatalysts. To this end, this thesis aims to design and synthesize 2D MOF nanosheets and 2D MOF-based hybrid nanosheets for electrocatalysis.

The first aspect of this thesis is about Ni-MOF nanosheets with high oxidation state for urea oxidation reaction (UOR). High oxidation state of metal cations is critical in achieving outstanding performance of many transition metal-based materials towards electrochemical oxidation reactions such as UOR, which acts as a vital half reaction for several practical applications. However, it is still a great challenge to explore such a kind of materials for high-performance oxidation reactions. Herein, 2D MOF comprising nickel species and organic ligand of 1,4-benzenedicarboxylic acid (BDC) is fabricated and explored as an electrocatalyst for UOR, which exhibits high activity (120 mA cm^{-2} at 1.6 V vs. RHE) and strong catalyst durability after continuous operation for 10 hours. The excellent UOR performance is due to high active site density of the 2D MOF, and high oxidation state of the nickel species, which are proved by both X-ray photoelectron spectroscopy and Synchrotron-based X-ray absorption near edge spectra. Our findings provide a suitable material for practical application of UOR, and this 2D MOF strategy could be used to fabricate other electrocatalyst with high oxidation state for a wide range of oxidation reactions.

The second aspect of this thesis is about Ni-BDC/$Ni(OH)_2$ hybrid nanosheets for oxygen evolution reaction (OER). Just like graphene, 2D MOF has an unwanted tendency to aggregate, which reduces the specific surface area. $Ni(OH)_2$ is a typical catalyst for OER, but the reaction activity is far from satisfactory probably due to its low oxidation state. The Ni-BDC/$Ni(OH)_2$ hybrid nanosheets prepared through a facile sonication-assisted solution method can perfectly solve these two problems. After hybridization with $Ni(OH)_2$, the large

surface area of Ni-BDC is well retained. Moreover, due to the strong electron interactions between BDC from Ni-BDC and Ni cations from $Ni(OH)_2$, the electronic structure of Ni cations from $Ni(OH)_2$ component can be well modified, leading to the generation of Ni cations with higher oxidation state, which surely contribute to enhanced OER activity. As a result, the Ni-BDC/$Ni(OH)_2$ hybrid nanosheets exhibited remarkable OER performance in 1.0 M KOH, outperforming pure Ni-BDC, $Ni(OH)_2$ and even commercial Ir/C.

The third aspect of this thesis is about Co-BDC/MoS_2 hybrid nanosheets for alkaline hydrogen evolution reaction (HER). Generally, the reaction activity of a catalyst for alkaline HER is about 2-3 orders of magnitude lower than that for acidic HER. This is because the hydrogen intermediate (H*) comes from the dissociation of water in alkaline solution, and this step introduces an additional energy barrier for alkaline HER. At present, the oxidation reaction (e.g. OER) performance of MOFs are comparable or even superior to benchmark noble metals, but the HER activities of MOFs are far from satisfactory. To this end, Co-BDC/MoS_2 hybrid nanosheets are constructed for alkaline HER. The pristine 2H-MoS_2 are transformed to 1T-MoS_2 partially after the hybridization. This is beneficial for HER as 1T-MoS_2 is a much better HER catalyst. Moreover, the well-constructed Co-BDC/MoS_2 interface is vital for alkaline HER, as both components play specific roles in different elementary steps of alkaline HER. In specific, Co-BDC facilitates the dissociation of water to provide enough protons to the nearby MoS_2, while phase-modified MoS_2 is favourable for the following H_2 generation. As expected, the as-fabricated Co-BDC/MoS_2 nanosheets exhibit remarkable HER performance in 1.0 M KOH, outperforming those of Co-BDC nanosheets, MoS_2 nanosheets and almost all the previously reported MOFs-based electrocatalysts.

Declaration

I certify that this work contains no material which has been accepted for the award of any other degree or diploma in my name, in any university or other tertiary institution and, to the best of my knowledge and belief, contains no material previously published or written by another person, except where due reference has been made in the text. In addition, I certify that no part of this work will, in the future, be used in a submission in my name, for any other degree or diploma in any university or other tertiary institution without the prior approval of the University of Adelaide and where applicable, any partner institution responsible for the joint-award of this degree.

I acknowledge that copyright of published works contained within this thesis resides with the copyright holder(s) of those works.

I also give permission for the digital version of my thesis to be made available on the web, via the University's digital research repository, the Library Search and also through web search engines, unless permission has been granted by the University to restrict access for a period of time.

Name of Candidate: Dongdong Zhu

Signature:

Date: 18/12/2018

Acknowledgments

First and foremost, my sincerest gratitude goes to my principle supervisor, Prof. Shizhang Qiao, who provided me a great opportunity to work in such a world-class research group in electrocatalysis area. I have learned a lot about how to be an independent and excellent researcher from Prof. Qiao. This thesis would not have been possible without his invaluable guidance and support in these four years. I also want to thank my co-supervisor, Dr. Chunxian Guo, for his insightful suggestions and help during my research.

I am very grateful for the financial support from the China Scholarship Council (CSC) and the University of Adelaide.

I would like to thank all the people who have helped me for the sample characterizations: Liang Wang and Dr. Yi Du from the University of Wollongong for the TEM test, Dr. Dawei Su from University of Technology Sydney for the BET measurements, Prof. Lei Zhang from the University of South China University of Technology for the XPS test, Ms Ruth Williams, Mr Ken Neubauer and Dr Lisa O'Donovan from the University of Adelaide for SEM and TEM tests. I have benefited a lot from their helps and discussions. Also, many thanks to Officers Michelle Fitton and Sue Earle, and Analytical Services Co-ordinator Dr. Qiuhong Hu for their administrative helps.

I am deeply indebted to all colleagues in Prof. Qiao's group at The University of Adelaide: Dr. Yao Zheng, Dr. Yan Jiao, Dr. Sheng Chen, Dr. Jingjing Duan, Dr. Bo You, Dr. Deepak Dubal, Dr. Ruifeng Zhou, Dr. Jingrun Ran, Dr. Lin Xiong, Dr. Bita Bayatsarmadi, Dr. Dongdong Li, Dr. Jinlong Liu, Fangxi Xie, Anthony Vasileff, Lei Liu, Yongqiang Zhao, Chao Ye, Xuesi Wang, Huanyu Jin, Chaochen Xu, Xing Zhi, Jieqiong Shan, Xin Liu, Tian Wen, Huan Li, Laiquan Li, Bingquan Xia, Xianlong Zhou, et al., for the discussion and help in research, and for the fun time we have shared in daily life.

I would like to thank my girlfriend Dr. Dandan Ma. It's so lucky to meet you in Adelaide, and we have lots of nice memories in Australia. Without your understanding and love, probably I cannot go through these four years. Finally, I am grateful to my parents in China. They didn't have chance to receive higher education at that time, but they know the importance of education and try their best to support me these years.

Chapter 1: Introduction

1.1 Significance of the Project

In order to meet the ever-increasing energy demand of the world while also preserve the environment, renewable and clean energy technologies including fuel cell, water splitting, metal-air batteries, and carbon dioxide conversion to fuel, have been widely investigated.[1-3] Electrocatalysis underpins these energy technologies, such as hydrogen evolution reaction (HER) and oxygen evolution reaction (OER) for water splitting, oxygen reduction reaction (ORR) and OER for metal-air batteries, ORR for fuel cell.[4-6] To achieve high energy efficiency of these reactions, advanced electrocatalysts are highly required to drive the sluggish kinetics.[7-8] Currently, the state-of-the-art electrocatalysts are noble metal-based catalysts such as Pt for ORR and HER, RuO_2 and IrO_2 for OER.[9] The high price, low abundance of noble metals greatly hinders the practical applications of these technologies. Therefore, developing low-cost, earth-abundant, stable and highly efficient non-noble metal-based electrocatalysts for these reactions are highly urgent and significant.[10]

Metal-organic frameworks (MOFs) are crystalline porous materials constructed by linking metal ions or clusters with organic ligands.[11-12] Since the first report in 1989, more than 20000 different MOFs are reported.[13] Due to their unique features such as tunable structures and functions, ultrahigh porosity and large surface area, MOFs have been widely investigated and applied in various areas such as gas separation and storage, biomedicine, catalysis and sensing.[14-15] As a subclass of MOFs, 2D MOFs also possess some advantages stemmed from 2D structure. Compared to bulk materials, higher percentages of metal atoms are exposed on the surface of 2D materials as active sites for catalysis. More inspiringly, these exposed metal atoms are coordinatively unsaturated with more dangling bonds, and hence contribute to higher catalytic activities.[16-17] Moreover, 2D materials lead to the formation of defeats, which can tailor the electronic structure of the 2D materials to achieve enhanced conductivity.[18] In all, 2D MOFs are quite promising for electrocatalysis owning to the aforementioned characteristics.

1.2 Research Objectives

The major goals of this thesis are to design 2D MOF nanosheets or 2D MOF-based hybrid nanosheets for electrocatalysis and get more insights into the reaction mechanisms of several

key electrocatalytic processes such as HER and OER. Specifically, the objectives of this thesis are:

- ***To fabricate*** ultrathin 2D Ni-BDC nanosheets with high oxidation state for urea oxidation reaction.
- ***To understand*** the importance of electronic structure and oxidation state of the electrocatalysts for oxidation reactions.
- ***To design*** novel 2D Ni-BDC/$Ni(OH)_2$ hybrid nanosheets through a facile sonication-assisted solution method for highly efficient oxygen evolution reaction.
- ***To overcome*** the shortcomings of pristine 2D MOFs by the hybridization with other 2D functional materials.
- ***To extend*** the application range of MOFs by constructing 2D Co-BDC/MoS_2 hybrid nanosheets for alkaline hydrogen evolution.
- ***To understand*** the important role of Co-BDC/MoS_2 interface for the enhanced alkaline HER performance.

1.3 Thesis Outline

This thesis is the outcomes of my PhD research presented in the form of journal publications. This thesis is about MOF nanosheets for electrocatalysis. Electrochemical carbon dioxide reduction reaction (CRR), which can directly convert unwanted carbon dioxide to useful chemicals and fuels, has drawn increasing attention from the academia and industry. Thus, recent progresses and challenges of this emerging and significant reaction is reviewed in the thesis. Then we discuss how the MOF nanosheets can be applied in electrocatalysis without any calcination treatment. Specifically, the chapters in the thesis are presented in the following sequence:

- ***Chapter 1*** introduces the significance of this project and outlines the research objectives and key contributions to the field of MOF and electrocatalysis.
- ***Chapter 2*** reviews the recent progresses and challenges of inorganic heterogeneous electrocatalysts for electrochemical carbon dioxide reduction reaction.
- ***Chapter 3*** presents 2D Ni-MOF nanosheets with high oxidation states for efficient electrocatalytic urea oxidation
- ***Chapter 4*** investigates 2D Ni-BDC/$Ni(OH)_2$ heterostructure for enhanced oxygen evolution reaction.
- ***Chapter 5*** studies 2D Co-BDC/MoS_2 Interface for enhanced alkaline hydrogen evolution.

- ***Chapter 6*** presents the conclusions and perspectives for further work on the design, application, and mechanisms of MOF nanosheets for electrocatalysis.

1.4 References

1. Anantharaj, S.; Ede, S. R.; Sakthikumar, K.; Karthick, K.; Mishra, S.; Kundu, S., Recent Trends and Perspectives in Electrochemical Water Splitting with an Emphasis on Sulfide, Selenide, and Phosphide Catalysts of Fe, Co, and Ni: A Review. ACS Catalysis 2016, 6 (12), 8069-8097.
2. Mistry, H.; Varela, A. S.; Kühl, S.; Strasser, P.; Cuenya, B. R., Nanostructured electrocatalysts with tunable activity and selectivity. Nature Reviews Materials 2016, 1, 16009.
3. Stamenkovic, V. R.; Mun, B. S.; Arenz, M.; Mayrhofer, K. J. J.; Lucas, C. A.; Wang, G.; Ross, P. N.; Markovic, N. M., Trends in electrocatalysis on extended and nanoscale Pt-bimetallic alloy surfaces. Nature Materials 2007, 6, 241.
4. Seh, Z. W.; Kibsgaard, J.; Dickens, C. F.; Chorkendorff, I.; Nørskov, J. K.; Jaramillo, T. F., Combining theory and experiment in electrocatalysis: Insights into materials design. Science 2017, 355 (6321), eaad4998.
5. Jiao, Y.; Zheng, Y.; Jaroniec, M.; Qiao, S. Z., Design of electrocatalysts for oxygen- and hydrogen-involving energy conversion reactions. Chemical Society Reviews 2015, 44 (8), 2060-2086.
6. Stamenkovic, V. R.; Strmcnik, D.; Lopes, P. P.; Markovic, N. M., Energy and fuels from electrochemical interfaces. Nature Materials 2016, 16, 57.
7. Luo, M.; Guo, S., Strain-controlled electrocatalysis on multimetallic nanomaterials. Nature Reviews Materials 2017, 2, 17059.
8. Zhang, B.; Zheng, X.; Voznyy, O.; Comin, R.; Bajdich, M.; García-Melchor, M.; Han, L.; Xu, J.; Liu, M.; Zheng, L.; García de Arquer, F. P.; Dinh, C. T.; Fan, F.; Yuan, M.; Yassitepe, E.; Chen, N.; Regier, T.; Liu, P.; Li, Y.; De Luna, P.; Janmohamed, A.; Xin, H. L.; Yang, H.; Vojvodic, A.; Sargent, E. H., Homogeneously dispersed, multimetal oxygen-evolving catalysts. Science 2016, aaf1525.
9. Roger, I.; Shipman, M. A.; Symes, M. D., Earth-abundant catalysts for electrochemical and photoelectrochemical water splitting. Nature Reviews Chemistry 2017, 1, 0003.

10. Zou, X.; Zhang, Y., Noble metal-free hydrogen evolution catalysts for water splitting. Chemical Society Reviews 2015, 44 (15), 5148-5180.
11. Jiao, L.; Wang, Y.; Jiang, H.-L.; Xu, Q., Metal–Organic Frameworks as Platforms for Catalytic Applications. Advanced Materials 2018, 30 (37), 1703663.
12. Zhao, Y.; Song, Z.; Li, X.; Sun, Q.; Cheng, N.; Lawes, S.; Sun, X., Metal organic frameworks for energy storage and conversion. Energy Storage Materials 2016, 2, 35-62.
13. Furukawa, H.; Cordova, K. E.; O'Keeffe, M.; Yaghi, O. M., The Chemistry and Applications of Metal-Organic Frameworks. Science 2013, 341 (6149), 1230444.
14. Wang, H.; Zhu, Q.-L.; Zou, R.; Xu, Q., Metal-Organic Frameworks for Energy Applications. Chem 2017, 2 (1), 52-80.
15. Yang, Q.; Xu, Q.; Jiang, H.-L., Metal–organic frameworks meet metal nanoparticles: synergistic effect for enhanced catalysis. Chemical Society Reviews 2017, 46 (15), 4774-4808.
16. Sun, Y.; Gao, S.; Lei, F.; Xie, Y., Atomically-thin two-dimensional sheets for understanding active sites in catalysis. Chemical Society Reviews 2015, 44 (3), 623-636.
17. Zhao, S.; Wang, Y.; Dong, J.; He, C.-T.; Yin, H.; An, P.; Zhao, K.; Zhang, X.; Gao, C.; Zhang, L.; Lv, J.; Wang, J.; Zhang, J.; Khattak, A. M.; Khan, N. A.; Wei, Z.; Zhang, J.; Liu, S.; Zhao, H.; Tang, Z., Ultrathin metal–organic framework nanosheets for electrocatalytic oxygen evolution. Nature Energy 2016, 1, 16184.
18. Duan, J.; Chen, S.; Zhao, C., Ultrathin metal-organic framework array for efficient electrocatalytic water splitting. Nature Communications 2017, 8, 15341.

Chapter 2: Literature Review

2.1 Introduction and Significance

This chapter reviews the recent advances in inorganic heterogeneous electrocatalysts for carbon dioxide reduction reaction (CRR). Carbon dioxide electroreduction is significantly important and attractive because it can not only reduce the accumulation of CO_2 in the atmosphere but also produce fuels and industrial chemicals, thus alleviating environmental problems and energy crisis simultaneously. Extensive studies have been carried out both experimentally and computationally to accelerate the development of electrocatalysis for CO_2 reduction. Though some reviews which are mainly focused on homogeneous catalysis for CO_2 reduction have been published before, there are few reviews which are specifically devoted to heterogeneous catalysis. Moreover, a great number of high-performance inorganic heterogeneous electrocatalysts for CO_2 reduction have been reported during these several years. These accumulated data and insights will certainly constitute new knowledge to the field of CO_2 reduction. Therefore, a timely and comprehensive review of heterogeneous electrocatalysts for CO_2 reduction presented here is meaningful to facilitate further research in this area.

Herein, our review paper is mainly about recent advances in both theoretical and experimental studies of heterogeneous electrocatalysis for CO_2 reduction. Besides metal electrocatalysts, which have been widely investigated throughout these years, our review also includes some other promising inorganic electrocatalysts like carbon-based materials, metal oxides and metal dichalcogenides. Very recently, these three groups of materials are proved to be good candidates as efficient electrocatalysts for CO_2 reduction. The reaction mechanism, some fundamental concepts and influential factors to the catalytic results are also presented in this review. However, though great achievements have been made in this research area, the technology is still far from practical application. Therefore, we also proposed several strategies including surface engineering, chemical modification, nanostructured catalysts, composite materials and reaction mechanism to boost the performance of heterogeneous electrocatalysts in this review.

2.2 Recent Advances in Inorganic Heterogeneous Electrocatalysts for Reduction of Carbon Dioxide

This chapter is included as it appears as a journal paper published by **Dongdong Zhu**, Jinlong Liu, Shi-Zhang Qiao, Recent advances in inorganic heterogeneous electrocatalysts for reduction of carbon dioxide, ***Advanced materials***, 2016, 28, 3423-3452.

Statement of Authorship

Title of Paper	Recent Advances in Inorganic Heterogeneous Electrocatalysts for Reduction of Carbon Dioxide
Publication Status	☑ Published ☐ Accepted for Publication ☐ Submitted for Publication ☐ Unpublished and Unsubmitted work written in manuscript style
Publication Details	Dongdong Zhu, Jinlong Liu, and Shi-Zhang Qiao, Recent Advances in Inorganic Heterogeneous Electrocatalysts for Reduction of Carbon Dioxide, Advanced Materials, 2016, 28, 3423–3452.

Principal Author

Name of Principal Author (Candidate)	Dongdong Zhu		
Contribution to the Paper	Project design and manuscript drafting.		
Overall percentage (%)	70%		
Certification:	This paper reports on original research I conducted during the period of my Higher Degree by Research candidature and is not subject to any obligations or contractual agreements with a third party that would constrain its inclusion in this thesis. I am the primary author of this paper.		
Signature		Date	18/12/2018

Co-Author Contributions

By signing the Statement of Authorship, each author certifies that:

i. the candidate's stated contribution to the publication is accurate (as detailed above);

ii. permission is granted for the candidate in include the publication in the thesis; and

iii. the sum of all co-author contributions is equal to 100% less the candidate's stated contribution.

Name of Co-Author	Jinlong Liu		
Contribution to the Paper	Discussion of this manuscript and manuscript revision. 20%		
Signature		Date	18/12/2018

Name of Co-Author	Shi-Zhang Qiao		
Contribution to the Paper	Supervision of the work and manuscript evaluation. 10%		
Signature		Date	19/Dec/2018

ADVANCED MATERIALS
www.advmat.de

Recent Advances in Inorganic Heterogeneous Electrocatalysts for Reduction of Carbon Dioxide

*Dong Dong Zhu, Jin Long Liu, and Shi Zhang Qiao**

In view of the climate changes caused by the continuously rising levels of atmospheric CO_2, advanced technologies associated with CO_2 conversion are highly desirable. In recent decades, electrochemical reduction of CO_2 has been extensively studied since it can reduce CO_2 to value-added chemicals and fuels. Considering the sluggish reaction kinetics of the CO_2 molecule, efficient and robust electrocatalysts are required to promote this conversion reaction. Here, recent progress and opportunities in inorganic heterogeneous electrocatalysts for CO_2 reduction are discussed, from the viewpoint of both experimental and computational aspects. Based on elemental composition, the inorganic catalysts presented here are classified into four groups: metals, transition-metal oxides, transition-metal chalcogenides, and carbon-based materials. However, despite encouraging accomplishments made in this area, substantial advances in CO_2 electrolysis are still needed to meet the criteria for practical applications. Therefore, in the last part, several promising strategies, including surface engineering, chemical modification, nanostructured catalysts, and composite materials, are proposed to facilitate the future development of CO_2 electroreduction.

1. Introduction

Since the industrial revolution in the 19th century, fossil fuels (i.e., coal, petroleum and natural gas) have been exploited as the main energy source to sustain our economy and society. The excessive depletion of fossil fuels gives rise to a series of problems.[1–3] On the one hand, with the fast development of the economy and the rapid growth of the population, the global demand for energy has been continuously increasing, while fossil fuels as non-renewable resources have very limited reserves, leading to an aggravated energy crisis. On the other hand, due to the huge consumption of fossil fuels, the as-emitted carbon dioxide (CO_2) has been constantly accumulating in the atmosphere year by year. By July 2015, the concentration of atmospheric CO_2 reached as high as 401.3 parts per million (ppm), which far exceeds the upper safety limit of 350 ppm for atmospheric CO_2.[4] The overproduction of CO_2 is believed to be a major contributor to some undesirable environmental changes, such as global warming, desertification, ocean acidification, etc. Therefore, alleviating the effects caused by the heavy CO_2 emission has become a pressing issue to the modern society.[5,6]

To solve the aforementioned problems, numerous studies have focused on energy- and environmental-related topics.[7–9] During the past several decades, fossil fuels have been partly replaced by clean and renewable energy sources (i.e., wind, tide, and solar) to mitigate CO_2 emission.[10] Despite the growth of renewable energy at an increasing rate, the percentage of these renewable sources is still very low (<5%) in today's overall energy consumption. In addition, most of these renewable sources are geographical, seasonal, and intermittent. Consequently, the full use of renewable energy is often concerned with energy conversion and storage technologies. Specifically, energy conversion and storage devices such as supercapacitors and rechargeable batteries (e.g., lithium-ion batteries) are supposed to level the electricity output. However, considering their low energy densities and high costs, the large-scale integration of these energy-storage devices into the grid can hardly be realized.[11,12] Apart from the development of renewable energy and related technologies, carbon capture and sequestration (CCS) has also been adopted to prevent the release of large quantities of CO_2 into the atmosphere.[13,14] Nevertheless, CCS technology is energy-consuming and expensive. Moreover, the risky leakage of stored CO_2 is a major concern with CCS, preventing large-scale CCS deployment from being commercialized. Accordingly, CO_2 fixation is still a great challenge for human beings worldwide.

In fact, an ideal solution is to convert atmospheric CO_2 into small organic molecules with improved energy density, such as carbon monoxide (CO), formic acid, methanol, methane, etc., using renewable energy.[15,16] Such a strategy can not only reduce the accumulation of CO_2 in the atmosphere, but also produce fuels and useful industrial chemicals, thus relieving our dependency on conventional fossil resources. To this end, various CO_2 reduction approaches, including electrochemical, photochemical, biochemical and thermochemical methods, have been proposed and intensively studied in the past decades.[17–20] Among these methods, reducing CO_2 with renewable electricity is particularly appealing, due to its moderate

D. D. Zhu, J. L. Liu, Prof. S. Z. Qiao
School of Chemical Engineering
University of Adelaide
Adelaide, SA 5005, Australia
E-mail: s.qiao@adelaide.edu.au
Prof. S. Z. Qiao
School of Materials Science and Engineering
Tianjin University
Tianjin 300072, China

DOI: 10.1002/adma.201504766

efficiency, controllable selectivity, simple reaction units, and enormous potential for real industrial applications.[21,22] Moreover, CO_2 electroreduction can also be regarded as a convenient way to store the renewable energies above in chemical forms.

Considering the fact that the linear CO_2 molecule is fully oxidized and extremely stable, efficient and robust electrocatalysts are needed to promote this kinetically sluggish reduction process.[18] Therefore, the performance of CO_2 electrochemical reduction essentially depends on the properties of the applied electrocatalysts. Electroreduction of CO_2 can be carried out via homogeneous or heterogeneous reactions. Correspondingly, electrocatalysts for CO_2 reduction are generally classified into homogeneous and heterogeneous catalysts.[23] In a typical homogeneous reduction of CO_2, electrocatalysts are organics or metal–organic molecules dissolved in electrolytes with unique active centers interacting with CO_2 molecules.[24,25] Owing to their special molecular structure, homogeneous electrocatalysts often exhibit excellent selectivity toward reduction of CO_2, thus attracting considerable attention and being widely investigated since the 1970s. Nevertheless, there are some disadvantages of homogeneous electrocatalysts, such as high cost, toxicity, and complicated post-separation, which hinder their real application in industry. On the contrary, inorganic heterogeneous electrocatalysts have stimulated more and more interest in recent years, due to their facile synthesis, environmental friendliness, outstanding efficiency, and great potential for large-scale applications.

A number of high-quality review articles covering homogeneous catalysis for electrochemical CO_2 reduction have been published,[23–27] while there are few reviews devoted entirely to heterogeneous catalysis. In spite of traditional metal electrocatalysts, which have been treated as typical electrodes for CO_2 electroreduction, a variety of new inorganic heterogeneous electrocatalysts have been reported in recent years with modest electrochemical results, in virtue of the rapid development of advanced nanotechnology and the giant progress in computational methods. More importantly, the emergence of these novel inorganic heterogeneous electrocatalysts has resulted in some mechanistic studies of CO_2 electroreduction. The accumulated data on CO_2 electroreduction constitute a new knowledge to this topic. Therefore, a timely and comprehensive review devoted to heterogeneous electrocatalysts for CO_2 reduction is definitely meaningful to stimulate further research in this area. The current review covers more than transition-metal (e.g., Cu, Ag, Au, and Sn) electrocatalysts.[28–31] As illustrated in **Scheme 1**, other promising electrocatalysts such as metal-free carbons (e.g., carbon nanotubes (CNTs) and carbon nanofibers (CNFs)),[32,33] transition-metal oxides (e.g., TiO_2 and SnO_2) and transition-metal dichalcogenides (MX_2, M = Mo, W; X = S, Se, Te)[34] are also summarized here. At the same time, some interesting reaction mechanisms associated with specific electrocatalysts are also described and discussed.

2. Fundamentals of Electrochemical CO_2 Reduction (ECR)

2.1. Reaction Mechanism of ECR

Electrochemical reduction of CO_2 is a multi-step reaction process generally involving two-, four-, six-, or eight-electron reaction pathways.[35] For heterogeneous catalysts applied in CO_2 reduction, the reaction often takes place at the electrode–electrolyte interface, where the electrode is a solid electrocatalyst while the electrolyte is usually an aqueous solution saturated with CO_2 by bubbling. Typically, this heterogeneous catalysis process involves three major steps: i) chemical adsorption of CO_2 on an electrocatalyst; ii) electron transfer and/or proton migration to cleave C–O bonds and/or form C–H bonds; and iii) configuration rearrangement of products to desorb them from the electrocatalyst surface and diffuse into the electrolyte.[36] The electrocatalyst employed and the electrode potential applied have a great influence on the final reduction products. In general, the reaction products are a mixture of carbon compounds

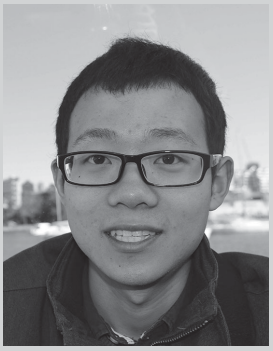

Dong Dong Zhu received his BE and ME degrees in materials science and engineering and materials engineering from Nanjing University of Science and Technology in 2011 and 2014, respectively. He is currently a Ph.D. candidate in chemical engineering under the supervision of Prof. Shi Zhang Qiao at the University of Adelaide. His current research is focused on the development of nanostructured materials for electrochemical CO_2 reduction, supercapacitors, and batteries.

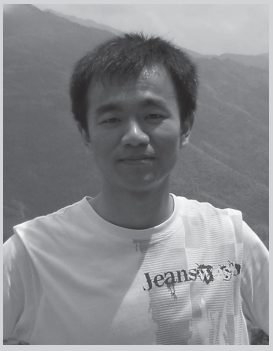

Jin Long Liu received his BE and ME degrees in Applied Chemistry from Central South University in 2011 and 2014, respectively. He is currently a Ph.D. candidate in chemical engineering under the supervision of Prof. Shi Zhang Qiao at The University of Adelaide. His current research is focused on the design and synthesis of functional materials for energy storage and catalysis.

Shi Zhang Qiao received his Ph.D. degree in chemical engineering from Hong Kong University of Science and Technology in 2000; he is currently a Chair Professor at the School of Chemical Engineering of The University of Adelaide, Australia. His research expertise is in nanomaterials for catalysis, drug and gene delivery, and energy storage and conversion.

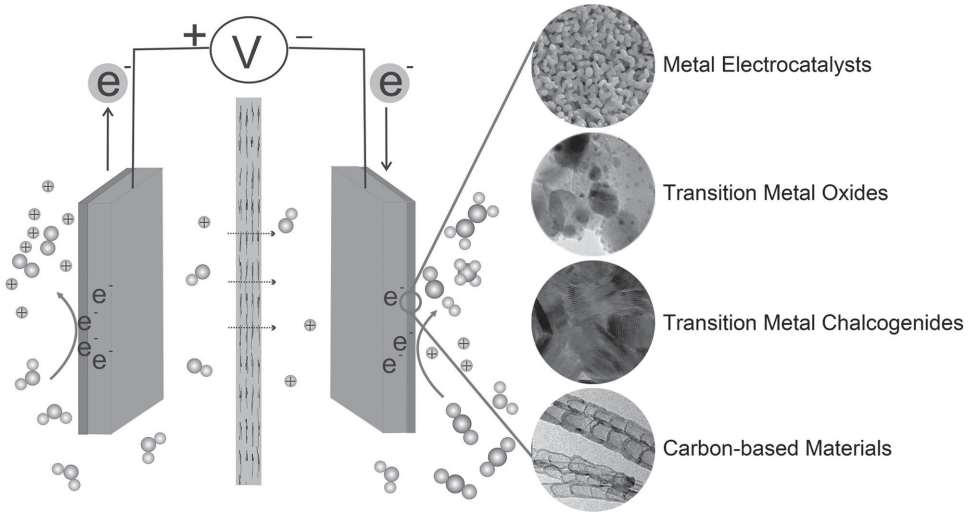

Scheme 1. Illustration of a reaction unit and four categories of the catalysts used for electrochemical CO_2 reduction.

with different oxidation states, and they often include carbon monoxide (CO), formate ($HCOO^-$) or formic acid (HCOOH), methane (CH_4), ethylene (C_2H_4), ethanol (C_2H_5OH), methanol (CH_3OH), etc.[37,38]

From a thermodynamic point of view, the equilibrium potentials of CO_2 reduction are comparable to that of the hydrogen evolution reaction (HER), as displayed in Reaction (R1)–(R7) (pH 7 in aqueous solution versus standard hydrogen electrode (SHE), 25 °C, 1 atmosphere gas pressure, and 1 M concentration of other solutes). This coincides well with the fact that H_2 is the major side-product for CO_2 electroreduction in aqueous electrolytes. Moreover, the small thermodynamic potential differences for CO_2 reduction products (Reaction (R1)—(R6)) indicate the reason why it is quite challenging to reduce CO_2 to the desirable product with good selectivity. However, the actual electrode potentials required to drive the reductions are much more negative than the equilibrium ones.[25]

$$CO_2 + 2H^+ + 2e^- \rightarrow CO + H_2O \quad E^0 = -0.52\ V \tag{R1}$$

$$CO_2 + 2H^+ + 2e^- \rightarrow HCOOH \quad E^0 = -0.61\ V \tag{R2}$$

$$CO_2 + 4H^+ + 4e^- \rightarrow HCHO + H_2O \quad E^0 = -0.51\ V \tag{R3}$$

$$CO_2 + 8H^+ + 8e^- \rightarrow CH_4 + 2H_2O \quad E^0 = -0.24\ V \tag{R4}$$

$$2CO_2 + 12H^+ + 12e^- \rightarrow C_2H_4 + 4H_2O \quad E^0 = -0.34\ V \tag{R5}$$

$$CO_2 + 6H^+ + 6e^- \rightarrow CH_3OH + H_2O \quad E^0 = -0.38V \tag{R6}$$

$$2H^+ + 2e^- \rightarrow H_2 \quad E^0 = -0.42\ V \tag{R7}$$

$$CO_2 + e^- \rightarrow CO_2^{\bullet-} \quad E^0 = -1.9\ V \tag{R8}$$

In fact, the large overpotential (the difference between the equilibrium potential and applied one) mainly originates from the first step of CO_2 reduction. As mentioned above, CO_2 electroreduction can be divided into three steps. In the first step, a key intermediate $CO_2^{\bullet-}$ is formed by one-electron transfer to a CO_2 molecule. Due to the enormous energy requirement to rearrange a linear molecule to a bent radical anion, the reaction occurs at −1.90 V versus SHE (Reaction (R8)).[24] The obtained $CO_2^{\bullet-}$ radical is highly reactive, then several proton-coupled multiple-electron-transfer reactions, which are thermodynamically more favorable, take place almost instantaneously. In a practical CO_2 electrocatalytic cell (Scheme 1), the oxygen evolution reaction (OER) takes place simultaneously at the anode electrode, and an ion exchange membrane is adopted to separate the cathode and anode compartments to prevent further oxidation of gaseous products formed from CO_2 reduction, only allowing the transfer of corresponding ions.[16]

2.2. Useful Notions in ECR

With respect to the evaluation and comparison of the performance of electrocatalysts for CO_2 reduction, it is necessary to clarify the definitions of several fundamental parameters.[39]

i) Onset potential. The onset potential refers to the applied voltage on the electrocatalyst versus the reference electrode, under which the desired product is yielded at a detectable amount. It should be noted that the onset potential is usually lower than the CO_2 reduction equilibrium potential, and the difference between them is identified as the overpotential.

ii) Faradaic efficiency (FE). The FE is defined as the percentage of electrons consumed for the formation of a given product. The FE can be simply calculated by Equation (1):

$$\varepsilon_{\text{Faradaic}} = \frac{\alpha n F}{Q} \tag{1}$$

where α is the number of electrons transferred (e.g., $\alpha = 8$ for reduction of CO_2 to CH_4), n is the number of moles for a

desired product, F refers to Faraday's constant (96 485 C mol^{-1}), while Q represents all the charge passed. The Faradaic efficiency is directly related to the product selectivity.

iii) The energetic efficiency (EE). The EE defines the overall energy utilization toward the desired product. The equation used to calculate EE is listed below:

$$\varepsilon_{\text{energetic}} = \frac{E_{\text{eq}}}{E_{\text{eq}} + \eta} \times \varepsilon_{\text{Faradaic}} \quad (2)$$

where E_{eq} is the equilibrium potential and η refers to the overpotential. Based on this equation, one can conclude that the high EE of CO_2 reduction arises from the combination of both a low overpotential and a high FE.

iv) The current density. The overall current density for CO_2 reduction is typically calculated via dividing the current by the geometric surface area of the working electrode. As a measure of the reaction rate, this parameter is crucial for practical applications, since it determines the electrolyzer size and the cost needed for the process. Moreover, the partial current density for a specific product can be acquired by multiplying the corresponding FE by the overall current density.

v) The Tafel plot. The Tafel plot connects the overpotential with the logarithm of the current density, which is very useful in evaluating the performance of electrocatalysts. In general, a smaller Tafel slope indicates better catalytic performance. In the case of CO_2 electroreduction, the Tafel slope is very useful for investigating the reaction mechanism. A Tafel slope of 118 mV dec^{-1} implies that the rate-determining step for CO_2 reduction is the generation of the $CO2^{\bullet-}$ key intermediate by the initial one-electron transfer step, while the slope of 59 mV dec^{-1} is indicative of a one-electron pre-equilibrium step before a later rate-limiting chemical step.[40]

2.3. Advantages and Challenges of ECR

Recently, electrocatalytic reduction of CO_2 has attracted extensive interest from both industry and academia due to its intrinsic advantages such as:

i) Fuels and useful chemical feedstocks can be obtained as final products, while the overall chemical consumption is just water and greenhouse-gas CO_2 since the electrolyte can be fully recycled;
ii) The electricity used can be derived from renewable resources, meaning that no extra CO_2 is generated during this reduction;
iii) The electrochemical reduction occurs under ambient pressures and temperatures;
iv) The reaction process can be controlled easily by adjusting the external parameters such as the applied potentials;
v) The modular characteristics of the electrocatalytic reaction system may enable its large-scale applications.[41]

Due to the enormous potential rewards, extensive studies have been done to accelerate the development of electrocatalysis for CO_2 reduction. However, up till now, none of the reported electrocatalysts have met the requirements for practical use. Several major scientific challenges still remain, such as:

i) Because of the high energy barrier for the formation of the $CO_2^{\bullet-}$ intermediate, a large overpotential is required, implying low energy efficiency of the reduction process;
ii) Hindered by the sluggish kinetics of CO_2 reduction and the limited mass transfer ability of CO_2 to the electrocatalyst surfaces, the reaction rates are rather low;
iii) Mixed products containing various gaseous and liquid species can be obtained from CO_2 reduction, in which case the product separation would be costly;
iv) During the reduction process, the catalytic active sites of electrocatalysts can be blocked or poisoned by reaction intermediates, by-products, and impurities from the electrolyte, resulting in severe deactivation.[42,43] In general, the lifetime of electrocatalysts reported so far is less than 100 h;
v) Since CO_2 reduction is performed in aqueous solutions, the competitive hydrogen evolution reaction (HER) should be considered.[44] As a significant side-reaction, which occurs with a much lower potential, the HER greatly influences the Faradaic efficiency and selectivity of CO_2 electrocatalysts;
vi) Compared with the HER, OER, and oxygen reduction reaction (ORR), CO_2 reduction is much more complicated due to many possible products and multiple coupling steps of electrons and protons. Thus, it is much more difficult to uncover the fundamental principles and exact reaction process of CO_2 reduction.

Overall, promising electrocatalysts for CO_2 reduction should feature a low overpotential, a high current density, and good stability, while simultaneously the HER should be strongly suppressed to yield desired products with high selectivity.

3. Electrocatalysts for Carbon Dioxide Reduction

3.1. Metal Electrocatalysts

During the past few decades, metal electrodes like Cu, Au, Sn etc. have been widely explored as electrocatalysts for CO_2 reduction.[45,46] In fact, the generation of the $CO_2^{\bullet-}$ intermediate has been regarded as a rate-determining step for CO_2 reduction in most cases. Therefore, one of the main functions of these electrocatalysts is to stabilize this key intermediate to achieve high energy efficiency for CO_2 reduction. Depending on the tendency to bind various intermediates and final products, metal electrodes can be classified into three groups.[21,47] As displayed in **Figure 1**, group 1 includes Sn, Hg, Pb, and In, etc., generating formate or formic acid as the main products. Metals belonging to this group can hardly bind the $CO_2^{\bullet-}$ intermediate, therefore formate or formic acid is formed through an outer-sphere mechanism.[47] Au, Ag, Zn, and Pd are typical representatives of the group 2 metals, which can bind *COOH tightly enough for further reduction. However, the obtained *CO intermediate is weakly bound to the metal surface. Thus, it desorbs readily from the surface and emerges as a predominant reaction product. Cu is the only metal belonging to the group 3, which is capable of binding and converting *CO intermediate to higher value-added

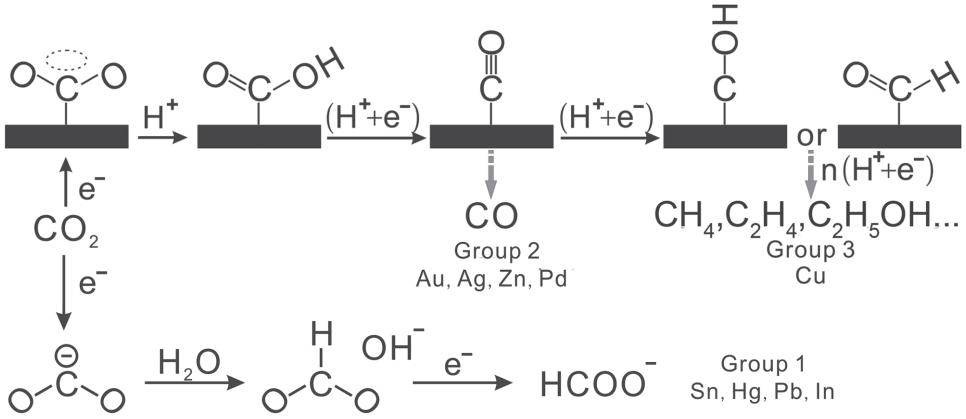

Figure 1. Reaction mechanism of electrochemical CO_2 reduction on metal electrodes in aqueous solutions.

products (such as hydrocarbons and alcohols) through *COH or *CHO intermediates. Overall, the major products generated by these three groups of catalysts are $HCOO^-$ (HCOOH), CO, and higher value-added products, respectively. As was mentioned above, a competitive process, HER, should not be forgotten in the case of CO_2 electrochemical reduction in aqueous solutions. As *CO intermediate is adsorbed strongly enough to exclude further reduction of CO_2, the HER almost exclusively occurs on metals like Pt, Ti, Fe, and Ni. Thus, tuning the binding energies of the key reaction intermediates is critical for final product selectivity and energy efficiency of CO_2 electroreduction. According to the principle of Sabatier, the best catalysts should feature appropriate interactions between reaction intermediates and surfaces of catalysts.[48–50]

In fact, the actual surface chemistry of transition metals during CO_2 reduction is even more complicated than the aforementioned theories.[51–53] Recently, Kuhl et al. performed CO_2 reduction on seven transition metals.[54] Interestingly, as displayed in **Figure 2**a, both methane and methanol were formed on Ag, Zn, Cu, Ni, and Pt metals. Meanwhile, only methane was generated on Fe, and methanol was produced on Au. The different oxophilicities between Au and Fe should contribute to those results. Because of a strong binding affinity for O, Fe should break the second C–O bond of the CO_2, leading to the formation of methane. In contrast, less-oxophilic Au prefers to keep the second C–O bond intact, and methanol is the only product. Therefore, it seems practical to obtain desired hydrocarbon or alcohol products by adjusting the binding strength of O_{ads}.

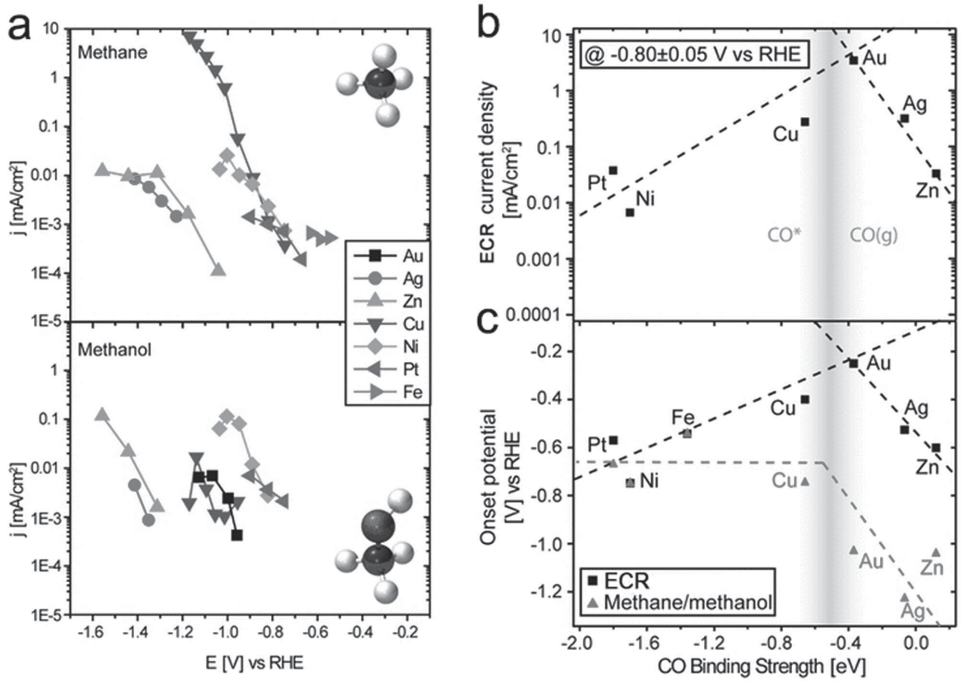

Figure 2. a) Partial current densities of methane and methanol on seven metals. b) Volcano plot of the current density for ECR at –0.8 V vs CO binding strength. c) Two distinct onset potentials plotted against CO binding energy: ECR and methane or methanol. The dashed lines are to guide the eye. Reproduced with permission.[54] Copyright 2014, The American Chemical Society.

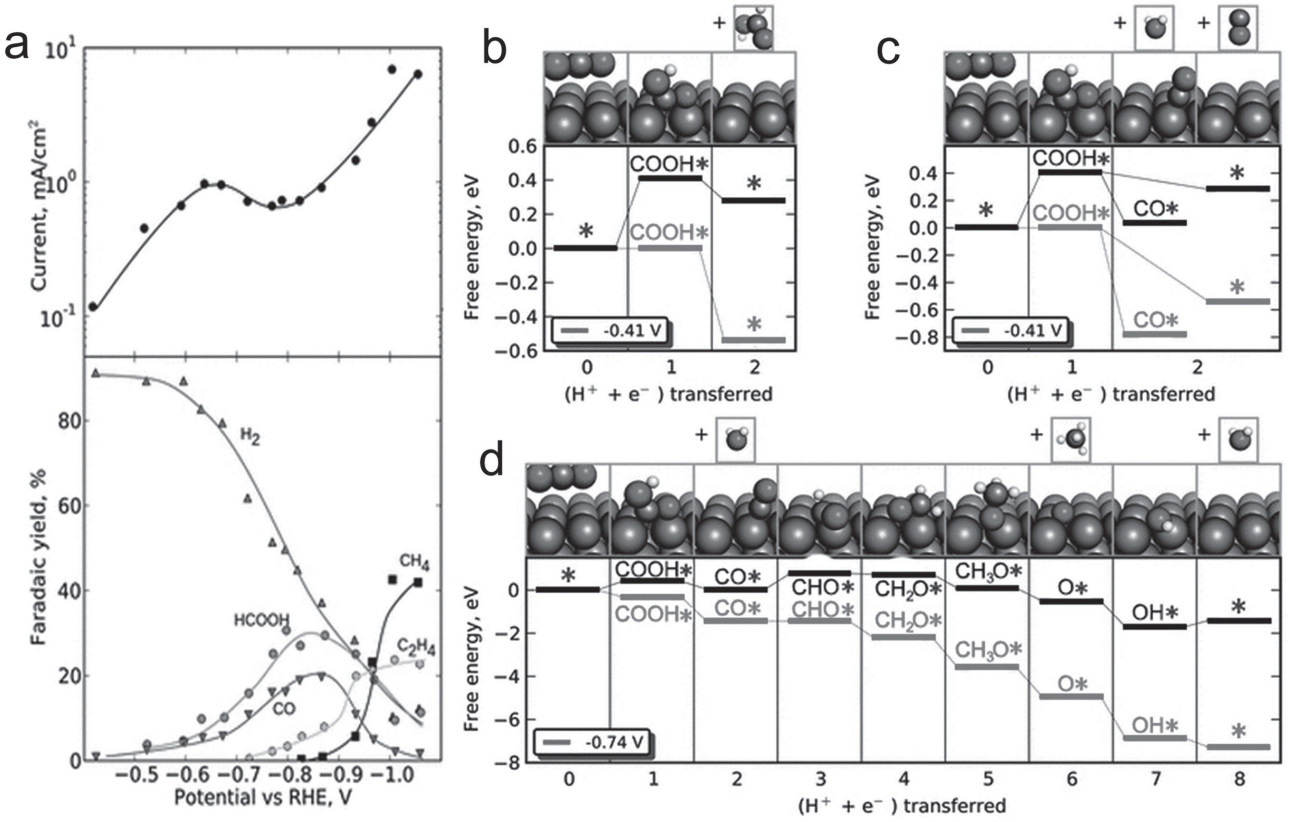

Figure 3. a) Product distribution and total current produced as a function of the applied potential (versus RHE) in the electrochemical reduction of CO_2 at a copper electrode in 0.1 M $KHCO_3$ (pH 6.8) at 18.5 °C. Free-energy diagrams for the lowest energy pathways leading to: b) HCOOH, c) CO, and d) CH_4. In each diagram, the black (higher) pathway represents the free energy at 0 V vs RHE and the grey (lower) pathway represents the free energy at the indicated potential. Reproduced with permission.[63] Copyright 2010, The Royal Society of Chemistry.

Furthermore, it was demonstrated that the catalytic activity and product selectivity greatly depend on the CO binding strength. The volcano-type plot for the CO_2 reduction activity is shown in Figure 2b,c with Au at the top, featuring both the highest current density and the lowest onset potential for CO_2 reduction. Owing to the lower CO binding strength, CO_2 activation becomes quite difficult on Ag and Zn, resulting in lower activity for CO_2 reduction than that of Au. However, for Cu, Ni, and Pt, which can bind *CO tightly, CO_2 activation seems to be facile, while it is difficult to further desorb CO or reduce it to other products. Importantly, as displayed in Figure 2c, a higher CO binding strength than that of Au is desired for the formation of methane and methanol. Interestingly, Pt, Ni, Fe, and Cu show similar onset potentials for the production of methane/methanol. Because of the high coverage of *CO intermediates on Pt, Ni, Fe, and Cu, the reduction of *CO is supposed to be the rate-determining step. Moreover, this rate-limiting step was shown to be rather insensitive to the CO binding strength, resulting in similar overpotentials. In contrast, for metals like Au, Ag, and Zn, a higher overpotential is needed for *CO reduction to compete with fast CO desorption.

3.1.1. Cu

Copper (Cu) is capable of directly converting CO_2 into varieties of hydrocarbons and alcohols.[55–57] These products are more valuable than CO or formate because they can be directly used in existing infrastructure with high energy densities. However, a relatively large overpotential (nearly 1 V) is required for the reduction, resulting in a low energy efficiency of the Cu electrode. Besides that, low product selectivity and fast deactivation of catalysts are typical barriers for practical use.[58,59] Thus, better understanding of the catalytic mechanism is of great significance for the future design of efficient and selective catalysts for CO_2 reduction.[60,61]

Reaction mechanisms: Pioneering research work on Cu electrodes was carried out by Hori in the 1980s.[62] He found that electrochemical reduction of CO_2 on a Cu electrode could effectively yield hydrocarbons and alcohols under ambient conditions. As displayed in **Figure 3**a, the product distribution varies significantly with applied potential. H_2, HCOOH, and CO are dominant reaction products at less-negative potentials, while CH_4 and C_2H_4 are preferentially produced at more negative potentials. These interesting phenomena can be explained by the following hypothesis. Initially, CO_2 is reduced to CO and HCOOH at less-negative potentials (more positive than –0.7 V vs RHE). Then, interfering with the cathodic HER, absorbed CO is further reduced to hydrocarbons and alcohols at more-negative potentials. In contrast, HCOOH is not further reduced. Therefore, CO is regarded as an intermediate species for CO_2 reduction on a Cu electrode.

Recently, Peterson et al. tried to explain CO_2 reduction on Cu electrodes by density functional theory (DFT) calculations.[63] In

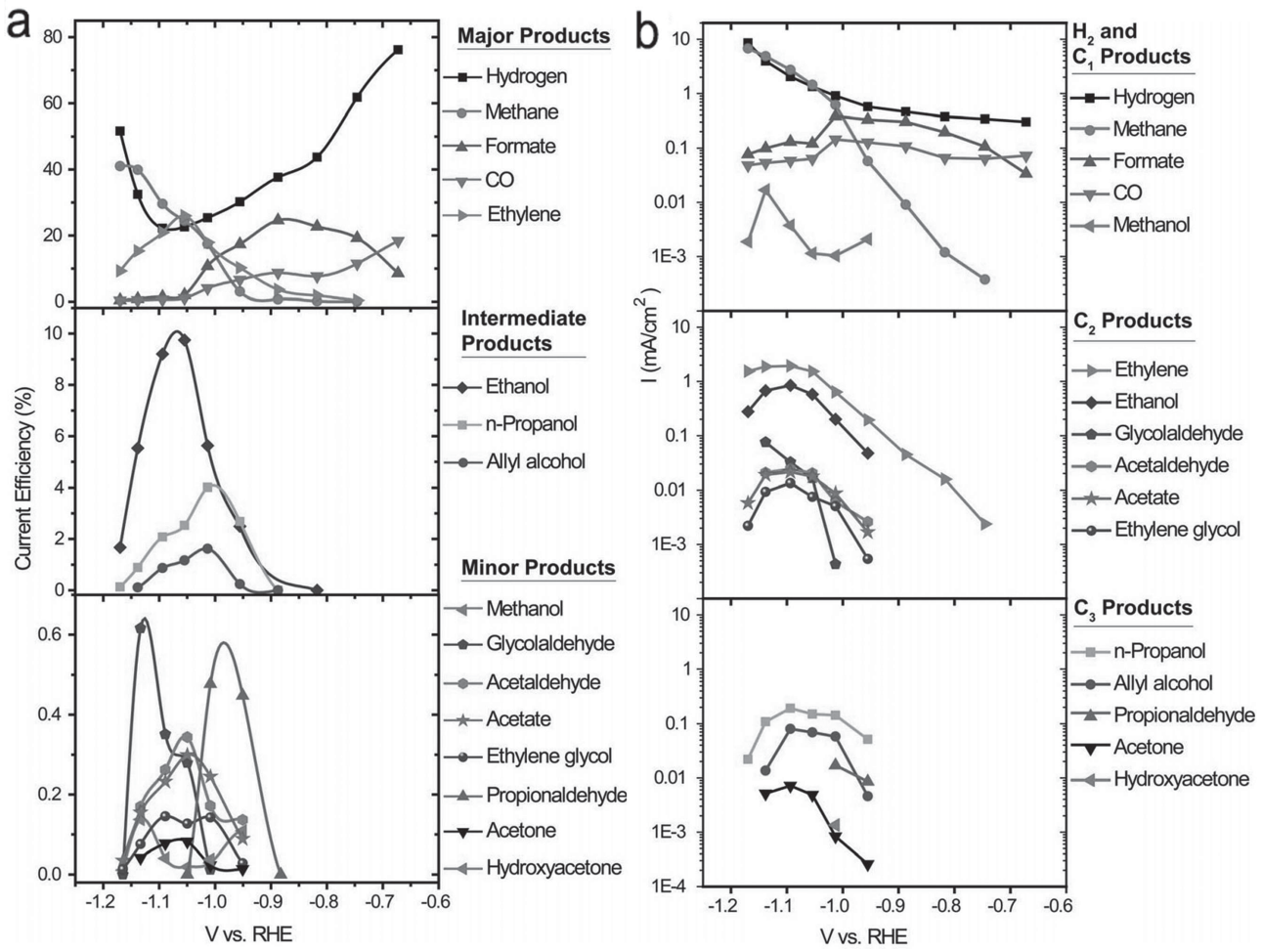

Figure 4. Electrochemical reduction of CO_2 performed at a copper electrode in 0.1 M $KHCO_3$ (pH 6.8) electrolyte. a) Current efficiency for major, intermediate range, and minor products as a function of potential. b) Tafel plot of the partial current going to each product. Reproduced with permission.[64] Copyright 2012, The Royal Society of Chemistry.

detail, the computational hydrogen electrode (CHE) model was applied to elucidate the exact reaction pathways for CO_2 reduction. Figure 3b shows the free-energy diagram for the lowest energy pathway to HCOOH. Firstly, adsorption of a proton–electron pair results in the formation of carboxyl (*COOH) species, and –0.41 V is required for this rate-determining step. Then, the obtained *COOH intermediate reacts with the second proton–electron pair to get the final product HCOOH. The route for CO production is also limited by the formation of *COOH. After that, by removing water, the *COOH intermediate is further reduced to *CO. Since *CO is weakly bonded, CO emerges as both a gas and a surface species for the reaction (Figure 3c). As illustrated in Figure 3d, the exact reaction pathway for CH_4 is $*CO_2 \rightarrow *COOH \rightarrow *CO \rightarrow *CHO \rightarrow *CH_2O \rightarrow *CH_3O \rightarrow CH_4$. Moreover, the reaction barrier of *CHO generation is significantly higher than that of *COOH generation. Therefore, for CH_4 formation, the rate-limiting step is the generation of the *CHO intermediate by protonation of *CO. This key step occurs at –0.74 V, which is consistent with the fact that CH_4 is produced at a more-negative range. The reduction of adsorbed *CO to *CHO is also considered to be the potential-limiting step for C_2H_4. However, the C–C bond in C_2H_4 is formed in a non-electrochemical way, while the CHE model is more suitable for simple proton-transfer reactions. Therefore, the CHE model is not applicable for the formation of C_2H_4. Moreover, the fluctuation of current density in Figure 3a can be attributed to surface coverage effects. The adsorbed *CO species on the Cu surface are responsible for the decreased overall current, since they block the active reaction sites. While the potential is negative enough to protonate the absorbed *CO intermediate, the catalyst surface is self-cleaned and some blocked catalytic active sites become free, resulting in recovered total current.

With the help of a highly sensitive reaction cell and advanced characterization techniques, 16 different products were detected on polycrystalline Cu surface by Jaramillo's group.[64] Notably, five of them including ethylene glycol, glycolaldehyde, hydroxyacetone, acetone, and glyoxal were reported for the first time. As illustrated in **Figure 4**a, the variety of reaction products is strongly related to the applied potential. In detail, four major products CO, formate, CH_4, and C_2H_4 were observed at less-negative potentials (–0.65 to –0.8 V vs RHE). Then, a significant

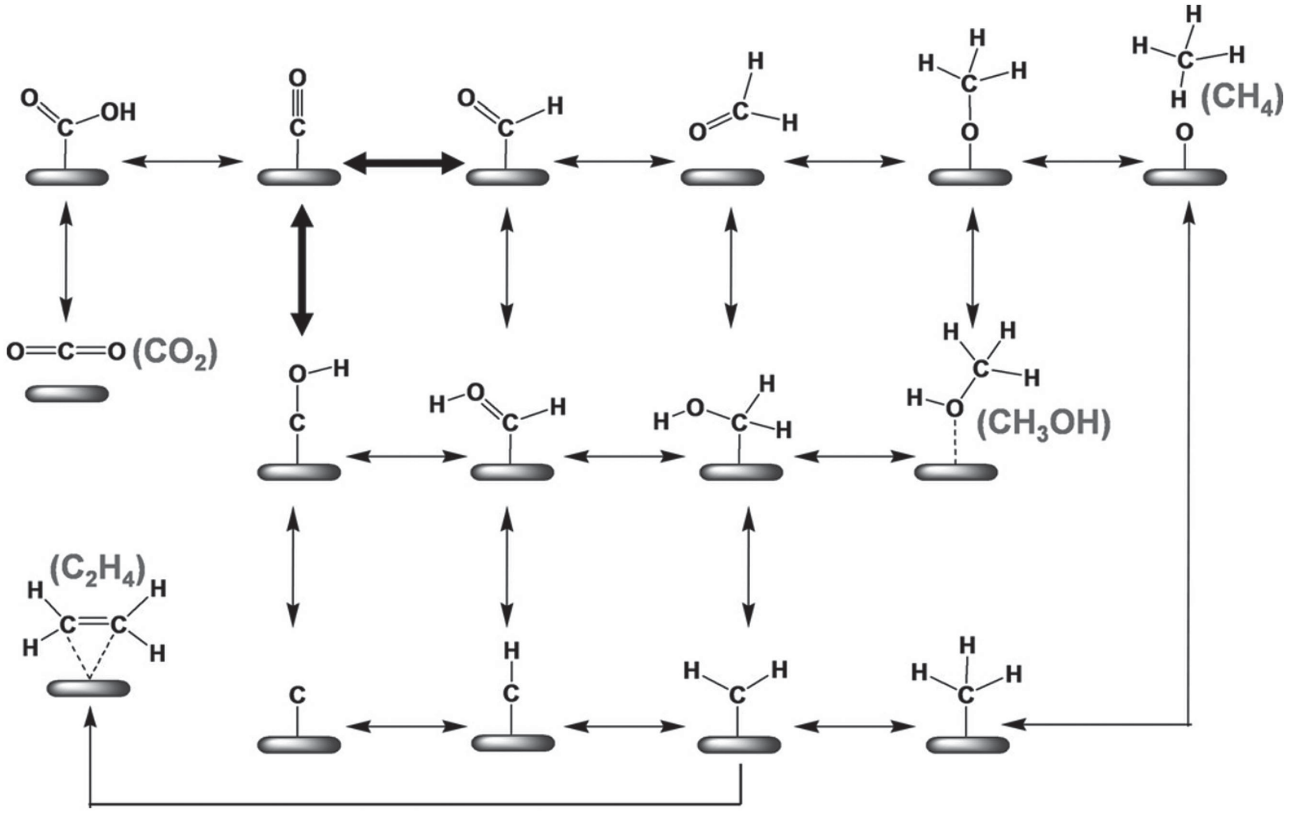

Figure 5. Proposed reaction pathways of CO_2 electroreduction to methane, methanol, and ethylene on Cu (111). Electrochemical elementary steps for CH_4 and CH_3OH formation involve electron and proton transfer, whereas C_2H_4 is produced through non-electrochemical CH_2 dimerization. H^++e^- reactants and H_2O products are omitted. Reproduced with permission.[65] Copyright 2013, Wiley-VCH.

number of C1–C3 intermediates or minor products emerged at the more-negative region (–0.9 to –1.1 V vs RHE). At the highly negative range (–1.1 V vs RHE), the current efficiency for all the products declined except that for H_2 and CH_4. Since electron and proton transfer became more facile at the highly negative range, as compared with C–C coupling, the reduction of C1 species to CH_4 was preferred. The Tafel plots in Figure 4b imply that the partial current densities of C2 and C3 products generally tracked that of C_2H_4. In order to explain the appearance of so many C2 and C3 products, several hypotheses were proposed. i) Different types of reaction sites on the Cu surface result in different products. ii) Different C1 species originating from the same type of surface sites are capable of coupling with each other to achieve diverse products at high overpotentials. However, according to the experimental findings, a completely novel opinion is ventured here. The repeated dihydroxylation of enol-like surface intermediates with $2H^+$ and $2e^-$ should be responsible for the formation of extensive C2 and C3 species.

Recently, Nie et al. found that the reduction pathways on the Cu electrode are determined by both the reaction free energy and the kinetics of the elementary steps.[65] As shown in **Figure 5**, *CO reduction to a *CHO (path I) or a *COH (path II) intermediate is regarded as the selectivity-determining step. As mentioned before, solely based on the free-energy analysis, Peterson et al. proposed that CH_4 is formed through the *CHO intermediate.[63] However, this conflicts with experimental fact that electrochemical reduction of CH_2O on the Cu electrode predominantly gives CH_3OH.[66] Since C–O bond dissociation and C–H formation occur on a metal surface, *CH_3O intermediates are required to bend to rearrange the C atom to the metal surface, leading to a high kinetic barrier for the formation of CH_4 from *CH_3O intermediate. Therefore, path I follows the following order: *CO → *CHO → *CH_2O → *CH_3O → CH_3OH. In contrast, both CH_4 and C_2H_4 originate through the further reduction of the *COH intermediate. A typical formation path for CH_4 is: *CO → *COH → *C → *CH → *CH_2 → *CH_3 → CH_4, which can be evidenced by the presence of graphitic carbon species during CO_2 reduction on the Cu surface.[67] Meanwhile, C_2H_4 should form through non-electrochemical *CH_2 dimerization. The activation barrier for *COH formation from *CO is much lower than that for *CHO, indicating that the dominant reduction products are CH_4 and C_2H_4, which is consistent with the experimental results.

The C–C bond can be formed on the Cu metal under ambient conditions during electrochemical reduction, while high temperatures and pressures are required in the gas phase Fischer–Tropsch process to produce higher hydrocarbons. Montoya et al. demonstrated that the C–C coupling between hydrogenated species (*CHO, *CH_2O) rather than bare *CO intermediates is kinetically more favorable in an electrochemical environment.[68] The degree of hydrogenation of *CO can be tailored by adjusting the applied potential, thus tuning the

activation barrier for C–C coupling. Therefore, *CO is protonated first, then the obtained *CH_xO species couple with each other to yield high-value-added products at room temperature.

In order to identify possible intermediates for CO_2 reduction, Schouten et al. investigated the reduction of several small organic molecules using online mass spectrometry (MS).[66] Examining the acquired experimental data with the former insights in this field, a new mechanism for CO_2 reduction was proposed. In detail, for the C2 reaction path, the CO dimer is formed by electrochemical dimerization of adsorbed CO intermediate. Then the CO dimer is reduced to enediol or oxametallacycle species, followed by further reduction to C_2H_4. Meanwhile, *CHO is regarded as the key intermediate for CH_4 formation, since CO can be activated by hydrogenation for further C–O bond breaking. Thus, the reaction pathway for CH_4 formation is predicted to be: *CO → *CHO → *CH_2 → *CH_3 → CH_4.

In conclusion, the study of the reaction mechanisms for CO_2 reduction on the Cu catalyst is still in its infancy, and different possible reaction pathways have been proposed to match the experimental results. Therefore, more efforts should be undertaken in this area to uncover the reaction mechanisms for CO_2 reduction, which is quite essential for developing highly efficient and selective catalysts.

Influential Factors: As discussed above, there are many possible reaction pathways and various final products for CO_2 electroreduction on the Cu electrodes. Though different theories have been proposed to uncover the details of the reduction, the debate is still going on. Actually, the reaction system of the Cu electrocatalyst can be even more complicated, since the catalytic ability and product selectivity are greatly influenced by many other important factors, which are briefly presented below.

i) Morphology. Tang et al. found that roughened polycrystalline Cu electrodes (Cu-nanoparticle-covered surface and sputtered surface) exhibited better electrocatalytic performance for CO_2 reduction than their smooth counterpart.[69] The high current density of the roughened Cu is simply attributed to higher specific surface area, which means more reaction active sites for CO_2 reduction and HER. Better selectivity of the roughened Cu toward hydrocarbon products implies the importance of surface morphology for CO_2 reduction. In contrast to the smooth surface, which is mainly composed of low-index crystal facets, the roughened surfaces possess a significant number of undercoordinated sites (edges, steps, and defects). As calculated by DFT, these low-coordination sites are more active for CO_2 reduction owing to lower energy barriers for the formation of key intermediates. Gonçalves et al. also reported that the morphology of the Cu electrode has a great impact on the product selectivity.[70] The major gaseous products for dendritic Cu are CO, methane, and ethylene. In contrast, C2 hydrocarbons (C_2H_4 and C_2H_6) are formed on the honeycomb and 3D structured Cu electrodes, while methane is suppressed. Recently, Sen et al. tested the performance of porous Cu nanofoams for CO_2 reduction.[71] As compared with smooth Cu electrodes, the overpotential of Cu nanofoams is about 200 mV lower. The distribution of products and their FEs are also significantly altered with changing morphology of the catalyst. A better selectivity for formic acid was achieved on the Cu nanofoams, while methane and ethylene are greatly suppressed to be minor products (FE < 2%).

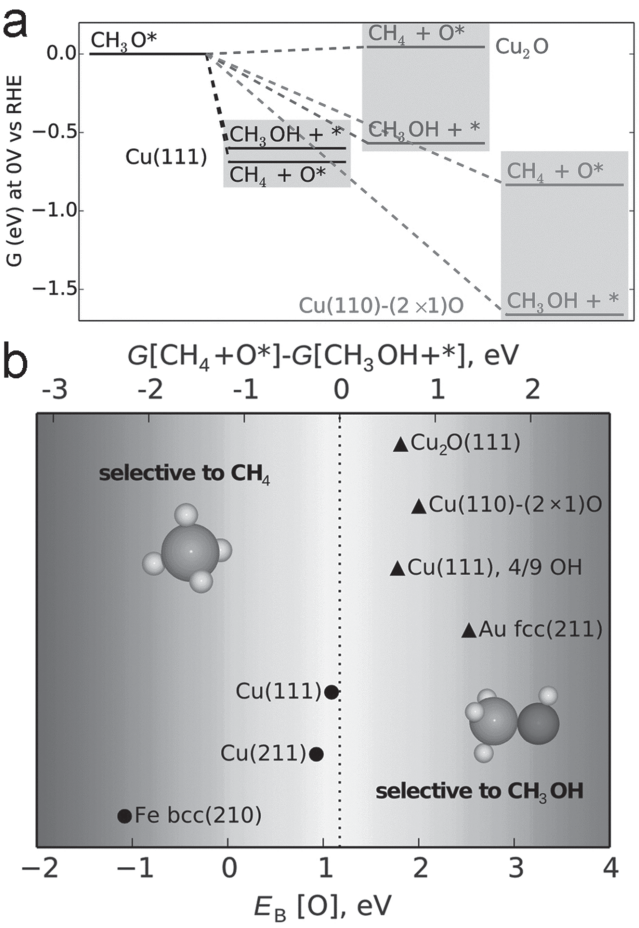

Figure 6. a) Free-energy diagram of the electrochemical step from CH_3O* on Cu (111), Cu_2O (111) and Cu (110)–(2 × 1) O. The step involves transfer of a proton and electron ($H^+ + e^-$) in the CHE model. b) Oxygen binding energy as an activity descriptor for CH_4/CH_3OH selectivity. The dashed line indicates the cutoff binding energy at which the thermodynamic selectivity of the elementary step changes between methane and methanol. Reproduced with permission.[75] Copyright 2015, The Royal Society of Chemistry.

ii) Surface Modification. Frese reported that CO_2 can be reduced to CH_3OH on oxidized Cu electrodes in 1991.[72] Since then, extensive studies on the modification of Cu electrodes have been reported.[73] Xiao et al. found that subsurface oxygen impurities could improve the binding strength of CO_2 molecules on the modified Cu, leading to lower overpotentials.[74] Moreover, the authors proposed that during CO_2 reduction, the carbon-modified Cu electrode had a better selectivity to HCOOH than CO. In order to identify the influence of the local surface environment, Zhang and Peterson investigated the selectivity of the *CH_3O intermediate by DFT.[75] As illustrated in **Figure 6**a, because of a lower free energy, CH_4 is thermodynamically more favorable on pure Cu surface (Cu (111)). In contrast, CH_3OH is preferred on both fully oxidized Cu (Cu_2O) and partially oxidized Cu (Cu (110) – (2×1) O) electrodes due to the reverse free-energy distribution. Moreover, hydroxyl (OH) coverage on the clean Cu surface results in the formation of CH_3OH, while CO coverage has little influence on the preference of final products. Therefore, by introducing a moderate

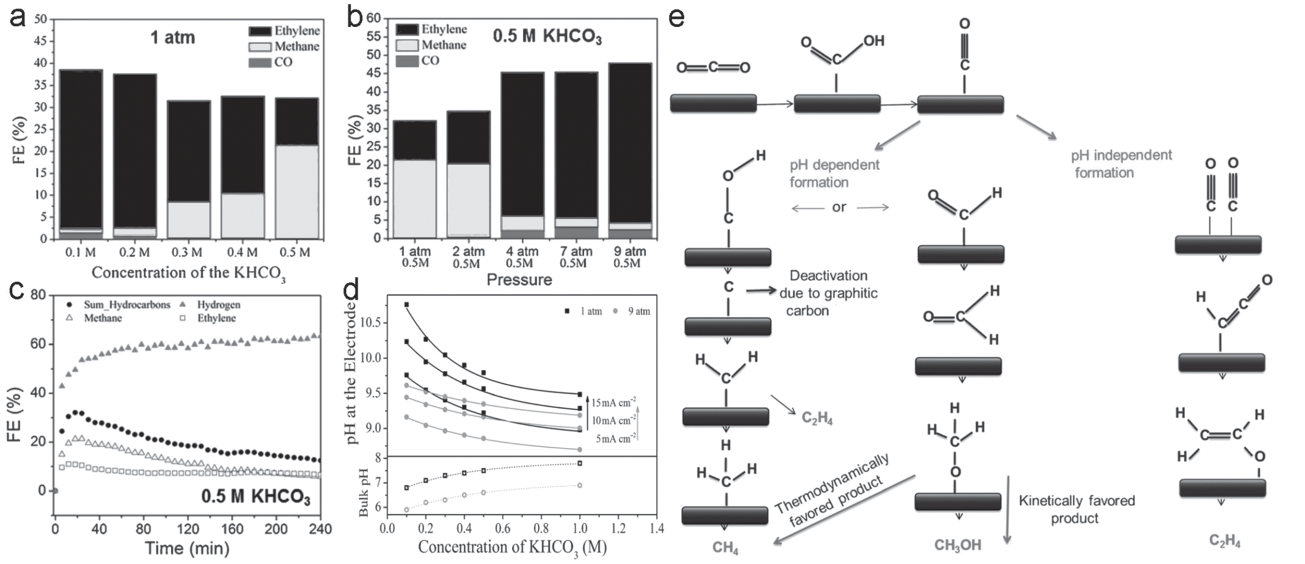

Figure 7. Product distributions for CO_2 reduction as a function of: a) electrolyte concentration, and b) CO_2 pressure. c) FE of the products versus time at 0.5 M $KHCO_3$ and 1 atm CO_2. d) Local pH at the electrode surface as a function of electrolyte concentration at different current densities and pressures and the corresponding bulk pH values. e) Proposed reaction scheme for CO_2 reduction. Reproduced with permission.[79] Copyright 2015, Wiley-VCH.

amount of oxygen (either oxidized surface or OH species), the reduction product would switch from CH_4 to CH_3OH on the Cu surface. According to the assumption of the $*CH_3O$ intermediate, the authors also proposed a simple descriptor for CH_4/CH_3OH selectivity in Figure 6b, indicating that the oxygen binding energy is a key factor determining the exact reaction pathway.

iii) Cu Metal Overlayers. Recently, Cu overlayers have been investigated for CO_2 reduction, as the tensile strain stemmed from lattice mismatch between Cu and substrate metal could alter the binding energies of the reaction intermediates.[76] Reske et al. performed CO_2 reduction on the Cu metal overlayers supported on the Pt substrate.[77] Introduction of a Cu monolayer altered significantly the nature of the Pt surface, as indicated by the much more negative onset potential for the HER. Moreover, the thickness of the Cu overlayers greatly influenced the reaction activity and product selectivity for CO_2 electrolysis. In detail, the partial current densities for methane and ethylene increased with the thickness of the Cu overlayers. Compared with Cu_{5nm}/Pt, Cu_{15nm}/Pt also exhibited better selectivity to methane than ethylene. Since electronic interaction between Pt and Cu atoms decreases with overlayer thickness, the strain effects should be mainly responsible for the above data obtained for Cu overlayers. However, despite the high current densities achieved on the Cu overlayers/Pt substrate, the FEs of hydrocarbons are significantly lower than those on the polycrystalline Cu. Varela et al. found that, due to the presence of *CO intermediates during CO_2 reduction, the morphology of the Cu overlayers changed from a continuous flat surface to a granular structure with the Pt surface partly exposed.[78] Therefore, the HER was promoted, leading to poor selectivity toward CO_2 reduction. Thus, the lattice strain should be seriously considered when designing advanced electrocatalysts for CO_2 reduction.

iv) Electrolyte and CO_2 Pressure. Recently, Kas et al. demonstrated that the hydrocarbon selectivity of Cu can be manipulated by process conditions.[79] As can be seen from **Figure 7**a,b, ethylene is the dominant product at low electrolyte concentration or high CO_2 pressure. The Faradaic efficiency of ethylene is almost constant, whereas that of methane declines significantly (Figure 7c). Moreover, because of the buffer capacity of the electrolyte, a lower concentration of $KHCO_3$ solution leads to a higher local pH at electrode surface (Figure 7d). As shown in Figure 7e, protonation of *CO is regarded as the rate-determining step for methane formation, which is greatly influenced by the pH value. Deactivation of methane seems to be caused by graphitic carbon formed through decomposition of intermediates. Meanwhile, ethylene is formed mainly through *CO coupling, and C–C coupling is a pH-independent process. Thus, high local pH arising from low electrolyte concentration should contribute to the formation of ethylene. Though higher CO_2 pressure results in lower local pH (Figure 7d), the corresponding high *CO surface coverage favors C–C coupling, thus promoting the generation of ethylene. Due to the release of OH^- through the HER and CO_2 reduction, a high local pH can be obtained through the high local current density, leading to the high selectivity to ethylene. In all, ethylene is favored to be produced on the Cu surface with low electrolyte concentration (high local pH), high local current density (high local pH), and high CO_2 pressure (high *CO coverage).

Nanoscaled Cu electrodes: Recently, Reske et al. fabricated Cu nanoparticles (NPs) with different sizes ranging from 2 to 15 nm for electrochemical CO_2 reduction.[80] As compared with the bulk Cu electrode, Cu NPs exhibit a dramatic increase in the overall current density, especially under 5 nm (**Figure 8**a). More interestingly, the product selectivity is greatly influenced by the particle size. As shown in Figure 8b, the formation of hydrocarbons (methane and ethylene) is suppressed on Cu

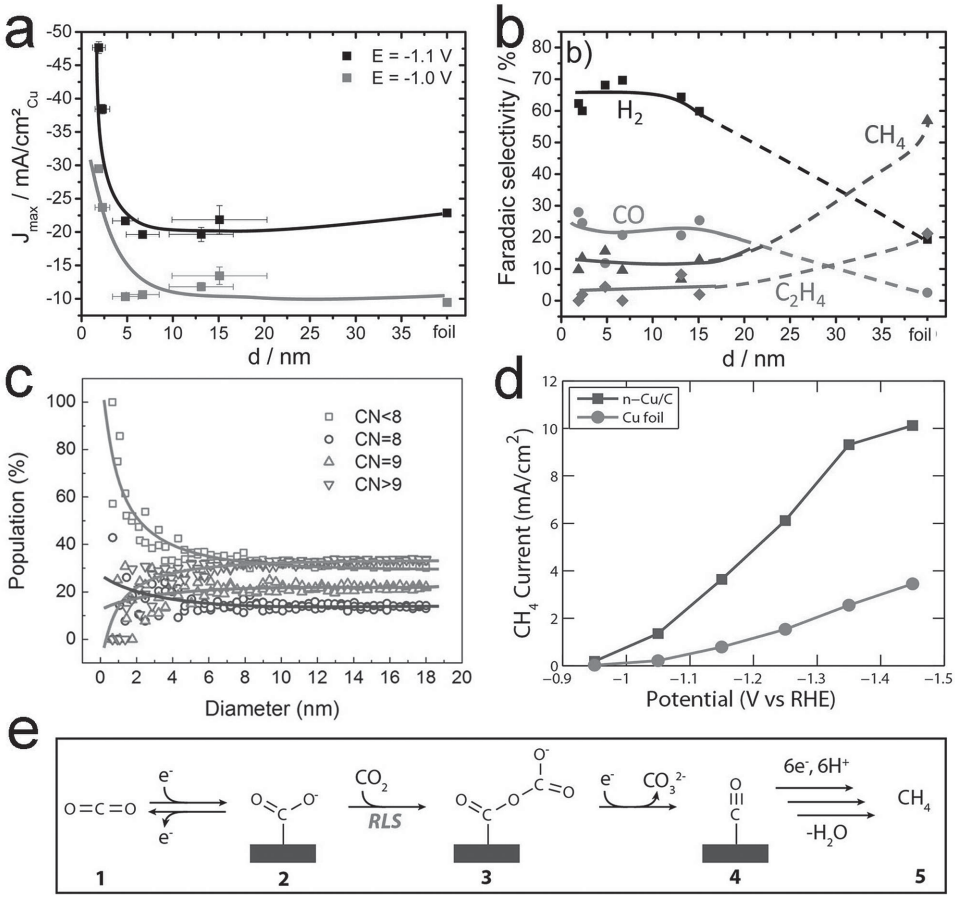

Figure 8. a) Particle-size effect during catalytic CO_2 electroreduction. The current densities at –1.1 and–1.0 V vs RHE as a function of Cu NP size. b) Particle-size dependence of the Faradaic selectivity for reaction products during CO_2 electroreduction on Cu NPs. c) Population (relative ratio) of surface atoms with a specific coordination number (CN) as a function of the particle diameter. Reproduced with permission.[80] Copyright 2014, The American Chemical Society. d) Comparison of methanation current density for n-Cu/C and copper foil electrodes. e) Proposed mechanism for the electrochemical reduction of CO_2 to methane, including an interesting rate-limiting step (RLS). Reproduced with permission.[81] Copyright 2014, The American Chemical Society.

NPs, whereas the HER becomes dominant with a high Faradaic efficiency over 60%. Though Cu NPs also possess a better selectivity to produce CO, the total Faradaic efficiency for CO_2 reduction still declines. Based on the modeling study, the high population of low-coordinated atoms (coordination number CN < 8) in Cu NPs seems to be responsible for this phenomenon (Figure 8c). The formation of *H and *COOH intermediates are the rate-determining steps for the production of H_2 and CO, respectively. Therefore, the higher binding strength between low-coordinated atoms and those key intermediates can undoubtedly promote the generation of H_2 and CO. However, due to the reduced mobility of *CO and *H, further hydrogenation of *CO becomes unfavorable, leading to smaller selectivity towards hydrocarbons.

However, Alivisatos's group found that methane generation was greatly enhanced on well-dispersed Cu nanoparticles (7.0 ± 0.4 nm) supported on glassy carbon (n-Cu/C).[81] A higher total current density and better selectivity to methane were achieved on an n-Cu/C electrode simultaneously, resulting in four-times greater partial current density for methane as compared with a Cu foil electrode (Figure 8d). The authors also discovered that the morphology of the deposited Cu has a dramatic impact on the catalytic methane production. The catalytic sites of isolated Cu nanoparticles are much more effective for methanation than those of dense aggregated nanoparticles. In fact, the reaction mechanism on n-Cu/C is distinct from that on Cu foil. The Tafel slope of n-Cu/C is approximately 60 mV dec^{-1}, indicating that one-electron pre-equilibrium process occurs prior to the rate-determining step. More interestingly, the partial current density for methane has a second-order dependence on the pressure of CO_2. Based on these insights, a completely novel reaction mechanism of CO_2 reduction on n-Cu/C is proposed as follows. Firstly, $CO_2^{\bullet-}$ is formed by a reversible one-electron-transfer pre-equilibrium reaction. Then, the obtained $CO_2^{\bullet-}$ reacts with another CO_2 molecule from solution to yield a CO_2–$CO_2^{\bullet-}$ intermediate by C–O coupling. This rate-determining step agrees well with the aforementioned second-order dependence. Finally, methane is produced by further reduction of the CO_2–$CO_2^{\bullet-}$ intermediate as displayed in Figure 8e.

Xie et al. also proved that the nanostructured Cu facilitates the reduction of CO_2.[82] The overpotential of a Cu nanoflower electrode was 400 mV lower than that on polycrystalline Cu

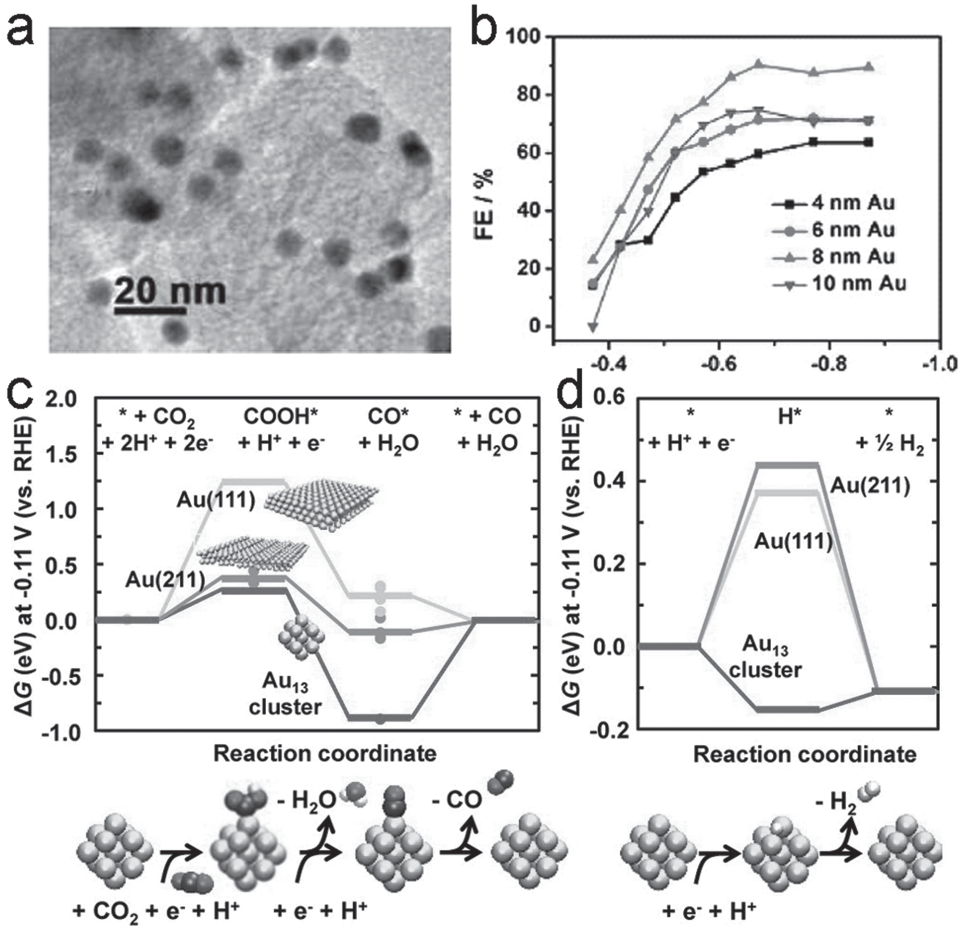

Figure 9. a) TEM image of C-Au NPs. b) Potential-dependent FEs for electrochemical reduction of CO_2 to CO on C-Au NPs with different sizes. c,d) Free-energy diagrams for electrochemical reduction of CO_2 to CO (c) and protons to hydrogen (d) on Au(111), Au(211), and a 13-atom Au cluster at –0.11 V. Reproduced with permission.[30] Copyright 2013, The American Chemical Society.

foil. Moreover, the high current density and better selectivity toward carbonaceous products are accomplished at the same time. The Cu nanoflower electrode also exhibited a better stability than that of Cu foil. Importantly, amorphous carbon was directly observed on the catalyst surface, which is consistent with the previous hypothesis. The thin carbon layer on the Cu nanoflower electrode surface can be regarded as a reaction intermediate, which is consumed quickly during hydrocarbon formation. In contrast, the thick carbon layer formed on the Cu foil turns out to be a poisoning species, which may block active reaction sites for further CO_2 reduction.

3.1.2. Au

Due to the ability to convert CO_2 to CO selectively and efficiently, Au has attracted a lot of attention, though the scarcity and high cost may hinder its practical use.[83] Zhu et al. fabricated a series of monodisperse Au nanoparticles (NPs) (**Figure 9**a) and tested their catalytic ability to reduce CO_2.[30] Among all the tested Au NPs, 8 nm Au NPs exhibited the highest FE up to 90% at –0.67V vs RHE (Figure 9b). Such a high selectivity of CO on Au NPs can be well explained by DFT. For Au (111) crystal faces (Figure 9c), a high free-energy (ΔG) increase between CO_2 and COOH* means that a large overpotential is needed for this process. On contrary, the free energy for the formation of COOH* on Au (211) is significantly lower than that on Au (111), indicating that the stepped surfaces are more active for CO_2 reduction. Though the formation of COOH* is relatively facile on Au_{13} cluster, the obvious ΔG increase in the last step makes the release of CO quite difficult. Furthermore, as compared with Au (111) and Au (211), the Au_{13} cluster is a better HER catalyst due to the much smaller ΔG increase (Figure 9d). These DFT calculations uncover the fact that the edge sites are more beneficial for CO evolution, while corner sites favor the HER. 8 nm Au NPs with 4 nm crystallite diameter can minimize the number of corner sites but provide enough edge sites, resulting in an excellent electrocatalytic performance for CO_2 reduction.

Since 1D nanowires have more edge sites but far fewer corner sites than NPs, Au nanowires are considered to be better candidates as efficient electrocatalysts for CO_2 reduction. Then, the same group further synthesized ultrathin Au nanowires (2 nm wide) by a facile seed-assisted growth method and tested their catalytic performance.[84] The positive onset potential (–0.2 V vs RHE), high Faradaic efficiency (94% at –0.35V vs RHE) and

a reasonable stability were achieved on 500 nm nanowires. According to DFT calculations, such outstanding catalytic results of Au nanowires originate from the high mass density of edge sites (16%), which favors CO formation, and the weak CO binding to these sites that facilitates the release of CO.

Mistry et al. also investigated the relationship between catalytic activity and Au NP size.[85] It was found that when the NP size decreased, the overall current density increased drastically. Due to a slight increase of CO production and a sharp increase in H_2, the Faradaic efficiency for CO_2 reduction dropped. Owing to significant number of low-coordinated sites on small Au NPs, both CO_2 reduction and the HER are promoted, even though the HER is more favored than CO_2 conversion to CO. Therefore, the CO/H_2 product ratio can be tuned by changing the size of the catalyst particles, which represents a great value for practical industrial applications.

Koh et al. fabricated a hierarchically structured Au film composed of nanoscale islands by the oxygen-plasma method.[86] Thanks to the expanded specific surface area, the Au island-type electrocatalyst showed an outstanding CO_2 reduction performance including enhanced current density, good selectivity for CO (FE > 95%) and relatively positive onset potential as compared with the Au foil. The performance of the Au island-type electrode was further improved by using an ionic liquid (1-butyl-3-methylimidazolium tetrafluoroborate ([BMIM]BF_4)), since the ionic liquid can reduce the overpotential by stabilizing the key $CO_2^{\bullet-}$ intermediate.[87] Despite improved CO_2 reduction activity, according to the analysis of the Tafel slopes, the rate-limiting step remains unchanged for the Au islands, and is still the formation of $CO_2^{\bullet-}$ intermediate by initial one-electron transfer.

More recently, Feng et al. reported that grain boundaries (GB) can play a significant role during CO_2 reduction on metal catalysts.[88] The vapor deposition method was adopted to deposit Au NPs on a carbon nanotube film (Au/CNT), as shown in **Figure 10**a. The grain boundaries can be clearly observed in the HRTEM image of the Au NPs shown in Figure 10b. In order to investigate the relationship between the catalytic activity and the GB density quantitatively, the GB surface density was tailored by thermal annealing. The GB density drops drastically as the annealing temperature increases. As compared with the annealed counterparts, the as-deposited Au/CNT electrode exhibited an extremely high CO partial current density (Figure 10c). The data shown in Figure 10d highlight the linear relationship between the GB density and the CO partial current density, indicating that a higher GB surface density results in an enhanced reaction activity for CO_2 reduction. Meanwhile, the HER was also found to be suppressed on the as-deposited Au/CNT. Moreover, the as-deposited Au/CNT electrode can survive for 12 h with still well-retained grain boundaries. Therefore, GB engineering seems to be promising for the development of highly efficient metal electrocatalysts for CO_2 reduction.

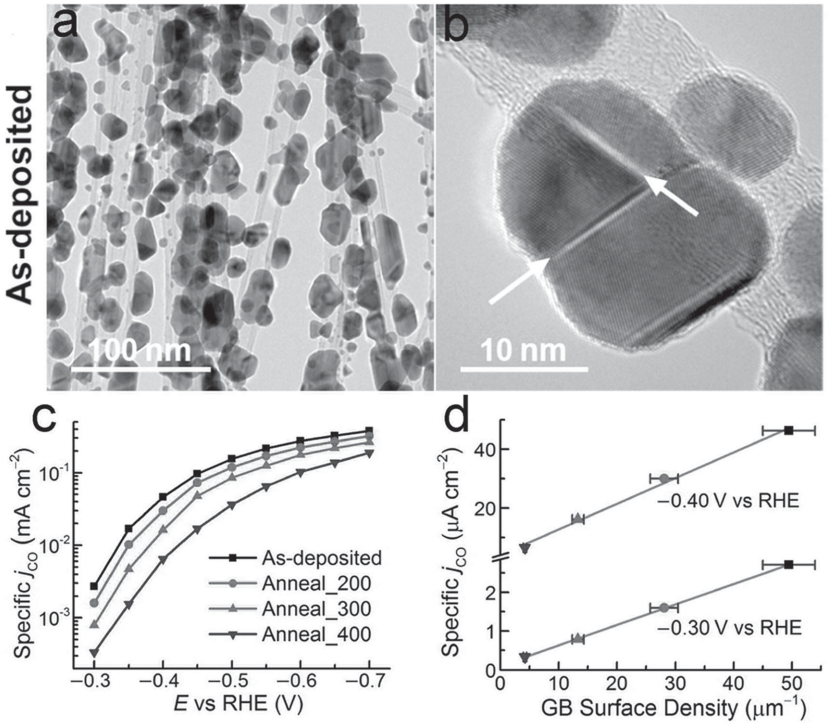

Figure 10. a,b) TEM images of as-deposited Au/CNT electrode. The left column shows the overview image of the electrode, and the right image shows some selected high-resolution TEM images of Au NPs. The arrows indicate grain boundaries in NPs. c) Specific current densities for CO production vs potential on different Au/CNT electrodes. d) Correlation between the specific CO current densities and GB surface density at low overpotentials. Reproduced with permission.[88] Copyright 2015, The American Chemical Society.

3.1.3. Ag

Ag is promising as a CO_2 reduction catalyst due to its relatively low overpotential and high selectivity.[89] Rosen et al. found that CO_2 can be exclusively converted to CO (FE > 95%) on a Ag catalyst with an overpotential smaller than 200 mV. Importantly, these outstanding results were achieved in 18 mol% 1-ethyl-3-methylimidazolium tetrafluoroborate (EMIM-BF_4) (a typical ionic liquid) solution.[90] As illustrated in **Figure 11**a, EMIM-BF_4 was expected to stabilize the $CO_2^{\bullet-}$ intermediate by forming complexes, thus significantly lowering the reaction barrier for CO_2 reduction. The same group also demonstrated that an appropriate water content in EMIM-BF_4 solution can accelerate CO_2 reduction to desired products.[91] Moreover, due to the better solubility of CO_2 and the suppressed HER in ionic liquids, the reaction rate of CO_2 reduction can be further enhanced. Interestingly, several reports show that ionic liquids can modulate the exact reaction process of CO_2 electroreduction, leading to different product selectivity.[92–94] Despite the high cost and ambiguous reaction mechanisms of CO_2 reduction in ionic liquids, they are still extensively applied in electrochemical CO_2 reduction studies.

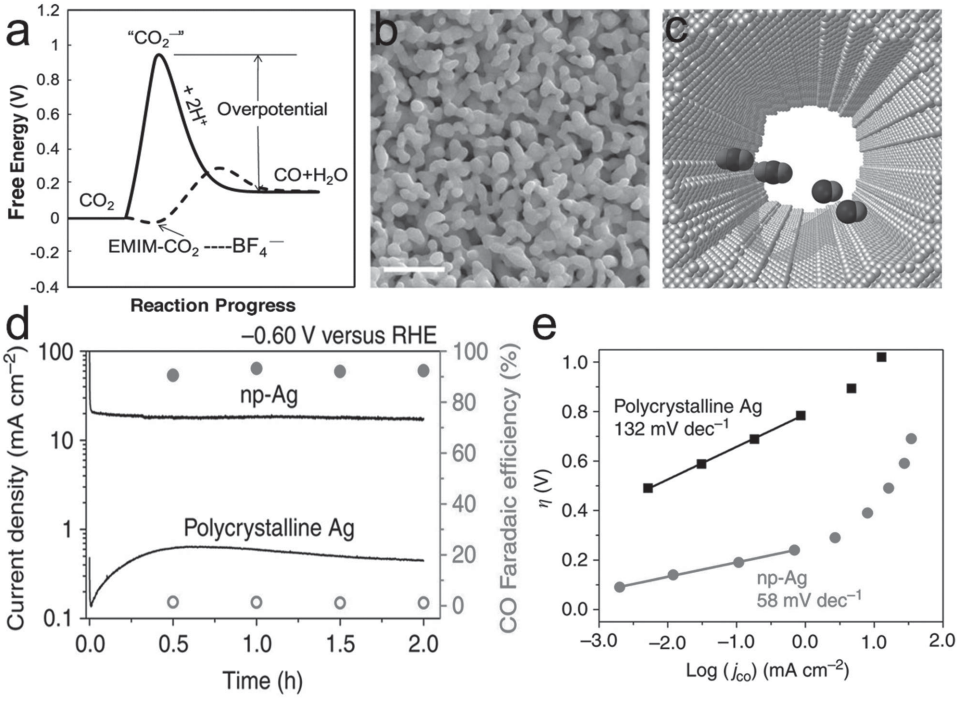

Figure 11. a) Scheme illustrating the free-energy changes during CO_2 reduction to CO in water or acetonitrile (solid line) or EMIM-BF_4 (dashed line). Reproduced with permission.[90] Copyright 2011, The American Association for the Advancement of Science. b) SEM image of de-alloyed np-Ag (scale bar, 500 nm). c) Schematic illustration of a nanopore in the silver electrocatalyst with highly curved internal surface. d) CO_2 reduction activity of np-Ag and polycrystalline silver at –0.60 V. Total current density versus time (left axis) and CO FE versus time (right axis). e) Overpotential versus CO production partial current density on polycrystalline silver and np-Ag. Reproduced with permission.[29] Copyright 2014, Nature Publishing Group.

Recently, Lu et al. fabricated a nanoporous silver (np-Ag) catalyst (Figure 11b) that is capable of converting CO_2 to CO with 92% selectivity at a moderate potential of –0.6 V vs RHE.[29] In contrast, as displayed in Figure 11d, the current density of polycrystalline Ag is much lower than that of np-Ag. In combination with an extremely poor FE (1.1%), the partial current density of CO on polycrystalline Ag is about 3000 times lower. However, the electrochemical surface area of np-Ag is only about 150 times larger than polycrystalline silver, meaning that the activity of the catalytic sites on np-Ag is about 20 times higher. It seems plausible that the intrinsically high activity of np-Ag arises from the stabilization of the $CO_2^{\bullet-}$ intermediates on the curved internal surface (Figure 11c). As can be seen from Figure 11e, the Tafel slope of np-Ag is 58 mV dec^{-1}, suggesting a fast initial electron-transfer step before the later rate-determining step, and this again confirms the stabilization of the $CO_2^{\bullet-}$ intermediate on np-Ag. Next, the same group further demonstrated that the low-coordinated surface atoms (steps or edges), which are more prevalent in nanostructured Ag catalysts, should be responsible for the enhanced catalytic activity and selectivity.[95] In fact, as compared to flat Ag surfaces, the activation energy needed to form *COOH intermediates from CO_2 is significantly reduced on these low-coordinated Ag atoms.

Salehi-Khojin et al. also demonstrated that an enhanced CO_2 reduction activity can be accomplished with Ag nanoparticles (NPs).[96] As the particle size decreased, the catalytic activity of the Ag NPs increased first, and then dropped dramatically when the particle size was smaller than 5 nm. In detail, the reaction rate of CO_2 reduction was about 10 times higher on 5 nm Ag NPs than that on the bulk Ag. The authors attributed these changes to the variation in binding energy of the key intermediates. Smaller particles possess higher binding energies than the bulk counterparts; therefore, the intermediates are better stabilized for further reduction, resulting in higher reaction rates. However, once the particles are too small (<5 nm), these intermediates bind too strongly to the surface, making it difficult to release the reaction product. Therefore, for ideal electrocatalysts, the binding strength of key intermediates should be appropriate: neither too strong nor too weak.

Thanks to the high sensitivity of the experimental setup used, 6 different products were observed on the Ag surface by Jaramillo's group.[97] As displayed in **Figure 12**a, H_2 and CO were the major products with a total FE over 90%, while formate, methanol, ethanol, and methane emerged as minor products. Obviously, the applied potential has a great influence on the selectivity between CO and H_2. H_2 dominates at low and high overpotentials, whereas CO surpasses H_2 at intermediate overpotentials. Interestingly, methanol, ethanol, and methane appear in a highly negative range with similar onset potentials, indicating the possibility of a common rate-limiting step. The authors proposed a possible mechanism for the reduction of CO_2 on the Ag surface (Figure 12b). Similar to the aforementioned Cu catalyst, the reaction pathway for CO formation is $CO_2 \rightarrow *CO_2 \rightarrow *COOH \rightarrow *CO \rightarrow CO$. As mentioned before, Ag is a typical group 2 metal that can bind *COOH strongly enough for further reduction to generate the *CO intermediate; therefore, it is quite difficult for formate to desorb easily from the catalyst surface, which makes formate a minor product in

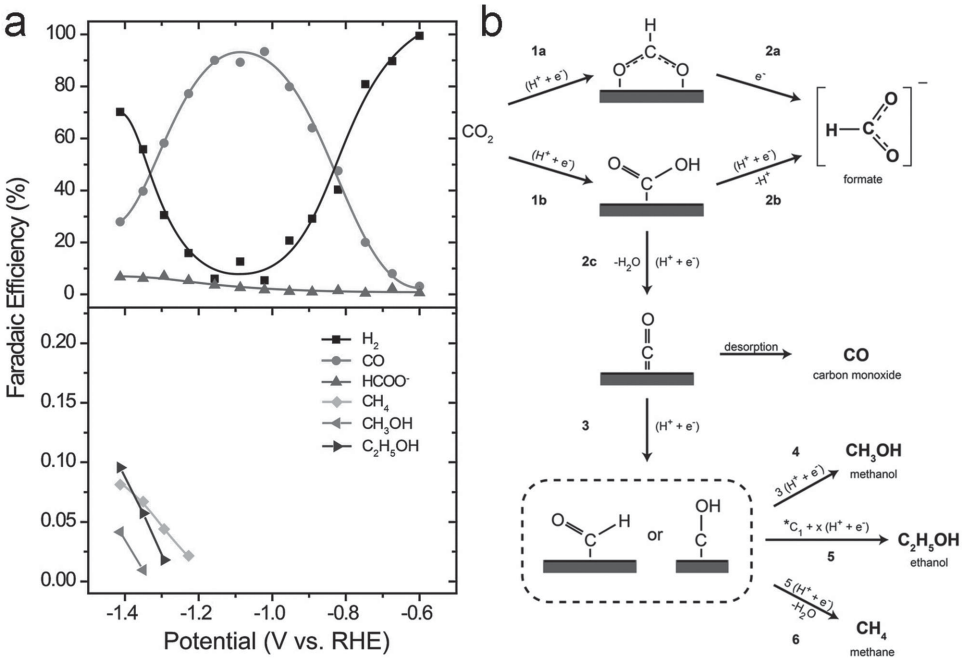

Figure 12. a) FE for each product as a function of potential. b) Possible mechanistic pathways for electrochemical reduction of CO_2 on silver. Reproduced with permission.[97] Copyright 2014, The Royal Society of Chemistry.

CO_2 reduction. Then, as the binding strength between the generated *CO intermediate and the Ag is so weak, CO can desorb easily and appears as the major product. However, because of the weak binding, it is also difficult to stabilize *CO intermediate for further reduction. Therefore, high overpotentials are required to promote the formation of *CHO or *COH intermediates. After this rate-determining step, methanol, ethanol, and methane can be generated by the reduction of *CHO or *COH intermediates. In contrast, the intermediate overpotentials are essential for selective conversion of CO_2 to CO, because they can facilitate the formation of the $*CO_2$ key intermediate without suppressing further CO evolution.

3.1.4. Other Metals

In fact, besides the aforementioned Au, Ag, and Cu electrodes, some other metals like Sn, Pd, Bi, Pb,[92] In,[98] and Pt[99,100] have also been investigated as potential electrocatalysts for CO_2 conversion. To have a better understanding of these metal catalysts, several of them, such as Sn, Pd, and Bi, are presented here.

Sn: In 1994, Hori et al. found that tin (Sn) can selectively convert CO_2 to formate, despite the fact that a high overpotential is required to achieve moderate current densities.[47] Since then, numerous studies on Sn catalyst for CO_2 reduction have been reported.[101–105] Bumroongsakulsawat and Kelsall found that both formate and CO can be obtained by reducing CO_2 on the Sn electrode.[106] Interestingly, the product selectivity was greatly influenced by the electrolyte, and a low pH was preferred for the conversion of CO to formate. The authors proposed that three different intermediates can appear during CO_2 reduction, and a lower pH promotes the protonation of $CO_2^{\bullet-}$ to form $CO_2H_2^{\bullet+}$, which is beneficial for the production of CO. Recently, Medina-Ramos et al. fabricated inexpensive Sn, Bi, Pb, and Sb catalysts by a facile electrodeposition method.[107] The as-fabricated Sn and Bi electrodes were capable of converting CO_2 to CO efficiently with the help of ionic liquids, while Pb was much less active and Sb even showed no activity for CO_2 reduction. In detail, a relatively high FE of CO (about 80%), an enhanced current density (7.2 mA cm^{-2}), and a good stability were achieved simultaneously on the Sn electrode with a small overpotential of about 200 mV. The XPS results indicate that the Sn electrode was composed of Sn^0 and $Sn^{2+/4+}$, and a similar composition has been previously observed on other Sn-based catalysts.[108] As will be discussed later, the catalytic performance of some metal electrodes can be significantly improved by the introduction of suitable metal oxides.

Pd: Palladium (Pd) is generally regarded as a group-2 metal for CO_2 reduction, giving CO as the main reaction product. However, because of the competitive HER, the FE of CO on Pd is below 30%, which is much lower than that of Au and Ag.[47,109] Recently, Gao et al. demonstrated that the catalytic performance of Pd nanoparticles for CO_2 reduction is greatly influenced by the particle size.[110] In general, small Pd NPs showed much higher CO FE and partial current density than large ones. Besides an 18.4-fold enhancement in the partial current density, the FE of CO also increased strikingly from 5.8% (10.3 nm) to 91.2% (3.7 nm) at −0.89V (vs RHE). In contrast to the aforementioned Au NPs, based on the DFT calculations, here both corner sites and edge sites (small Pd NPs) can facilitate CO_2 adsorption and formation of the key intermediate *COOH. Meanwhile, CO_2 prefers to stay away from terrace sites (large Pd NPs), and a higher free energy is required for *COOH formation. Therefore, the size effect observed on Pd NPs is attributed to the different ratios of corner, edge, and terrace sites.

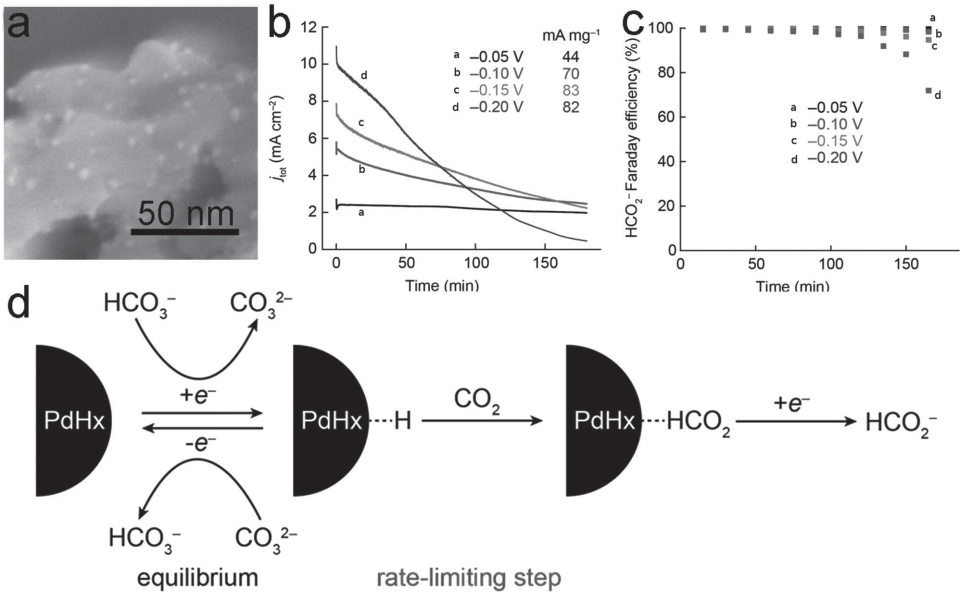

Figure 13. a) SEM image of Pd/C electrode before CO_2 electroreduction. b) Total geometric current density vs time and the mass activity for HCO_2^- synthesis averaged over 3 h. c) HCO_2^- Faraday efficiency vs time in CO_2-saturated 2.8 M $KHCO_3$. d) Electrohydrogenation mechanism for CO_2 reduction on Pd/C. Adapted with permission.[114] Copyright 2015, The American Chemical Society.

Meanwhile, several early studies found that Pd can also selectively convert CO_2 to formate. Unfortunately, the reaction current densities were extremely low, or the Pd electrode deactivated quickly.[111–113] Very recently, Min and Kanan prepared Pd/C electrocatalysts for CO_2 reduction.[114] As displayed in **Figure 13**a, small Pd nanoparticles (5 nm) were well-dispersed on carbon particles. The as-fabricated Pd/C electrode can selectively reduce CO_2 to formate with high current density at a small overpotential (Figure 13b,c). Though the catalyst deactivated significantly during a 3 h experiment, the average mass activity was still as high as 83 mA mg^{-1} at –0.15V vs RHE. Interestingly, based on electrokinetic results, a completely new mechanism for CO_2 reduction to formate was proposed, as shown in Figure 13d. The first step is the formation of Pd hydride on the surface, and then CO_2 is reduced by adsorbed hydrogen in an electro-hydrogenation way. As compared to the formation of $CO_2^{\bullet-}$ intermediates in most cases, this rate-limiting step is more facile to occur, resulting in a low overpotential for CO_2 reduction on Pd. Moreover, the authors attributed the deactivation of the Pd electrode to CO poisoning. By simply removing CO with air exposure, the catalytic activity can be well restored.

Bi: Due to its relatively low price and nontoxic character, bismuth (Bi) has drawn some attention recently as an intriguing electrocatalyst for CO_2 reduction. Dimeglio and Rosenthal electrodeposited a Bi-based material containing metallic Bi^0 and Bi^{3+} ions onto a glassy carbon electrode (GCE).[93] Besides the commonly applied supporting electrolyte consisting of MeCN and $TBAPF_6$ (tetrabutylammonium hexafluorophosphate), ionic liquids (ILs) were also used for CO_2 reduction, as they can help to stabilize the key intermediates. In detail, in combination with $[BMIM]BF_4$, the Bi-modified electrode selectively (95% FE) reduced CO_2 to CO with moderate partial current density (5.51 mA cm^{-2}) at an overpotential below 200 mV.[84] The authors believed that the enhanced catalytic activity may arise from the metastable surface of the Bi^0/Bi^{3+} material, or the interface between Bi^{3+} and Bi^0 sites can further stabilize $CO_2^{\bullet-}$ intermediates.

Then, the same research group obtained Bi-based material from an organic Bi^{3+} precursor by in situ electrodeposition.[94] Significantly, the organic electrolyte used for the fabrication of the aforementioned Bi-based catalyst can be directly used for further CO_2 reduction. Furthermore, the imidazolium-based IL was proved to be bifunctional, since it not only promoted CO_2 activation, but also served as the supporting electrolyte. Thus, without the aforementioned expensive $TBAPF_6$, the as-fabricated Bi-modified electrode was also highly efficient in converting CO_2 to CO. In summary, this relatively inexpensive system exhibited superior electrocatalytic results for CO_2 reduction, such as enhanced partial current density (25–30 mA cm^{-2}), low overpotential (less than 250 mV), and comparable high energy efficiency (nearly 80%) to that of noble metals.

3.1.5. Oxide-Derived Metals

Recently, metallic electrodes derived from corresponding metal oxides have seemed promising to promote catalytic performance for CO_2 reduction. Chen and Kanan found that, as compared with a normal Sn electrode coated with a thin native SnO_x film, an electrodeposited Sn/SnO_x composite exhibited greatly enhanced the current density and Faradaic efficiency for CO_2 reduction.[115] In contrast, an etched Sn electrode with a freshly exposed Sn^0 surface showed an extremely low CO_2 reduction Faradaic efficiency (<1%). Although the exact reaction mechanism on the Sn/SnO_x composite is still to be determined, SnO_x seems to stabilize the $CO_2^{\bullet-}$ intermediate. Moreover, Baruch et al. investigated CO_2 reduction on the native Sn surface

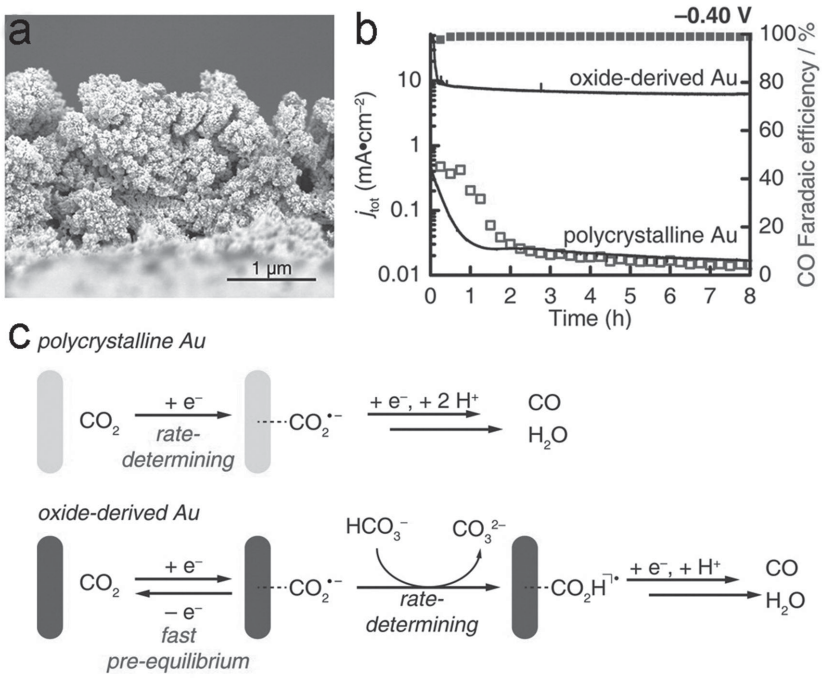

Figure 14. a) Cross-sectional SEM image of the oxide-derived Au NPs. b) Total current density vs time (left axis) and FE for CO production vs time (right axis) on the oxide-derived Au and polycrystalline Au at –0.4V vs RHE. c) Proposed mechanisms for CO_2 reduction to CO on the polycrystalline Au and oxide-derived Au. Reproduced with permission.[119] Copyright 2012, The American Chemical Society.

using in situ attenuated total reflectance infrared (ATR-IR) spectroscopy.[116] The intense peaks in the ATR-IR spectrum indicate the formation of surface-bound tin carbonates. Since $Sn_6O_4(OH)_4$ nanoparticles produced much more formate than SnO_2 nanoparticles at a less-negative potential, Sn^{2+} was proposed to be an active catalytic site for CO_2 reduction. Therefore, the authors suggested that the native surface SnO_2 was reduced to Sn^{2+} species first, and then reacted with CO_2 to form the surface-bound carbonates, which were further reduced to formate. In this case the surface-bound carbonates are regarded as key intermediates, not $CO_2^{\bullet-}$. These results undoubtedly confirm that SnO_x participates in the CO_2 reduction on the Sn surface, suggesting that metal/metal oxide can be an efficient catalyst for CO_2 reduction.

Li and Kanan successfully fabricated an oxide-derived (OD) Cu electrode as a superior CO_2 electrocatalyst, which was formed by in situ electrochemical reduction of the thermally grown Cu_2O layer.[28] The OD Cu electrode (derived from a thick Cu_2O layer formed at 500 °C) was able to efficiently convert CO_2 into CO and HCOOH at a much lower overpotential than polycrystalline Cu. A high current density and a very good stability were also achieved at the same time. These exceptional results may arise from the highly active reaction sites on the grain boundaries formed during conversion of the solid Cu_2O phase to OD Cu.[117] Thus, engineering of metal surfaces to produce enough active catalytic sites, for instance, by reducing thick metal oxide layers to metallic electrodes, can be an attractive approach to boost the catalytic performance. Kas et al. also performed CO_2 reduction on the OD Cu nanoparticles,[118] and found that the thickness of the parent Cu_2O layer dominated the product distribution, while the initial orientation of Cu_2O crystals had only minor influence.

Since then, this fascinating method has been widely used for other metals such as Au,[119] Sn,[31] and Pb.[120] Chen and Kanan obtained the OD Au nanoparticles (**Figure 14**a) by reducing thick Au oxide films.[119] The obtained OD Au electrode showed much higher current density than that of the polycrystalline Au at –0.4 V in Figure 14b. The CO Faradaic efficiency of OD Au was approximately 96%, while the HER took place almost exclusively on the polycrystalline Au electrode. As illustrated in Figure 14c, in the case of polycrystalline Au, the initial electron transfer to CO_2 is the rate-determining step (114 mV dec^{-1}), which needs a high overpotential to overcome the barrier. In contrast, a fast one-electron pre-equilibrium step occurs before the rate-determining one (56 mV dec^{-1}) on the OD Au electrode. The proposed mechanisms suggest that OD Au better stabilizes the key $CO_2^{\bullet-}$ intermediate than the polycrystalline Au does, leading to a greatly enhanced catalytic performance.

Then, the same group reported that OD Pb can largely suppress the HER while maintaining the activity of CO_2 reduction.[120] In fact, the partial current densities of formate on the OD Pb electrode and Pb foil were similar. However, as compared to Pb foil, the OD Pb possessed a 700-fold lower activity for the HER in a 0.25 M Na_2CO_3 electrolyte, leading to a greatly enhanced Faradaic efficiency. Based on the experimental data, the thin metastable Pb oxide formed on the Pb surface should be responsible for the difference in the product selectivity. The Pb oxide seems to be passive for the HER, while the reaction activity for CO_2 reduction is not compromised. Thanks to the high density of defects, the formation of metastable Pb oxide is more facile on OD Pb. Therefore, OD Pb showed higher coverage of Pb oxide, and the selectivity difference actually arose from the coverage difference.

Recently, Zhang et al. synthesized OD Sn by electroreduction of SnO_2 nanoparticles, which were prepared by a hydrothermal method.[31] The as-fabricated OD Sn/carbon black exhibited significantly improved current density as compared with electrodeposited Sn (**Figure 15**a). The current efficiency of formate was also enhanced from 35% (electrodeposited Sn) to 86% (OD Sn derived from 5 nm SnO_2) at –1.8 V. Interestingly, the catalytic performance of OD Sn was heavily dependent on the particle size. As displayed in Figure 15b, the FE value of formate increased with decreasing particle size until a peak value at 5 nm SnO_2 NPs. According to the test of OH^- adsorption, a smaller particle size led to a stronger surface binding strength. It is well known that poor stabilization of the key $CO_2^{\bullet-}$ intermediate means that a high overpotential is needed to conquer the barrier. However, binding $CO_2^{\bullet-}$ too strongly should also be prohibited, since it makes further protonation of $CO_2^{\bullet-}$ and the final product desorption unfavorable. Thus, the

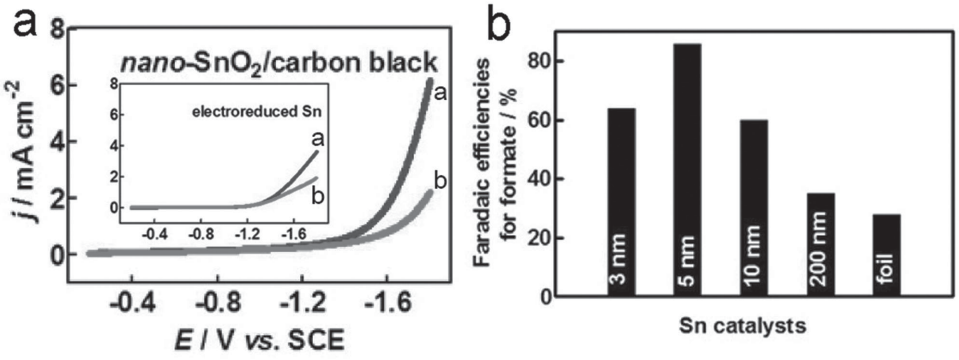

Figure 15. a) Single reductive linear sweep voltammetric scans at 50 mV s^{-1} in 0.1 M $NaHCO_3$ solution saturated with N_2 (line b) and CO_2 (1 atm, line a) at reduced nano-SnO_2/carbon black, and the inset image is at electrodeposited Sn particles. b) Particle-size dependence of FEs for CO_2 reduction to formate on Sn catalysts. Adapted with permission.[31] Copyright 2014, The American Chemical Society.

best catalytic performance was achieved on OD Sn with an optimized binding energy. Moreover, OD Sn/graphene displayed a much higher current density (10.2 mA cm^{-2}) than that of OD Sn/carbon black, due to the stronger electronic interactions between OD Sn and graphene.[121]

However, in contrast to former studies, Kim et al. demonstrated that the metal oxide, which was typically regarded as a starting material for OD metal, also participated in CO_2 reduction.[122] With the help of surface and bulk sensitive techniques, the Cu_2O electrode was found to be only partially reduced during electrolysis, leading to the formation of a Cu_2O surface layer on the top of bulk OD Cu. Besides CO and formate, metallic Cu favors the formation of CH_4, while the Cu_2O electrode (Cu_2O/OD Cu) showed better selectivity toward C_2H_4. The overpotential of the Cu_2O electrode was about 200 mV lower than that of metallic Cu. Though the authors considered that both the surface metal oxide and the bulk metal contributed to these different results, further research is still needed to identify whether the metal, the metal oxide, or the interface between them provides the reaction active sites for CO_2 reduction on the OD metals.

3.1.6. Metal Alloys

As mentioned above, the reaction activity and product selectivity of CO_2 reduction are heavily dependent on the binding strength of the key intermediates. Recently, alloying has drawn much attention, since it can enhance the performance of metal catalysts by tuning the stabilization degree of key intermediates. Xu et al. found that, besides the improved stability of Cu nanoparticles, the incorporation of Au also resulted in lowering the overpotential for CO_2 reduction.[123] Zhao et al. demonstrated that Au_3Cu alloy nanocrystals exhibited larger current densities than Au nanoparticles. Furthermore, the product distribution was also different. Au nanoparticles favored CO formation while Au_3Cu alloy nanocrystals promoted the production of formate, methane and ethylene.[124] Jia et al. also discovered that the enhanced production of highly valued alcohols could be achieved on the nanostructured Cu–Au alloy, and the total FE of methanol and ethanol was nearly 30%.[125]

In order to better understand the fundamentals of alloying for catalysis, Kim et al. tested the performance of CO_2 electrolysis on bimetallic Au–Cu nanoparticle monolayers.[126] Not surprisingly, the number of obtained products increased with increasing Cu content. As displayed in **Figure 16**a, the incorporation of Au promoted CO evolution, and Au_3Cu showed the peak activity for CO generation. Meanwhile, formate, methane, ethylene, and H_2 were suppressed. The authors attributed the preference of CO formation on Au–Cu NPs to both electronic and geometric effects. The lower d-band levels indicate weaker binding on transition metals; according to Figure 16b, the binding strength of *COOH and *CO should shift upwards from Au, Au–Cu, to Cu (electronic effect). Here, the binding strength mainly stems from the interaction between carbon atoms and active reaction sites. Therefore, the reaction activity of CO formation on Au–Cu NPs should lie between Au and Cu. However, this was in contrast to the results shown in Figure 16a, meaning that the catalytic activity of Au–Cu is not only determined by the electronic effect. In fact, the geometric effect caused by the local atom arrangement should also be considered. Due to the fact that Cu atom next to the Au–C bond can possibly form another bond with oxygen from *COOH (Figure 16c), *COOH could be further stabilized. Thus, Au–Cu NPs stabilize *COOH intermediates better than *CO does, which is beneficial for CO formation. Meanwhile, better stabilization of *COOH makes the desorption of formate or formic acid from the surface of Au_3Cu nanoparticles more difficult, which is confirmed by the relatively low turnover of formic acid (see Figure 16c). In summary, thanks to electronic and geometric effects in metal-alloy catalysts, the binding energies of key intermediates can be adjusted, which results in a better catalytic performance than that of monometallic catalysts.

Recently, Guo et al. fabricated monodisperse Cu–Pt nanocrystals (NCs) with different atomic ratios for CO_2 electrocatalysis.[127] Among all the as-fabricated samples, the Cu_3Pt NCs exhibited the highest current density and best selectivity toward CH_4. As mentioned above, the reaction path for the formation of CH_4 on the Cu electrode could be $\rightarrow$ *CO_2 $\rightarrow$ *COOH $\rightarrow$ *CO $\rightarrow$ *HCO $\rightarrow$ ... $\rightarrow$ CH_4. Meanwhile, as a typical electrocatalyst for the HER, Pt shows great affinity for protons. Therefore, the incorporation of Pt was performed to facilitate

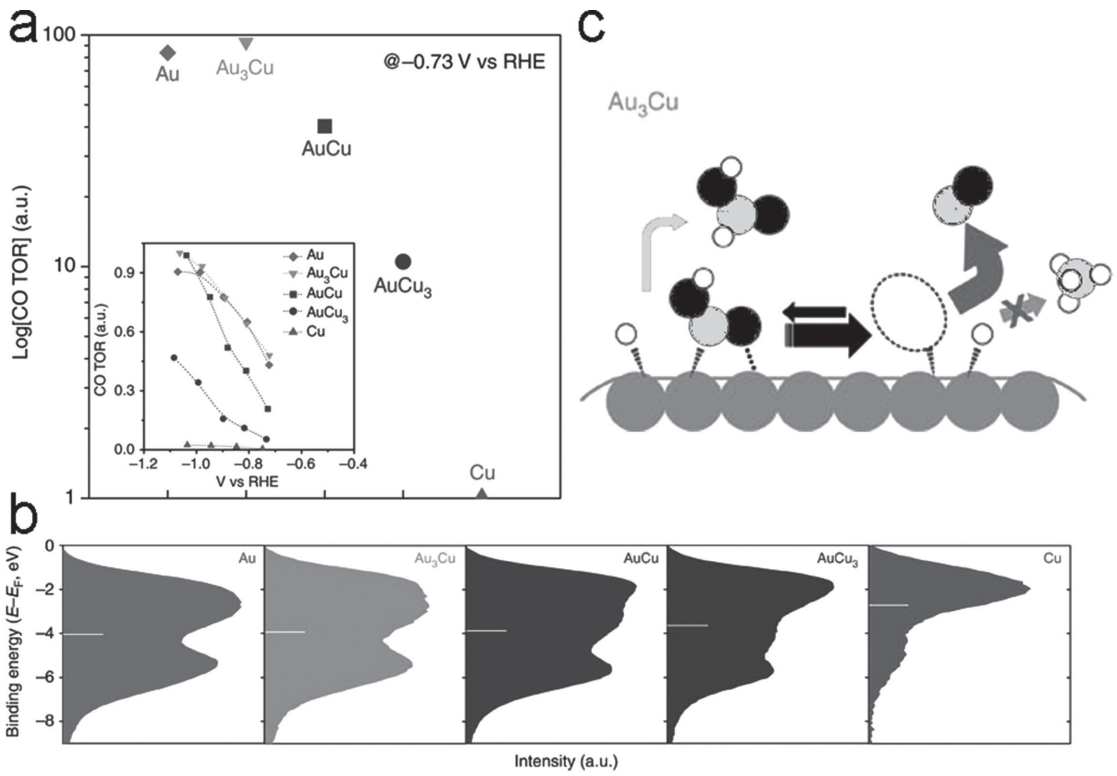

Figure 16. a) Relative turnover rates (TORs) of carbon monoxide compared at –0.73 V vs RHE. The inset shows the relative CO TOR as a function of potential. b) Surface valence-band photoemission spectra of Au–Cu bimetallic nanoparticles. The white bar indicates the center of gravity. c) Scheme showing the proposed mechanism for CO_2 reduction on the catalyst surface of Au_3Cu nanoparticles. The filled circles denote C (light grey), O (black), and H (white). Additional binding between COOH and the catalyst surface is presented as a dotted line. The arrows indicate the pathway to each product: dark gray for CO, light gray for formate, and the crossed arrow for hydrocarbons. Larger arrows indicate higher turnover. Adapted with permission.[126] Copyright 2014, Nature Publishing Group.

protonation of adsorbed *CO, resulting in an enhanced FE for CH_4. However, the atomic ratio of Cu and Pt should be optimized, since too much Pt means a low density of adsorbed *CO intermediates, which certainly limits the catalytic performance of the Cu–Pt NCs. Interestingly, this composition-dependent activity for CO_2 reduction was also demonstrated by others on Cu–Pt alloy nanocubes.[128]

Rasul et al. synthesized a Cu–In bimetallic electrode by electrodepositing In on OD Cu.[129] Besides comparable total current densities with those measured with OD Cu, the as-fabricated Cu–In electrode was able to efficiently convert CO_2 to CO with a high FE of 90% at –0.5 V vs RHE. According to the DFT calculations, In atoms preferred to be at the edge sites of the Cu icosahedron. In contrast to earlier reports, the electronic structure of Cu was only slightly influenced by the incorporation of In. In fact, the presence of In greatly affected the adsorption ability of neighboring Cu, and H adsorption became unfavorable, while the CO adsorption energy was nearly unchanged, leading to better selectivity of the Cu–In electrode toward CO. Thus, Cu–In bimetallic electrocatalysts may have great potential for practical applications in the future since there is no precious-metal component in their structure.

Recently, some computational research on the CO_2 reduction on metal alloys has been reported.[130–133] Hirunsit et al. investigated the performance of Cu-based alloys (Cu_3X) for CO_2 reduction by DFT calculations.[134] The protonation of *CO to produce *COH or *HCO intermediates was regarded as the rate-determining step for most Cu-based alloys, except for Cu_3Au and Cu_3Co. Moreover, alloying had also a great influence on the selectivity between the *COH and the *HCO intermediates. Since a higher degree of electron transfer is needed to form *COH from *CO, stronger *CO adsorption on metal alloys would be beneficial for the formation of *COH. In contrast to pure metals, the catalytic activity of Cu-based alloys did not follow the volcano-type relationship. Such a non-volcano relationship indicates that different Cu-based alloy surfaces favor formation of different intermediates, which diversifies the distribution of products. In other words, as compared to pure Cu catalyst, the CO_2 electroreduction activity and selectivity can be modified by alloying copper with different transition metals. For instance, Cu_3Rh energetically benefits the formation of CH_4, whereas CH_3OH production is more favorable on Cu_3Pd and Cu_3Pt.

To explore potential electrocatalysts that can efficiently convert CO_2 to high-valued methanol, Back et al. took the binding energies of *CO, *OH, and *H intermediates into account.[135] Besides optimal *CO binding energy, *H adsorption strength should be weak enough to suppress unwanted HER. Importantly, the reduction product of $*OCH_3$ is closely related to the *OH binding energy. The weak binding strength of *OH means that $*OCH_3$ can be easily removed to form methanol, while strong binding strength leads to the generation of methane.

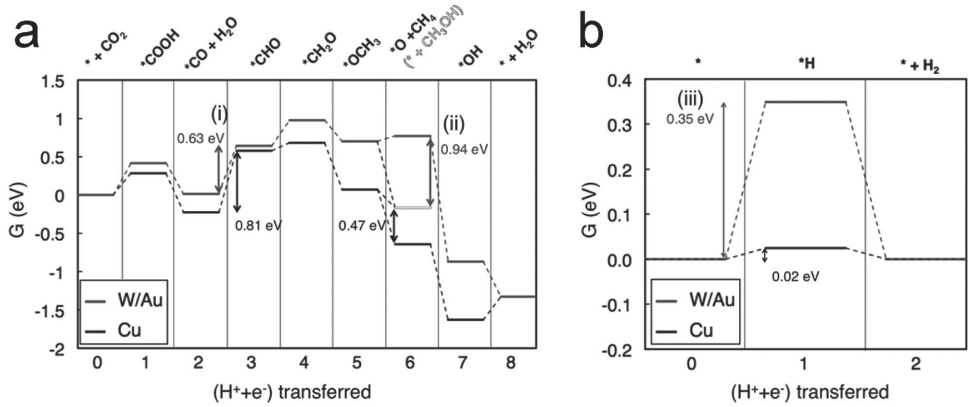

Figure 17. a,b) Free-energy diagram for electroreduction of CO_2 to CH_4 or CH_3OH (shown in light gray) (a) and H_2 evolution reactions at zero electrode potential ($U = 0$ V) for Cu (lower) and W/Au (upper) (b). Each reaction step involves a proton–electron pair ($H^+ + e^-$) transferred from the solution to the electrode. The asterisk alone represents a clean slab, while *CO, for example, represents the CO-adsorbed surface. Adapted with permission.[135] Copyright 2014, The American Chemical Society.

Based on these three criteria, the authors suggested that the W–Au alloy could exhibit better performance than Cu. As displayed in **Figure 17**a, for both W–Au alloy and Cu, the rate-limiting step in CO_2 reduction is the generation of *CHO from the *CO intermediate. The free-energy difference between the W–Au alloy (0.63 eV) and Cu (0.81 eV) indicates that the W–Au alloy has a lower overpotential for CO_2 reduction. The protonation of $*OCH_3$ is regarded as the selectivity-determining step for methanol and methane. Due to the obvious free-energy difference (0.94 eV), the W–Au alloy shows better selectivity toward methanol, while methane is the major product on the Cu electrode. Figure 18b shows that the W–Au alloy (0.35 eV) can efficiently suppress unwanted HER as compared to Cu (0.02 eV). In conclusion, alloying can be effective to promote the performance of metal catalysts when the binding energies are properly adjusted.

3.2. Transition-Metal Oxides

As mentioned above, a variety of metal electrodes have been investigated for CO_2 electrolysis. Meanwhile, only a few transition-metal oxides such as TiO_2, FeO_x, and Cu_2O, etc. have been reported as potential electrocatalysts for CO_2 reduction.[136–139] Furthermore, most of them exhibited reasonable catalytic performance only in the presence of organic solvents. Chu et al. confirmed that a nanostructured TiO_2 film (n-TiO_2) was able to convert CO_2 to low-density polyethylene (LDPE) with a moderate current efficiency (14%) in [EMIM]BF_4-H_2O solution.[140] The authors proposed that Ti^{4+} was reduced to Ti^{3+} species first, then it reacted with CO_2 to form $CO_2^{\bullet-}$ intermediates. An ionic liquid could promote the formation of *CO from the $CO_2^{\bullet-}$ intermediates, while the high pressure induced by the unique nanoporous structure of the TiO_2 film helped to polymerize $*CH_2$ to LDPE. Then, Ramesha et al. again demonstrated that the electrocatalytic ability of n-TiO_2 originated from the Ti^{3+} sites, which were converted from Ti^{4+}.[141] The interaction between CO_2 and catalytically active Ti^{3+} sites made the initial one-electron transfer step more facile. Here, methanol was obtained on n-TiO_2 with high FEs (nearly 90%) in organic solution. Interestingly, the introduction of small cations restrained the performance of n-TiO_2 due to their possible interaction with Ti^{3+} sites,[142] making them unavailable for CO_2 reduction.

Recently, Ma et al. synthesized a Ag–TiO_2 composite as an electrocatalyst for CO_2 reduction (**Figure 18**a).[143] Excellent catalytic results including a high FE of CO (>90%) and a remarkable CO partial current density (>100 mA cm^{-2}) were achieved with the Ag–TiO_2 composite in aqueous solution. Importantly, the performance of Ag–TiO_2 was comparable to that of unsupported Ag nanoparticles, meaning that the Ag loading can be significantly reduced (Figure 18b). In contrast, it is difficult to reduce CO_2 on a bare TiO_2 electrode in aqueous solution. The synergistic effects between TiO_2 and Ag are responsible for the CO_2 reduction. As illustrated in Figure 18c, Ti^{III} species generated by the reduction of TiO_2 not only facilitate the formation of the key $CO_2^{\bullet-}$ intermediates, but also improve their stabilization. Then, Ag nanoparticles adhered on TiO_2 further reduce the $CO_2^{\bullet-}$ intermediate to CO. Thus, metal/metal-oxide hybrids seem to be fascinating candidates for efficient reduction of CO_2 at acceptable costs. Moreover, TiO_2 is also regarded as a typical photocatalyst for CO_2 reduction.[144–146] Therefore, in spite of the great challenges ahead, it seems quite attractive to reduce CO_2 in a photochemically assisted electrocatalytic way.

Tin oxides have been reported to catalyze the CO_2 reduction on Sn electrodes. However, only a few studies on tin (IV) oxide (SnO_2) for CO_2 electrolysis have been reported, possibly due to the fact that SnO_2 can be readily reduced to metallic Sn. Recently, Lee et al. investigated CO_2 reduction on SnO_2 nanocatalysts.[147] Interestingly, it was demonstrated that both the pH of the electrolyte and the applied potentials can be optimized to achieve a high catalytic activity and good stability on SnO_2. In detail, the SnO_2 electrode stayed intact at high pH values, while it was reduced in situ to Sn at pH 8.42. Moreover, the SnO_2 electrode exhibited a better performance than Sn at pH 10.2 and –0.6 V (vs RHE), as evidenced by the higher FE (67.6%) for formate and better stability. In fact, the equilibrium concentrations in the CO_2-HCO_3^--CO_3^{2-} system were determined by the pH values of the electrolyte. The relatively high concentration of HCO_3^- species at pH 10.2 contributed to the better selectivity for formate, as formate was predominantly

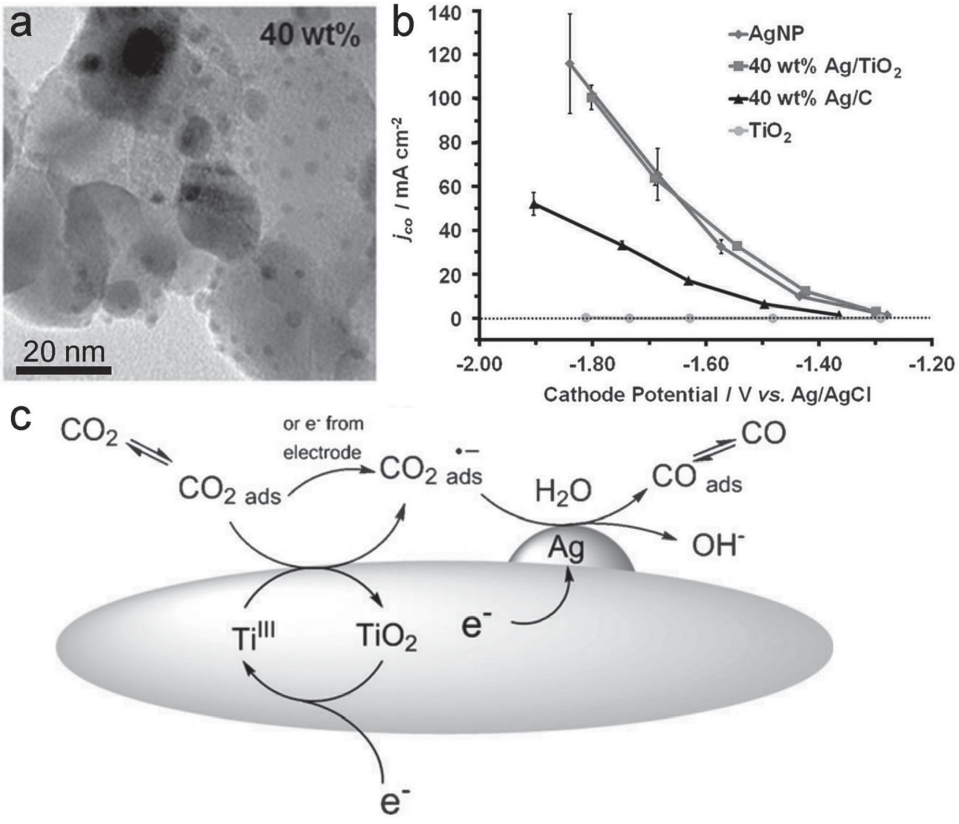

Figure 18. a) TEM image of 40 wt% Ag/TiO_2: the dark spheres or dots are Ag particles and the larger gray structures denote TiO_2. b) Partial current density for CO production on four catalysts: 40 wt% Ag/TiO_2, 40 wt% Ag/C, Ag NP, and TiO_2. c) A schematic diagram of the proposed pathway for CO_2 reduction to CO on the Ag/TiO_2 catalyst. Reproduced with permission.[143] Copyright 2014, Wiley-VCH.

generated by the reduction of HCO_3^-, whereas CO was formed through CO_2 reduction.[148] In contrast to the metal electrodes mainly used in neutral or near-neutral solutions, some metal oxides prefer alkaline conditions to achieve better activity and structure stability.

Recently, molybdenum dioxide (MoO_2) was also identified as a promising electrocatalyst for CO_2 reduction in organic solutions by Oh et al.[149] Not surprisingly, both the temperature and the water concentration in organic solvent influenced the catalytic performance of the MoO_2 microparticles. Formate and oxalate were shown to be the major products at room temperature, whereas CO and oxalate were generated with greatly enhanced current densities at –20 °C. The product distribution could be also adjusted by water concentration, although the catalytic activity would be partially compromised. Furthermore, the authors also proved that the catalytic ability originated from the MoO_2 microparticles, rather than from the metal Mo nanoparticles formed in situ. Sekimoto et al. found that doped gallium oxide (Ga_2O_3) could efficiently convert CO_2 to formic acid with high FEs exceeding 80%.[150] In fact, Sn and Si dopants mainly contributed to the improved conductivity of Ga_2O_3, while the Ga_2O_3 itself could effectively reduce CO_2. As indicated by DFT calculations, formate ($HCOO\text{-}Ga_2O_3$) was considered to be the key intermediate for CO_2 reduction on Ga_2O_3, and the stable state of the adsorbed formate was responsible for the good selectivity to formic acid.

3.3. Transition-Metal Chalcogenides

Transition-metal chalcogenides (TMCs) are chemical compounds consisting of at least one transition-metal element and one chalcogen anion. Due to their occurrence in many stoichiometries (such as monochalcogenides (e.g., ZnS), dichalcogenides (e.g., MoS_2), trichalcogenides (e.g., MoS_3), and tetrachalcogenides (e.g., VS_4)) and structures, TMCs have been widely studied during the past several decades.[151–155] Although oxygen belongs to group VIA of the periodic table, which is also defined as a chalcogen group; the term chalcogenide generally refers to sulfides, selenides, and tellurides, rather than oxides. Consequently, it is necessary to discuss this group of materials individually. To the best of our knowledge, it is also the first summary of TMCs as electrocatalysts for CO_2 reduction.

In 1997, Hara et al. investigated the effect of adsorbed sulfide ion (S^{2-}) on metal electrodes (i.e., Fe, Ni, Pd, Cu, Zn, Ag, and Pt) on the electrochemical reduction of CO_2.[156] Their study showed that the product selectivity could be changed markedly after treating metal electrodes with Na_2S aqueous solution. According to the current–potential curve, the authors speculated that S^{2-} adsorbed on the surface of metal electrodes could prevent the formation of adsorbed CO. However, the conclusion was only based on the electrochemical investigation without additional characterization of the treated metal electrodes. Probably, due to the Na_2S treatment, the surface

of metal electrodes was partially oxidized into sulfides, which resulted in a different product selectivity. Direct evidence for such behavior was the color change of the electrodes, especially Cu and Ag electrodes whose surfaces changed to gray and black, respectively. Obviously, more efforts should be devoted to the study of TMC electrocatalysts.

Unfortunately, TMCs as electrocatalysts for CO_2 reduction have not received much attention, although chalcogenides are well known due to the abundance of diverse metal ores on the planet. For example, it was recently found that black smokers in deep-sea hydrothermal vents contain plenty of transition-metal sulfides, such as $CuFeS_2$ and FeS_2. More importantly, such a discovery led to a hypothesis to uncover the chemical evolution in the prebiotic ocean and the early evolution of energy metabolism in ancient Earth, that is, the transition-metal sulfides are likely to serve as electrocatalysts for CO_2 reduction at the interface between the vent and the cold ocean.[157,158] To validate such a hypothesis, Yamaguchi et al. synthesized iron sulfide and Ni-containing iron sulfides via a hydrothermal method and evaluated their energetics for electrocatalytic CO_2 reduction by mimicking the CO_2-saturated ancient ocean.[158] As expected, the as-synthesized Fe_3S_4 (greigite) exhibited some electrocatalytic activity to reduce CO_2 into CO and CH_4. Namely, as compared to pure FeS, the poly(allylamine hydrochloride) (PAH)-modified $FeNi_2S_4$ (violarite) showed much better efficiency (ca. 85 fold) and selectivity for CO_2 reduction. Evidently, all these results point out that the Ni-doped FeS can function as an efficient electrocatalyst for CO_2 reduction, thereby demonstrating the validity of the aforementioned hypothesis. Due to the fact that CO_2 in the ancient ocean could be effectively be reduced into CO and CH_4 naturally, clarification of the role of TMCs in CO_2 electroreduction is crucial for the fixation of CO_2 in the future.

As a new class of two-dimensional layer-structured materials, transition-metal dichalcogenides (MX_2) show great potential for diverse applications such as hydrodesulfurization, sensing, catalysis, and energy storage.[159–162] The versatility of MX_2 originates from their unique crystalline and electronic structure. Specifically, each single sheet of MX_2 is composed of a layer of metal atoms sandwiched between two layers of chalcogen atoms by covalent bonding, and adjacent MX_2 sheets stack via van der Waals interactions.[161] Interestingly, the conductivity and catalytic ability of transition-metal dichalcogenides can be different for various polymorphs. Lukowski et al. found that the semiconducting 2H-MoS_2 phase could be converted to metallic 1T-MoS_2 with greatly enhanced catalytic activity by chemical exfoliation.[163]

Among the various MX_2 species, MoS_2 is of particular interest due to its abundance, low price, facile synthesis, and prominent catalytic features. During the last decade, MoS_2 has been widely employed as a catalyst for the HER, the ORR, and water splitting.[164–166] Despite its highlighted applications in these fields, only a few reports are available on its electrocatalytic performance toward CO_2 reduction. Using DFT, Chan et al. discussed the possibility of using MoS_2 and $MoSe_2$ as electrocatalysts for CO_2 reduction.[167] Importantly, the DFT calculations indicated that the edge sites in MoS_2 and $MoSe_2$, namely, the bridging S and Se atoms respectively, could selectively bind the key CO_2 reduction intermediates (i.e., *COOH and *CHO) and promote subsequent reaction steps, whereas CO could be effectively bound on the edge metal atoms in MoS_2 and $MoSe_2$ and possibly further reduced to hydrocarbons and/or alcohols. These results theoretically predicted superior CO_2 reduction activity over many transition-metal catalysts. Moreover, Ni-doped MoS_2 was also studied due to the fact that the S edge could be easily doped with transition metals to intentionally tune the binding energies of the intermediates. In this case, both the number of S edges and the binding energy of the CO intermediate are reduced, thus making CO_2 reduction possible. In order to design catalysts for CO_2 reduction with better efficiency and selectivity, the authors pointed out that the edge sites should be maximized and particular edges should be also stabilized.

Inspired by the fact that MoS_2 shows a very good performance for water splitting comparable to that of Pt catalysts,[168–170] Asadi et al. studied electrochemical CO_2 reduction on the Mo-terminated edges of MoS_2 (**Figure 19**a,b) in EMIM-BF_4.[34] Unsurprisingly, the layer-stacked bulk MoS_2 with Mo-terminated edges displayed an excellent CO_2-reduction performance in terms of the current density (65 mA cm^{-2} at −0.764 V vs RHE), overpotential (ca. 54 mV), FE (ca. 98% for CO at −0.764 V vs RHE), selectivity, and stability, which were superior with respect to Ag NPs and the bulk Ag (Figure 19c). These experimental findings also verified the theoretical prediction by Chan et al.[167] Moreover, DFT calculations revealed that the superior catalytic performance can be attributed to the metallic character, low work function (3.9 eV) and the high d-electron density on the Mo-terminated edges of MoS_2, which is almost one order of magnitude higher than that of Ag atoms on the surface of Ag film. To authenticate their understanding and further improve the performance of MoS_2, the authors then synthesized vertically aligned MoS_2 nanosheets with more available Mo atoms on the edges as active sites (Figure 19d,e). As expected, a further improvement in the CO_2 reduction current density (i.e., 130 mA cm^{-2} at −0.764 V vs RHE) was observed for the vertically aligned MoS_2 (Figure 19f). All these theoretical and experimental reports demonstrate the potential of MX_2 as novel and advanced electrocatalysts for CO_2 reduction. Nevertheless, the current research on MX_2 as a CO_2-reduction electrocatalyst is very limited and only focused on MoS_2. More extensive studies directed toward other MX_2 such as $MoSe_2$ and WS_2 would be desirable. A better understanding of the catalytic mechanism on MX_2 is urgently needed to open new avenues for the development of improved electrocatalysts for CO_2 reduction.

3.4. Carbon-Based Materials

In addition to transition metals and transition-metal compounds as electrocatalysts for CO_2 reduction, renewable metal-free catalysts, especially nanocarbon-based catalysts, have become increasingly attractive because of their distinct properties over conventional CO_2 electrocatalysts. One of the most prominent features of these catalysts is the ability of carbon atoms to assemble into a variety of nanocarbon materials with different dimensions and structures, for example, one-dimensional carbon nanotubes (CNT) and carbon nanofibers (CNF), and two-dimensional graphene. More importantly,

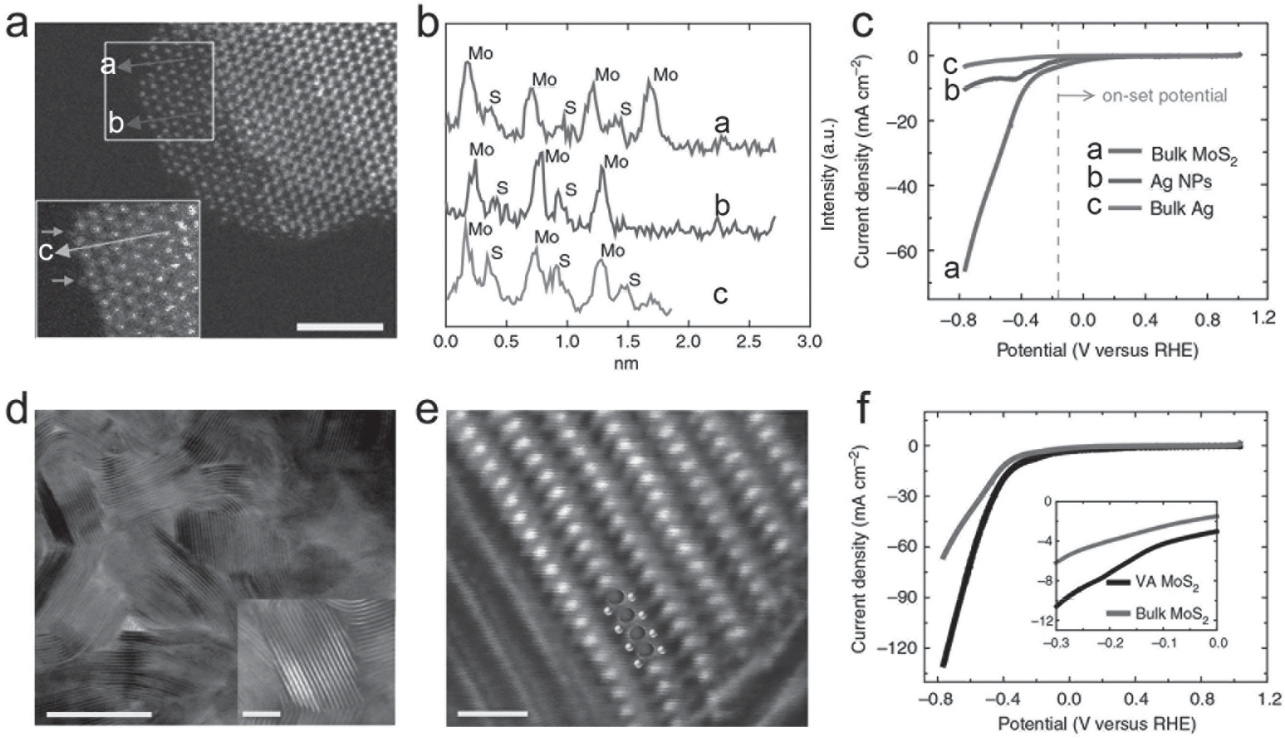

Figure 19. a) Raw grayscale high-angle annular dark-field (HAADF) and low-angle annular dark-field (LAADF) image (inset) of MoS_2 edges (scale bar, 5 nm). b) The line scans (arrows a and b toward edges) identifying Mo atoms to be the terminating atoms. An additional light atom (arrow c line scan) occupying what should be a Mo position, most probably a carbon atom, from the STEM substrate. c) Cyclic voltammetry (CV) curves for bulk MoS_2, Ag NPs, and bulk Ag performed in CO_2-saturated 96 mol% water and 4 mol% EMIM-BF_4 solution. d) Annular bright-field (ABF) STEM images of vertically aligned MoS_2 (scale bar, 20 nm). STEM analysis (inset) showing the vertically aligned texture of MoS_2 nanoflakes (scale bar, 5 nm). e) High-resolution HAADF STEM image of vertically aligned MoS_2 (scale bar, 2 nm). Mo atoms are brighter and larger in size in comparison to sulfur atoms due to high atomic number. f) CO_2 reduction performance of the bulk MoS_2 and vertically aligned MoS_2 represented by VA MoS_2. Adapted with permission.[34] Copyright 2014, Nature Publishing Group.

these nanocarbon materials possess many intrinsic advantages, including high surface area, outstanding conductivity, excellent chemical stability, and remarkable mechanical strength, which are expected to boost the catalytic performance for electrochemical CO_2 reduction. Besides, they are inexpensive, environmentally friendly and easily available at large quantities. However, pure nanocarbon materials possess a very small catalytic activity toward electrochemical CO_2 reduction because the neutral carbon atoms show negligible ability to activate CO_2 molecules or adsorb the $CO_2^{-\bullet}$ intermediate. Fortunately, it is easy and effective to manipulate the structure and chemical state of nanocarbon materials by introducing heteroatoms (e.g., B, N, P, and S) during the synthesis process or post-treatment, thus changing the atomic charge and spin density of some carbon atoms as active sites for CO_2 reduction. From the standpoint of materials engineering, this class of materials is ideal for the design of future electrocatalysts, capable for converting CO_2 into desired products with high efficiency and selectivity.

Recently, Kumar et al. reported polyacrylonitrile-based heteroatomic CNFs as renewable and metal-free electrocatalysts for CO_2 reduction, which exhibited remarkable catalytic ability for selective reduction of CO_2 to CO at very low overpotential (0.17 V) (**Figure 20**a).[33] As compared to the bulk Ag and Ag nanoparticles (200, 40, and 5 nm), the as-prepared CNFs achieved a highest current density that was ca. 13 times and 4 times higher than those of the bulk Ag and 5-nm Ag nanoparticles, respectively (Figure 20b). To elucidate the CO_2-reduction mechanism, they further examined and carefully compared the X-ray photoelectron spectra (XPS) of N_{1s} in CNFs before and after electrochemical CO_2 reduction (Figure 20c,d). It was found that the peak area of the pyridinic nitrogen remained almost constant, eliminating the possibility of the direct participation of nitrogen heteroatoms in the CO_2 reduction. Conversely, this comparison proved that the oxidized carbon atoms in the CNFs are responsible for the CO_2 reduction. On the basis of XPS analysis and previous reports, the authors proposed a possible reaction mechanism for the CO_2 electroreduction in the EMIM-BF_4 ionic-liquid electrolyte (see Figure 20g). Specifically, the oxidized carbon atoms are initially reduced during a redox cycling process. The dissolved CO_2 molecules coordinate with EMIM cations to form an intermediate EMIM---CO_2 complex, which then adsorb on the reduced carbon atoms. Next, the reduced carbon atoms are reoxidized to their initial state, which is accompanied by CO_2 reduction to CO. Finally, the produced CO is released. During this heterogeneous catalysis process, the active carbon atoms are renewable to maintain the catalytic activity of CNFs. In conclusion, the catalytic proficiency of the as-prepared CNFs can be attributed to the redistribution of charge and spin density owing to the interaction between the doped nitrogen atoms and their adjacent carbon atoms.

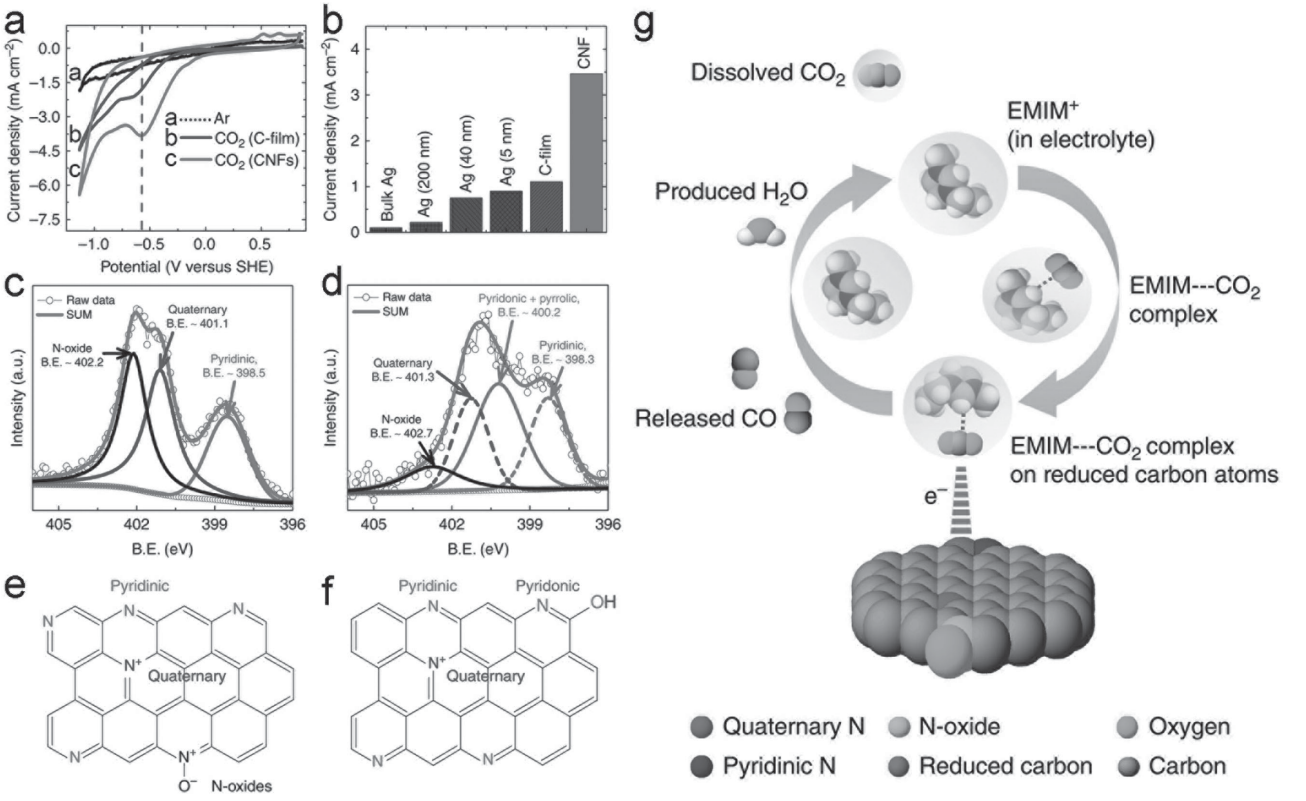

Figure 20. a) CVs for CO_2 reduction in Ar-saturated (curve a) and CO_2-saturated pure EMIM-BF_4 on a carbon-film electrode (curve b) and CNF electrode (curve c). b) Absolute current density for CO_2 reduction on different electrodes in EMIM-BF_4 electrolyte. c,d) Deconvoluted N1s spectra of CNFs before (c) and after (d) electrochemical experiments. e,f) The corresponding atomic structure on the basis of XPS analysis. g) Schematic illustration of the CO_2 reduction mechanism. Adapted with permission.[33] Copyright 2013, Nature Publishing Group.

More recently, Zhang et al. fabricated polyethylenimine-functionalized N-doped graphenated carbon nanotubes (denoted as PEI-NGCNT) with a 3D hierarchical structure for electrochemical CO_2 reduction to formate.[32] Under optimum conditions, the FE for formate could achieve 85% with a high current density up to 9.5 mA cm^{-2}. The PEI layer greatly intensifies CO_2 adsorption with high capacity and selectivity. As a co-catalyst, PEI also significantly reduces the catalytic overpotential by helping to stabilize the $CO_2^{\bullet-}$ key intermediates together with N-doped carbon, resulting in an improved FE, as well as a higher current density. More interestingly, the outstanding electrocatalytic performance correlates with the synergistic effects between N-doping and the PEI overlayer. In fact, a PEI layer can boost the performance of carbon materials only in the presence of N-doping. This study shows that, besides heteroatom doping, functionalization of nanocarbon materials by means of organic molecules with high adsorption affinity and selectivity toward CO_2 can be another effective strategy to further maximize the performance of electrocatalytic CO_2 reduction.

Wu et al. synthesized heavily N-doped CNTs (NCNTs) arrays by a liquid CVD method to obtain a highly efficient, selective, and stable catalyst for electrocatalytic reduction of CO_2 to CO.[171] The multiwalled NCNTs are bamboo-shaped with a homogeneous N distribution and a total N content up to 5 atom% (**Figure 21**a–c). Specifically, the N configurations are pyridinic, pyrrolic, and graphitic with N contents of 1.5, 1.1, and 2.4 atom%, respectively (Figure 21d,e). Unprecedented overpotential (–0.18 V) and selectivity toward production of CO (80%) have been observed on the as-obtained NCNTs. Based on the computational hydrogen electrode (CHE) model and DFT simulations, the binding energies of *COOH and *CO were calculated in an attempt to address the significant role of the N dopant and understand the mechanism of CO_2 electroreduction to CO (Figure 21f). Intriguingly, the most preferable and selective site toward CO production is pyridinic N because it possesses the strong COOH binding and facilitates CO desorption at the same time. Meanwhile, both pyrrolic N and graphitic N also display better activity and selectivity than that of pristine CNTs. Undoubtedly, these experimental and theoretical findings definitely shed some light on the design and modification of carbon nanostructures to further enhance the electrocatalytic reduction of CO_2.

Moreover, Nakata et al. reported that the boron-doped diamond (BDD) is capable of reducing CO_2 to HCHO with high FE (74%).[172] Interestingly, the electrolyte used can be methanol, aqueous NaCl, or even seawater. HCHO is proposed to form as follows:

$$CO_2 + 2H^+ + 2e^- \rightarrow HCOOH \quad \text{(R9)}$$

$$HCOOH + 2H^+ + 2e^- \rightarrow HCHO + H_2O \quad \text{(R10)}$$

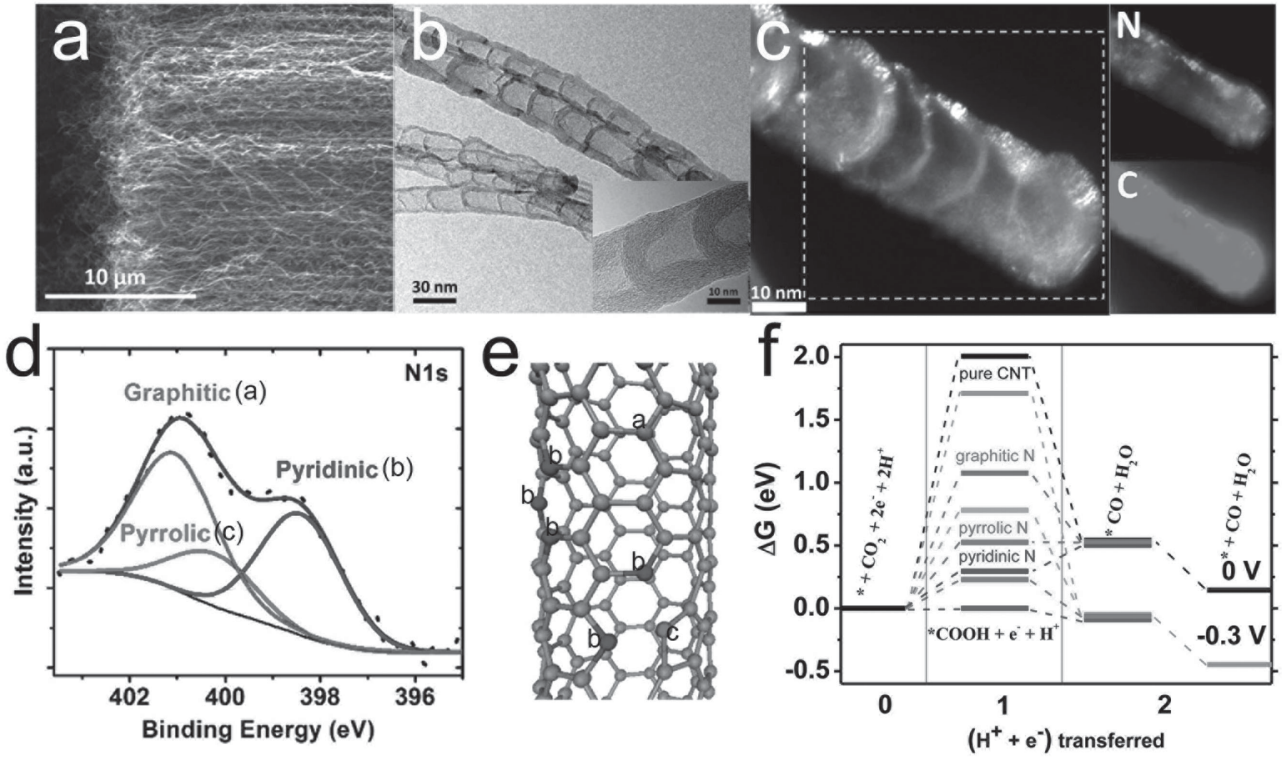

Figure 21. a) SEM images of NCNTs. b) TEM images of NCNTs (the inset shows a single multiwall NCNT). c) Electron energy loss spectroscopy (EELS) elemental mapping of N and C. d) Representative XPS of N 1s for NCNTs. The N 1s spectrum is deconvoluted into three peaks representing three different N functionalities. e) Schematic illustration of graphitic (a), pyrrolic (b), and pyridinic (c) N configurations. f) The calculated free-energy diagram for CO_2 electroreduction to CO on pristine CNTs and NCNTs. Adapted with permission.[171] Copyright 2015, The American Chemical Society.

The BDD electrode can effectively reduce CO_2 to HCHO due to the presence of sp^3-bonded carbon atoms. As compared to the sp^2-bonded carbon atoms in glassy carbon, they are particularly effective in the process of converting HCOOH to HCHO. Meanwhile, the intrinsic wide potential window of BDD can greatly suppress the HER, making it promising for practical applications.

4. Conclusions and Outlook

CO_2 electroreduction has attracted great attention because of the following advantages: i) the level of atmospheric CO_2 can be greatly reduced to alleviate various unfavorable effects caused by global warming; ii) the reaction products generated in CO_2 electroreduction are useful chemical feedstocks or fuels, which can probably help to mitigate the energy crisis; iii) it is a convenient way to store renewable electricity in high-energy-density chemical forms. Due to the intrinsic inertia of CO_2 molecules, highly efficient and robust electrocatalysts are required to promote this sluggish reaction. These catalysts can significantly reduce the reaction barriers for CO_2 reduction by helping to stabilize the key reaction intermediates. Different catalysts tend to bind various intermediates to a different extent, leading to the generation of diverse products. In other words, by rational design of the catalysts, it is possible to selectively reduce CO_2 to desirable products. In order to stimulate further research interest in this area, a timely and comprehensive overview of inorganic heterogeneous electrocatalysts for CO_2 reduction is presented here. According to the elemental composition, these catalysts can be categorized into four groups: metals, metal oxides, metal chalcogenides, and carbon-based materials. **Table 1** illustrates the most recent achievements in the development of electrocatalysts for CO_2 reduction.

Recently, due to the enormous potential rewards, extensive experimental and computational studies have been done to accelerate the development of electrocatalysis for CO_2 reduction. However, in spite of the great efforts, it still seems quite challenging to efficiently reduce CO_2 to desirable products. In fact, the current catalytic technologies in this area are far from the requirements for widespread applications. Scientific problems including high overpotential, low catalytic activity, poor product selectivity, and unsatisfactory catalyst stability still require further attention. Importantly, for electrochemical CO_2 reduction, the binding strength of various reaction intermediates to electrocatalysts is the key factor governing the catalytic activity and final distribution of products. Therefore, it should be seriously taken into consideration during design of high-performance electrocatalysts for CO_2 reduction. In view of the former research devoted to CO_2 electroreduction and other energy-related topics, we propose several major strategies to boost the performance of heterogeneous electrocatalysts:

i) Surface engineering. The electrocatalyst surface has a great impact on the final catalytic performance, especially for metal catalysts. As compared to metals with smooth surfaces, their

Table 1. The performance of recently reported electrocatalysts for CO_2 reduction.

Electrode	Potential vs RHE [V]	Current Density [mA cm^{-2}]	Products (Faradaic Efficiency [%])	Electrolyte	Reference (Year)
Cu (10 nm)	−1.1	20	H_2 (64%), CO (22%), CH_4 (10%), C_2H_4 (4%)	0.1 M $KHCO_3$	[80] (2014)
Cu	−1.25	9	CH_4 (80%), H_2 (13%)	0.1 M $NaHCO_3$	[81] (2014)
Ag	−0.60	18	CO (92%)	0.5 M $KHCO_3$	[29] (2014)
Ag	−1.35	10	H_2 (55%), CO (40%)	0.1 M $KHCO_3$	[97] (2014)
Au (8 nm)	−0.67		CO (90%)	0.5 M $KHCO_3$	[30] (2013)
Au	−0.35		CO (94%)	0.5 M $KHCO_3$	[84] (2014)
Au (3.2 nm)	−1.2	100	H_2 (80%), CO (20%),	0.1 M $KHCO_3$	[85] (2014)
Au	−0.45		CO (90%)	0.5 M $NaHCO_3$	[88] (2015)
Pd (3.7 nm)	−0.89	9	CO (91.2%)	0.1 M $KHCO_3$	[110] (2015)
Pd	−0.15	7	Formate (95%)	2.8 M $KHCO_3$	[114] (2015)
OD Au	−0.4	10	CO (98%)	0.5 M $NaHCO_3$	[119] (2012)
OD Cu	−0.5	2.7	CO (40%), HCOOH (33%)	0.5 M $NaHCO_3$	[28] (2012)
Sn/SnOx	−0.7	1.8	CO (58%), HCOOH (40%)	0.5 M $NaHCO_3$	[115] (2012)
Sn/graphene	−1.16	10.2	Formate (93.6%)	0.1 M $NaHCO_3$	[31] (2014)
Au_3Cu	−0.73	3	CO (64.7%), formate (3.11%)	0.1 M $KHCO_3$	[126] (2014)
Cu–In	−0.6	1	CO (38%), HCOOH (34%)	0.1 M $KHCO_3$	[129] (2015)
Ag/TiO_2	−0.8	101	CO (>90%)	1 M KOH	[143] (2014)
MoS_2	−0.764	65	CO (98%)	H_2O/EMIM-BF_4	[34] (2014)
PEI-NCNT	−1.16	7.2	Formate (85%)	0.1 M $KHCO_3$	[32] (2014)
CNF	−0.25	4	CO	EMIM-BF_4	[33] (2013)
BDD	−0.9	0.08	HCHO (65%), HCOOH (14%)	0.1 M MeOH (TBAP)	[172] (2014)
NCNT	−0.28	0.9	CO (80%)	0.1 M $KHCO_3$	[171] (2015)

roughened counterparts have higher current densities due to the larger electrochemical active surface area. More importantly, the roughened surfaces possess significantly more low-coordination sites (edges, steps, defects) than smooth ones, which have better intrinsic reaction activity for CO_2 reduction. Besides the surface morphology effect, surface impurities and metal overlayers should also be considered. Meanwhile, the OD metal method has been also successfully applied to obtain various metals like Cu, Sn, Au, and Pb, showing a greatly enhanced catalytic activity. Although no definite mechanism has been confirmed yet, it seems plausible that high densities of grain boundaries are produced during metal formation through the constrained metal-oxide lattice, and the highly active sites present on the formed grain boundaries contribute to the enhanced CO_2 reduction activity.

ii) Chemical modification. Since Gong et al. discovered that N-doped carbon nanotube arrays exhibited superb ORR performance,[173] doped carbon materials have been extensively investigated as electrocatalysts for the ORR, OER, and HER.[174–178] In contrast, pure carbon materials show a very small catalytic activity. Recently, N-doped carbon materials have been demonstrated to be efficient electrocatalysts for CO_2 reduction, as discussed in Section 3.4. Moreover, the improved catalytic activities of the metal alloys clearly show the importance of chemical modification. Thanks to the electronic and geometric effects, the binding strengths of different intermediates to metal alloys can be adjusted to the appropriate values, leading to better catalytic performance than monometallic catalysts. Moreover, according to computational simulations, Lim et al. also found that p-block dopants in metals can effectively modulate the reaction energetics.[179] Thus, sulfur- and arsenic-doped Ag are expected to have both low overpotential and satisfying stability for CO_2 reduction, again confirming the significance of chemical modification.

iii) Nanostructured catalysts. Nanotechnology has been extensively employed in the energy storage (Li-ion batteries, supercapacitors, metal–air batteries, etc.) and catalysis (electrocatalysis, photocatalysis, etc.) fields for a long time.[180–185] Meanwhile, it is well known that the activity of electrocatalysts is closely related to both the number of total surface active sites and the intrinsic activity of each reaction site.[186] For CO_2 electroreduction, despite some debate still going on, nanostructuring has been proved to notably improve the catalytic performance in most cases. Not surprisingly, nanostructured catalysts usually possess larger electrochemical surface area than the bulk materials, resulting in a larger amount of catalytically active sites. More importantly, nanostructured catalysts have a great portion of low-coordinated (corner, edge and step) sites whose catalytic behavior is distinct from the fully coordinated sites of bulk materials.[187] Considering the continuous improvement in the technology to synthesize nanomaterials, further nanostructured materials (such as nanowire arrays, core–shell structures, mesoporous films,

hollow structures, etc.) can be developed as promising electrocatalysts for CO_2 reduction.

iv) Composite materials. Liang et al. found that despite Co_3O_4 or graphene alone showing very small catalytic activity toward ORR, a strongly coupled Co_3O_4–graphene hybrid exhibited surprisingly high activity for both the ORR and the OER.[188] Since then, a variety of composite catalysts have been designed for the ORR, OER, and HER to achieve better electrocatalytic activity and stability.[189–193] Recently, Zheng et al. reported extraordinary HER results for a g-C_3N_4@N-graphene composite originating from the chemical and electronic coupling between both components.[194] This method was also shown to be applicable for CO_2 electroreduction. Zhang et al. attributed the superior catalytic performance of the Sn–graphene composite to its strong electronic interactions.[31] Since the electronic structure of Sn NPs is modified by the introduction of graphene, both CO_2 adsorption and further CO_2 reduction were promoted. As mentioned above, thanks to the synergistic effect, both Ag–TiO_2 and PEI–NCNT composites are able to selectively reduce CO_2 to desirable products with reasonable activity. Therefore, various composites such as metal–carbon, metal–metal oxide, metal chalcogenide–carbon, etc. can be explored as potential electrocatalysts for CO_2 reduction.[195,196]

v) Reaction mechanism. Due to a much more complicated reaction process, the current knowledge of the reaction mechanisms for CO_2 electroreduction is severely limited. However, better understanding of the fundamentals of CO_2 electroreduction is urgently needed to accelerate further developments in this research area.[197] Thanks to the significant advances in DFT calculations and computer science, nowadays it has become possible to investigate electrocatalysts at the atomic level by computational methods. Despite the simplified models used in theoretical studies for CO_2 electroreduction, the DFT method has been identified as a powerful tool to explain experimental results and predict promising new catalysts. Meanwhile, advanced characterization techniques such as scanning transmission electron microscopy (STEM), near edge X-ray absorption fine structure (NEXAFS), surface X-ray scattering (SXS), etc. also benefit research into electrochemical reduction of CO_2, as they are capable of providing more information about the structural and chemical properties of the catalysts. Moreover, in situ techniques, which have been widely used in battery and catalysis science,[198–203] can probe the morphology and electronic structure of the electrode under catalytic conditions, thus yielding new insights into the nature of CO_2 electroreduction.

In addition, some other influential factors should be considered to make this technology more practical. In some cases of CO_2 electroreduction, low current densities are caused by the limited mass transport of CO_2 to the cathode surface. Therefore, the design of reactors such as gas-diffusion cells and liquid-flow cells, or solid polymer electrolytes can be adapted to partly address this issue.[204,205] Meanwhile, ionic liquids have been demonstrated as another appealing approach to promote the performance of electrocatalysts in CO_2 reduction. As compared to aqueous electrolytes, they have some desirable characteristics such as high CO_2 solubility, and wide potential windows. More importantly, the reaction barrier for CO_2 reduction can be significantly reduced while hydrogen formation can be greatly suppressed in the presence of ionic liquids.[206,207] Moreover, from the perspective of material science, more potential inorganic candidates, including metal nitrides, metal phosphides, metal carbides, and metal borides, can be explored to discover new catalysts with intrinsic high catalytic activity toward CO_2 reduction. Despite the fact that, at present, almost all research interest is focused on the cathode electrodes (CO_2 electroreduction), the catalytic performance of the anode (OER) should not be ignored, as both of them determine the overall cell efficiency.[208] Other parameters like CO_2 pressure, reaction temperature, pH values, and alkali cations of electrolyte[209,210] can also affect the final results for CO_2 electroreduction. Lastly, in order to make this technology economically feasible for long-term commercial applications, catalyst degradation or poisoning should be suppressed to the lowest levels.

In summary, recent work has indicated the possibility of producing hydrocarbon fuels from undesirable CO_2, as well as renewable electricity in the presence of advanced electrocatalysts. Despite the great challenges ahead, there is a sincere hope that continuous and extensive research in this area will result in the development of highly efficient, robust, and relatively cheap catalysts for CO_2 reduction in the near future, thus leaving a carbon neutral world for human beings.

Acknowledgements

D.D.Z. and J.L.L. contributed equally to this work. The authors gratefully acknowledge financial support from the Australian Research Council (ARC) through the Discovery Project programs (DP130104459, DP140104062, and DP1601048866) and from the Natural Science Foundation of China (No. 21576202).

Received: September 28, 2015
Revised: November 29, 2015
Published online: March 21, 2016

[1] M. S. Dresselhaus, I. L. Thomas, *Nature* **2001**, *414*, 332.
[2] S. Chu, A. Majumdar, *Nature* **2012**, *488*, 294.
[3] J. G. Canadell, C. Le Quéré, M. R. Raupach, C. B. Field, E. T. Buitenhuis, P. Ciais, T. J. Conway, N. P. Gillett, R. A. Houghton, G. Marland, *Proc. Natl. Acad. Sci. USA* **2007**, *104*, 18866.
[4] P. Tans, R. Keeling, NOAA/ESRL,http://www.esrl.noaa.gov/gmd/ccgg/trends/, accessed: August, **2015**.
[5] D. R. Feldman, W. D. Collins, P. J. Gero, M. S. Torn, E. J. Mlawer, T. R. Shippert, *Nature* **2015**, *519*, 339.
[6] M. E. Mann, *Proc. Natl. Acad. Sci. USA* **2009**, *106*, 4065.
[7] G. A. Olah, G. K. S. Prakash, A. Goeppert, *J. Am. Chem. Soc.* **2011**, *133*, 12881.
[8] S. Perathoner, G. Centi, *ChemSusChem* **2014**, *7*, 1274.
[9] N. S. Lewis, D. G. Nocera, *Proc. Natl. Acad. Sci. USA* **2006**, *103*, 15729.
[10] D. Larcher, J. M. Tarascon, *Nat. Chem.* **2015**, *7*, 19.
[11] B. Scrosati, K. M. Abraham, W. V. Schalkwijk, J. Hassoun, *Lithium Batteries: Advanced Technologies and Applications*, John Wiley & Sons, Hoboken, NJ, USA **2013**.

[12] G. P. Wang, L. Zhang, J. J. Zhang, *Chem. Soc. Rev.* **2012**, *41*, 797.
[13] R. S. Haszeldine, *Science* **2009**, *325*, 1647.
[14] S. Chu, *Science* **2009**, *325*, 1599.
[15] M. Aresta, A. Dibenedetto, A. Angelini, *Chem. Rev.* **2014**, *114*, 1709.
[16] E. V. Kondratenko, G. Mul, J. Baltrusaitis, G. O. Larrazábal, J. P. Ramírez, *Energy Environ. Sci.* **2013**, *6*, 3112.
[17] S. N. Habisreutinger, L. Schmidt-Mende, J. K. Stolarczyk, *Angew. Chem. Int. Ed.* **2013**, *52*, 7372.
[18] A. M. Appel, J. E. Bercaw, A. B. Bocarsly, H. Dobbek, D. L. DuBois, M. Dupuis, J. G. Ferry, E. Fujita, R. Hille, P. J. Kenis, C. A. Kerfeld, R. H. Morris, C. H. Peden, A. R. Portis, S. W. Ragsdale, T. B. Rauchfuss, J. N. Reek, L. C. Seefeldt, R. K. Thauer, G. L. Waldrop, *Chem. Rev.* **2013**, *113*, 6621.
[19] G. A. Ozin, *Adv. Mater.* **2015**, *27*, 1957.
[20] W. Wang, S. Wang, X. Ma, J. Gong, *Chem. Soc. Rev.* **2011**, *40*, 3703.
[21] J. P. Jones, G. K. S. Prakash, G. A. Olah, *Isr. J. Chem.* **2014**, *54*, 1451.
[22] D. T. Whipple, P. J. A. Kenis, *J. Phys. Chem. Lett.* **2010**, *1*, 3451.
[23] C. Costentin, M. Robert, J. M. Saveant, *Chem. Soc. Rev.* **2013**, *42*, 2423.
[24] E. E. Benson, C. P. Kubiak, A. J. Sathrum, J. M. Smieja, *Chem. Soc. Rev.* **2009**, *38*, 89.
[25] J. Schneider, H. Jia, J. T. Muckerman, E. Fujita, *Chem. Soc. Rev.* **2012**, *41*, 2036.
[26] J. M. Savéant, *Chem. Rev.* **2008**, *108*, 2348.
[27] M. R. Dubois, D. L. Dubois, *Acc. Chem. Res.* **2009**, *42*, 1974.
[28] C. W. Li, M. W. Kanan, *J. Am. Chem. Soc.* **2012**, *134*, 7231.
[29] Q. Lu, J. Rosen, Y. Zhou, G. S. Hutchings, Y. C. Kimmel, J. G. Chen, F. Jiao, *Nat. Commun.* **2014**, *5*, 3242.
[30] W. Zhu, R. Michalsky, O. Metin, H. Lv, S. Guo, C. J. Wright, X. Sun, A. A. Peterson, S. Sun, *J. Am. Chem. Soc.* **2013**, *i*, 16833.
[31] S. Zhang, P. Kang, T. J. Meyer, *J. Am. Chem. Soc.* **2014**, *136*, 1734.
[32] S. Zhang, P. Kang, S. Ubnoske, M. K. Brennaman, N. Song, R. L. House, J. T. Glass, T. J. Meyer, *J. Am. Chem. Soc.* **2014**, *136*, 7845.
[33] B. Kumar, M. Asadi, D. Pisasale, S. Sinha-Ray, B. A. Rosen, R. Haasch, J. Abiade, A. L. Yarin, A. Salehi-Khojin, *Nat. Commun.* **2013**, *4*, 2819.
[34] M. Asadi, B. Kumar, A. Behranginia, B. A. Rosen, A. Baskin, N. Repnin, D. Pisasale, P. Phillips, W. Zhu, R. Haasch, R. F. Klie, P. Král, J. Abiade, A. Salehi-Khojin, *Nat. Commun.* **2014**, *5*, 4470.
[35] R. J. Lim, M. Xie, M. A. Sk, J. M. Lee, A. Fisher, X. Wang, K. H. Lim, *Catal. Today* **2014**, *233*, 169.
[36] R. Schlogl, *Angew. Chem. Int. Ed.* **2015**, *54*, 3465.
[37] J. Qiao, Y. Liu, F. Hong, J. Zhang, *Chem. Soc. Rev.* **2014**, *43*, 631.
[38] J. Albo, M. A. Guerra, P. Castaño, A. Irabien, *Green Chem.* **2015**, *17*, 2304.
[39] H. R. M. Jhong, S. Ma, P. J. A. Kenis, *Curr. Opin. Chem. Eng.* **2013**, *2*, 191.
[40] E. Gileadi, *Electrode Kinetics for Chemists, Engineers, and Materials Scientists*, Wiley-VCH, Weinheim, Germany **1993**.
[41] A. S. Agarwal, Y. Zhai, D. Hill, N. Sridhar, *ChemSusChem* **2011**, *4*, 1301.
[42] M. Gangeri, S. Perathoner, S. Caudo, G. Centi, J. Amadou, D. Bégin, C. P. Huu, M. J. Ledoux, J. P. Tessonnier, D. S. Su, R. Schlögl, *Catal. Today* **2009**, *143*, 57.
[43] S. A. Akhade, W. Luo, X. Nie, N. J. Bernstein, A. Asthagiri, M. J. Janik, *Phys. Chem. Chem. Phys.* **2014**, *16*, 20429.
[44] Y. J. Zhang, V. Sethuraman, R. Michalsky, A. A. Peterson, *ACS Catal.* **2014**, *4*, 3742.
[45] Y. Hori, K. Kikuchi, S. Suzuki, *Chem. Lett.* **1985**, *14*, 1695.
[46] Y. Hori, *Modern Aspects of Electrochemistry*, Springer, New York **2008**.
[47] Y. Hori, H. Wakebe, T. Tsukamoto, O. Koga, *Electrochim. Acta* **1994**, *39*, 1833.
[48] E. Roduner, *Chem. Soc. Rev.* **2014**, *43*, 8226.
[49] R. V. Santen, M. Neurock, *Handbook of Heterogeneous Catalysis*, Wiley-VCH, Weinheim, Germany **2008**.
[50] D. C. Grenoble, M. M. Estadt, D. F. Ollis, *J. Catal.* **1981**, *67*, 90.
[51] A. A. Peterson, J. K. Nørskov, *J. Phys. Chem. Lett.* **2012**, *3*, 251.
[52] C. Shi, H. A. Hansen, A. C. Lausche, J. K. Norskov, *Phys. Chem. Chem. Phys.* **2014**, *16*, 4720.
[53] H. A. Hansen, J. B. Varley, A. A. Peterson, J. K. Nørskov, *J. Phys. Chem. Lett.* **2013**, *4*, 388.
[54] K. P. Kuhl, T. Hatsukade, E. R. Cave, D. N. Abram, J. Kibsgaard, T. F. Jaramillo, *J. Am. Chem. Soc.* **2014**, *136*, 14107.
[55] C. S. Chen, A. D. Handoko, J. H. Wan, L. Ma, D. Ren, B. S. Yeo, *Catal. Sci. Technol.* **2015**, *5*, 161.
[56] M. Gattrell, N. Gupta, A. Co, *J. Electroanal. Chem.* **2006**, *594*, 1.
[57] Y. Hori, I. Takahashi, O. Koga, N. Hoshi, *J. Phys. Chem. B* **2002**, *106*, 15.
[58] X. Nie, W. Luo, M. J. Janik, A. Asthagiri, *J. Catal.* **2014**, *312*, 108.
[59] Y. Hori, H. Konishi, T. Futamura, A. Murata, O. Koga, H. Sakurai, K. Oguma, *Electrochim. Acta* **2005**, *50*, 5354.
[60] K. J. Schouten, Z. Qin, E. P. Gallent, M. T. Koper, *J. Am. Chem. Soc.* **2012**, *134*, 9864.
[61] F. C. Vallejo, M. T. Koper, *Angew. Chem.* **2013**, *125*, 7423.
[62] Y. Hori, A. Murata, R. Takahashi, *J. Chem. Soc., Faraday Trans. 1* **1989**, *85*, 2309.
[63] A. A. Peterson, F. A. Pedersen, F. Studt, J. Rossmeisl, J. K. Nørskov, *Energy Environ. Sci.* **2010**, *3*, 1311.
[64] K. P. Kuhl, E. R. Cave, D. N. Abram, T. F. Jaramillo, *Energy Environ. Sci.* **2012**, *5*, 7050.
[65] X. Nie, M. R. Esopi, M. J. Janik, A. Asthagiri, *Angew. Chem. Int. Ed.* **2013**, *52*, 2459.
[66] K. J. P. Schouten, Y. Kwon, C. J. M. van der Ham, Z. Qin, M. T. M. Koper, *Chem. Sci.* **2011**, *2*, 1902.
[67] D. W. DeWulf, T. Jin, A. J. Bard, *J. Electrochem. Soc.* **1989**, *136*, 1686.
[68] J. H. Montoya, A. A. Peterson, J. K. Nørskov, *ChemCatChem* **2013**, *5*, 737.
[69] W. Tang, A. A. Peterson, A. S. Varela, Z. P. Jovanov, L. Bech, W. J. Durand, S. Dahl, J. K. Norskov, I. Chorkendorff, *Phys. Chem. Chem. Phys.* **2012**, *14*, 76.
[70] M. R. Gonçalves, A. Gomes, J. Condeço, T. R. C. Fernandes, T. Pardal, C. A. C. Sequeira, J. B. Branco, *Electrochim. Acta* **2013**, *102*, 388.
[71] S. Sen, D. Liu, G. T. R. Palmore, *ACS Catal.* **2014**, *4*, 3091.
[72] K. W. Frese, *J. Electrochem. Soc.* **1991**, *138*, 3338.
[73] M. Le, M. Ren, Z. Zhang, P. T. Sprunger, R. L. Kurtz, J. C. Flake, *J. Electrochem. Soc.* **2011**, *158*, E45.
[74] J. Xiao, A. Kuc, T. Frauenheim, T. Heine, *J. Mater. Chem. A* **2014**, *2*, 4885.
[75] Y. J. Zhang, A. A. Peterson, *Phys. Chem. Chem. Phys.* **2015**, *17*, 4505.
[76] D. Friebel, F. Mbuga, S. Rajasekaran, D. J. Miller, H. Ogasawara, R. A. Mori, D. Sokaras, D. Nordlund, T. C. Weng, A. Nilsson, *J. Phys. Chem. C* **2014**, *118*, 7954.
[77] R. Reske, M. Duca, M. Oezaslan, K. J. P. Schouten, M. T. M. Koper, P. Strasser, *J. Phys. Chem. Lett.* **2013**, *4*, 2410.
[78] A. S. Varela, C. Schlaup, Z. P. Jovanov, P. Malacrida, S. Horch, I. E. L. Stephens, I. Chorkendorff, *J. Phys. Chem. C* **2013**, *117*, 20500.
[79] R. Kas, R. Kortlever, H. Yılmaz, M. T. M. Koper, G. Mul, *ChemElectroChem* **2015**, *2*, 354.
[80] R. Reske, H. Mistry, F. Behafarid, B. R. Cuenya, P. Strasser, *J. Am. Chem. Soc.* **2014**, *136*, 6978.

[81] K. Manthiram, B. J. Beberwyck, A. P. Alivisatos, *J. Am. Chem. Soc.* **2014**, *136*, 13319.
[82] J. F. Xie, Y. X. Huang, W. W. Li, X. N. Song, L. Xiong, H. Q. Yu, *Electrochim. Acta* **2014**, *139*, 137.
[83] D. R. Kauffman, D. Alfonso, C. Matranga, H. Qian, R. Jin, *J. Am. Chem. Soc.* **2012**, *134*, 10237.
[84] W. Zhu, Y. J. Zhang, H. Zhang, H. Lv, Q. Li, R. Michalsky, A. A. Peterson, S. Sun, *J. Am. Chem. Soc.* **2014**, *136*, 16132.
[85] H. Mistry, R. Reske, Z. Zeng, Z. J. Zhao, J. Greeley, P. Strasser, B. R. Cuenya, *J. Am. Chem. Soc.* **2014**, *136*, 16473.
[86] J. H. Koh, H. S. Jeon, M. S. Jee, E. B. Nursanto, H. Lee, Y. J. Hwang, B. K. Min, *J. Phys. Chem. C* **2015**, *119*, 883.
[87] B. A. Rosen, J. L. Haan, P. Mukherjee, B. Braunschweig, W. Zhu, A. Salehi-Khojin, D. D. Dlott, R. I. Masel, *J. Phys. Chem. C* **2012**, *116*, 15307.
[88] X. Feng, K. Jiang, S. Fan, M. W. Kanan, *J. Am. Chem. Soc.* **2015**, *137*, 4606.
[89] N. Hoshi, M. Kato, Y. Hori, *J. Electroanal. Chem.* **1997**, *440*, 283.
[90] B. A. Rosen, A. Salehi-Khojin, M. R. Thorson, W. Zhu, D. T. Whipple, P. J. Kenis, R. I. Masel, *Science* **2011**, *334*, 643.
[91] B. A. Rosen, W. Zhu, G. Kaul, A. Salehi-Khojin, R. I. Masel, *J. Electrochem. Soc.* **2013**, *160*, H138.
[92] L. Sun, G. K. Ramesha, P. V. Kamat, J. F. Brennecke, *Langmuir* **2014**, *30*, 6302.
[93] J. L. DiMeglio, J. Rosenthal, *J. Am. Chem. Soc.* **2013**, *135*, 8798.
[94] J. Medina-Ramos, J. L. DiMeglio, J. Rosenthal, *J. Am. Chem. Soc.* **2014**, *136*, 8361.
[95] J. Rosen, G. S. Hutchings, Q. Lu, S. Rivera, Y. Zhou, D. G. Vlachos, F. Jiao, *ACS Catal.* **2015**, *5*, 4293.
[96] A. Salehi-Khojin, H. R. M. Jhong, B. A. Rosen, W. Zhu, S. Ma, P. J. A. Kenis, R. I. Masel, *J. Phys. Chem. C* **2013**, *117*, 1627.
[97] T. Hatsukade, K. P. Kuhl, E. R. Cave, D. N. Abram, T. F. Jaramillo, *Phys. Chem. Chem. Phys.* **2014**, *16*, 13814.
[98] Z. M. Detweiler, J. L. White, S. L. Bernasek, A. B. Bocarsly, *Langmuir* **2014**, *30*, 7593.
[99] K. Dhar, C. Cavallotti, *J. Phys. Chem. A* **2014**, *118*, 8676.
[100] C. Shi, C. P. O'Grady, A. A. Peterson, H. A. Hansen, J. K. Norskov, *Phys. Chem. Chem. Phys.* **2013**, *15*, 7114.
[101] S. Kapusta, N. Hackerman, *J. Electrochem. Soc.* **1983**, *130*, 607.
[102] Anawati, G. S. Frankel, A. Agarwal, N. Sridhar, *Electrochim. Acta* **2014**, *133*, 188.
[103] R. L. Machunda, H. Ju, J. Lee, *Curr. Appl. Phys.* **2011**, *11*, 986.
[104] P. Bumroongsakulsawat, G. H. Kelsall, *Electrochim. Acta* **2015**, *159*, 242.
[105] J. Wu, P. P. Sharma, B. H. Harris, X. D. Zhou, *J. Power Sources* **2014**, *258*, 189.
[106] P. Bumroongsakulsawat, G. H. Kelsall, *Electrochim. Acta* **2014**, *141*, 216.
[107] J. Medina-Ramos, R. C. Pupillo, T. P. Keane, J. L. DiMeglio, J. Rosenthal, *J. Am. Chem. Soc.* **2015**, *137*, 5021.
[108] J. Wu, F. G. Risalvato, S. Ma, X. D. Zhou, *J. Mater. Chem. A* **2014**, *2*, 1647.
[109] K. Ohkawa, K. Hashimoto, A. Fujishima, Y. Noguchi, S. Nakayama, *J. Electroanal. Chem.* **1993**, *345*, 445.
[110] D. Gao, H. Zhou, J. Wang, S. Miao, F. Yang, G. Wang, J. Wang, X. Bao, *J. Am. Chem. Soc.* **2015**, *137*, 4288.
[111] C. J. Stalder, S. Chao, M. S. Wrighton, *J. Am. Chem. Soc.* **1984**, *106*, 3673.
[112] N. Furuya, T. Yamazaki, M. Shibata, *J. Electroanal. Chem.* **1997**, *431*, 39.
[113] B. I. Podlovchenko, E. A. Kolyadko, S. Lu, *J. Electroanal. Chem.* **1994**, *373*, 185.
[114] X. Min, M. W. Kanan, *J. Am. Chem. Soc.* **2015**, *137*, 4701.
[115] Y. Chen, M. W. Kanan, *J. Am. Chem. Soc.* **2012**, *134*, 1986.
[116] M. F. Baruch, J. E. Pander, J. L. White, A. B. Bocarsly, *ACS Catal.* **2015**, *5*, 3148.
[117] C. W. Li, J. Ciston, M. W. Kanan, *Nature* **2014**, *508*, 504.
[118] R. Kas, R. Kortlever, A. Milbrat, M. T. Koper, G. Mul, J. Baltrusaitis, *Phys. Chem. Chem. Phys.* **2014**, *16*, 12194.
[119] Y. Chen, C. W. Li, M. W. Kanan, *J. Am. Chem. Soc.* **2012**, *134*, 19969.
[120] C. H. Lee, M. W. Kanan, *ACS Catal.* **2015**, *5*, 465.
[121] S. Zhang, Y. Shao, H. G. Liao, J. Liu, I. A. Aksay, G. Yin, Y. Lin, *Chem. Mater.* **2011**, *23*, 1079.
[122] D. Kim, S. Lee, J. D. Ocon, B. Jeong, J. K. Lee, J. Lee, *Phys. Chem. Chem. Phys.* **2015**, *17*, 824.
[123] Z. Xu, E. Lai, Y. Shao-Horn, K. Hamad-Schifferli, *Chem. Commun.* **2012**, *48*, 5626.
[124] W. Zhao, L. Yang, Y. Yin, M. Jin, *J. Mater. Chem. A* **2014**, *2*, 902.
[125] F. Jia, X. Yu, L. Zhang, *J. Power Sources* **2014**, *252*, 85.
[126] D. Kim, J. Resasco, Y. Yu, A. M. Asiri, P. Yang, *Nat. Commun.* **2014**, *5*, 4948.
[127] X. Guo, Y. Zhang, C. Deng, X. Li, Y. Xue, Y. M. Yan, K. Sun, *Chem. Commun.* **2015**, *51*, 1345.
[128] X. Zhao, B. Luo, R. Long, C. Wang, Y. Xiong, *J. Mater. Chem. A* **2015**, *3*, 4134.
[129] S. Rasul, D. H. Anjum, A. Jedidi, Y. Minenkov, L. Cavallo, K. Takanabe, *Angew. Chem. Int. Ed.* **2015**, *54*, 2146.
[130] N. Artrith, A. M. Kolpak, *Nano Lett.* **2014**, *14*, 2670.
[131] M. Karamad, V. Tripkovic, J. Rossmeisl, *ACS Catal.* **2014**, *4*, 2268.
[132] P. Hirunsit, *J. Phys. Chem. C* **2013**, *117*, 8262.
[133] S. Lysgaard, J. S. Myrdal, H. A. Hansen, T. Vegge, *Phys. Chem. Chem. Phys.* **2015**, *17*, 28270.
[134] P. Hirunsit, W. Soodsawang, J. Limtrakul, *J. Phys. Chem. C* **2015**, *119*, 8238.
[135] S. Back, H. Kim, Y. Jung, *ACS Catal.* **2015**, *5*, 965.
[136] R. Arrigo, M. E. Schuster, S. Wrabetz, F. Girgsdies, J. P. Tessonnier, G. Centi, S. Perathoner, D. S. Su, R. Schlogl, *ChemSusChem* **2012**, *5*, 577.
[137] A. N. Grace, S. Y. Choi, M. Vinoba, M. Bhagiyalakshmi, D. H. Chu, Y. Yoon, S. C. Nam, S. K. Jeong, *Applied Energy* **2014**, *120*, 85.
[138] N. Kumari, N. Sinha, M. A. Haider, S. Basu, *Electrochim. Acta* **2015**, *177*, 21.
[139] N. Ullah, I. Ali, M. Jansen, S. Omanovic, *Can. J. Chem. Eng.* **2015**, *93*, 55.
[140] D. Chu, G. Qin, X. Yuan, M. Xu, P. Zheng, J. Lu, *ChemSusChem* **2008**, *1*, 205.
[141] G. K. Ramesha, J. F. Brennecke, P. V. Kamat, *ACS Catal.* **2014**, *4*, 3249.
[142] B. H. Meekins, P. V. Kamat, *ACS Nano* **2009**, *3*, 3437.
[143] S. Ma, Y. Lan, G. M. Perez, S. Moniri, P. J. Kenis, *ChemSusChem* **2014**, *7*, 866.
[144] T. Inoue, A. Fujishima, S. Konishi, K. Honda, *Nature* **1979**, *277*, 637.
[145] L. Liu, H. Zhao, J. M. Andino, Y. Li, *ACS Catal.* **2012**, *2*, 1817.
[146] J. Yu, J. Low, W. Xiao, P. Zhou, M. Jaroniec, *J. Am. Chem. Soc.* **2014**, *136*, 8839.
[147] S. Lee, J. D. Ocon, Y. Son, J. Lee, *J. Phys. Chem. C* **2015**, *119*, 4884.
[148] N. Sreekanth, K. L. Phani, *Chem. Commun.* **2014**, *50*, 11143.
[149] Y. Oh, H. Vrubel, S. Guidoux, X. Hu, *Chem. Commun.* **2014**, *50*, 3878.
[150] T. Sekimoto, M. Deguchi, S. Yotsuhashi, Y. Yamada, T. Masui, A. Kuramata, S. Yamakoshi, *Electrochem. Commun.* **2014**, *43*, 95.
[151] Q. H. Wang, K. Kalantar-Zadeh, A. Kis, J. N. Coleman, M. S. Strano, *Nat. Nanotechnol.* **2012**, *7*, 699.
[152] D. Jariwala, V. K. Sangwan, L. J. Lauhon, T. J. Marks, M. C. Hersam, *ACS Nano* **2014**, *8*, 1102.

[153] H. Wang, H. Feng, J. Li, *Small* **2014**, *10*, 2165.
[154] R. Lv, J. A. Robinson, R. E. Schaak, D. Sun, Y. Sun, T. E. Mallouk, M. Terrones, *Acc. Chem. Res.* **2015**, *48*, 56.
[155] H. Wang, H. Yuan, S. S. Hong, Y. Li, Y. Cui, *Chem. Soc. Rev.* **2015**, *44*, 2664.
[156] K. Hara, A. Tsuneto, A. Kudo, T. Sakata, *J. Electroanal. Chem.* **1997**, *434*, 239.
[157] R. Nakamura, T. Takashima, S. Kato, K. Takai, M. Yamamoto, K. Hashimoto, *Angew. Chem. Int. Ed.* **2010**, *49*, 7692.
[158] A. Yamaguchi, M. Yamamoto, K. Takai, T. Ishii, K. Hashimoto, R. Nakamura, *Electrochim. Acta* **2014**, *141*, 311.
[159] G. Berhault, M. P. Rosa, A. Mehta, M. J. Yácaman, R. R. Chianelli, *Appl. Catal. A: Gen.* **2008**, *345*, 80.
[160] J. S. Kim, H. W. Yoo, H. O. Choi, H. T. Jung, *Nano Lett.* **2014**, *14*, 5941.
[161] J. N. Coleman, M. Lotya, A. O'Neill, S. D. Bergin, P. J. King, U. Khan, K. Young, A. Gaucher, S. De, R. J. Smith, I. V. Shvets, S. K. Arora, G. Stanton, H.-Y. Kim, K. Lee, G. T. Kim, G. S. Duesberg, T. Hallam, J. J. Boland, J. J. Wang, J. F. Donegan, J. C. Grunlan, G. Moriarty, A. Shmeliov, R. J. Nicholls, J. M. Perkins, E. M. Grieveson, K. Theuwissen, D. W. McComb, P. D. Nellist, V. Nicolosi, *Science* **2011**, *331*, 568.
[162] A. Ambrosi, Z. Sofer, M. Pumera, *Small* **2015**, *11*, 605.
[163] M. A. Lukowski, A. S. Daniel, F. Meng, A. Forticaux, L. Li, S. Jin, *J. Am. Chem. Soc.* **2013**, *135*, 10274.
[164] Y. Li, H. Wang, L. Xie, Y. Liang, G. Hong, H. Dai, *J. Am. Chem. Soc.* **2011**, *133*, 7296.
[165] T. Wang, J. Zhuo, Y. Chen, K. Du, P. Papakonstantinou, Z. Zhu, Y. Shao, M. Li, *ChemCatChem* **2014**, *6*, 1877.
[166] Z. Yin, B. Chen, M. Bosman, X. Cao, J. Chen, B. Zheng, H. Zhang, *Small* **2014**, *10*, 3536.
[167] K. Chan, C. Tsai, H. A. Hansen, J. K. Nørskov, *ChemCatChem* **2014**, *6*, 1899.
[168] T. Wang, D. Gao, J. Zhuo, Z. Zhu, P. Papakonstantinou, Y. Li, M. Li, *Chem. Eur. J.* **2013**, *19*, 11939.
[169] H. I. Karunadasa, E. Montalvo, Y. Sun, M. Majda, J. R. Long, C. J. Chang, *Science* **2012**, *335*, 698.
[170] B. Hinnemann, P. G. Moses, J. Bonde, K. P. Jørgensen, J. H. Nielsen, S. Horch, I. Chorkendorff, J. K. Nørskov, *J. Am. Chem. Soc.* **2005**, *127*, 5308.
[171] J. Wu, R. M. Yadav, M. Liu, P. P. Sharma, C. S. Tiwary, L. Ma, X. Zou, X.-D. Zhou, B. I. Yakobson, J. Lou, P. M. Ajayan, *ACS Nano* **2015**, *9*, 5364.
[172] K. Nakata, T. Ozaki, C. Terashima, A. Fujishima, Y. Einaga, *Angew. Chem. Int. Ed.* **2014**, *126*, 890.
[173] K. Gong, F. Du, Z. Xia, M. Durstock, L. Dai, *Science* **2009**, *323*, 760.
[174] Y. Zhao, R. Nakamura, K. Kamiya, S. Nakanishi, K. Hashimoto, *Nat. Commun.* **2013**, *4*, 2390.
[175] S. Chen, J. Duan, M. Jaroniec, S. Z. Qiao, *Adv. Mater.* **2014**, *26*, 2925.
[176] Y. Zheng, Y. Jiao, L. H. Li, T. Xing, Y. Chen, M. Jaroniec, S. Z. Qiao, *ACS Nano* **2014**, *8*, 5290.
[177] J. Zhang, Z. Zhao, Z. Xia, L. Dai, *Nat. Nanotechnol.* **2015**, *10*, 444.
[178] Y. Zheng, Y. Jiao, M. Jaroniec, Y. Jin, S. Z. Qiao, *Small* **2012**, *8*, 3550.
[179] H. K. Lim, H. Shin, W. A. Goddard, Y. J. Hwang, B. K. Min, H. Kim, *J. Am. Chem. Soc.* **2014**, *136*, 11355.
[180] H. Xia, C. Hong, B. Li, B. Zhao, Z. Lin, M. Zheng, S. V. Savilov, S. M. Aldoshin, *Adv. Funct. Mater.* **2015**, *25*, 627.
[181] C. Wang, L. Wu, H. Wang, W. Zuo, Y. Li, J. Liu, *Adv. Funct. Mater.* **2015**, *25*, 3524.
[182] J. Xie, H. Zhang, S. Li, R. Wang, X. Sun, M. Zhou, J. Zhou, X. W. Lou, Y. Xie, *Adv. Mater.* **2013**, *25*, 5807.
[183] F. Cheng, J. Shen, B. Peng, Y. Pan, Z. Tao, J. Chen, *Nat. Chem.* **2011**, *3*, 79.
[184] T. Y. Ma, S. Dai, M. Jaroniec, S. Z. Qiao, *J. Am. Chem. Soc.* **2014**, *136*, 13925.
[185] X. Zhang, F. Han, B. Shi, S. Farsinezhad, G. P. Dechaine, K. Shankar, *Angew. Chem. Int. Ed.* **2012**, *124*, 12904.
[186] M. S. Faber, S. Jin, *Energy Environ. Sci.* **2014**, *7*, 3519.
[187] Q. Lu, J. Rosen, F. Jiao, *ChemCatChem* **2015**, *7*, 38.
[188] Y. Liang, Y. Li, H. Wang, J. Zhou, J. Wang, T. Regier, H. Dai, *Nat. Mater.* **2011**, *10*, 780.
[189] Y. Li, W. Zhou, H. Wang, L. Xie, Y. Liang, F. Wei, J. C. Idrobo, S. J. Pennycook, H. Dai, *Nat. Nanotechnol.* **2012**, *7*, 394.
[190] Y. Hou, A. B. Laursen, J. Zhang, G. Zhang, Y. Zhu, X. Wang, S. Dahl, I. Chorkendorff, *Angew. Chem. Int. Ed.* **2013**, *52*, 3621.
[191] T. Wang, J. Zhuo, K. Du, B. Chen, Z. Zhu, Y. Shao, M. Li, *Adv. Mater.* **2014**, *26*, 3761.
[192] Z. Zhuang, W. Sheng, Y. Yan, *Adv. Mater.* **2014**, *26*, 3950.
[193] Y. Liang, Y. Li, H. Wang, H. Dai, *J. Am. Chem. Soc.* **2013**, *135*, 2013.
[194] Y. Zheng, Y. Jiao, Y. Zhu, L. H. Li, Y. Han, Y. Chen, A. Du, M. Jaroniec, S. Z. Qiao, *Nat. Commun.* **2014**, *5*, 3783.
[195] D. H. Lim, J. H. Jo, D. Y. Shin, J. Wilcox, H. C. Ham, S. W. Nam, *Nanoscale* **2014**, *6*, 5087.
[196] Y. Koo, R. Malik, N. Alvarez, L. White, V. N. Shanov, M. Schulz, B. Collins, J. Sankar, Y. Yun, *RSC Adv.* **2014**, *4*, 16362.
[197] Y. Jiao, Y. Zheng, M. Jaroniec, S. Z. Qiao, *Chem. Soc. Rev.* **2015**, *44*, 2060.
[198] T. Masuda, H. Fukumitsu, K. Fugane, H. Togasaki, D. Matsumura, K. Tamura, Y. Nishihata, H. Yoshikawa, K. Kobayashi, T. Mori, K. Uosaki, *J. Phys. Chem. C* **2012**, *116*, 10098.
[199] V. S. Myers, A. I. Frenkel, R. M. Crooks, *Langmuir* **2012**, *28*, 1596.
[200] C. M. Wang, X. Li, Z. Wang, W. Xu, J. Liu, F. Gao, L. Kovarik, J. G. Zhang, J. Howe, D. J. Burton, Z. Liu, X. Xiao, S. Thevuthasan, D. R. Baer, *Nano Lett.* **2012**, *12*, 1624.
[201] B. Lassalle-Kaiser, D. Merki, H. Vrubel, S. Gul, V. K. Yachandra, X. Hu, J. Yano, *J. Am. Chem. Soc.* **2015**, *137*, 314.
[202] J. Y. Huang, L. Zhomg, C. M. Wang, J. P. Sullivan1, W. Xu, L. Q. Zhang, S. X. Mao, N. S. Hudak, X. H. Liu, A. Subramanian, H. Fan, L. Qi, A. Kushima, J. Li, *Science* **2010**, *330*, 1515.
[203] N. Kornienko, J. Resasco, N. Becknell, C. M. Jiang, Y. S. Liu, K. Nie, X. Sun, J. Guo, S. R. Leone, P. Yang, *J. Am. Chem. Soc.* **2015**, *137*, 7448.
[204] Q. Wang, H. Dong, H. Yu, H. Yu, *J. Power Sources* **2015**, *279*, 1.
[205] L. M. Aeshala, R. Uppaluri, A. Verma, *Phys. Chem. Chem. Phys.* **2014**, *16*, 17588.
[206] Z. Zhang, C. Wu, J. Ma, J. Song, H. Fan, J. Liu, Q. Zhu, B. Han, *Green Chem.* **2015**, *17*, 1633.
[207] T. C. Berto, L. Zhang, R. J. Hamers, J. F. Berry, *ACS Catal.* **2015**, *5*, 703.
[208] S. Ma, R. Luo, S. Moniri, Y. Lan, P. J. A. Kenis, *J. Electrochem. Soc.* **2014**, *161*, F1124.
[209] D. T. Whipple, E. C. Finke, P. J. A. Kenis, *Electrochem. Solid-State Lett.* **2010**, *13*, B109.
[210] M. R. Thorson, K. I. Siil, P. J. A. Kenis, *J. Electrochem. Soc.* **2013**, *160*, F69.

Chapter 3: Two-Dimensional Metal-Organic Frameworks with High Oxidation States for Efficient Electrocatalytic Urea Oxidation

3.1 Introduction and Significance

High oxidation state of metal cations is critical in achieving outstanding performance of many transition metal-based materials towards electrochemical oxidation reactions such as urea oxidation reaction (UOR), which acts as a vital half reaction for several practical applications. However, currently it still remains quite challenging to modulate oxidation state of metal cations via facile and effective methods. Our study presents a new method to generate metal cations with high oxidation state by introducing 1,4-benzenedicarboxylic acid (BDC) ligands to modify the electronic structures of metal species. The as-fabricated ultrathin 2-D Ni-MOF nanosheets exhibit remarkable activity, favorable kinetics, and strong durability towards UOR. The highlights of this work include:

1. Novel strategy for achieving high oxidation state. In this work, high oxidation state of nickel cations is achieved by strong interaction between Ni species and BDC ligands, which draw electrons from the Ni species. This is completely different from previous reports, in which the oxidation state of metal species is generally adjusted by hybridizing with other materials.

2. 2-D MOF for electrolysis. Ultrathin 2-D Ni-MOF is directly used as an electrocatalyst for UOR without any post-treatment. To the best of our knowledge, this is also the first example that MOF is applied in urea electrolysis area.

3. Remarkable activity and stability. Ultrathin 2-D Ni-MOF nanosheets exhibit low onset potential (1.36 V vs. RHE to achieve 10 mA cm^{-2}), high anodic current density (120 mA cm^{-2} at 1.6 V vs. RHE) and good stability (10 h) for UOR. The anodic current density can be further enhanced to 292 mA cm^{-2} (1.6 V vs. RHE) by depositing 2-D MOF on conductive nickel foam, outperforming the state-of-the-art UOR catalysts.

4. Reasonable mechanism. The excellent UOR performance is found to be partially from the high active site density of the 2-D MOF, and largely from high oxidation state of the nickel species, which is proved by both X-ray photoelectron spectroscopy and Synchrotron-based X-ray absorption near edge spectra.

3.2 Two-Dimensional Metal-Organic Frameworks with High Oxidation States for Efficient Electrocatalytic Urea Oxidation

This chapter is included as it appears as a journal paper published by **Dongdong Zhu**, Chunxian Guo, Jinlong Liu, Liang Wang, Yi Du, Shi-Zhang Qiao, Two-dimensional metal-organic frameworks with high oxidation states for efficient electrocatalytic urea oxidation, ***Chemical Communications***, 2017, 53, 10906-10909.

Statement of Authorship

Title of Paper	Two-Dimensional Metal-Organic Frameworks with High Oxidation States for Efficient Electrocatalytic Urea Oxidation
Publication Status	☑ Published ☐ Accepted for Publication ☐ Submitted for Publication ☐ Unpublished and Unsubmitted work written in manuscript style
Publication Details	Dongdong Zhu, Chunxian Guo, Jinlong Liu, Liang Wang, Yi Du, and Shi-Zhang Qiao, Two-Dimensional Metal-Organic Frameworks with High Oxidation States for Efficient Electrocatalytic Urea Oxidation, Chemical Communications, 2017, 53, 10906–10909.

Principal Author

Name of Principal Author (Candidate)	Dongdong Zhu		
Contribution to the Paper	Project design, sample synthesis, most of the characterizations, electrochemical tests, data analysis, and manuscript drafting.		
Overall percentage (%)	70%		
Certification:	This paper reports on original research I conducted during the period of my Higher Degree by Research candidature and is not subject to any obligations or contractual agreements with a third party that would constrain its inclusion in this thesis. I am the primary author of this paper.		
Signature		Date	18/12/2018

Co-Author Contributions

By signing the Statement of Authorship, each author certifies that:

i. the candidate's stated contribution to the publication is accurate (as detailed above);

ii. permission is granted for the candidate in include the publication in the thesis; and

iii. the sum of all co-author contributions is equal to 100% less the candidate's stated contribution.

Name of Co-Author	Chunxian Guo		
Contribution to the Paper	Discussion and supervision of this project, and manuscript revision. 5%		
Signature		Date	18/12/2018

Name of Co-Author	Jinlong Liu		
Contribution to the Paper	Assistance with electrocatalytic testing and analysis. 5%		
Signature		Date	18/12/2018

Name of Co-Author	Liang Wang		
Contribution to the Paper	Assistance with TEM characterization. 5%		
Signature		Date	18.12.2018

Name of Co-Author	Yi Du		
Contribution to the Paper	Assistance with TEM characterization. 5%		
Signature		Date	18.12.2018

Name of Co-Author	Shi-Zhang Qiao		
Contribution to the Paper	Supervision of the work, and manuscript evaluation. 10%		
Signature		Date	19/Dec/2018

ChemComm

COMMUNICATION

View Article Online
View Journal | View Issue

Cite this: *Chem. Commun.*, 2017, 53, 10906

Received 15th August 2017,
Accepted 13th September 2017

DOI: 10.1039/c7cc06378d

rsc.li/chemcomm

Two-dimensional metal–organic frameworks with high oxidation states for efficient electrocatalytic urea oxidation†

Dongdong Zhu,[a] Chunxian Guo,[a] Jinlong Liu,[a] Liang Wang,[b] Yi Du[b] and Shi-Zhang Qiao *[a]

A two-dimensional metal–organic framework (MOF) comprising nickel species and an organic ligand of benzenedicarboxylic acid is fabricated and explored as an electrocatalyst for urea oxidation reaction (UOR). The excellent UOR performance is found to be partially due to the high active site density of the two-dimensional MOF, and largely because of the high oxidation state of the nickel species.

An appropriate oxidation state of metal cations is critical in achieving outstanding performance of many transition-metal based electrocatalysts towards electrochemical oxidation reactions.[1,2] In terms of oxygen evolution reaction (OER), metal cations are oxidized to higher valence states before the onset of the reaction, and these highly oxidative metal cations are supposed as catalytic active sites.[3] Interestingly, Bell *et al.* discovered that a metal support can modify the oxidation state of deposited cobalt oxide, and enhanced oxidation of cobalt oxide is beneficial to improve OER activity.[4] Therefore, it seems possible to promote the performance of oxidation reactions by tailoring the oxidation state of metal cations. The Pd/PANI/Pd nanotube array exhibited better catalytic performance than the Pd nanotube array towards ethanol oxidation reaction (EOR). Due to electron transfer from Pd to PANI, Pd with a high oxidation state was formed, which contributed to enhanced EOR activity.[5] Despite the aforementioned reports, currently it remains quite challenging to modulate the oxidation states of metal cations *via* facile and effective methods.

As a promising hydrogen storage material, urea is cheap, stable, relatively nontoxic, and easy for storage and transportation, and has an energy density of 16.9 MJ L^{-1}, which is even higher than compressed or liquid hydrogen, making urea an ideal alternative to hydrogen as an energy source for fuel cells that utilize urea oxidation reaction (UOR) and oxygen reduction reaction.[6] Moreover, compared with OER (1.23 V *vs.* RHE), which is a typical anodic reaction for water splitting, the theoretical potential of UOR (0.37 V *vs.* RHE) is significantly lower. Hence, UOR has great potential to replace OER for more efficient water splitting to produce hydrogen.[7] Additionally, a large amount of urea that is produced from industrial, agricultural and human wastewater always pollutes atmosphere and groundwater, causing severe health problems for human beings, and UOR is an efficient way to purify urea-rich wastewater, eliminating these potential hazards.[8] However, UOR is a six-electron transfer process ($CO(NH_2)_2 + 6OH^- \rightarrow N_2 + 5H_2O + CO_2 + 6e^-$) with complicated gas evolution steps, suffering from intrinsically sluggish kinetics. Thus, high-performance electrocatalysts are highly required to reduce the reaction barriers for UOR. Since Botte *et al.* demonstrated that nickel displayed higher oxidation current densities than noble metals (Pt, Rh, Pt–Ir) for urea electrolysis in alkaline media,[9] nickel-based materials, such as $Ni(OH)_2$,[10] Ni–Zn–Co,[11] $Ni_{1.5}Mn_{1.5}O_4$,[12] *etc.*, have been widely investigated as electrocatalysts for UOR. Unfortunately, these nickel-based UOR catalysts generally suffer from low catalytic activity and relatively poor stability. Recently, metallic $Ni(OH)_2$ nanosheets demonstrated good stability for UOR but the catalytic activity was not satisfactory, with a low peak current density of 36 mA cm^{-2}.[13] Overall, despite these tremendous efforts, currently all the reported UOR catalysts are still far from requirements, which greatly hinders urea-related technologies for practical applications.

Ultrathin two-dimensional (2-D) materials represent an emerging class of nanomaterials that have been widely investigated for catalysis, energy storage and conversion, and electronic and optoelectronic devices, owing to their appealing properties such as compelling electronic properties, high specific surface area, outstanding mechanical strength, excellent optical transparency, *etc.*[14,15] In particular, ultrathin 2-D metal–organic framework (MOF) nanosheets, constructed by joining metal ions with organic linkers, possess high percentages of metal atoms exposed on the surface, and these coordinatively unsaturated metal sites with more dangling bonds are highly desirable for electrocatalysis.[16]

[a] *School of Chemical Engineering, University of Adelaide, Adelaide, SA 5005, Australia. E-mail: s.qiao@adelaide.edu.au*
[b] *Institute for Superconducting and Electronic Materials (ISEM), University of Wollongong, Wollongong, NSW 2525, Australia*

† Electronic supplementary information (ESI) available: Experimental section, supplementary figures and tables. See DOI: 10.1039/c7cc06378d

Moreover, the electronic structures of metal sites in MOFs are influenced by organic ligands through strong interactions, making it possible to achieve high oxidation states of metal cations. Therefore, considering the unique physicochemical properties as well as tailorable electronic structures, 2-D MOFs with high oxidation states may offer a great opportunity as promising electrocatalyts towards oxidation reactions such as UOR.

In this study, we fabricate a kind of 2-D MOF comprising nickel species and organic ligands of benzenedicarboxylic acid (BDC), and discover that ultrathin nickel-based metal–organic framework (Ni-MOF) nanosheets have high oxidation states of nickel cations, which is confirmed by X-ray photoelectron spectroscopy and synchrotron-based X-ray absorption near-edge spectra. The high oxidation state of nickel cations is attributed to the strong interaction between the Ni species and benzenedicarboxylic acid (BDC) ligands, which draw electrons from the Ni species. This strategy to achieve a high oxidation state at the molecular level is completely different from previous reports, in which the oxidation state of metal cations is generally adjusted by hybridizing with other materials. Due to the nickel cations with high oxidation states and a large number of catalytic active sites, the as-fabricated ultrathin 2-D Ni-MOF nanosheets exhibit remarkable performance for UOR, outperforming the state-of-the-art UOR catalysts.

As illustrated in Fig. 1, Ni-MOF nanosheets were fabricated *via* a facile sonication-assisted solution method by adding the organic ligands (BDC) into the solution of metal salt (nickel chloride hexahydrate) (see the ESI† for a detailed experimental process). The scanning electron microscopy (SEM) image in Fig. 2a shows that the as-fabricated sample has an obvious sheet morphology, and the presence of wrinkles reveals good flexibility of the sample. The transmission electron microscopy (TEM) images (Fig. 2b and Fig. S2, ESI†) again confirm the sheet-like morphology with a lateral size of several hundred nanometers, while the transparent characteristic of the nanosheet indicates its ultrathin thickness. Since these nanosheets are extremely sensitive to electron beam irradiation, very low accelerating voltage (80 kV) was applied during the scanning transmission electron microscopy (STEM) test to get more information. Fig. 2c displays that the lattice spacing of the nanosheet is around 1.05 nm. The inserted selected-area electron diffraction (SAED) pattern in Fig. 2c reveals the single-crystalline nature of the nanosheet. Energy-dispersive spectroscopy (EDS) (Fig. S1b, ESI†) confirms that the obtained nanosheets are composed of C, O and Ni without other impurities, and the elemental mapping in Fig. 2d suggests that these elements are uniformly distributed throughout the whole nanosheet.

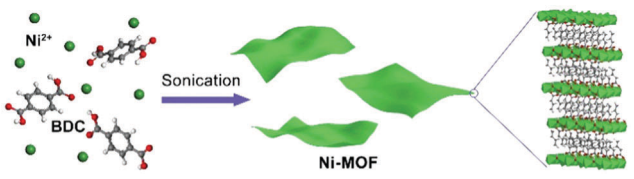

Fig. 1 Schematic illustration of the synthesis process for Ni-MOF nanosheets.

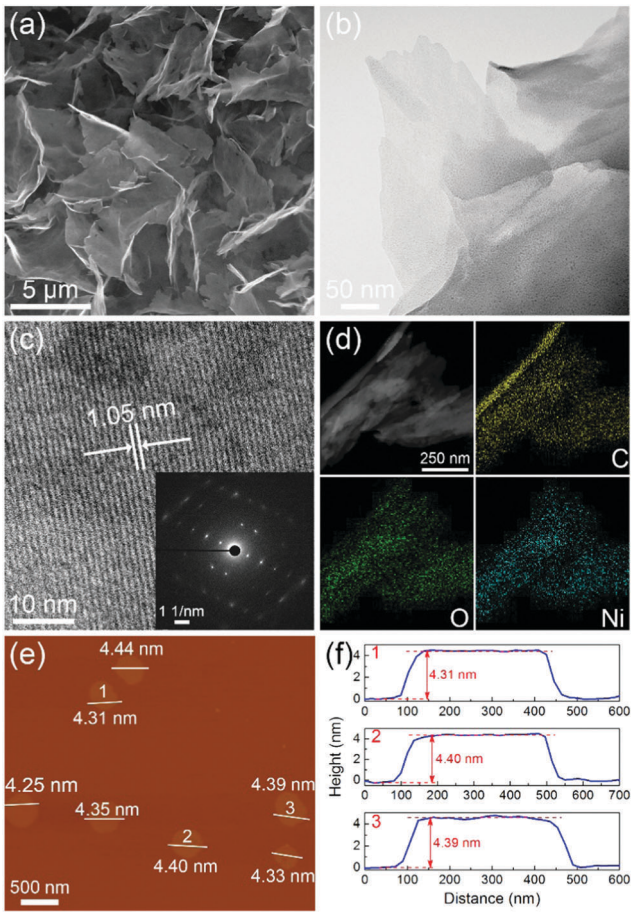

Fig. 2 (a and b) SEM and TEM images of Ni-MOF. (c) HRTEM image and SAED pattern (inset) of Ni-MOF. (d) Elemental mapping of Ni-MOF. (e and f) AFM image of Ni-MOF and the corresponding height profiles along the marked white lines.

To evaluate the exact thickness of the nanosheets, atomic force microscopy (AFM) was applied. As can be seen from Fig. 2e, the height of the nanosheets is around 4.3–4.4 nm, corresponding to five metal coordination layers or four BDC coordination layers (Fig. 1). Fig. 2f further implies that the nanosheets have relatively flat surfaces. All of these results undoubtedly confirm the successful fabrication of flexible ultrathin nanosheets, which are quite appealing for electrocatalysis applications. The ultrathin nanosheets expose more metal active sites for the catalytic reaction, while the open pores between flexible nanosheets surely would promote the mass transfer of the electrolyte and the diffusion of gas products.[17] For the purpose of comparison, $Ni(OH)_2$ nanosheets (Fig. S4, ESI†) were also synthesized here *via* a facile hydrothermal method.[18]

The crystal structure of the ultrathin nanosheets was further analyzed by powder X-ray diffraction (PXRD). Fig. S5a (ESI†) reveals that the PXRD pattern of the obtained nanosheets is consistent with the simulated diffraction pattern, implying the successful fabrication of Ni-MOFs. Moreover, the observed diffraction peak appeared at 8.8° is assigned to the (200) plane of Ni-MOFs, which agrees well with the lattice spacing of

1.05 nm in Fig. 2c.[19] In this structure, every Ni atom is octahedrally coordinated by six O atoms from BDC ligands or hydroxyls, and these Ni-based pseudo octahedra are further connected with each other in the (200) plane to form metal coordination layers, which are separated by BDC molecules.[16]

X-ray photoelectron spectroscopy (XPS) is further employed to gain information about surface electronic state and chemical composition of the samples. As displayed in Fig. 3a, the Ni 2p XPS spectrum of $Ni(OH)_2$ shows two main peaks positioned at 856.1 and 873.6 eV, which are assigned to Ni $2P_{3/2}$ and Ni $2P_{1/2}$, together with two corresponding satellite peaks located at 861.7 and 880.6 eV. The spin-energy separation of two main peaks is 17.5 eV, which is the characteristic of a $Ni(OH)_2$ phase.[20] Interestingly, Ni-MOF exhibits a similar Ni 2p spectrum, which is also composed of two main peaks, along with two satellite peaks. However, compared to $Ni(OH)_2$, all the Ni 2P peaks of Ni-MOF shift noticeably to higher binding energies. Specifically, for Ni $2P_{3/2}$ main peak, the binding energy of Ni-MOF is 1.5 eV higher than that of $Ni(OH)_2$ (Table S1, ESI†), indicating a higher oxidation state of Ni cations in Ni-MOF.

Synchrotron-based X-ray absorption near-edge spectra (XANES) technique was further used to reveal the local electronic structure of Ni-MOFs. The absorption edge energy of XANES is very sensitive to the oxidation state of target element.[21] As displayed in Fig. 3b, the Ni L-edge of Ni-MOF shifts to higher energy than that of $Ni(OH)_2$, indicating a lower electron density at the Ni site in Ni-MOF.[22,23] It is supposed that comparing with hydroxyl, BDC acts as a better electron acceptor which attracts more electrons from Ni through Ni–O bond, resulting in higher oxidation state of Ni cations in Ni-MOF, which agrees with previous XPS results. In conclusion, all the results above clearly demonstrated that ultrathin Ni-MOF nanosheets with high oxidation state were successfully synthesized.

To evaluate the catalytic performance of ultrathin Ni-MOF nanosheets for UOR, a series of electrochemical measurements were carried out using a three-electrode configuration. Fig. 4a shows the linear sweep voltammetry (LSV) curves of the Ni-MOF catalyst deposited on a glassy carbon electrode in different electrolytes. Since the approximate concentration of urea in human urine is 0.33 M, and this is also the benchmark for most previous reports, 0.33 M urea was used here for UOR test.[24] As displayed in Fig. 4a, OER takes place in 1.0 M KOH, with an obvious oxidation peak at around 1.4 V (*vs.* reversible hydrogen electrode, RHE), which can be attributed to the formation of NiOOH species.[25] After the addition of urea, Ni-MOF exhibits a greatly enhanced anodic current density for UOR. Interestingly, the onset potential of UOR is quite close to the potential where NiOOH appears, suggesting that the newly generated NiOOH species are active sites for UOR, which is consistent with previous reports about nickel-based catalysts for UOR.[13] Fig. 4b shows the LSV curves of Ni-MOF, $Ni(OH)_2$ and commercial 20% Pt/C in 1.0 M KOH containing 0.33 M urea. Obviously, the anodic current of Ni-MOF has a dramatic increase as the potential becomes more positive, while other two samples only show very limited increase. Specifically, Ni-MOF requires a potential of 1.36 V (*vs.* RHE) to drive a current density of 10 mA cm^{-2}, which is significantly lower than those of $Ni(OH)_2$ (1.46 V) and Pt/C (1.64 V). In fact, this value obtained from the glassy carbon electrode is comparable or even lower than previous reported catalysts based on nickel foam or carbon cloth, including carbon/Ni–Fe (1.39 V), Ni_2P (1.38 V), L-MnO_2 (1.37 V) and so on (Table S2, ESI†).[26–28] Moreover, Ni-MOF also exhibits higher current density (120 mA cm^{-2}) than both $Ni(OH)_2$ (41 mA cm^{-2}) and Pt/C (6 mA cm^{-2}) at 1.6 V (*vs.* RHE) in Fig. S11 (ESI†). The current density of Ni-MOF can be further enhanced to 292 mA cm^{-2} by depositing it on conductive nickel foam (Fig. S10, ESI†), which outperforms state-of-the-art catalysts as shown in Table S2 (ESI†).

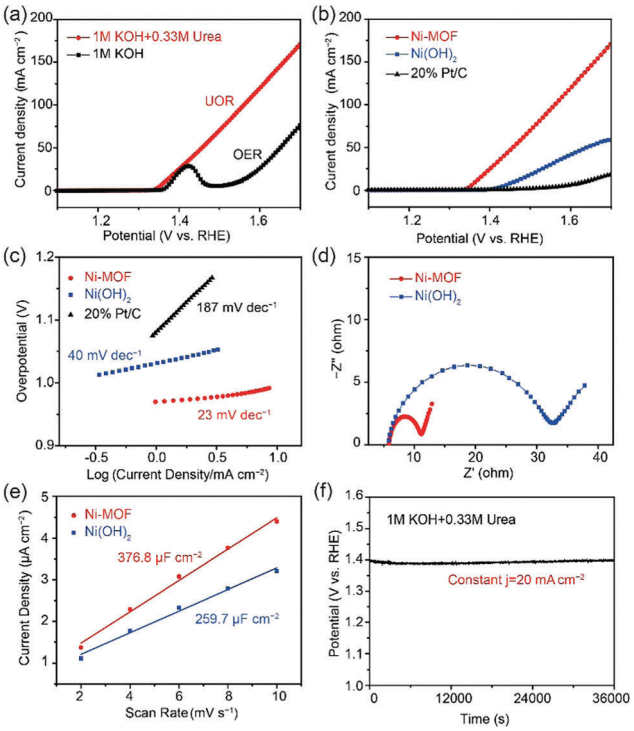

Fig. 4 (a) LSV curves of Ni-MOF in 1 M KOH electrolyte with and without 0.33 M urea at a scan rate of 10 mV s^{-1}. (b) LSV curves of Ni-MOF, $Ni(OH)_2$ and 20% Pt/C. (c) Tafel plots of Ni-MOF, $Ni(OH)_2$ and 20% Pt/C. (d) Nyquist plots of Ni-MOF and $Ni(OH)_2$. (e) Current density as a function of the scan rate to give the double-layer capacitance (C_{dl}) for Ni-MOF and $Ni(OH)_2$. (f) Galvanostatic experiment of Ni-MOF at a constant current density of 20 mA cm^{-2} for 36 000 s.

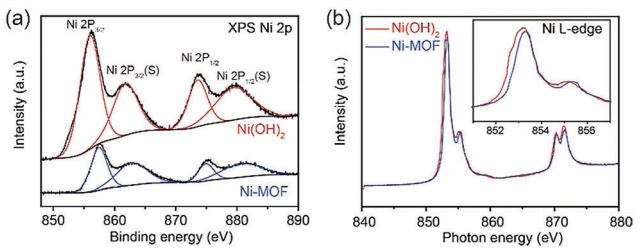

Fig. 3 (a) XPS Ni2p spectra of $Ni(OH)_2$ and Ni-MOF. (b) Synchrotron XANES Ni L-edge spectra of $Ni(OH)_2$ and Ni-MOF, and the inset shows the magnified absorption curve between 851.0 eV and 857.0 eV.

The outstanding UOR catalytic behavior of Ni-MOF is further evidenced by Tafel plots in Fig. 4c. The Tafel slope of Ni-MOF is only 23 mV dec^{-1}, which is much smaller than those of $Ni(OH)_2$ (40 mV dec^{-1}) and Pt/C (187 mV dec^{-1}). Such a small Tafel slope of Ni-MOF indicates its favorable reaction kinetics for UOR, which is also a desirable feature for practical applications. Electrochemical impedance spectroscopy (EIS) test was conducted to provide more insights into the electrode kinetics during UOR. Typical Nyquist plots of Ni-MOF and $Ni(OH)_2$ carried out at same potential of 1.6 V (*vs.* RHE) are displayed in Fig. 4d. The semicircular diameter of Ni-MOF (5.3 Ω) is much smaller than that of $Ni(OH)_2$ (26.9 Ω), revealing that Ni-MOF has a remarkably smaller charge transfer resistance during UOR.

The overall activity of a catalyst is determined by both the number of active sites and the intrinsic activity of every single site. The double-layer capacitance (C_{dl}), which is proportional to the electrochemical active surface area, was measured by cyclic voltammograms which were collected at a non-faradaic potential region (0.06 to 0.16 V *vs.* Ag/AgCl, Fig. S8 and S9, ESI†). As can be seen from Fig. 4e, the C_{dl} of Ni-MOF is 376.8 μF cm^{-2}, which is only 1.45 times higher than that of $Ni(OH)_2$, revealing that the high active site density of Ni-MOF nanosheets only makes a small contribution to the exceptional UOR performance. Therefore, the significant enhancement in the activity of Ni-MOF for UOR is mainly attributed to its higher intrinsic activity. Recent studies discovered that introducing more highly oxidized metal species in catalysts would promote oxidation reactions.[4,22] Previous XPS and XANES results confirm higher oxidation states of Ni cations in Ni-MOFs, which should be responsible for improved intrinsic catalytic activity. Aside from catalytic activity, stability is another crucial factor of the electrocatalysts for industrial applications. A galvanostatic experiment for Ni-MOF was performed at a constant current density of 20 mA cm^{-2}. As can be seen from Fig. 4f, Ni-MOF nanosheets exhibit strong durability with maintained UOR activity of over 36 000 s. All the results above clearly demonstrate Ni-MOFs as a highly efficient and stable catalyst for UOR.

In summary, we discovered Ni-MOF as a novel electrocatalyst for UOR. The ultrathin Ni-MOF nanosheets exhibit remarkable activity, favorable kinetics, and strong durability towards UOR. In addition to the high active site density of ultrathin Ni-MOF nanosheets, the exceptional UOR results are mainly attributed to high oxidation states of the nickel species. This study demonstrates Ni-MOF as a promising candidate for urea-related practical applications including purification of urea-rich wastewater, urea-assisted hydrogen production and direct urea fuel cells. More significantly, this work may shed light on heterogeneous catalyst design at the molecular level. By introducing appropriate molecules, the local electronic environment of metal cations can be well modified, thus making it possible to design advanced electrocatalysts with high oxidation states for a wide range of oxidation reactions.

This work was financially supported by the Australian Research Council (ARC) through the Discovery Project Programs (DP140104062, DP160104866, DP170104464 and LP160100927) and the National Natural Science Foundation of China (No. 21576202). XANES measurements were undertaken on the soft X-ray beamline at the Australian Synchrotron. D. D. Zhu acknowledges the financial support from the Chinese Scholarship Council (CSC).

Conflicts of interest

There are no conflicts to declare.

Notes and references

1 B. S. Yeo and A. T. Bell, *J. Phys. Chem. C*, 2012, **116**, 8394.
2 Z. Zhuang, W. Sheng and Y. Yan, *Adv. Mater.*, 2014, **26**, 3950.
3 L. Trotochaud, S. L. Young, J. K. Ranney and S. W. Boettcher, *J. Am. Chem. Soc.*, 2014, **136**, 6744.
4 B. S. Yeo and A. T. Bell, *J. Am. Chem. Soc.*, 2011, **133**, 5587.
5 A.-L. Wang, H. Xu, J.-X. Feng, L.-X. Ding, Y.-X. Tong and G.-R. Li, *J. Am. Chem. Soc.*, 2013, **135**, 10703.
6 R. Lan, S. Tao and J. T. S. Irvine, *Energy Environ. Sci.*, 2010, **3**, 438.
7 R. Ding, L. Qi, M. Jia and H. Wang, *Nanoscale*, 2014, **6**, 1369.
8 N. Kakati, J. Maiti, K. S. Lee, B. Viswanathan and Y. S. Yoon, *Electrochim. Acta*, 2017, **240**, 175.
9 B. K. Boggs, R. L. King and G. G. Botte, *Chem. Commun.*, 2009, 4859.
10 D. Wang, W. Yan, S. H. Vijapur and G. G. Botte, *J. Power Sources*, 2012, **217**, 498.
11 W. Yan, D. Wang and G. G. Botte, *Appl. Catal., B*, 2012, **127**, 221.
12 S. Periyasamy, P. Subramanian, E. Levi, D. Aurbach, A. Gedanken and A. Schechter, *ACS Appl. Mater. Interfaces*, 2016, **8**, 12176.
13 X. Zhu, X. Dou, J. Dai, X. An, Y. Guo, L. Zhang, S. Tao, J. Zhao, W. Chu, X. C. Zeng, C. Wu and Y. Xie, *Angew. Chem., Int. Ed.*, 2016, **55**, 12465.
14 C. Tan, X. Cao, X.-J. Wu, Q. He, J. Yang, X. Zhang, J. Chen, W. Zhao, S. Han, G.-H. Nam, M. Sindoro and H. Zhang, *Chem. Rev.*, 2017, **117**, 6225.
15 Y. Sun, S. Gao, F. Lei and Y. Xie, *Chem. Soc. Rev.*, 2015, **44**, 623.
16 S. Zhao, Y. Wang, J. Dong, C.-T. He, H. Yin, P. An, K. Zhao, X. Zhang, C. Gao, L. Zhang, J. Lv, J. Wang, J. Zhang, A. M. Khattak, N. A. Khan, Z. Wei, J. Zhang, S. Liu, H. Zhao and Z. Tang, *Nat. Energy*, 2016, **1**, 16184.
17 J. Duan, S. Chen and C. Zhao, *Nat. Commun.*, 2017, **8**, 15341.
18 Z. Li, X. Dou, Y. Zhao and C. Wu, *Inorg. Chem. Front.*, 2016, **3**, 1021.
19 L. Zhao, B. Dong, S. Li, L. Zhou, L. Lai, Z. Wang, S. Zhao, M. Han, K. Gao, M. Lu, X. Xie, B. Chen, Z. Liu, X. Wang, H. Zhang, H. Li, J. Liu, H. Zhang, X. Huang and W. Huang, *ACS Nano*, 2017, **11**, 5800.
20 Y.-Z. Su, K. Xiao, N. Li, Z.-Q. Liu and S.-Z. Qiao, *J. Mater. Chem. A*, 2014, **2**, 13845.
21 J. Wu, Z. Ren, S. Du, L. Kong, B. Liu, W. Xi, J. Zhu and H. Fu, *Nano Res.*, 2016, **9**, 713.
22 C. Guo, Y. Zheng, J. Ran, F. Xie, M. Jaroniec and S. Z. Qiao, *Angew. Chem., Int. Ed.*, 2017, **56**, 8539.
23 D. Wang, J. Zhou, Y. Hu, J. Yang, N. Han, Y. Li and T.-K. Sham, *J. Phys. Chem. C*, 2015, **119**, 19573.
24 R. P. Forslund, J. T. Mefford, W. G. Hardin, C. T. Alexander, K. P. Johnston and K. J. Stevenson, *ACS Catal.*, 2016, **6**, 5044.
25 G.-F. Chen, T. Y. Ma, Z.-Q. Liu, N. Li, Y.-Z. Su, K. Davey and S.-Z. Qiao, *Adv. Funct. Mater.*, 2016, **26**, 3314.
26 S. Chen, J. Duan, A. Vasileff and S. Z. Qiao, *Angew. Chem., Int. Ed.*, 2016, **55**, 3804.
27 G. Das, R. M. Tesfaye, Y. Won and H. H. Yoon, *Electrochim. Acta*, 2017, **237**, 171.
28 D. Liu, T. Liu, L. Zhang, F. Qu, G. Du, A. M. Asiri and X. Sun, *J. Mater. Chem. A*, 2017, **5**, 3208.

Supporting Information

Two-dimensional metal−organic frameworks with high oxidation state for efficient electrocatalytic urea oxidation

*Dongdong Zhu, Chunxian Guo, Jinlong Liu, Liang Wang, Yi Du, and Shizhang Qiao**

D. D. Zhu, Dr. C. X. Guo, J. L. Liu, Prof. S. Z. Qiao
School of Chemical Engineering, University of Adelaide, Adelaide, SA 5005, Australia
E-mail: s.qiao@adelaide.edu.au

L. Wang, Dr. Y. Du
Institute for Superconducting and Electronic Materials (ISEM), University of Wollongong, Wollongong, NSW 2525, Australia

1. Experimental Section

1.1 Materials

All chemicals, including N, N-Dimethylformamide (DMF), 1,4-benzenedicarboxylic acid (BDC), anhydrous ethanol, Triethylamine (TEA), Nickel(II) chloride hexahydrate ($NiCl_2 \cdot 6H_2O$), hexamethylenetetramine, Pt/C (20 wt% of Pt on Vulcan XC72), Nafion (15 wt%) were purchased from Sigma-Aldrich and used without further purification. Milli-Q water with a resistance of 18.2 MΩ was used in all experiments.

1.2 Synthesis of Ni-MOF nanosheets

32 mL DMF, 2 mL ethanol, and 2 mL water were firstly mixed in a 100mL glass bottle (Duran Schott). Then 0.75 mmol BDC and 0.75 mmol $NiCl_2 \cdot 6H_2O$ were added in the bottle, respectively. After the solution was stirred for 5 mins, 0.8 mL TEA was injected into the solution. Afterwards, the glass bottle was continuously ultrasonicated for 8 hours under ambient conditions. The resulting product was collected via centrifugation, washed with ethanol for 4 times, and dried by vacuum freeze-drying.

1.3 Synthesis of $Ni(OH)_2$ nanosheets

0.5 mmol $NiCl_2 \cdot 6H_2O$ and 168 mg hexamethylenetetramine were dissolved in 27 mL water and 3 mL ethanol under vigorous stirring. Then the solution was transferred into a 40 mL Teflon-lined stainless steel autoclave. The autoclave was sealed and heated at 120 °C for 12 h. After the autoclave was naturally cooled down to room temperature, the product was collected via centrifugation, washed with water for 4 times, and dried by vacuum freeze-drying.

1.4 Characterizations

The morphology of the samples was characterized by field emission scanning electron microscopy (SEM, QUANTA 450), transmission electron microscopy (TEM, Tecnai G2 Spirit, which operates at an accelerating voltage of 200 KV) and scanning transmission electron microscopy (STEM, JEOL JEM-ARM200F, which operates at an accelerating voltage of 80 KV) equipped with energy dispersive spectrometer (EDS), and atomic force microscopy (AFM, Asylum Research MFP-3D). The structure, and chemical composition of the samples were characterized by powder X-ray diffractometer (PXRD, Cu-target Bruker D8 Advance), X-ray photoelectron spectroscopy (XPS, ESCALab250) and Synchrotron-based X-ray absorption near edge spectra (XANES).The XANES measurements were carried out on the soft X-ray spectroscopy beamline at the Australian Synchrotron, which is equipped with a hemispherical electron analyser and a microchannel plate detector that enables a simultaneous recording of the total and partial electron yields.

1.5 Electrochemical Measurements

Electrocatalyst inks were prepared by mixing active material with carbon black and Nafion. Specifically, 5 mg Ni-MOF was dispersed in 1 mL H_2O, then 300 μL carbon black (3mg ml^{-1}) and 35 μL Nafion (5%) were added in the solution and sonicated over 1 h. Glassy carbon electrodes with an area of 0.196 cm^2 were polished to a mirror finish before use. Then, 10 μL of the electrocatalyst ink was drop-cast onto the electrode, and the electrocatalyst layer was dried overnight. For comparison, $Ni(OH)_2$, Pt/C were prepared by using same method on glassy carbon electrode, except that no carbon black was added for Pt/C. Ni-MOF/Ni foam was obtained by dropping 50 μL ink of Ni-MOF on 1cm^2 Ni foam.

Electrochemical tests were carried out in a three-electrode system on a workstation (CHI 760D Instruments, Inc., USA). Ag/AgCl (4 M KCl) electrode and carbon rod were used as the reference and counter electrodes, respectively. The reversible hydrogen electrode (RHE) potentials were obtained by the following equation: E(RHE) = E(Ag/AgCl) + 0.205 + 0.059 × pH. 1 M KOH and 0.33 M urea solution was used as the electrolyte for urea oxidation reaction test. A flow of N_2 (ultra-high-grade purity, Airgas) was maintained in the electrolyte during the test.

Before data collection, the working electrodes were scanned by cyclic voltammetry (CV) plots until the signals were stabilized. The linear sweep voltammetry (LSV) curves were recorded with a scan rate of 10 mV s^{-1}. Electrochemical impedance spectroscopy (EIS) was measured in the frequency range from 0.1 Hz to 100 kHz with an initial potential of 1.6 V (vs. RHE). The electrical double layer capacitor (C_{dl}) of the samples were obtained from CV plots in a small potential range of 0.06−0.16 V (vs. Ag/AgCl). The electrode durability was tested by Galvanostatic method, which was conducted at 20 mA cm^{-2} for 36000 s.

2. Supplementary Figures and Tables

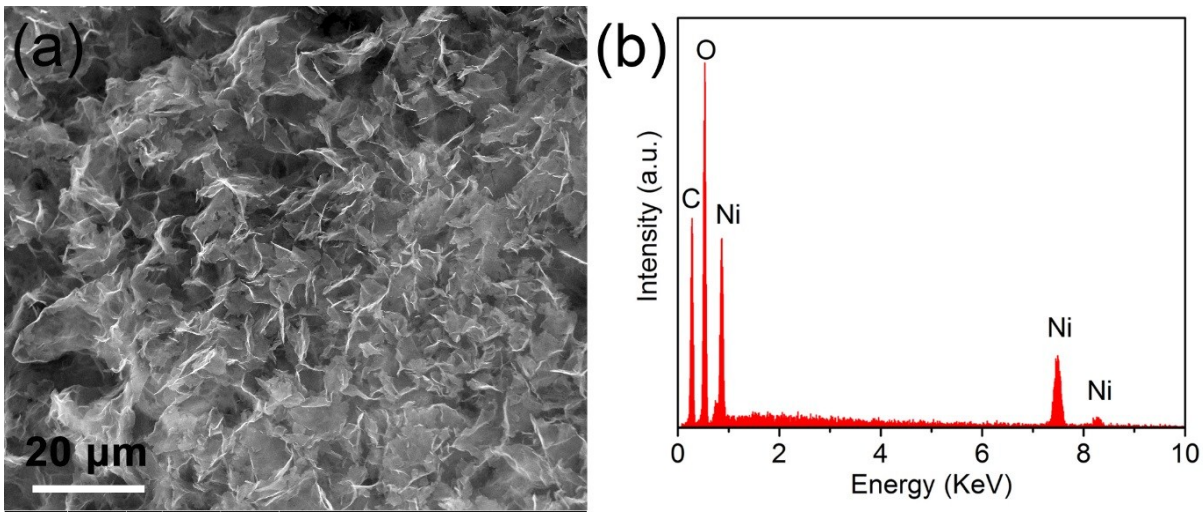

Fig. S1 (a) SEM image of Ni-MOF. (b) EDS spectrum of Ni-MOF.

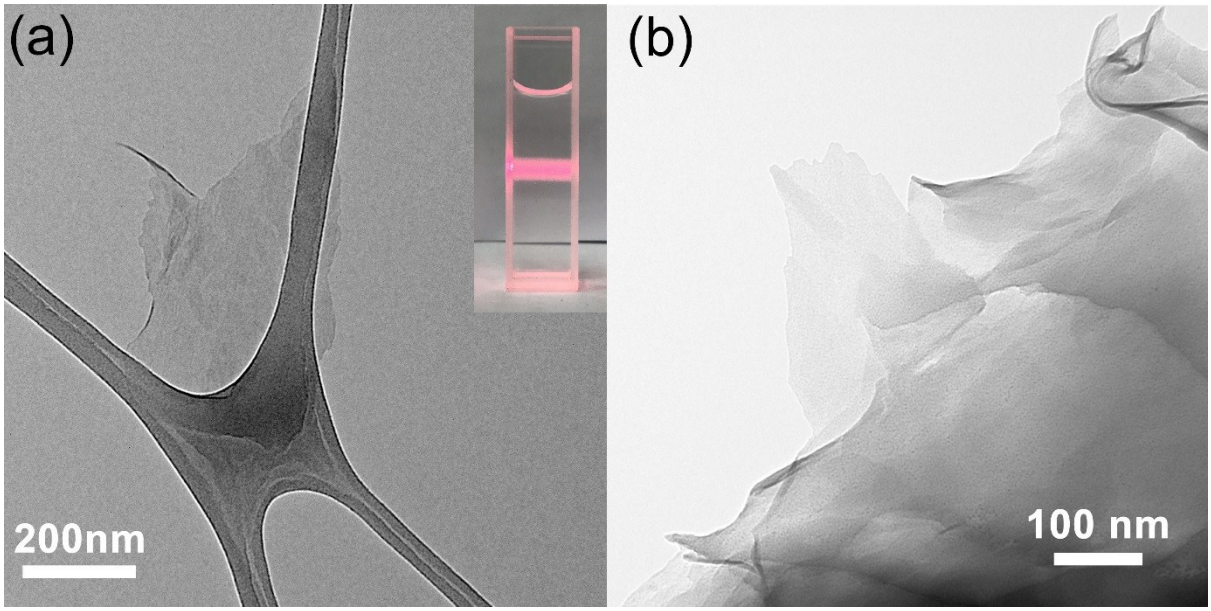

Fig. S2 (a, b) TEM images of Ni-MOF. The inset in S2a shows the Tyndall effect of the 2D Ni-MOF colloidal solution in water.

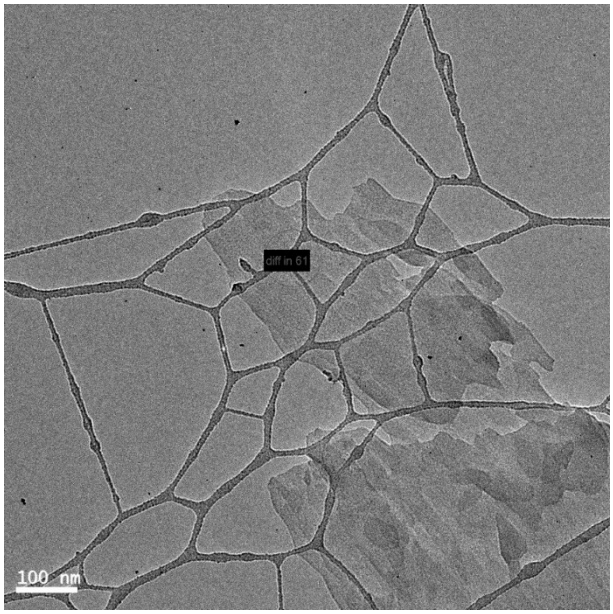

Fig. S3 The black square shows the area for SAED.

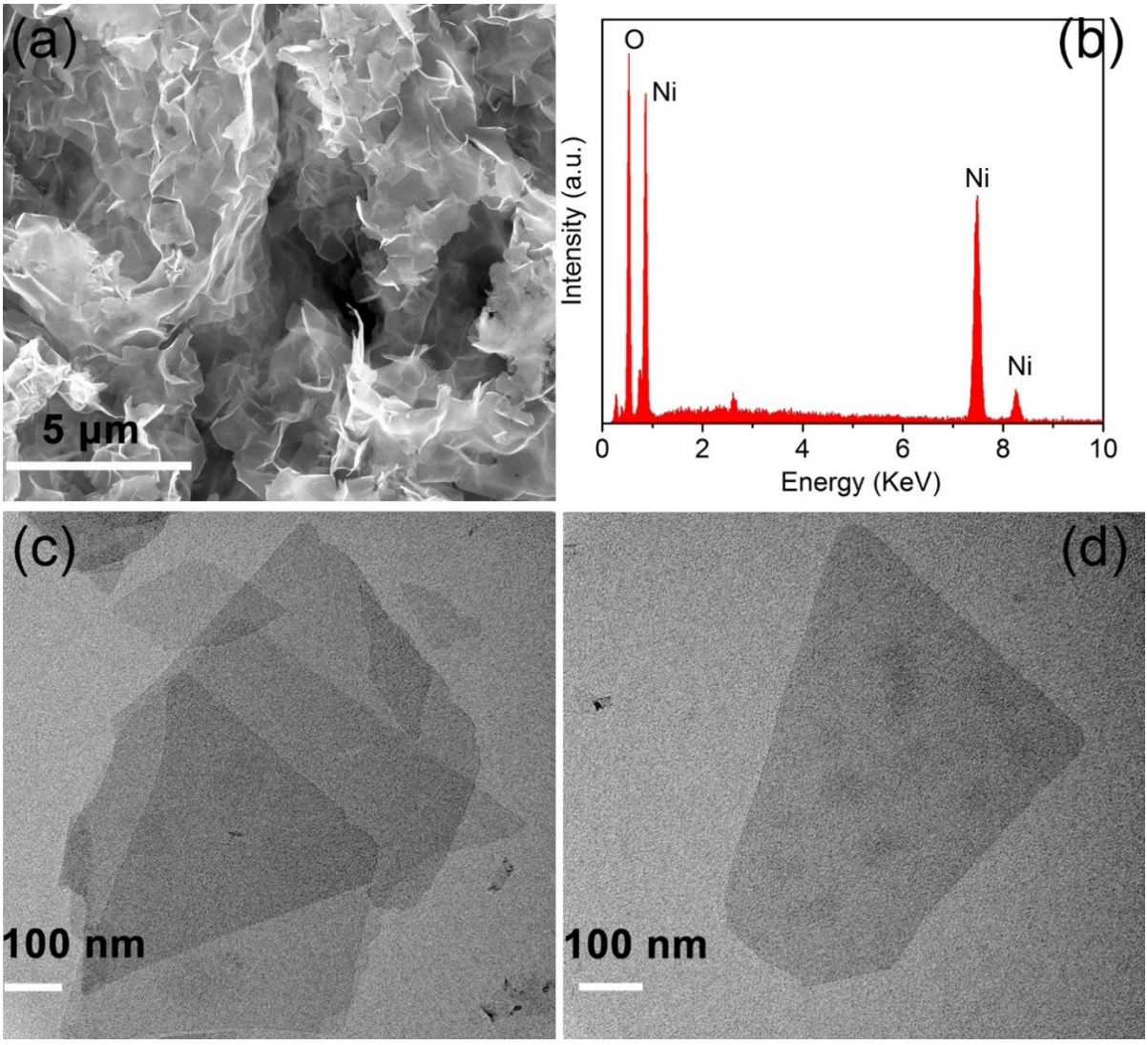

Fig. S4 (a) SEM, (b) EDS and (c,d) TEM images of $Ni(OH)_2$ nanosheets.

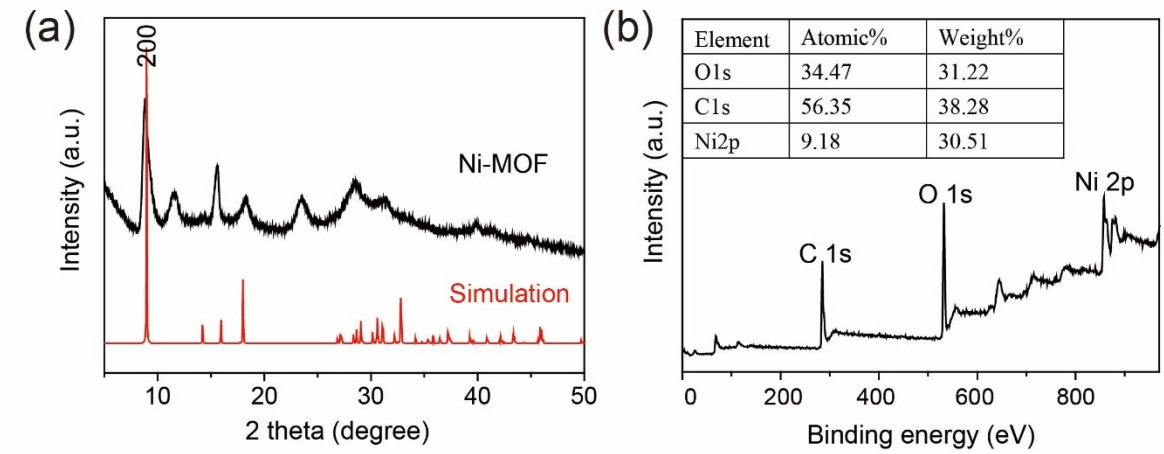

Fig. S5 (a) PXRD pattern of Ni-MOF and the simulated diffraction pattern based on the crystal structure. Two peaks with 2θ at 11.6 and 23.3˚ correspond to d-spacing of 7.6 and 3.8 Å, which should be related to layered materials. The similar results have been observed in previous works.[1-3] (b) XPS survey spectrum of Ni-MOF.

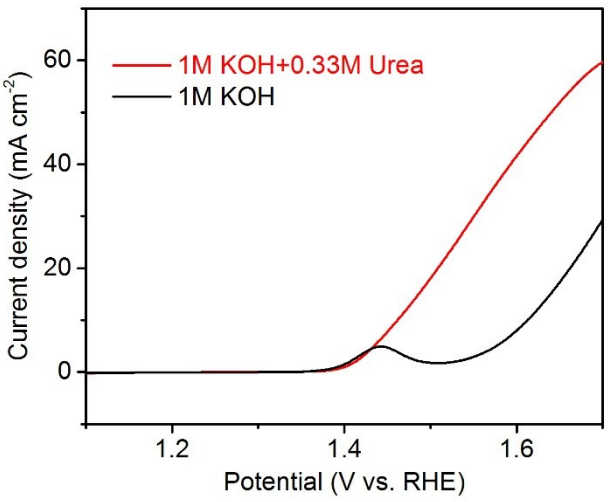

Fig. S6 LSV curves of $Ni(OH)_2$ in 1 M KOH electrolyte with and without 0.33M urea at a scan rate of 10mV s^{-1}.

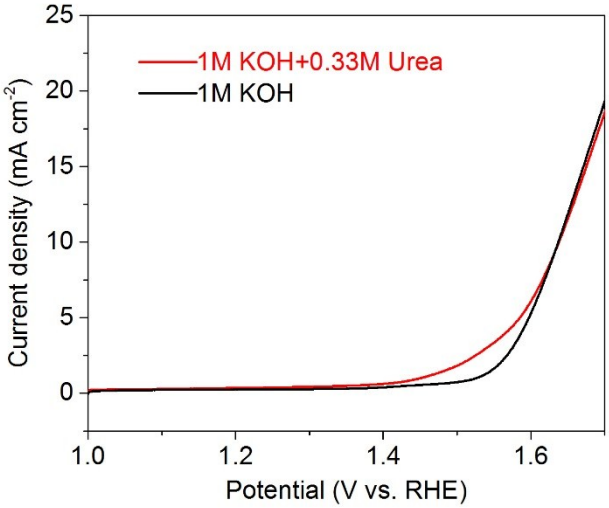

Fig. S7 LSV curves of 20% Pt/C in 1 M KOH electrolyte with and without 0.33M urea at a scan rate of 10mV s^{-1}.

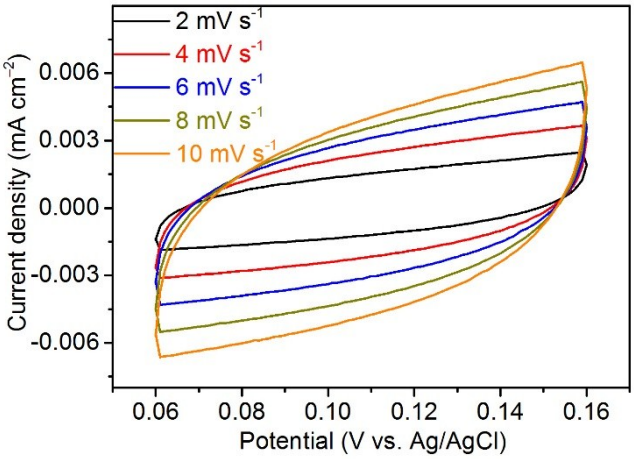

Fig. S8 CV curves recorded for Ni-MOF in a potential window (0.06 to 0.16 V vs Ag/AgCl) without faradaic processes.

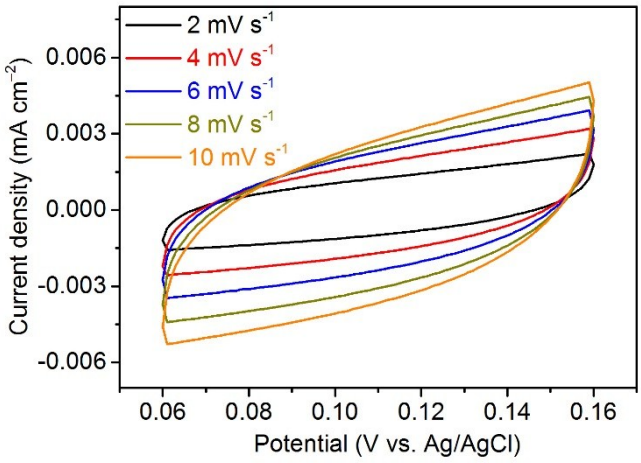

Fig. S9 CV curves recorded for $Ni(OH)_2$ in a potential window (0.06 to 0.16 V vs Ag/AgCl) without faradaic processes.

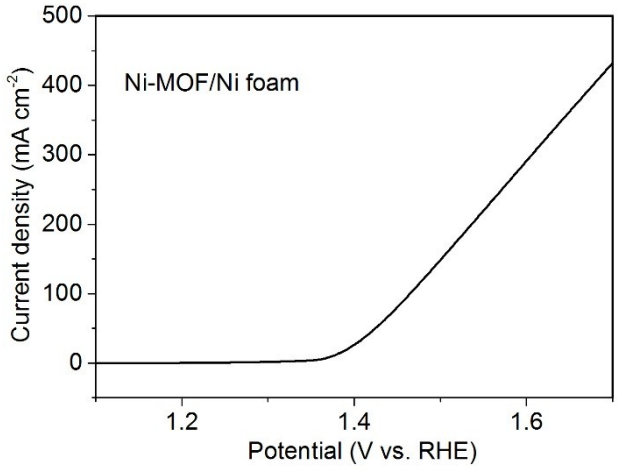

Fig. S10 LSV curve of Ni-MOF deposited on nickel foam.

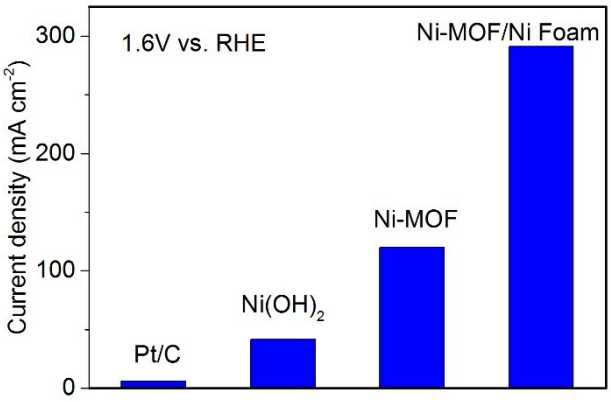

Fig. S11 (a) Current densities of Ni-MOF, $Ni(OH)_2$, Pt/C and Ni-MOF/Ni foam at 1.6V vs. RHE.

Table S1. Comparison of peak positions of Ni 2P for Ni-MOF and $Ni(OH)_2$ in XPS spectrum.

	Ni $2P_{3/2}$ (eV)	**Ni $2P_{3/2}$ (S) (eV)**	**Ni $2P_{1/2}$ (eV)**	**Ni $2P_{1/2}$ (S) (eV)**
Ni-MOF	857.6	862.6	875.1	881.4
$Ni(OH)_2$	856.1	861.7	873.6	880.6

Table S2. Comparison of the UOR activity between recently reported electrode materials.

Catalyst	**Potential @ 10 mA cm^{-2} (V vs. RHE)**	**Current density @ 1.6V (vs. RHE) (mA cm^{-2})**	**Substrate**	**Reference**
Ni-MOF	1.36	120	Glassy carbon	This work
$Ni(OH)_2$	1.46	41	Glassy carbon	This work
Ni-MOF	1.37	292	Nickel foam	This work
Metallic $Ni(OH)_2$	1.39	36 (peak current)	Glassy carbon	Angew. Chem. Int. Ed., **2016**, 55, 12465
Ni_2P	1.38	180	Carbon cloth	J. Mater. Chem. A, **2017**, 5, 3208
Ni_3N	1.35	130	Carbon cloth	Inorg. Chem. Front., **2017**, 4, 1120
Carbon/Ni-Fe	1.39	80	nickel foam	Electrochem. Acta, **2017**, 227, 210

Ni-Cr	1.38	90	Glassy carbon	ChemCatChem, 10.1002/cctc.201700451
NiO-Fe_2O_3	1.40	50	Graphene aerogel	Electrochem. Acta, **2017**, 237, 171
$LaNiO_3$	1.39	NA	Glassy carbon	ACS Catal., **2016**, 6, 5044
Ni-Co	1.53	20	Glassy carbon	Sci. Rep., **2014**, 4, 5863
Graphene-$Ni(OH)_2$	1.52	20	Glassy carbon	Electrochim. Acta, **2013**, 89, 732
L-MnO_2	1.37	170	Graphene–nickel foam	Angew. Chem. Int. Ed., **2016**, 55, 3804
S-MnO_2	1.33	260	Graphene–nickel foam	Angew. Chem. Int. Ed., **2016**, 55, 3804
MnO_2/$MnCo_2O_4$	1.33	270	Nickel foam	J. Mater. Chem. A, **2017**, 5, 7825

References

1 C. X. Guo, K. Sun, J. Ouyang and X. Lu, *Chem. Mater.*, 2015, **27**, 5813.

2 A. V. Murugan, B. B. Kale, C.-W. Kwon, G. Campet and K. Vijayamohanan, *Journal of Materials Chemistry*, 2001, **11**, 2470.

3 V. Petkov, P. N. Trikalitis, E. S. Bozin, S. J. L. Billinge, T. Vogt and M. G. Kanatzidis, *J. Am. Chem. Soc.*, 2002, **124**, 10157.

Chapter 4: 2D Metal-Organic Framework/$Ni(OH)_2$ Heterostructure for Enhanced Oxygen Evolution Reaction

4.1 Introduction and Significance

2D metal-organic frameworks (MOFs) are widely regarded as promising electrocatalysts for oxygen evolution reaction (OER). However, 2D MOFs have an unwanted tendency to aggregate, which severely limits its potential application. We fabricated a novel 2D MOF-$Ni(OH)_2$ heterostructure via a facile sonication-assisted solution method. Due to rational material design, the large surface area of MOF is well maintained. More impressively, because of the strong electron interactions between MOF and $Ni(OH)_2$, the electronic structure of $Ni(OH)_2$ component is well modified, leading to the generation of $Ni(OH)_2$ with higher oxidation state, which is highly desirable for OER. As expected, the as-fabricated Ni-BDC/$Ni(OH)_2$ (BDC stands for 1,4-benzenedicarboxylate, $C_8H_4O_4$) hybrid nanosheets exhibited significantly improved OER performance when compared with pure Ni-BDC, $Ni(OH)_2$ and commercial Ir/C. Highlights of this work include:

1. New strategy to synthesise 2D MOF-based hybrid materials. Novel Ni-BDC/ $Ni(OH)_2$ hybrid nanosheets were obtained via a facile sonication-assisted solution method. The simple strategy developed here can be readily extended to the preparation of other 2D MOF-based hybrid nanosheets, such as MOF-MoS_2, MOF-Metal oxide and MOF-Graphene, etc, which surely will draw much attention from the research area of catalysis, battery, gas separation and storage, sensing, etc.

2. Rational catalyst design. Coupling Ni-BDC with $Ni(OH)_2$ significantly prevents its aggregation, and the obtained Ni-BDC/$Ni(OH)_2$ nanosheets provide larger surface areas for electrocatalysis. The strong interactions between $Ni(OH)_2$ and Ni-BDC decrease the electron density around Ni atoms in $Ni(OH)_2$. Thus, Ni cations with higher oxidation states are achieved in $Ni(OH)_2$ component, which contributes greatly to the outstanding OER activity of Ni-BDC/$Ni(OH)_2$. Therefore, both the number of active sites and intrinsic activity of each active site are increased in this rationally designed material.

3. Excellent activity and stability. The as-fabricated Ni-BDC/$Ni(OH)_2$ hybrid nanosheets exhibit high activity, favourable kinetics (41 mV dec^{-1}) and strong durability (20 h) towards alkaline OER. In detail, the current density of Ni-BDC/$Ni(OH)_2$ is 82.5 mA cm^{-2} at 1.6 V (vs.

RHE), which is significantly greater than that for Ni-BDC (5.5 times), $Ni(OH)_2$ (20.6 times), and Ir/C (3.0 times).

4.2 2D Metal-Organic Framework/$Ni(OH)_2$ Heterostructure for Enhanced Oxygen Evolution Reaction

This chapter is included as it appears as a journal paper published by **Dongdong Zhu**, Jinlong Liu, Liang Wang, Yi Du, Yao Zheng, Kenneth Davey and Shi-Zhang Qiao, 2D Metal-Organic Framework/$Ni(OH)_2$ Heterostructure for Enhanced Oxygen Evolution Reaction, ***submitted***.

Statement of Authorship

Title of Paper	2D Metal-Organic Framework/$Ni(OH)_2$ Heterostructure for Enhanced Oxygen Evolution Reaction
Publication Status	☐ Published ☐ Accepted for Publication ☑ Submitted for Publication ☐ Unpublished and Unsubmitted work written in manuscript style
Publication Details	Dongdong Zhu, Jinlong Liu, Liang Wang, Yi Du, Yao Zheng, Kenneth Davey, and Shi-Zhang Qiao, 2D Metal-Organic Framework/$Ni(OH)_2$ Heterostructure for Enhanced Oxygen Evolution Reaction, submitted.

Principal Author

Name of Principal Author (Candidate)	Dongdong Zhu		
Contribution to the Paper	Project design, sample synthesis, most of the characterizations, electrochemical tests, data analysis, and manuscript drafting.		
Overall percentage (%)	60%		
Certification:	This paper reports on original research I conducted during the period of my Higher Degree by Research candidature and is not subject to any obligations or contractual agreements with a third party that would constrain its inclusion in this thesis. I am the primary author of this paper.		
Signature		Date	18/12/2018

Co-Author Contributions

By signing the Statement of Authorship, each author certifies that:

i. the candidate's stated contribution to the publication is accurate (as detailed above);

ii. permission is granted for the candidate in include the publication in the thesis; and

iii. the sum of all co-author contributions is equal to 100% less the candidate's stated contribution.

Name of Co-Author	Jinlong Liu		
Contribution to the Paper	Assistance with electrocatalytic testing and analysis. 5%		
Signature		Date	18/12/2018

Name of Co-Author	Liang Wang		
Contribution to the Paper	Assistance with TEM characterization. 5%		
Signature		Date	18.12.2018

Name of Co-Author	Yi Du		
Contribution to the Paper	Assistance with TEM characterization. 5%		
Signature		Date	18.12.2018

Name of Co-Author	Yao Zheng		
Contribution to the Paper	Discussion of the project and manuscript revision. 5%		
Signature		Date	19/12/2018

Name of Co-Author	Kenneth Davey		
Contribution to the Paper	Assistance with manuscript editing and polishing. 5%		
Signature		Date	19 December 2018

Name of Co-Author	Shi-Zhang Qiao		
Contribution to the Paper	Supervision of the work, and manuscript evaluation. 15%		
Signature		Date	19/Dec/2018

Journal Name

ARTICLE

2D Metal-Organic Framework/$Ni(OH)_2$ Heterostructure for Enhanced Oxygen Evolution Reaction

Received 00th January 20xx,
Accepted 00th January 20xx

DOI: 10.1039/x0xx00000x

www.rsc.org/

Dongdong Zhu,[a] Jinlong Liu,[a] Liang Wang,[b] Yi Du,[b] Yao Zheng,[a] Kenneth Davey[a] and Shi-Zhang Qiao*[a]

2D metal-organic frameworks (MOFs) are widely regarded as promising electrocatalysts for oxygen evolution reaction (OER). This results from inherent properties such as large portion of surface coordinatively unsaturated metal atoms, rapid mass transfer and enhanced conductivity. However, 2D MOFs have a strong tendency to aggregate, which severely limits their potential application for OER. Here, novel 2D Ni-BDC/$Ni(OH)_2$ (BDC stands for 1,4-benzenedicarboxylate, $C_8H_4O_4$) hybrid nanosheets are synthesized via a facile sonication-assisted solution method. Because of the rational material design, the large surface area of Ni-BDC is maintained. Significantly, after coupling, the electronic structure of Ni atoms in $Ni(OH)_2$ component is well modified, leading to the generation of Ni cations with higher oxidation states, which are desirable for OER. The as-prepared Ni-BDC/$Ni(OH)_2$ exhibits high activity, favorable kinetics and strong durability towards the OER. Specifically, the OER current density of Ni-BDC/$Ni(OH)_2$ is 82.5 mA cm^{-2} at 1.6 V versus reversible hydrogen electrode (RHE), which is significantly greater than that of Ni-BDC (5.5 times), $Ni(OH)_2$ (20.6 times) and Ir/C (3.0 times). Moreover, the sonication-assisted method developed in this work can be readily adapted for preparation of various 2D MOF-based hybrid functional materials.

Introduction

Clean and renewable energy technologies such as fuel cells, water splitting and metal-air batteries, are being widely investigated to meet increasing global energy demands while also preserve the world environment.[1-3] Electrochemical processes including hydrogen evolution reaction (HER), oxygen evolution reaction (OER), oxygen reduction reaction (ORR), and carbon dioxide reduction reaction (CRR) play critical roles in these technologies.[4-8] Highly active electrocatalysts are urgently needed to reduce high overpotentials associated with sluggish kinetics of these processes. From a theoretical perspective, the reaction activity of an electrocatalyst is determined by both the number of active sites and the intrinsic activity of each site.[9, 10] Constructing ultrathin 2D nanosheets is hypothesized to be an ideal way to expose more active sites.[11] Application of the Sabatier principle indicates that a catalyst with appropriate surface binding energies for reaction intermediates will provide optimal catalytic activity.[5] Basically, the binding energy of the reaction intermediates to the catalyst surface is determined largely by the electronic structure of the catalyst itself.[12] Therefore, engineering the electronic structure of the catalyst through modification of its composition and physical structure should be a means to enhance its intrinsic activity.[13] However, it is still quite challenging to rationally design an electrocatalyst with both increased number of active sites and improved intrinsic activity.

Metal-organic frameworks (MOFs), an important class of porous crystalline materials, are composed of metal-containing nodes and organic linkers with strong coordination bonds.[14-16] They have emerged in a wide range of fields, including gas storage and separation, catalysis, biomedicine and chemical sensing due to inherent characteristics such as tunable structure, ultrahigh specific surface area and uniform pore size distribution.[17-21] In particular, 2D MOF nanosheets have recently drawn increasing attention for electrocatalysis owing to their appealing properties: nanometer thickness and high porosity enable rapid mass transfer, while rich defects originated from ultrathin nature of the nanosheets contribute to enhanced conductivity.[22, 23] Importantly, a high percentage of metal atoms are exposed on the surface of 2D MOF nanosheets as accessible active sites, and these coordinatively unsaturated metal sites have more dangling bonds that could facilitate the interaction with reaction intermediates, which are highly desirable for catalysis.[24] Further, by using appropriate organic ligands, the electronic structure of metal nodes can be purposely tailored to obtain metal cations with high oxidation states in 2D MOF. It is known for example that highly oxidative metal cations can promote the performance of oxidation reactions, such as OER, urea oxidation reaction, and

[a] School of Chemical Engineering, The University of Adelaide, Adelaide, SA 5005, Australia. E-mail: s.qiao@adelaide.edu.au
[b] Institute for Superconducting and Electronic Materials (ISEM), University of Wollongong, Wollongong, NSW 2525, Australia.
† Electronic Supplementary Information (ESI) available: See DOI: 10.1039/x0xx00000x

ethanol oxidation reaction.[25, 26] However, a signifcant drawback is that 2D MOFs have a strong tendency to aggregate. This severely hinders their practical application in electrochemical surface-related reactions. Therefore, it is highly essential to prevent such aggregation to retain the large surface area.

OER underpins various energy conversion technologies, and the state-of-the-art electrocatalysts for this sluggish reaction are noble metals such as RuO_2 and IrO_2.[27, 28] However, scarcity and expense restrict their large-scale applications. Therefore, earth-abundant and less expensive transition metal-based compounds have been widely investigated as alternatives.[29, 30] Among these, $Ni(OH)_2$ is considered attractive because of its intrinsic water oxidation ability, high stability and resistance to corrosion.[31-33] Although numerous efforts have been devoted to exploring efficient catalysts based on $Ni(OH)_2$, currently the OER performance of $Ni(OH)_2$ is still far from satisfactory. This is thought to result from a relatively low oxidation state of the nickel cations.[25] Accordingly, in order to achieve superior OER property, the electronic structure of $Ni(OH)_2$ needs to be well modified to optimize adsorption of the reaction intermediates on its surface.

In this contribution, a novel 2D MOF/$Ni(OH)_2$ heterostructure, Ni-BDC/$Ni(OH)_2$ (BDC stands for 1,4-benzenedicarboxylate, $C_8H_4O_4$), was designed and fabricated as an efficient OER electrocatalyst. In this hybrid material system, the large surface area of Ni-BDC is maintained. Meanwhile, due to the strong electron interactions between $Ni(OH)_2$ and Ni-BDC, the electronic structure of $Ni(OH)_2$ is well modified, giving rise to the formation of $Ni(OH)_2$ with higher oxidation states, which is favourable for the OER. As a result, the as-fabricated Ni-BDC/$Ni(OH)_2$ hybrid nanosheets exhibited significantly improved OER performance, which is superior to the individual components and even surpasses benchmark commercial Ir/C catalyst.

Results and Discussion

Figure 1 schematically shows the fabrication process of Ni-BDC/$Ni(OH)_2$. Firstly, $Ni(OH)_2$ nanosheets were synthesized via a simple hydrothermal method using $NiCl_2{\cdot}6H_2O$ and hexamethylenetetramine as precursors.[34] The as-fabricated

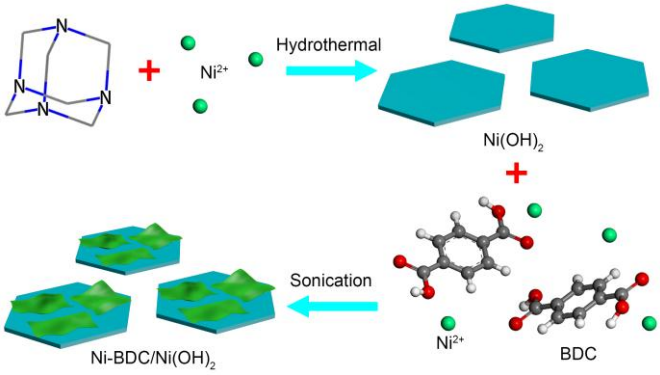

Fig. 1 Schematic illustration of the synthesis process for the Ni-BDC/$Ni(OH)_2$ hybrid nanosheets.

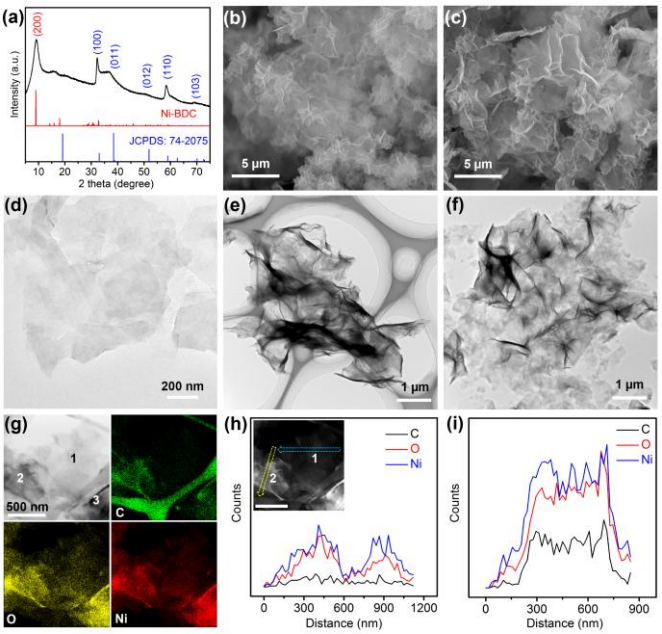

Fig. 2 (a) XRD pattern for Ni-BDC/$Ni(OH)_2$. (b, c) SEM images for $Ni(OH)_2$ and Ni-BDC/$Ni(OH)_2$. (d–f) TEM images of $Ni(OH)_2$, Ni-BDC, and Ni-BDC/$Ni(OH)_2$. (g) TEM image of Ni-BDC/$Ni(OH)_2$ and corresponding elemental mapping. (h, i) EDS line scan for area 1 and 2 as indicated in HAADF-STEM image of Ni-BDC/$Ni(OH)_2$ (inset).

$Ni(OH)_2$ nanosheets were added into the solution containing organic ligands (BDC) and $NiCl_2{\cdot}6H_2O$, and then Ni-BDC/$Ni(OH)_2$ hybrid nanosheets were obtained by a facile sonication-assisted solution method (*see* Experimental Section).

Successful fabrication of Ni-BDC/$Ni(OH)_2$ was confirmed by powder X-ray diffraction (XRD). As is seen in Figure 2a, in addition to the characteristic peaks arising from $Ni(OH)_2$ (JCPDS: 74-2075), there is a distinct diffraction peak centered at two-theta of 9°, which can be well assigned to the (200) plane of Ni-BDC (No. 985792, Cambridge Crystallographic Data Center).[35] The crystal structure of Ni-BDC (Figure S1) indicates that each nickel atom is octahedrally coordinated by six oxygen atoms from BDC ligands or hydroxyls. These nickel-based pseudo-octahedra connect with each other in the lattice plane (200) to form nickel-oxygen layers that are separated by organic BDC layers.[24] Scanning electron microscopy (SEM) images (Figure 2b and Figure S2) reveal that the as-fabricated $Ni(OH)_2$ sample has an obvious sheet-like morphology. After depositing Ni-BDC (Figures S3) on the surface of $Ni(OH)_2$, the nanosheet morphology is maintained, and the lateral size of the obtained hybrid nanosheets is about several micrometers (Figure 2c and Figures S4). The transmission electron microscopy (TEM) image of Figure 2d indicates that $Ni(OH)_2$ nanosheets have smooth surface without any obvious wrinkles. Meanwhile, the TEM image in Figure 2e gives the nanosheet morphology of pure Ni-BDC. Of note, the presence of wrinkles and folds reveals its good flexibility, which is quite similar to the behavior of graphene. It is evident from contrasting the TEM image for Ni-BDC/$Ni(OH)_2$ (Figure 2f) that flexible Ni-BDC nanosheets are clearly attached to the relatively flat $Ni(OH)_2$ nanosheets.

In order to get more insights into the coupling of Ni-BDC and $Ni(OH)_2$, energy dispersive X-ray spectroscopy (EDS) mapping test was carried out. As exhibited in Figure 2g, the corresponding elemental mapping confirms the existence of C, O, and Ni in Ni-BDC/$Ni(OH)_2$, which is in good agreement with XRD results (Figure 2a) and EDS spectrum (Figure S5). More significantly, for Ni-BDC/$Ni(OH)_2$ hybrid nanosheets, the only elemental difference between Ni-BDC and $Ni(OH)_2$ is carbon. It is concluded therefore that the different distributions of C and O, Ni indicate that Ni-BDC nanosheets (area 2,3 in Figure 2g) are clearly deposited on the surface of the $Ni(OH)_2$ nanosheets (area 1 in Figure 2g). The corresponding high-angle annular dark field (HAADF)-scanning tunneling electron microscopy (STEM) image of Ni-BDC/$Ni(OH)_2$ is given as the inset in Figure 2h. EDS line scan was performed on area 1 and 2 (inset of Figure 2h) to garner additional evidence. The line-profile analysis in Figure 2h demonstrates that the signal for C is negligible for area 1. This confirms that area 1 is pure $Ni(OH)_2$. By contrast, Figure 2i shows a strong signal for C in area 2, which reveals the existence of Ni-BDC in area 2. Moreover, at a distance between 0 and 200 nm (Figure 2i), the signal of C is significantly low. As the signal for C is strong in the middle of area 2, it is concluded that Ni-BDC is deposited on $Ni(OH)_2$ in area 2, which agrees well with previous EDS mapping results (Figure 2g). In all, it is evident that the purposefully designed Ni-BDC/$Ni(OH)_2$ hybrid nanosheets were in fact successfully fabricated.

X-ray photoelectron spectroscopy (XPS) measurements were further carried out to analyze surface chemical states of the samples. Figure 3a shows the high-resolution Ni 2p XPS spectra of $Ni(OH)_2$ and Ni-BDC. To be specific, the Ni 2p spectrum for $Ni(OH)_2$ displays two main peaks located at 855.6 and 873.4 eV (Figure S6) together with two shakeup satellite peaks, which are attributed to Ni $2p_{3/2}$ and Ni $2p_{1/2}$, respectively. The spin-energy separation between these two main peaks is 17.8 eV, which verifies the $Ni(OH)_2$ phase.[36] The Ni 2p spectrum distribution for Ni-BDC is similar to that for $Ni(OH)_2$, but all the Ni 2p peaks are obviously shifted to higher binding energy regions (Figure S6), indicating that the Ni atoms in Ni-BDC possess lower electron densities than in $Ni(OH)_2$. Therefore, it is concluded that BDC draws more electrons from the Ni cations through Ni–O bonds compared with hydroxyl, demonstrating that BDC is a meaningfully better electron acceptor.[25] The formation process of the Ni-BDC/$Ni(OH)_2$ hybrid nanosheets is proposed as follows: $Ni(OH)_2$ partially loses hydroxyls in the weak acid environment during sonication, and then the deprotonated BDC ligands could react with these coordinatively unsaturated Ni atoms of $Ni(OH)_2$ to generate the Ni-BDC/$Ni(OH)_2$ heterostructure. Based on previous XPS results, an interaction mechanism of $Ni(OH)_2$ and Ni-BDC from Ni-BDC/$Ni(OH)_2$ is proposed in Figure 3b. By coupling with Ni-BDC, the local electronic environment of Ni atoms in $Ni(OH)_2$ can be manipulated. In brief, some hydroxyls of $Ni(OH)_2$ are replaced by BDC, which means that Ni atoms lose more electrons, allowing for the formation of Ni cations with higher oxidation states in the $Ni(OH)_2$ component of the hybrid material. From an experimental point of view, it is however difficult to solely investigate the change in oxidation state of the Ni cations in $Ni(OH)_2$ because both Ni-BDC and $Ni(OH)_2$ possess Ni cations.

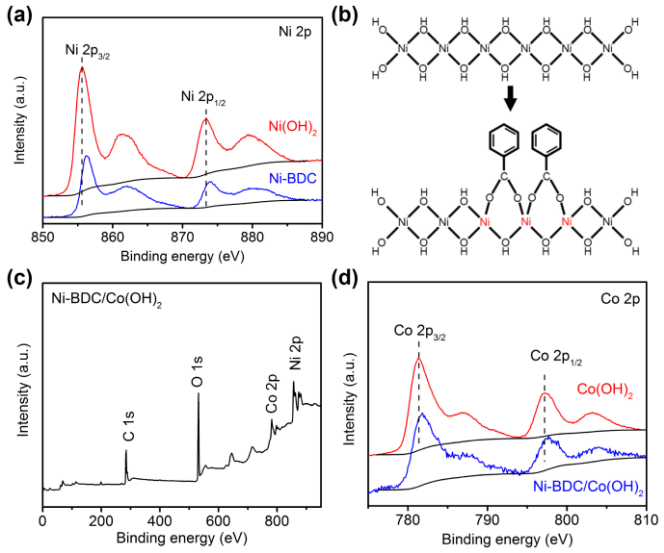

Fig. 3 (a) Ni 2p XPS spectra for $Ni(OH)_2$ and Ni-BDC. (b) Proposed interaction mechanism of $Ni(OH)_2$ and Ni-BDC from Ni-BDC/$Ni(OH)_2$. (c) XPS survey spectrum for Ni-BDC/$Co(OH)_2$. (d) Co 2p XPS spectra for $Co(OH)_2$ and Ni-BDC/$Co(OH)_2$.

To nevertheless demonstrate the hypothesis that the introduction of Ni-BDC can improve the oxidation state of $Ni(OH)_2$, a similar material system, Ni-BDC/$Co(OH)_2$ was designed and fabricated. As displayed in Figure 3c, the XPS survey spectrum of Ni-BDC/$Co(OH)_2$ shows distinct signals for Co, Ni, O and C, in line with its elemental mapping and EDS results (Figure S7), suggesting the successful fabrication of the Ni-BDC/$Co(OH)_2$ heterostructure. After coupling with Ni-BDC, all the Co 2p peaks of $Co(OH)_2$ shift noticeably to higher binding energy regions as shown in Figure 3d. Specifically, for Co $2p_{3/2}$ main peak, the binding energy for Ni-BDC/$Co(OH)_2$ is 0.5 eV higher than that for $Co(OH)_2$ (Figure S8), reflecting a higher oxidation state of Co cations in Ni-BDC/$Co(OH)_2$, and this is consistent well with former assumption. It is concluded that through careful fabrication of MOF-metal hydroxide heterostructure, the electronic structure of the metal cations in the metal hydroxide can be purposefully tailored, which is of great significance for achieving highly active and efficient electrocatalysts.

To assess the electrocatalytic performance towards the OER, Ni-BDC/$Ni(OH)_2$ hybrid nanosheets were tested in a typical three-electrode cell containing 1.0 M KOH solution. To permit direct comparison, pristine Ni-BDC, $Ni(OH)_2$ and commercial Ir/C with the same mass loading were also tested. Figure 4a presents linear sweep voltammetry (LSV) curves of the samples (IR corrected) at a slow scan rate of 1 mV s^{-1} (this rate was used to minimize the influence from capacitance behavior). Impressively, Ni-BDC/$Ni(OH)_2$ exhibits the highest current densities among all the samples at the potential beyond 1.55 V (vs. RHE), directly confirming that the coupling of $Ni(OH)_2$ and Ni-BDC can significantly improve the catalytic activity. The overpotential required to achieve a current density of 10 mA cm^{-2} is a key evaluation parameter for OER.[37] As displayed in Figure 4b, the overpotential for Ni-BDC/$Ni(OH)_2$ is only 320 mV,

which is considerably smaller than that for Ni-BDC (358 mV), $Ni(OH)_2$ (395 mV), and even Ir/C (332 mV). Moreover, this enhanced OER performance of Ni-BDC/$Ni(OH)_2$ is validated by current densities at a fixed overpotential as shown in Figure 4c. At an overpotential of 370 mV, the current density for Ni-BDC/$Ni(OH)_2$ is 82.5 mA cm^{-2}, which is 5.5, 20.6 and 3.0 times higher than that for Ni-BDC, $Ni(OH)_2$ and Ir/C, respectively. More impressively, as shown in Table S1, the OER performance of Ni-BDC/$Ni(OH)_2$ is superior to that of many other recently reported electrocatalysts based on MOF or $Ni(OH)_2$ in alkaline environment.[38-42] The excellent OER performance of Ni-BDC/$Ni(OH)_2$ is further testified through Tafel plots. A low Tafel plot is favorable for practical application, as it means a remarkably enhanced OER rate can be achieved with an increase in overpotential.[43] As depicted in Figure 4d, Ni-BDC/$Ni(OH)_2$ exhibits the lowest Tafel slope of 41 mV dec^{-1} among all the samples, indicating its most rapid OER kinetics. In addition to catalytic activity, stability is another critical criterion for evaluating a catalyst. As can be seen in Figure 4e, no obvious potential shift is observed in the LSV curves for Ni-BDC/$Ni(OH)_2$ sample after 2500 cyclic voltammetry (CV) cycles. Moreover, the chronopotentiometric curve in Figure 4f demonstrates that Ni-BDC/$Ni(OH)_2$ has strong durability with maintained OER activity for 20 hours at a constant current density of 10 mA cm^{-2}. All the results above clearly demonstrate that Ni-BDC/$Ni(OH)_2$ is an efficient and stable catalyst for OER.

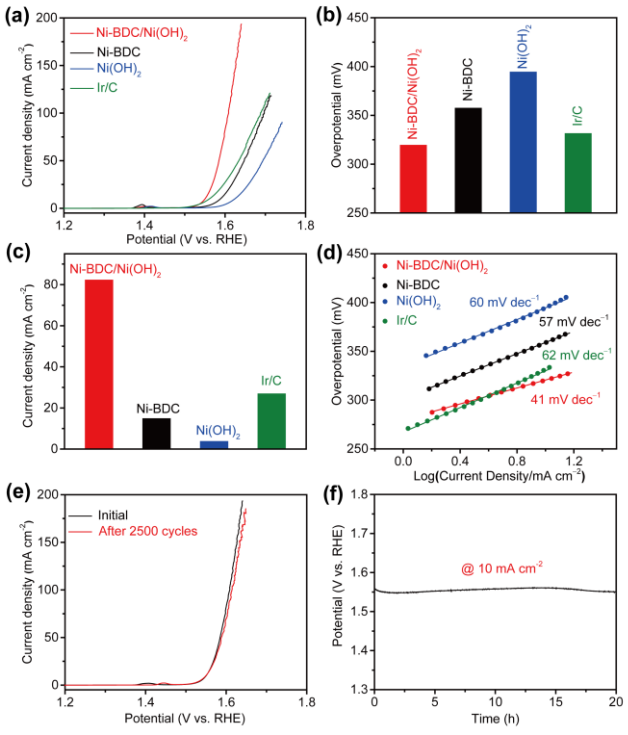

Fig. 4 (a) OER LSV curves for Ni-BDC/$Ni(OH)_2$, Ni-BDC, $Ni(OH)_2$ and Ir/C in 1.0 M KOH at a scan rate of 1 mV s^{-1}. (b) Overpotentials for Ni-BDC/$Ni(OH)_2$, Ni-BDC, $Ni(OH)_2$ and Ir/C required to deliver 10 mA cm^{-2}. (c) OER current densities for Ni-BDC/$Ni(OH)_2$, Ni-BDC, $Ni(OH)_2$ and Ir/C at 1.6 V vs. RHE. (d) Tafel plots for Ni-BDC/$Ni(OH)_2$, Ni-BDC, $Ni(OH)_2$ and Ir/C. (e) LSV curves for Ni-BDC/$Ni(OH)_2$ recorded before and after 2500 CV cycles. (f) Chronopotentiometric response of Ni-BDC/$Ni(OH)_2$ at a constant current density of 10 mA cm^{-2} for 20 hours.

Since the activity of a catalyst is controlled by both the number of active sites and intrinsic activity of each site, it is necessary to investigate the electrochemically active surface area (ECSA) to estimate the number of exposed active sites and probe the intrinsic activity.[44] To this end, the double-layer capacitance (C_{dl}), which is proportional to the ECSA, was obtained via using CV measurements under different scan rates in a non-Faradaic potential window (Figure 5a, S9 and S10).[45] As can be seen in Figure 5b, the C_{dl} for Ni-BDC/$Ni(OH)_2$ is 1070 μF cm^{-2}, which is meaningfully greater than that for both pure Ni-BDC (416 μF cm^{-2}) and $Ni(OH)_2$ (576 μF cm^{-2}), implying that the coupling of Ni-BDC and $Ni(OH)_2$ significantly improves the ECSA, which contributes greatly to the exceptional OER activity of Ni-BDC/$Ni(OH)_2$. To investigate the intrinsic activity of the samples, the apparent current density was further normalized to the corresponding ECSA. The normalization curves in Figure 5c reveal that the OER activity of Ni-BDC is remarkably higher than that for $Ni(OH)_2$, which agrees well with previous reports that metal cations with higher oxidation state in electrocatalysts are favorable for oxidation reactions.[25] Notably, the Ni-BDC/$Ni(OH)_2$ hybrid nanosheets exhibit greatest intrinsic activity for OER. Based on such a comparison, constructing Ni-BDC/$Ni(OH)_2$ heterostructure not only exposes more active sites, but also improves the intrinsic activity. Electrochemical impedance spectroscopy (EIS) was performed to gain more insights to the charge-transfer kinetics at the electrode/electrolyte interface. According to the Nyquist plots (Figure 5d), the semicircular diameter of $Ni(OH)_2$, Ni-BDC and Ni-BDC/$Ni(OH)_2$ are 82, 36 and 15 Ω, respectively, manifesting that Ni-BDC/$Ni(OH)_2$ has the smallest charge transfer resistance during OER process.

It is concluded that the demonstrated superior OER activity of Ni-BDC/$Ni(OH)_2$ can be attributed to rational design of its composition and structure. Firstly, the aggregation of Ni-BDC is significantly mitigated by coupling with $Ni(OH)_2$, and the

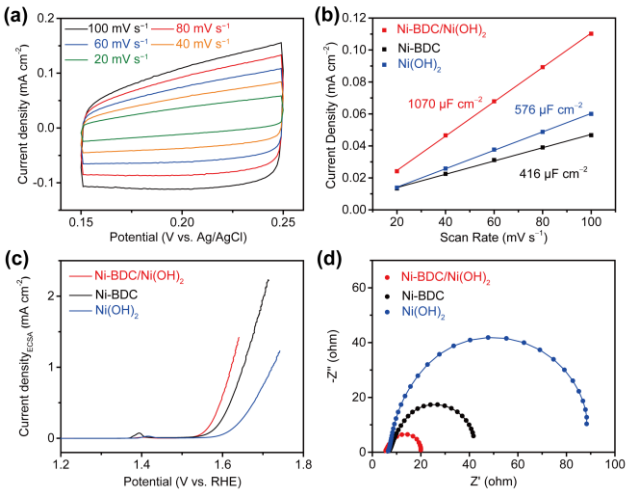

Fig. 5 (a) CV curves for Ni-BDC/$Ni(OH)_2$ at scan rates from 20 to 100 mV s^{-1}. (b) Current density as a function of scan rate to derive C_{dl} for Ni-BDC/$Ni(OH)_2$, Ni-BDC and $Ni(OH)_2$. (c) OER LSV curves for Ni-BDC/$Ni(OH)_2$, Ni-BDC and $Ni(OH)_2$ from Figure. 4a normalized to the ECSA. (d) Nyquist plots for Ni-BDC/$Ni(OH)_2$, Ni-BDC and $Ni(OH)_2$ measured at 1.56 V vs. RHE.

obtained Ni-BDC/$Ni(OH)_2$ nanosheets can provide a larger active surface area for OER. Secondly, at the interface between $Ni(OH)_2$ and Ni-BDC, strong interactions between Ni atoms from $Ni(OH)_2$ and neighbouring BDC from Ni-BDC could decrease the electron density around the Ni atoms. Therefore, Ni cations with higher oxidation states are achieved in $Ni(OH)_2$ component, which contribute greatly to boosting the intrinsic OER activity of Ni-BDC/$Ni(OH)_2$.[46-48] Thirdly, from the point of view of structure, 2D materials own some intrinsic advantages for electrocatalysis. Comparing with bulk counterparts, more atoms are exposed on the surface of Ni-BDC/$Ni(OH)_2$ nanosheets as active sites, and these coordinatively unsaturated metal atoms are favorable for OER.[49, 50] Moreover, the unique nanosheet structure with high porosity facilitates rapid mass transport of electrolyte to the reaction sites and the release of gaseous O_2 product.[51] Collectively, all these features of Ni-BDC/$Ni(OH)_2$ hybrid nanosheets are responsible for the fascinating OER performance.

Conclusions

In summary, Ni-BDC/$Ni(OH)_2$ hybrid nanosheets were successfully fabricated via a simple sonication-assisted solution method. Compared to pure Ni-BDC or $Ni(OH)_2$, a larger electrochemical surface area is achieved in Ni-BDC/$Ni(OH)_2$. More importantly, due to the strong electron interactions between $Ni(OH)_2$ and Ni-BDC, the electronic structure of Ni atoms in $Ni(OH)_2$ is well manipulated, resulting in the formation of Ni cations with higher oxidation state, which evidently enhance the OER activity. As a consequence, both the number of active sites and intrinsic activity of each active site are increased in this rationally designed material. Benefitting from these merits, Ni-BDC/$Ni(OH)_2$ exhibited superior activity, favorable kinetics and outstanding stability towards alkaline OER, outperforming the performance of each component and even commercial Ir/C catalyst. Considering the composition versatility of 2D materials, a collection of 2D MOF-based hybrid nanosheets (MOF-MoS_2, MOF-metal oxide, MOF-graphene, etc.) can be obtained, which are quite promising for a wide range of applications including catalysis, battery, gas separation and storage, sensing, and so on.

Experimental

Chemicals

All chemicals, including hexamethylenetetramine, nickel(II) chloride hexahydrate ($NiCl_2{\cdot}6H_2O$), N, N-dimethylformamide (DMF), 1,4-benzenedicarboxylic acid (BDC), anhydrous ethanol, triethylamine (TEA), Ir/C (20 wt.% of Ir on Vulcan XC72), Nafion (15 wt.%) were purchased from Sigma-Aldrich and used without further purification. Milli-Q water with a resistance of 18.2 MΩ was used in all experiments.

Synthesis of Ni-BDC/$Ni(OH)_2$ hybrid nanosheets

Firstly, $Ni(OH)_2$ nanosheets were fabricated by a simple hydrothermal method. In details, 120 mg $NiCl_2{\cdot}6H_2O$ and 168 mg hexamethylenetetramine were dissolved in a mixed solution of 27 mL water and 3 mL ethanol under vigorous stirring for 20 min. Then the resulting solution was transferred into a 40 mL Teflon-lined stainless steel autoclave. The autoclave was sealed and heated at 120 °C for 12 h. After the autoclave was naturally cooled down to room temperature, the product was collected via centrifugation, washed with water for four times, and dried by vacuum freeze-drying.

Afterwards, the Ni-BDC/$Ni(OH)_2$ hybrid nanosheets were obtained by a sonication-assisted solution method. Typically, 16 mg $Ni(OH)_2$ was dispersed in a mixed solution (32 mL DMF, 2 mL ethanol and 2 mL water) in a 100 mL glass bottle (Duran Schott). Next, 0.06 mmol BDC and 0.06 mmol $NiCl_2{\cdot}6H_2O$ were added in the bottle. After the solution was stirred for 5 min, 0.2 mL TEA was injected into the solution. Subsequently, the glass bottle was continuously ultrasonicated for 4 h under ambient conditions. The resulting product was collected via centrifugation, washed with ethanol for four times, and dried at 60 °C in a vacuum oven.

To permit comparison, pure Ni-BDC was generated via the similar method. In brief, 32 mL DMF, 2 mL ethanol and 2 mL water were firstly mixed in a 100 mL glass bottle. Then 0.75 mmol BDC and 0.75 mmol $NiCl_2{\cdot}6H_2O$ were added in the bottle, respectively. After the solution was stirred for 5 min, 0.8 mL TEA was injected into the solution. Afterwards, the glass bottle was continuously ultrasonicated for 8 h under ambient conditions. The final product was collected via centrifugation, washed with ethanol for four times, and dried at 60 °C in a vacuum oven.

Material Characterizations

The morphology of the samples was characterized by field emission scanning electron microscopy (SEM, QUANTA 450) equipped with energy dispersive spectrometer (EDS), transmission electron microscopy (TEM, Tecnai G2 Spirit, which operates at an accelerating voltage of 200 kV) and scanning transmission electron microscopy (STEM, JEOL JEM-ARM200F, which operates at an accelerating voltage of 80 kV) equipped with EDS. The powder XRD data was collected by Rigaku MiniFlex 600 with Cu Kα radiation at a scan rate of 1° min^{-1}. XPS measurements were carried out on ESCALab250 using Al Kα radiation.

Electrochemical Measurements

Electrocatalyst inks were prepared by mixing active material with carbon black and Nafion. Specifically, 5 mg Ni-BDC/$Ni(OH)_2$ hybrid nanosheets were dispersed in 1 mL H_2O, and then 500 µL carbon black (2 mg ml^{-1}) and 100 µL Nafion (1 wt.%) were added in the solution and sonicated for 1 h. Glassy carbon electrodes with an area of 0.196 cm^2 were polished to a mirror finish prior to use. Then, 10 µL of the electrocatalyst ink was drop-cast onto the electrode and the electrocatalyst layer was dried overnight. To permit comparison, $Ni(OH)_2$, Ni-BDC and Ir/C inks were prepared using the same method and loaded on glassy carbon electrode, except that no carbon black was added for Ir/C.

Electrochemical tests were carried out in a three-electrode glass cell (Pine Research Instruments, USA) on a workstation (CHI 760D Instruments, Inc., USA). Ag/AgCl (4 M KCl) electrode and carbon rod were used as the reference and counter electrodes, respectively. The reversible hydrogen electrode (RHE) potentials were obtained by the following equation: E(RHE) = E(Ag/AgCl) + 0.205 + 0.059 × pH. 1.0 M KOH solution was used as the electrolyte for the OER test. A flow of O_2 (ultra-high-grade purity, Airgas) was maintained in the electrolyte during the test in order to ensure the O_2/H_2O equilibrium at 1.23 V vs. RHE. Therefore, the overpotential (η) for OER was calculated as follows: η = E(RHE) − 1.23 V.

Before data collection, the working electrodes were scanned by cyclic voltammetry (CV) until the signals were stabilized. The linear sweep voltammetry (LSV) curves were recorded with a scan rate of 1 mV s^{-1}. The current density was normalized to the geometrical surface area. Electrochemical impedance spectroscopy (EIS) was measured in the frequency range from 0.1 Hz to 100 kHz with an amptitude of 5 mV at a potential of 1.56 V (vs. RHE). IR compensation of LSV curves was performed using the solution resistance estimated from EIS measurements. The capacitance of double layer (C_{dl}) of the samples were obtained via CV technique in a non-Faradaic potential range of 0.15 to 0.25 V (vs. Ag/AgCl). The specific capacitance for a flat surface is generally found to be in the range of 20 to 60 μF cm^{-2}. Herein, a value of 40 μF cm^{-2} was used in the calculations for the electrochemical active surface area.[52] The electrode durability was tested by repetitive CV scans for 2500 cycles in a potential window of 0.2 to 0.55 V (vs. Ag/AgCl) and chronopotentiometry measurement at 10 mA cm^{-2} for 20 h.

Conflicts of interest

The authors declare no competing financial interest.

Acknowledgements

This work was financially supported by the Australian Research Council (ARC) through the Discovery Project programs (DP140104062, DP160104866, DP170104464 and LP160100927) and the National Natural Science Foundation of China (No. 21576202). D. D. Zhu acknowledges the financial support from the Chinese Scholarship Council (CSC). The authors also thank Laiquan Li, Fangxi Xie, Huanyu Jin, and Dr. Chunxian Guo for very useful discussions.

Notes and references

1. M. S. Faber and S. Jin, *Energy Environ. Sci.*, 2014, **7**, 3519-3542.
2. H. Mistry, A. S. Varela, S. Kühl, P. Strasser and B. R. Cuenya, *Nat. Rev. Mater.*, 2016, **1**, 16009.
3. V. R. Stamenkovic, D. Strmcnik, P. P. Lopes and N. M. Markovic, *Nat. Mater.*, 2017, **16**, 57.
4. X. Zou and Y. Zhang, *Chem. Soc. Rev.*, 2015, **44**, 5148-5180.
5. D. D. Zhu, J. L. Liu and S. Z. Qiao, *Adv. Mater.*, 2016, **28**, 3423-3452.
6. W. Xia, A. Mahmood, Z. Liang, R. Zou and S. Guo, *Angew. Chem. Int. Ed.*, 2016, **55**, 2650-2676.
7. J. Liu, D. Zhu, C. Guo, A. Vasileff and S.-Z. Qiao, *Adv. Energy Mater.*, 2017, **7**, 1700518.
8. J. Liu, D. Zhu, Y. Zheng, A. Vasileff and S.-Z. Qiao, *ACS Catal.*, 2018, **8**, 6707-6732.
9. Z. W. Seh, J. Kibsgaard, C. F. Dickens, I. Chorkendorff, J. K. Nørskov and T. F. Jaramillo, *Science*, 2017, **355**, eaad4998.
10. J. Liu, Y. Zheng, Y. Jiao, Z. Wang, Z. Lu, A. Vasileff and S.-Z. Qiao, *Small*, 2018, **14**, 1704073.
11. J. Bao, X. Zhang, B. Fan, J. Zhang, M. Zhou, W. Yang, X. Hu, H. Wang, B. Pan and Y. Xie, *Angew. Chem.*, 2015, **127**, 7507-7512.
12. Y. Jiao, Y. Zheng, M. Jaroniec and S. Z. Qiao, *Chem. Soc. Rev.*, 2015, **44**, 2060-2086.
13. J. K. Nørskov, T. Bligaard, J. Rossmeisl and C. H. Christensen, *Nat. Chem.*, 2009, **1**, 37.
14. H. Furukawa, K. E. Cordova, M. O'Keeffe and O. M. Yaghi, *Science*, 2013, **341**, 1230444.
15. A. Schoedel, M. Li, D. Li, M. O'Keeffe and O. M. Yaghi, *Chem. Rev.*, 2016, **116**, 12466-12535.
16. S. Dang, Q.-L. Zhu and Q. Xu, *Nat. Rev. Mater.*, 2017, **3**, 17075.
17. L. Sun, M. G. Campbell and M. Dincă, *Angew. Chem. Int. Ed.*, 2016, **55**, 3566-3579.
18. B. Li, H. M. Wen, Y. Cui, W. Zhou, G. Qian and B. Chen, *Adv. Mater.*, 2016, **28**, 8819-8860.
19. L. Jiao, Y. Wang, H. L. Jiang and Q. Xu, *Adv. Mater.*, 2017, 1703663.
20. X. Cao, C. Tan, M. Sindoro and H. Zhang, *Chem. Soc. Rev.*, 2017, **46**, 2660-2677.
21. Z. Liang, C. Qu, W. Guo, R. Zou and Q. Xu, *Adv. Mater.*, 2018, **30**, 1702891.
22. J. Duan, S. Chen and C. Zhao, *Nat. Commun.*, 2017, **8**, 15341.
23. M. Zhao, Y. Huang, Y. Peng, Z. Huang, Q. Ma and H. Zhang, *Chem. Soc. Rev.*, 2018, **47**, 6267-6295.
24. S. Zhao, Y. Wang, J. Dong, C.-T. He, H. Yin, P. An, K. Zhao, X. Zhang, C. Gao, L. Zhang, J. Lv, J. Wang, J. Zhang, A. M. Khattak, N. A. Khan, Z. Wei, J. Zhang, S. Liu, H. Zhao and Z. Tang, *Nat. Energy*, 2016, **1**, 16184.
25. D. Zhu, C. Guo, J. Liu, L. Wang, Y. Du and S.-Z. Qiao, *Chem. Commun.*, 2017, **53**, 10906-10909.
26. A.-L. Wang, H. Xu, J.-X. Feng, L.-X. Ding, Y.-X. Tong and G.-R. Li, *J. Am. Chem. Soc.*, 2013, **135**, 10703-10709.
27. B. Zhang, X. Zheng, O. Voznyy, R. Comin, M. Bajdich, M. García-Melchor, L. Han, J. Xu, M. Liu, L. Zheng, F. P. García de Arquer, C. T. Dinh, F. Fan, M. Yuan, E. Yassitepe, N. Chen, T. Regier, P. Liu, Y. Li, P. De Luna, A. Janmohamed, H. L. Xin, H. Yang, A. Vojvodic and E. H. Sargent, *Science*, 2016, **352**, 333-337.
28. M. Tahir, L. Pan, F. Idrees, X. Zhang, L. Wang, J.-J. Zou and Z. L. Wang, *Nano Energy*, 2017, **37**, 136-157.
29. L. Han, S. Dong and E. Wang, *Adv. Mater.*, 2016, **28**, 9266-9291.
30. I. Roger, M. A. Shipman and M. D. Symes, *Nat. Rev. Chem.*, 2017, **1**, 0003.
31. M. Gao, W. Sheng, Z. Zhuang, Q. Fang, S. Gu, J. Jiang and Y. Yan, *J. Am. Chem. Soc.*, 2014, **136**, 7077-7084.
32. J. Xie, X. Zhang, H. Zhang, J. Zhang, S. Li, R. Wang, B. Pan and Y. Xie, *Adv. Mater.*, 2017, **29**, 1604765.
33. C. Luan, G. Liu, Y. Liu, L. Yu, Y. Wang, Y. Xiao, H. Qiao, X. Dai and X. Zhang, *ACS Nano*, 2018, **12**, 3875-3885.
34. Z. Li, X. Dou, Y. Zhao and C. Wu, *Inorg. Chem. Front.*, 2016, **3**, 1021-1027.

35. G. Hai, X. Jia, K. Zhang, X. Liu, Z. Wu and G. Wang, *Nano Energy*, 2018, **44**, 345-352.
36. H. B. Li, M. H. Yu, F. X. Wang, P. Liu, Y. Liang, J. Xiao, C. X. Wang, Y. X. Tong and G. W. Yang, *Nat. Commun.*, 2013, **4**, 1894.
37. C. C. McCrory, S. Jung, J. C. Peters and T. F. Jaramillo, *J. Am. Chem. Soc.*, 2013, **135**, 16977-16987.
38. C. Tang, H. S. Wang, H. F. Wang, Q. Zhang, G. L. Tian, J. Q. Nie and F. Wei, *Adv. Mater.*, 2015, **27**, 4516-4522.
39. X.-F. Lu, P.-Q. Liao, J.-W. Wang, J.-X. Wu, X.-W. Chen, C.-T. He, J.-P. Zhang, G.-R. Li and X.-M. Chen, *J. Am. Chem. Soc.*, 2016, **138**, 8336-8339.
40. K. Fan, H. Chen, Y. Ji, H. Huang, P. M. Claesson, Q. Daniel, B. Philippe, H. Rensmo, F. Li, Y. Luo and L. Sun, *Nat. Commun.*, 2016, **7**, 11981.
41. L. Zhao, B. Dong, S. Li, L. Zhou, L. Lai, Z. Wang, S. Zhao, M. Han, K. Gao, M. Lu, X. Xie, B. Chen, Z. Liu, X. Wang, H. Zhang, H. Li, J. Liu, H. Zhang, X. Huang and W. Huang, *ACS Nano*, 2017, **11**, 5800-5807.
42. X.-L. Wang, L.-Z. Dong, M. Qiao, Y.-J. Tang, J. Liu, Y. Li, S.-L. Li, J.-X. Su and Y.-Q. Lan, *Angew. Chem. Int. Ed.*, 2018, **57**, 9660-9664.
43. S. Anantharaj, S. R. Ede, K. Sakthikumar, K. Karthick, S. Mishra and S. Kundu, *ACS Catal.*, 2016, **6**, 8069-8097.
44. M. S. Faber, R. Dziedzic, M. A. Lukowski, N. S. Kaiser, Q. Ding and S. Jin, *J. Am. Chem. Soc.*, 2014, **136**, 10053-10061.
45. Y. Yin, J. Han, Y. Zhang, X. Zhang, P. Xu, Q. Yuan, L. Samad, X. Wang, Y. Wang, Z. Zhang, P. Zhang, X. Cao, B. Song and S. Jin, *J. Am. Chem. Soc.*, 2016, **138**, 7965-7972.
46. B. S. Yeo and A. T. Bell, *J. Am. Chem. Soc.*, 2011, **133**, 5587-5593.
47. G. Liu, P. Li, G. Zhao, X. Wang, J. Kong, H. Liu, H. Zhang, K. Chang, X. Meng, T. Kako and J. Ye, *J. Am. Chem. Soc.*, 2016, **138**, 9128-9136.
48. C. Guo, Y. Zheng, J. Ran, F. Xie, M. Jaroniec and S. Z. Qiao, *Angew. Chem. Int. Ed.*, 2017, **56**, 8539-8543.
49. Y. Sun, S. Gao, F. Lei and Y. Xie, *Chem. Soc. Rev.*, 2015, **44**, 623-636.
50. L. Liang, H. Cheng, F. Lei, J. Han, S. Gao, C. Wang, Y. Sun, S. Qamar, S. Wei and Y. Xie, *Angew. Chem. Int. Ed.*, 2015, **54**, 12004-12008.
51. C. Tan, X. Cao, X.-J. Wu, Q. He, J. Yang, X. Zhang, J. Chen, W. Zhao, S. Han, G.-H. Nam, M. Sindoro and H. Zhang, *Chem. Rev.*, 2017, **117**, 6225-6331.
52. C. Zhang, Y. Huang, Y. Yu, J. Zhang, S. Zhuo and B. Zhang, *Chem. Sci.*, 2017, **8**, 2769-2775.

Supporting Information

2D Metal-Organic Framework/$Ni(OH)_2$ Heterostructure for Enhanced Oxygen Evolution Reaction

Dongdong Zhu,[a] Jinlong Liu,[a] Liang Wang,[b] Yi Du,[b] Yao Zheng,[a] Kenneth Davey[a] and Shi-Zhang Qiao*[a]

[a] School of Chemical Engineering, The University of Adelaide, Adelaide, SA 5005, Australia
E-mail: s.qiao@adelaide.edu.au

[b] Institute for Superconducting and Electronic Materials (ISEM), University of Wollongong, Wollongong, NSW 2525, Australia

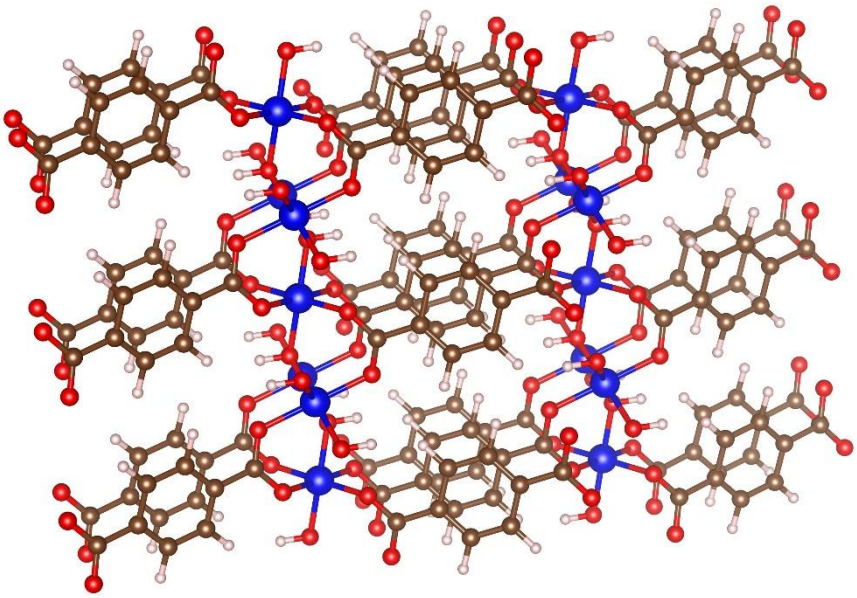

Figure S1. Crystal structure of Ni-BDC. Color scheme for atom representation: blue for Ni, red for O, grey for C and white for H.

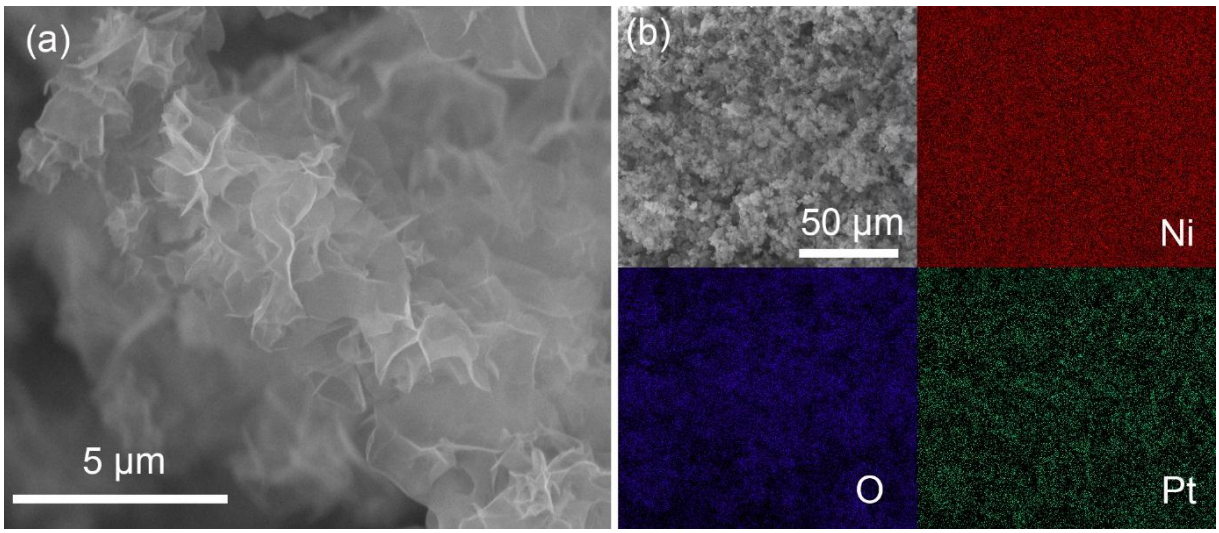

Figure S2. a) SEM image of $Ni(OH)_2$. b) Element mapping of $Ni(OH)_2$ for the selected area.

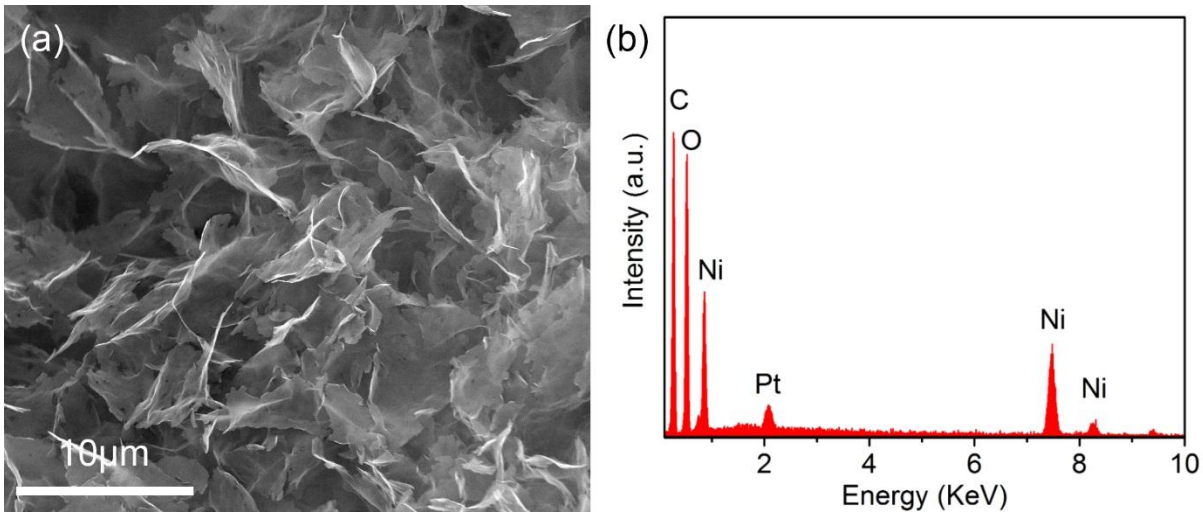

Figure S3. a) SEM image of Ni-BDC. b) EDS spectrum of Ni-BDC.

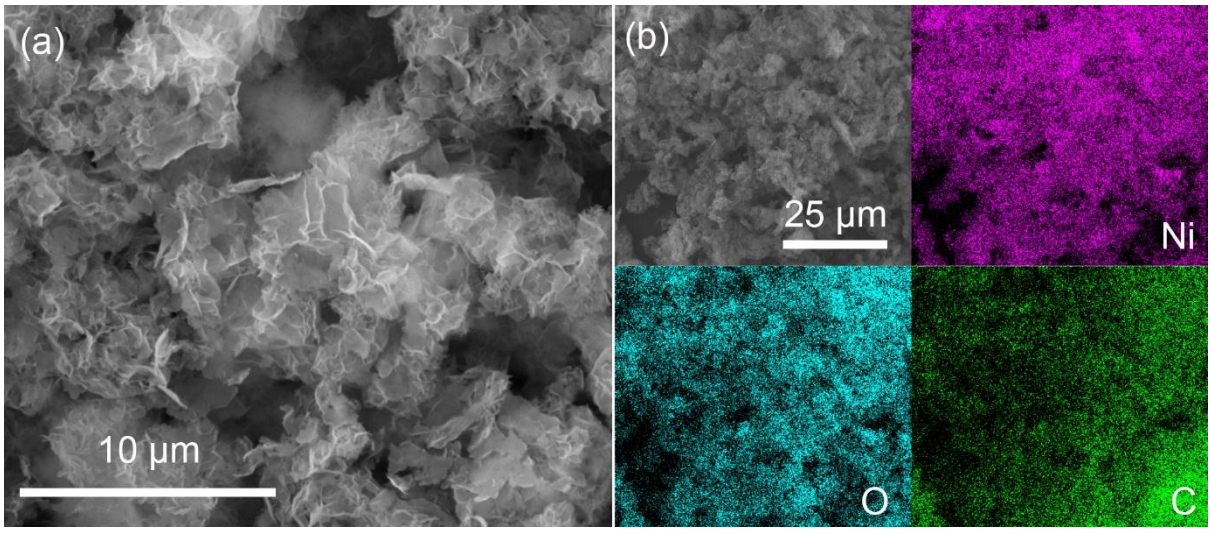

Figure S4. a) SEM image of Ni-BDC/$Ni(OH)_2$. b) Element mapping of Ni-BDC/$Ni(OH)_2$ for the selected area.

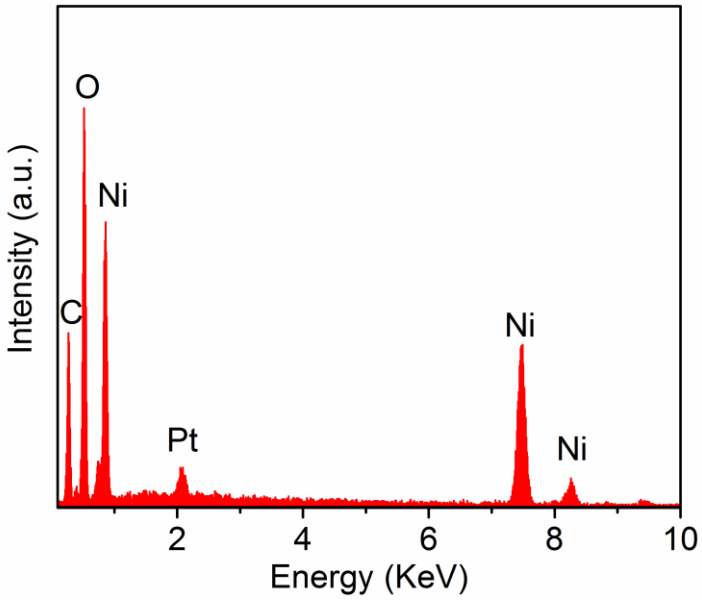

Figure S5. EDS spectrum for Ni-BDC/$Ni(OH)_2$ containing Ni, O and C.

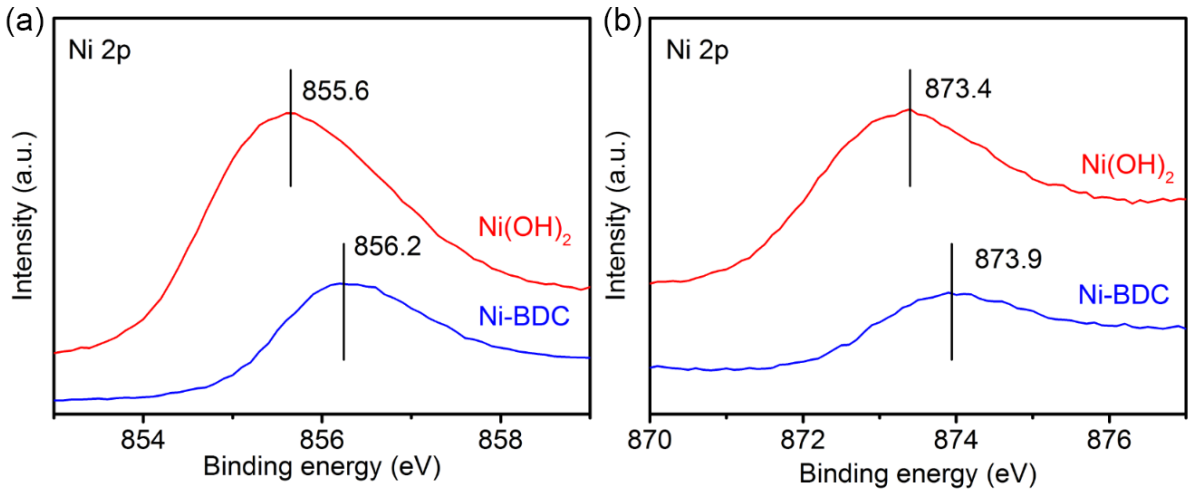

Figure S6. a) Magnified XPS spectra of Ni $2p_{3/2}$ for $Ni(OH)_2$ and Ni-BDC. b) Magnified XPS spectra of Ni $2p_{1/2}$ for $Ni(OH)_2$ and Ni-BDC.

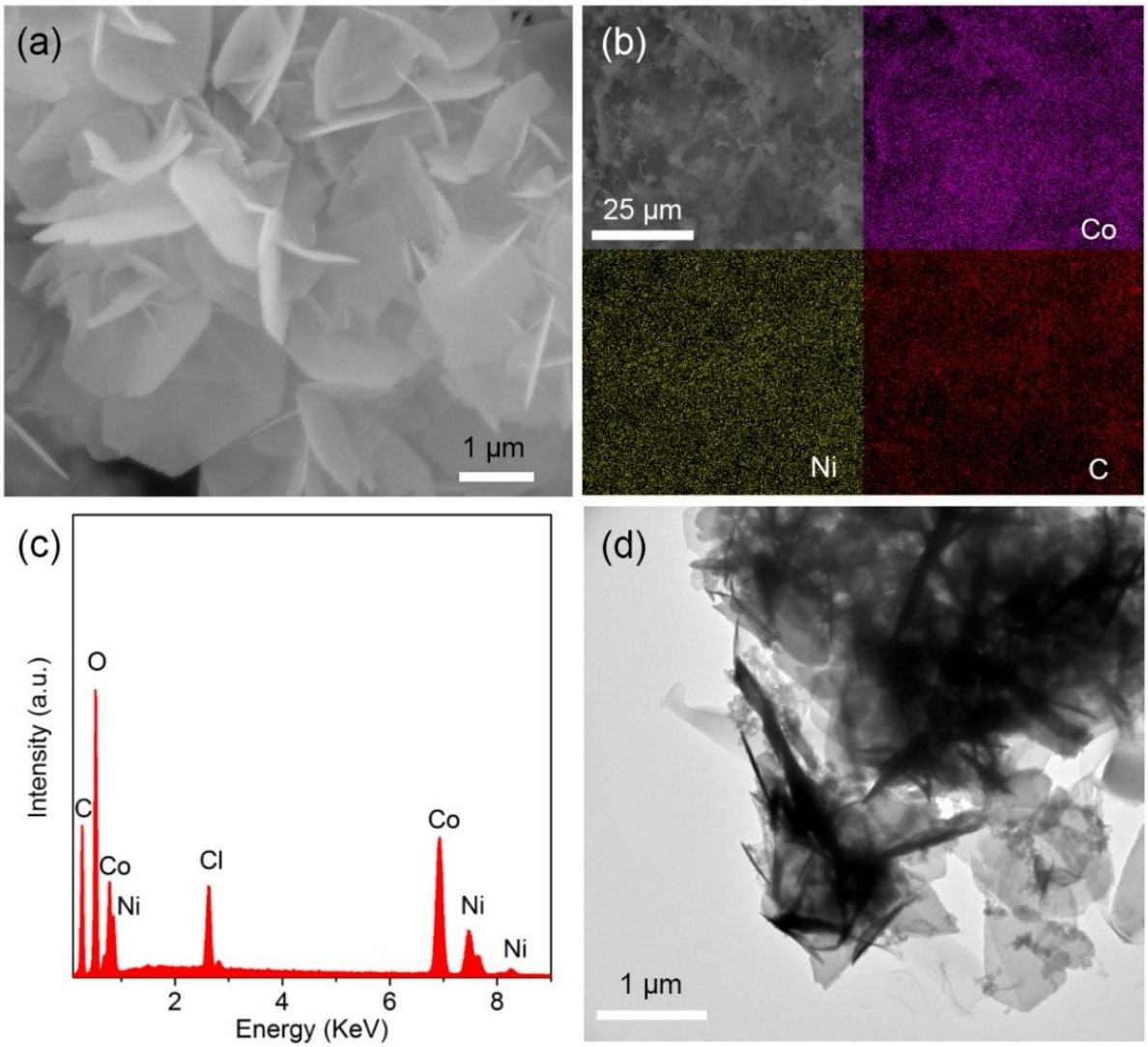

Figure S7. a) SEM image of $Co(OH)_2$ nanosheets. b) Element mapping of Ni-BDC/$Co(OH)_2$ for the selected area. c) EDS spectrum of Ni-BDC/$Co(OH)_2$. d) TEM image of Ni-BDC/$Co(OH)_2$. The $Co(OH)_2$ nanosheets were fabricated by a homogeneous precipitation method (Adv. Mater. Interfaces 2018, 5, 1700709). The as-fabricated $Co(OH)_2$ nanosheets were added to the solution containing BDC and $NiCl_2$ $6H_2O$, and Ni-BDC/$Co(OH)_2$ hybrid nanosheets were obtained by the same sonication-assisted solution method as for Ni-BDC/$Ni(OH)_2$.

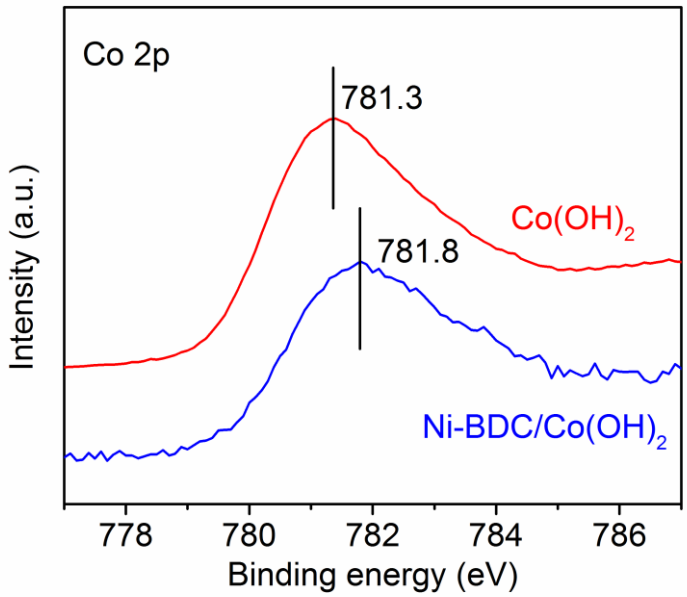

Figure S8. Magnified XPS spectra of Co $2p_{3/2}$ for $Co(OH)_2$ and Ni-BDC/$Co(OH)_2$.

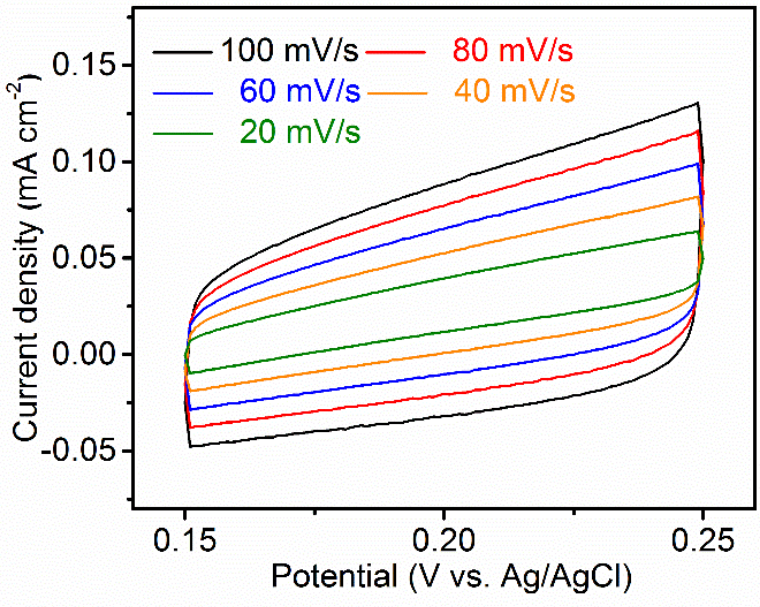

Figure S9. CV curves of $Ni(OH)_2$ at scan rates from 20 to 100 mV s^{-1}.

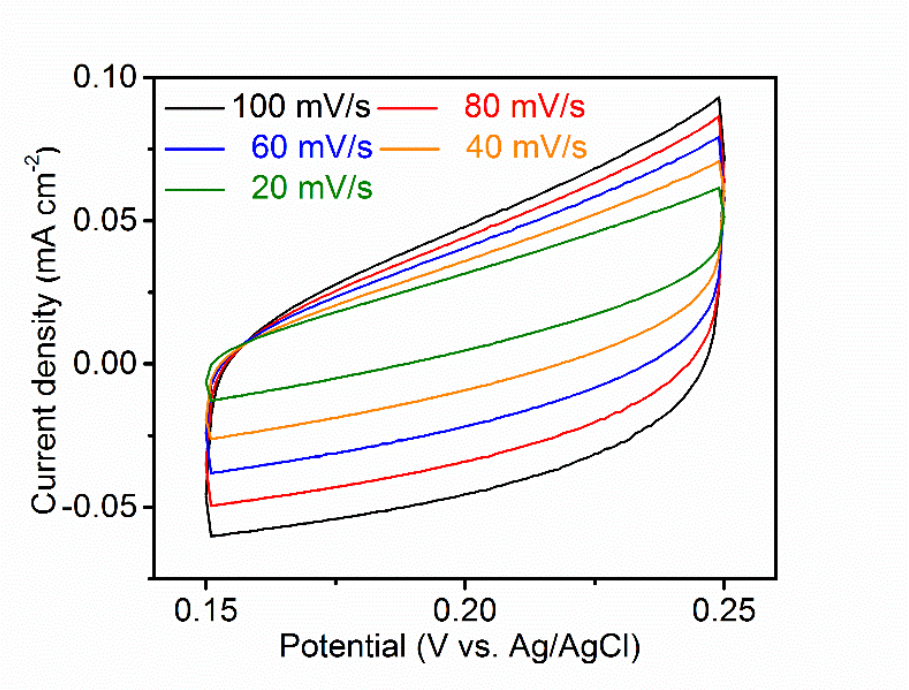

Figure S10. CV curves of Ni-BDC at scan rates from 20 to 100 mV s^{-1}.

Table S1. Comparison of OER activity between MOF-based or $Ni(OH)_2$-based catalysts deposited on glassy carbon or FTO in alkaline solution.

Catalyst	Overpotential @ 10 mA cm^{-2} (mV)	Current density @ 1.6V (vs. RHE) (mA cm^{-2})	Tafel slop (mV dec^{-1})	Reference
Ni-BDC/$Ni(OH)_2$	320	82.5	41	This work
Ni-BDC	358	15.1	57	This work
$Ni(OH)_2$	395	4.0	60	This work
NNU-23 (Fe_2Ni-MOF)	365	11	81.8	Angew. Chem. Int. Ed. **2018**, 57, 9660.
$Co_2(\mu\text{-}OH)_2$(bbta)	387	6	N/A	J. Am. Chem. Soc. **2016**, 138, 8336.
$Ti_3C_2T_x$–CoBDC nanosheets	410	4	48.2	ACS Nano **2017**, 11, 5800.
Co-BDC nanosheets	371	10	103	Nat. Energy, **2016**, 1, 16184.
Ni-BDC nanosheets	321	20	65	Nat. Energy, **2016**, 1, 16184.
NiPc–MOF	390	8	74	J. Mater. Chem. A, **2018**, 6, 1188.
β-$Ni(OH)_2$ nanomeshes	NA	100	132	Adv. Mater. **2017**, 29, 1604765
$Ni_{0.75}V_{0.25}$-LDH nanosheets	318	27 (1.58V vs. RHE)	50	Nat. Commun. **2016**, 7, 11981.
NiFe LDH/graphene	337	20	45	Adv. Mater. **2015**, 27, 4516.
α-$Ni(OH)_2$ hollow spheres	331	45	42	J. Am. Chem. Soc. **2014**, 136, 7077.
MWCNTs/$Ni(OH)_2$	474	< 5	87	J. Mater. Chem. A, **2014**, 2, 11799.
CoMn LDH nanoplates	324	NA	43	J. Am. Chem. Soc. **2014**, 136, 16481

Chapter 5: Engineering 2D Metal-Organic Frameworks/MoS_2 Interface for Enhanced Alkaline Hydrogen Evolution

5.1 Introduction and Significance

2D metal-organic frameworks (MOFs) have been widely investigated as electrocatalysts for oxygen evolution reaction (OER). However, there are only a few reports on MOFs for hydrogen evolution reaction (HER), and these reported MOFs generally suffer from extremely low HER activities. We fabricated novel 2D Co-BDC/MoS_2 (BDC stands for 1,4-benzenedicarboxylate, $C_8H_4O_4$) hybrid nanosheets via a facile sonication-assisted solution method. The introduction of Co-BDC induces the partial phase-transfer of MoS_2 from 2H-phase to 1T-phase. More impressively, the well-designed Co-BDC/MoS_2 is favourable for alkaline HER. Co-BDC with optimum binding strength to hydroxyl and H_2O facilitates the adsorption and dissociation of H_2O to provide enough protons to the nearby MoS_2, while MoS_2 contributes to the generation and desorption of H_2. As expected, the as-fabricated Co-BDC/MoS_2 hybrid nanosheets exhibited significantly improved HER performance when compared with pure Co-BDC, MoS_2 and almost all the reported MOFs-based HER electrocatalysts. Highlights of this work include:

1. Phase transfer. It is discovered for the first time that coupling MOF (Co-BDC) with MoS_2 could promote the phase transfer from 2H-MoS_2 to 1T-MoS_2. The electronic conductivity of metallic 1T-MoS_2 is about 10^7 times higher than that of 2H-MoS_2. More importantly, 1T-MoS_2 activates the inert basal planes of 2H-MoS_2 to provide more active sites for HER, contributing to greatly enhanced HER activity.

2. Interface for alkaline HER. The well-designed Co-BDC/MoS_2 interface is of high significance for alkaline HER. Co-BDC can speed up the rate-limiting water dissociation step of alkaline HER, while modified MoS_2 enables to promote the subsequent hydrogen generation step. The as-fabricated Co-BDC/MoS_2 hybrid nanosheets only need a small overpotential of 248 mV to reach −10 mA cm^{-2}, while this value for previously reported MOFs is around 300−700 mV.

3. Design 2D MOF-based hybrid materials for more applications. Generally, the performance of pristine MOFs for HER is far from satisfactory. In this contribution, by combing 2D MOFs with MoS_2, the alkaline HER performance is significantly improved. Therefore, by coupling

MOFs with other functional materials selectively, the application of MOFs can be expanded to more research areas.

5.2 Engineering 2D Metal-Organic Frameworks/MoS_2 Interface for Enhanced Alkaline Hydrogen Evolution

This chapter is included as it appears as a journal paper published by **Dongdong Zhu**, Jinlong Liu, Yongqiang Zhao, Yao Zheng and Shi-Zhang Qiao, Engineering 2D Metal-Organic Frameworks/MoS_2 Interface for Enhanced Alkaline Hydrogen Evolution, ***submitted.***

Statement of Authorship

Title of Paper	Engineering 2D Metal-Organic Frameworks/MoS_2 Interface for Enhanced Alkaline Hydrogen Evolution,
Publication Status	☐ Published ☐ Accepted for Publication ☑ Submitted for Publication ☐ Unpublished and Unsubmitted w ork w ritten in manuscript style
Publication Details	Dongdong Zhu, Jinlong Liu, Yongqiang Zhao, Yao Zheng and Shi-Zhang Qiao, Engineering 2D Metal-Organic Frameworks/MoS_2 Interface for Enhanced Alkaline Hydrogen Evolution, submitted.

Principal Author

Name of Principal Author (Candidate)	Dongdong Zhu		
Contribution to the Paper	Project design, sample synthesis, most of the characterizations, electrochemical tests, data analysis, and manuscript drafting.		
Overall percentage (%)	70%		
Certification:	This paper reports on original research I conducted during the period of my Higher Degree by Research candidature and is not subject to any obligations or contractual agreements with a third party that would constrain its inclusion in this thesis. I am the primary author of this paper.		
Signature		Date	18/12/2018

Co-Author Contributions

By signing the Statement of Authorship, each author certifies that:

i. the candidate's stated contribution to the publication is accurate (as detailed above);

ii. permission is granted for the candidate in include the publication in the thesis; and

iii. the sum of all co-author contributions is equal to 100% less the candidate's stated contribution.

Name of Co-Author	Jinlong Liu		
Contribution to the Paper	Assistance with electrocatalytic testing and analysis. 5%		
Signature		Date	18/12/2018

Name of Co-Author	Yongqiang Zhao		
Contribution to the Paper	Assistance with TEM characterization. 5%		
Signature		Date	19/12/2018

Please cut and paste additional co-author panels here as required.

Name of Co-Author	Yao Zheng			
Contribution to the Paper	Discussion of the project and manuscript revision. 5%			
Signature			Date	19/12/2018

Name of Co-Author	Shi-Zhang Qiao			
Contribution to the Paper	Supervision of the work, and manuscript evaluation. 15%			
Signature			Date	19/Dec/2018

DOI: 10.1002/((please add manuscript number))
Article type: Communication

Engineering 2D Metal-Organic Frameworks/MoS_2 Interface for Enhanced Alkaline Hydrogen Evolution

*Dongdong Zhu, Jinlong Liu, Yongqiang Zhao, Yao Zheng and Shi-Zhang Qiao**

D. D. Zhu, J. L. Liu, Y. Q. Zhao, Dr. Y. Zheng, Prof. S. Z. Qiao
School of Chemical Engineering, The University of Adelaide, Adelaide, SA 5005, Australia
E-mail: s.qiao@adelaide.edu.au

Keywords: 2D material, metal-organic framework, MoS_2, electrocatalysis, hydrogen evolution reaction

2D metal-organic frameworks (MOFs) have been widely investigated for electrocatalysis because of their unique characteristics such as large specific surface area, tunable structures and enhanced conductivity. However, most of the works are focused on oxygen evolution reaction (OER). There are very limited number of reports on MOFs for hydrogen evolution reaction (HER), and generally these reported MOFs suffer from unsatisfactory HER activities. In this contribution, novel 2D Co-BDC/MoS_2 (BDC stands for 1,4-benzenedicarboxylate, $C_8H_4O_4$) hybrid nanosheets are synthesized via a facile sonication-assisted solution strategy. The introduction of Co-BDC induces the phase transfer from semiconducting 2H-MoS_2 to metallic 1T-MoS_2 partially. Compared with 2H-MoS_2, 1T-MoS_2 can activate the inert basal plane to provide more catalytic active sites, which contributes significantly to improving HER activity. The well-designed Co-BDC/MoS_2 interface is vital for alkaline HER, as Co-BDC enables to speed up the sluggish water dissociation (rate-limiting step for alkaline HER), and modified MoS_2 is favorable for the subsequent hydrogen generation step. As expected, the resultant 2D Co-BDC/MoS_2 hybrid nanosheets demonstrate remarkable catalytic activity and good stability towards alkaline HER, outperforming those of bare Co-BDC, MoS_2 and almost all the previously reported MOFs-based electrocatalysts.

1. Introduction

Metal-organic frameworks (MOFs), a relatively new class of crystalline porous materials, are constructed by linking metal ions or clusters with organic ligands through the principle of coordination chemistry.[1] Due to the fascinating features including tunable structures and functions, high porosity, and large specific surface area, MOFs have aroused widespread interests in a large variety of fields such as gas separation and storage, catalysis, energy conversion and storage, sensors, and biomedicine.[2] As a subclass of MOFs, 2D MOFs have recently attracted increasing attention for electrocatalysis owing to their intrinsic advantages.[3] Nanometer thickness and high porosity of 2D MOF nanosheets guarantee fast mass transport and superior electron transfer. High percentages of metal atoms are exposed on the surface as active sites, and these exposed atoms are coordinatively unsaturated, which are favorable for electrocatalysis.[4] At present, numerous MOFs have been demonstrated as efficient electrocatalysts for oxidation reactions such as oxygen evolution reaction (OER) and urea oxidation reaction.[5] By contrast, there are only a few reports on MOFs for hydrogen evolution reaction (HER), and these reported MOFs suffer from low HER activities. Generally, very high overpotentials of 300−700 mV are required for MOFs to reach a HER current density of −10 mA cm^{-2}.[6]

Molybdenum disulfide (MoS_2) has been widely investigated as a promising alternative to Pt for acidic HER because of its near-optimal hydrogen adsorption free energy in theory, high chemical corrosion resistance, earth abundance, and low cost.[7] There are four polymorphs of MoS_2 including trigonal phase (1T), hexagonal phases (1H or 2H), and rhombohedral phase (3R).[8] Among them, semiconducting 2H-MoS_2 is thermodynamically stable, and the most common form in nature.[9] However, 2H-MoS_2 suffers from low catalytic activity for HER due to its low electron conductivity and very limited number of active sites. Specifically, only unsaturated sulfur atoms at the edges of 2H-MoS_2 are active, while the (0001) basal planes are catalytically inert.[10] By contrast, 1T-MoS_2 is metallic with outstanding electronic

conductivity, which is 10^7 times higher than that of 2H-MoS_2.[11] More significantly, 1T-MoS_2 can activate the inert basal planes to provide more active sites for the HER, resulting in greatly enhanced HER activity.[12] Therefore, by improving the conductivity and increasing the number of active sites simultaneously, phase engineering is regarded as an efficient method to promote the HER performance of MoS_2.[13] Despite great efforts have been made to evidently increase the HER activities of MoS_2 in acid medium, it still remains to be a big challenge to improve the alkaline HER performance of MoS_2 due to its sluggish kinetics in basic environment.[14]

From the point of view of practical applications, alkaline HER is more appealing than acidic HER, as acidic fog is easily formed in acid environment, which inevitably corrodes the reaction cell and contaminates the generated hydrogen.[15] Moreover, few OER (anodic half reaction of water splitting) catalysts can survive in acid solutions under high overpotentials for a long time.[16] In spite of these advantages, generally the reaction rate of HER in alkaline media is about two to three orders of magnitude lower than that in acid media.[17] For acidic HER, the hydrogen intermediate (H*) comes from the hydronium ions, and hydrogen adsorption free energy is supposed as the sole descriptor for the reaction activity. However, in alkaline solutions, H* is formed by the dissociation of water, which may introduce an additional energy barrier and very likely becomes the rate-determining step.[18] Thus, both water dissociation and hydrogen adsorption should be carefully considered when designing highly efficient electrocatalysts for alkaline HER.[19] As mentioned before, MoS_2 possesses near-optimal hydrogen adsorption, which is highly desirable for acidic HER.[20] However, the poor water dissociation capability of MoS_2 stemmed from improper hydroxyl adsorption contributes to poor HER performances in alkaline solutions.[21] Therefore, introducing a water dissociation promoter is supposed to be an efficient way to accelerate the alkaline HER process of MoS_2.[22]

Inspired by aforementioned hypotheses, novel 2D Co-BDC/MoS_2 hybrid nanosheets (BDC stands for 1,4-benzenedicarboxylate, $C_8H_4O_4$), were designed and fabricated as efficient electrocatalysts for alkaline HER. Importantly, the successful deposition of Co-BDC on MoS_2 nanosheets induces the partial transfer of MoS_2 from 2H phase to 1T phase, which is a much better electrocatalyst for HER. Meanwhile, the constructed Co-BDC/MoS_2 interface is highly desirable for alkaline HER, whereby Co-BDC promotes the sluggish water dissociation, and the modified MoS_2 contributes to the generation and desorption of hydrogen. As expected, the as-fabricated Co-BDC/MoS_2 nanosheets exhibit improved HER performance compared with each component and almost all the reported MOF-based HER catalysts in alkaline solutions.

2. Results and Discussion

The synthetic procedure of Co-BDC/MoS_2 hybrid nanosheets is schematically depicted in **Figure 1**. Firstly, bulk MoS_2 was exfoliated to MoS_2 nanosheets via a modified Li-ion intercalation method.[23] Then, the as-synthesized MoS_2 nanosheets were dispersed in the solution containing organic ligands (BDC) and cobalt salt (cobalt chloride hexahydrate), and Co-BDC/MoS_2 nanosheets were obtained by a simple sonication-assisted solution method (see Experimental Section for more details).

The successful fabrication of Co-BDC/MoS_2 was first demonstrated by powder X-ray diffraction (XRD). As displayed in Figure S1, after the exfoliation of bulk MoS_2, all the diffraction peaks of obtained MoS_2 nanosheets are well indexed to hexagonal MoS_2 (JCPDS card No. 37-1492).[24] As for Co-BDC/MoS_2 hybrid nanosheets (**Figure 2**a), in addition to the characteristic peaks arising from MoS_2, there are two more distinct peaks appeared, which can be well assigned to the (200) and (400) planes of Co-BDC.[25] In fact, Co-BDC is isostructural to the previously reported Ni-BDC (No. 985792, space group of *C2/m*, Cambridge Crystallographic Data Center), and the atomic arrangement of Co-BDC is defined in Figure S2.[4] In detail, each cobalt atom is octahedrally coordinated by six oxygen atoms from BDC ligands or hydroxyls, and these cobalt-based pseudo octahedra are further edge/corner

connected with each other in the lattice plane (200) to form cobalt-oxygen layers, which are separated by BDC ligands.[26] The morphology of the samples was characterized by scanning electron microscopy (SEM) and transmission electron microscopy (TEM). The as-exfoliated MoS_2 sample (Figure 2b, S3 and S4) has an obvious nanosheet morphology, and the presence of ripples and corrugations reveals its good flexibility.[27] Notably, after hybridization with Co-BDC (Figure S5), the obtained Co-BDC/MoS_2 sample maintains the 2D nanosheet feature, which is confirmed by high-angle annular dark field scanning tunneling electron microscopy (HAADF-STEM) image in Figure 2c. The SEM and TEM images of Co-BDC/MoS_2 (Figure S6 and S7) further indicate its sheet-like morphology with a lateral size of several micrometers. Energy dispersive X-ray (EDX) spectroscopy result in Figure S8 confirms that Co-BDC/MoS_2 hybrid nanosheets are composed of Mo, S, C, O, and Co without other impurities. Furthermore, as displayed in Figure 2d, the homogeneous distribution of Mo, S, and Co elements again demonstrates the uniform hybridization of Co-BDC and MoS_2.

X-ray photoelectron spectroscopy (XPS) measurements were carried out to investigate the surface electronic state and chemical composition of the samples. The XPS survey spectrum of Co-BDC/MoS_2 (Figure S9) shows obvious additional Co peaks at 781 eV and 798 eV when compared with that of pure MoS_2 (Figure S10), which suggests the successful incorporation of Co-BDC. For the bare MoS_2 nanosheets, the Mo 3d spectrum consists of peaks located at 229.5 eV and 232.6 eV (**Figure 3**a), which are well assigned to Mo $3d_{5/2}$ and Mo $3d_{3/2}$, respectively.[12a] After the hybridization with Co-BDC, the obtained Co-BDC/MoS_2 exhibits the similar Mo 3d spectrum distribution with that of MoS_2, but all the peaks shift noticeably to lower binding energy regions. To be specific, for the Mo $3d_{5/2}$ peak, the binding energy of Co-BDC/MoS_2 is 0.5 eV lower than that of MoS_2. Similarly, the S 2p spectrum can also be deconvoluted into two peaks, which are attributed to S $2p_{3/2}$ and S $2p_{1/2}$. As displayed in Figure 3b, for Co-BDC/MoS_2, the binding energies of S $2p_{3/2}$ and S $2p_{1/2}$ are negatively shifted by 0.35 eV and 0.4 eV, respectively, compared with those of pure MoS_2 nanosheets.

These results demonstrate the existence of strong electronic interactions between Co-BDC and MoS_2, again confirms the successful fabrication of Co-BDC/MoS_2 hybrid nanosheets. More importantly, the downshifted binding energies of both Mo 3d and S 2p after hybridization indicate noticeable charge transfer from Co-BDC to MoS_2, meaning that the electron densities around Mo and S atoms are increased in the Co-BDC/MoS_2 hybrid nanosheets. Previous reports demonstrate that introducing more electrons to 2H-MoS_2 will facilitate its phase transfer to 1T-MoS_2.[28] Therefore, it is supposed that Co-BDC could effectively donate electrons to promote the phase transition of MoS_2 in Co-BDC/MoS_2. The deconvolution of XPS Mo 3d peaks for 2H-MoS_2 and 1T-MoS_2 is thereby used to identify the existence of 1T and 2H phase.[29] As shown in Figure 3c, only 2H-MoS_2 (red lines) is observed in the MoS_2 nanosheets, while the additional peaks (green lines) appeared in Co-BDC/MoS_2 reveal the partial phase transformation of MoS_2 from 2H-phase to 1T-phase after depositing Co-BDC on MoS_2 nanosheets.[12a] In order to further confirm the appearance of 1T-MoS_2 in Co-BDC/MoS_2, Raman spectroscopy was further applied. As can be seen in Figure 3d, MoS_2 nanosheets exhibit typical Raman shifts of 377 and 404 cm^{-1} for the in-plane E^1_{2g} and out-of-plane A_{1g} modes, in accordance with previously reported 2H-MoS_2.[30] As for Co-BDC/MoS_2, besides E^1_{2g} and A_{1g}, three additional peaks including J_1 (146 cm^{-1}), E_{1g} (279 cm^{-1}), and J_3 (336 cm^{-1}) appear, which are characteristic features of 1T-MoS_2.[31] Normally, J_1 and J_3 peaks are attributed to the phonon modes in 1T-MoS_2 superlattice structure, and E_{1g} verifies the dominant octahedral coordination of Mo in 1T-MoS_2.[32] Moreover, the peaks at 111 and 123 cm^{-1} are also observed in the Raman spectra of 1T-MoS_2 in previous literatures, despite the attributes of these peaks are still not clear.[33] Accordingly, all these results validate that Co-BDC/MoS_2 hybrid nanosheets were successfully synthesized. Of note, the introduced Co-BDC in the hybrid material resulted in the partial phase transfer of MoS_2 from 2H-phase to 1T-phase.

The electrocatalytic performance of Co-BDC/MoS_2 for alkaline HER was evaluated using a typical three-electrode electrochemical cell with a rotating disk electrode (RDE) in Ar-saturated 1.0 M KOH solution. For comparison, pristine Co-BDC, MoS_2 and the benchmark commercial Pt-C with the same mass loading were also tested. As can be seen from the IR-corrected linear sweep voltammetry (LSV) curves in **Figure 4**a, Co-BDC/MoS_2 exhibits higher HER current densities than Co-BDC and MoS_2, directly confirming that the coupling of Co-BDC and MoS_2 allows for a profoundly enhanced alkaline HER activity. Especially, the HER onset overpotential of Co-BDC/MoS_2 is only 155 mV, which is far better than those of Co-BDC (421 mV) and MoS_2 (229 mV). Moreover, as a typical reference metric for HER, the overpotential value to afford a HER current density of −10 mA cm^{-2} is frequently employed.[34] Co-BDC/MoS_2 requires a relatively low overpotential of 248 mV to achieve −10 mA cm^{-2} (Figure S11), considerably smaller than those of Co-BDC (529 mV) and MoS_2 (349 mV). The high HER activity of Co-BDC/MoS_2 is also validated by the larger current density at fixed overpotential. For example, Co-BDC/MoS_2 delivers a current density of −32.3 mA cm^{-2} at −0.3 V versus reversible hydrogen electrode (RHE), which is significantly greater than those of MoS_2 (−4.3 mA cm^{-2}) and Co-BDC (−0.45 mA cm^{-2}). In addition, the HER activity of as-synthesized Co-BDC/MoS_2 is comparable or even superior to many previously reported MOF-based or MoS_2-based electrocatalysts (Table S1).

Figure 4b shows Tafel plots of the samples derived from corresponding polarization curves, which provide more insights to the reaction kinetics of the catalysts. The Tafel slop of MoS_2 (109 mV dec^{-1}) is close to 120 mV dec^{-1}, suggesting that water dissociation (Volmer step) is the rate-determining step for bare MoS_2 in alkaline environment.[35] However, the Tafel slope of Co-BDC/MoS_2 is dramatically decreased to 86 mV dec^{-1}, demonstrating that the combination of Co-BDC and MoS_2 could effectively facilitate the kinetics of the prior water dissociation step.[21a, 36] To further clarify the electrocatalytic behavior of the samples, electrochemical impedance spectroscopy (EIS) test was carried out, and the corresponding

Nyquist plots are displayed in Figure 4c and S12. The semicircular diameter of Co-BDC/MoS_2 (6 Ω) is obviously smaller than those of MoS_2 (36 Ω) and Co-BDC (280 Ω), suggesting that Co-BDC/MoS_2 has a remarkably lower charge-transfer resistance at the electrode-electrolyte interface during the HER process, which matches well with the superior alkaline HER activity of Co-BDC/MoS_2.

Aside from the catalytic activity, stability is another critical criterion for the evaluation of a HER catalyst. Therefore, the long-term operating durability of Co-BDC/MoS_2 electrode was assessed by using cyclic voltammetry (CV) and chronopotentiometry techniques in alkaline solution. As displayed in Figure 4d, after 2000 CV cycles, the polarization curve only shows negligible potential shift. In particular, the overpotential required to deliver −30 mA cm^{-2} is increased by only 9 mV. The inset chronopotentiometric curve again confirms the relatively good stability of Co-BDC/MoS_2 sample for 15 h at a constant current density of −10 mA cm^{-2}. All the results above clearly support that Co-BDC/MoS_2 can function as an efficient and stable catalyst for alkaline HER.

With the establishment of physical properties and electrochemical results, the high HER activity of Co-BDC/MoS_2 hybrid nanosheets can be ascribed to the following three aspects. 1) morphology engineering: 2D morphology of Co-BDC/MoS_2 promotes the mass transfer and exposes more metal atoms on the surface as active sites for the reaction; 2) interface engineering: it is generally accepted that alkaline HER includes prior water dissociation to form H* (Volmer step) and following hydrogen generation (Tafel step or Heyrovsky step).[21b] In this regard, the well-designed Co-BDC/MoS_2 interface is vital for the outstanding alkaline HER performance, as both Co-BDC and MoS_2 play specific roles in different elementary steps. Co-BDC is a highly efficient OER catalyst in alkaline solution, which is capable of binding and dissociating hydroxyl species efficiently.[4] Therefore, as shown in **Figure 5**, it is supposed that Co-BDC nanosheets with optimum binding strength to hydroxyl and H_2O facilitate the adsorption and dissociation of H_2O to provide enough protons to the nearby

MoS_2, while MoS_2 nanosheets act as reaction active sites for the generation and desorption of H_2. 3) electronic engineering: by coupling Co-BDC with MoS_2, the semiconducting 2H-MoS_2 is partially transformed to metallic 1T-MoS_2, which is highly desirable for electrocatalysis. More importantly, for 2H-MoS_2, the active sites are limited to the edge sites only, while the majority part (the basal plane) is catalytically inert. By contrast, the obtained 1T-MoS_2 could activate the basal plane to provide more reaction active sites.[12a] Moreover, previous reports show that the HER kinetics of MoS_2 can be accelerated by increasing its electronic density.[37] Specifically, the adsorption strength of H* is weakened on the surface of electron-rich MoS_2, which could promote the following H* recombination and hydrogen release process.[38] Previous XPS results confirm that high electron density of MoS_2 is achieved in Co-BDC/MoS_2 duo to the significant electron transfer from Co-BDC to MoS_2. Consequently, the electron-modified MoS_2 in Co-BDC/MoS_2 makes H_2 generation step more facile, which contributes greatly to the enhanced overall alkaline HER activity. Collectively, benefitting from these three advantageous engineering strategies, the resultant Co-BDC/MoS_2 hybrid nanosheets achieve outstanding HER performance in the alkaline environment.

3. Conclusion

In summary, a novel 2D Co-BDC/MoS_2 hybrid nanocomposite was synthesized via a facile sonication-assisted solution method. Here, Co-BDC acts as an electron donor, and coupling Co-BDC with MoS_2 induces the partial phase transfer from 2H-MoS_2 to 1T-MoS_2. This is evidenced by both XPS and Raman results. Compared with pristine 2H-MoS_2, besides the notably enhanced conductivity, 1T-MoS_2 activates the inert basal plane to expose more catalytic active sites, which is highly desirable for the HER. More importantly, the well-constructed Co-BDC/MoS_2 interface is of high significance for alkaline HER, as Co-BDC speeds up the rate-determining water dissociation step of alkaline HER, and electron-rich MoS_2 is favorable for the following H_2 generation step. These merits resulted in significantly enhanced HER performance of Co-BDC/MoS_2 when compared with bare Co-BDC and MoS_2

in the alkaline environment. Therefore, by rational design of MOF-based hybrids which combine MOFs with other functional materials selectively, the application of MOFs could be extended to more research areas.

4. Experimental Section

4.1 Materials

All chemicals, including bulk molybdenum (IV) sulfide (MoS_2), n-butyllithium solution (2.5 M in hexanes), hexane (anhydrous, 95%), N,N-dimethylformamide (DMF), ethanol, cobalt (II) chloride hexahydrate ($CoCl_2 \cdot 6H_2O$), 1,4-benzenedicarboxylic acid (BDC), triethylamine (TEA), Pt-C (20 wt.% of Pt on Vulcan XC72), Nafion (15 wt.%) were purchased from Sigma-Aldrich and used without further purification. Milli-Q water with a resistance of 18.2 MΩ was used in all experiments.

4.2 Synthesis of Co-BDC/MoS_2 hybrid nanosheets

MoS_2 nanosheets were fabricated by chemical exfoliation of bulk MoS_2. Firstly, 780 mg bulk MoS_2 powders were immersed in 4 mL n-butyllithium solution (2.5 M in hexane) for 2 days in a flask filled with argon gas. Then the mixture was centrifuged and washed with hexane for three times to remove excessive Li and organic residues. Afterwards, the as-prepared Li_xMoS_2 precursor was exfoliated in 400 mL water by ultrasonication for 1 h. Then the product was collected via centrifugation, washed with water for four times to remove excessive lithium cations and unexfoliated materials, and dried at 60 ℃ in a vacuum oven to obtain MoS_2 nanosheets.

Co-BDC/MoS_2 hybrid nanosheets were obtained by a sonication-assisted solution method. In detail, 40.8 mg MoS_2 nanosheets were dispersed in a mixed solution (32 mL DMF, 2 mL ethanol and 2 mL water) in a 100 mL glass bottle (Duran Schott). Next, 0.1 mmol BDC and 0.1 mmol $CoCl_2 \cdot 6H_2O$ were added in the bottle. Then the solution was stirred for 10 min, and 0.2 mL TEA was injected into the solution. Afterwards, the glass

bottle was ultrasonicated for 3 h under ambient conditions. The resulting product was collected via centrifugation, washed with ethanol for four times, and dried at 60 ℃ in a vacuum oven.

For comparison, the sonication-assisted solution method was also applied to generate pure Co-BDC. In brief, 32 mL DMF, 2 mL ethanol and 2 mL water were mixed in a 100 mL glass bottle firstly. Then 0.75 mmol BDC and 0.75 mmol $CoCl_2$ $6H_2O$ were added in the bottle. After the solution was stirred for 10 min, 0.8 mL TEA was injected into the solution. Afterwards, the glass bottle was continuously ultrasonicated for 8 h under ambient conditions. The final product was collected via centrifugation, washed with ethanol for four times, and dried at 60 ℃ in a vacuum oven.

4.3 Material Characterizations

XRD patterns were recorded on Rigaku MiniFlex 600 with Cu Kα radiation at a scan rate of $1\,^{\circ}\,min^{-1}$. The morphology and microstructure of the samples were observed by field-emission scanning electron microscopy (SEM, QUANTA 450) equipped with energy dispersive X-ray (EDX) detector, and scanning transmission electron microscopy (STEM, Tecnai G2 F30) equipped with EDX detector. XPS measurements were carried out on ESCALab250 using Al Kα radiation, and all the binding energies were referenced to C 1s peak at 284.8 eV. Raman spectra were acquired by iHR550 Raman microscopy (HORIBA scientific).

4.4 Electrochemical Measurements

Electrocatalyst inks were prepared by mixing active material with carbon black and Nafion. Typically, 10 mg Co-BDC/MoS_2 hybrid nanosheets were dispersed in 2 mL water, and then 1 mL carbon black (2 mg ml^{-1}) and 200 μL Nafion (1 wt.%) were added in the solution and sonicated for 1 h. Next, 10 μL of the electrocatalyst ink was transferred onto a glassy carbon rotating disk electrode (0.196 cm^2) serving as a working electrode. To permit

comparison, MoS_2, Co-BDC and Pt-C inks were prepared using the same method and loaded on glassy carbon electrode, except that no carbon black was added for Pt-C. Electrochemical tests were carried out in a three-electrode glass cell (Pine Research Instruments, USA) on an electrochemical workstation (CHI 760D Instruments, Inc., USA). The reference electrode was an Ag/AgCl in 4 M KCl solution and the counter electrode was a graphite rod. The reversible hydrogen electrode (RHE) potentials were obtained by the following equation: E(RHE) = E(Ag/AgCl) + 0.205 + 0.059 × pH. 1.0 M KOH solution was used as the electrolyte for the HER test. A flow of Ar was maintained over the electrolyte during the experiment to eliminate dissolved oxygen. The working electrode was rotated at 1600 rpm to remove the hydrogen gas generated on the catalyst surface. Before data collection, the working electrodes were scanned by cyclic voltammetry (CV) until the signals were stabilized. The linear sweep voltammetry (LSV) curves were recorded with a scan rate of 5 mV s^{-1}. The current density was normalized to the geometrical surface area. Electrochemical impedance spectroscopy (EIS) was measured in the frequency range from 0.1 Hz to 100 kHz with an amptitude of 5 mV at a potential of −0.47 V (vs. RHE). IR compensation of LSV curves was performed using the solution resistance estimated from EIS measurements. The electrode durability was tested by repetitive CV scans for 2000 cycles in a potential window of −1.2 to −1.3 V (vs. Ag/AgCl) and chronopotentiometry measurement at a constant current density of −10 mA cm^{-2} for 15 h.

Supporting Information

Supporting Information is available from the Wiley Online Library or from the author.

Acknowledgements

This work was financially supported by the Australian Research Council (ARC) through the Discovery and Linkage Project programs (DP140104062, DP160104866, DP170104464, and LP160100927). D. D. Zhu acknowledges the financial support from the Chinese Scholarship Council (CSC). The authors also thank Dr. Chunxian Guo, Dr. Jingjing Duan, Dr. Bo You, and Binwei Zhang for very useful discussions.

Received: ((will be filled in by the editorial staff))
Revised: ((will be filled in by the editorial staff))
Published online: ((will be filled in by the editorial staff))

References

[1] a) H. Furukawa, K. E. Cordova, M. O'Keeffe, O. M. Yaghi, *Science* **2013**, 341; b) L. Jiao, Y. Wang, H.-L. Jiang, Q. Xu, *Adv. Mater.* **2018**, 30, 1703663; c) X. Cao, C. Tan, M. Sindoro, H. Zhang, *Chem. Soc. Rev.* **2017**, 46, 2660.

[2] a) J. Liu, D. Zhu, C. Guo, A. Vasileff, S.-Z. Qiao, *Adv. Energy Mater.* **2017**, 7, 1700518; b) Z. Liang, C. Qu, W. Guo, R. Zou, Q. Xu, *Adv. Mater.* **2018**, 30, 1702891.

[3] M. Zhao, Y. Huang, Y. Peng, Z. Huang, Q. Ma, H. Zhang, *Chem. Soc. Rev.* **2018**, 47, 6267.

[4] S. Zhao, Y. Wang, J. Dong, C.-T. He, H. Yin, P. An, K. Zhao, X. Zhang, C. Gao, L. Zhang, J. Lv, J. Wang, J. Zhang, A. M. Khattak, N. A. Khan, Z. Wei, J. Zhang, S. Liu, H. Zhao, Z. Tang, *Nat. Energy* **2016**, 1, 16184.

[5] a) D. Zhu, C. Guo, J. Liu, L. Wang, Y. Du, S.-Z. Qiao, *Chem. Commun.* **2017**, 53, 10906; b) J. Duan, S. Chen, C. Zhao, *Nat. Commun.* **2017**, 8, 15341; c) K. Rui, G. Zhao, Y. Chen, Y. Lin, Q. Zhou, J. Chen, J. Zhu, W. Sun, W. Huang, S. X. Dou, *Adv. Funct. Mater.* **2018**, 28, 1801554; d) X.-L. Wang, L.-Z. Dong, M. Qiao, Y.-J. Tang, J. Liu, Y. Li, S.-L. Li, J.-X. Su, Y.-Q. Lan, *Angew. Chem. Int. Ed.* **2018**, 57, 9660; e) J. Huang, Y. Li, R.-K. Huang, C.-T. He, L. Gong, Q. Hu, L. Wang, Y.-T. Xu, X.-Y. Tian, S.-Y. Liu, Z.-M. Ye, F. Wang, D.-D. Zhou, W.-X. Zhang, J.-P. Zhang, *Angew. Chem. Int. Ed.* **2018**, 57, 4632.

[6] a) J.-S. Qin, D.-Y. Du, W. Guan, X.-J. Bo, Y.-F. Li, L.-P. Guo, Z.-M. Su, Y.-Y. Wang, Y.-Q. Lan, H.-C. Zhou, *J. Am. Chem. Soc.* **2015**, 137, 7169; b) A. J. Clough, J. W.

Yoo, M. H. Mecklenburg, S. C. Marinescu, *J. Am. Chem. Soc.* **2015**, 137, 118; c) R. Dong, M. Pfeffermann, H. Liang, Z. Zheng, X. Zhu, J. Zhang, X. Feng, *Angew. Chem. Int. Ed.* **2015**, 54, 12058; d) Y.-P. Wu, W. Zhou, J. Zhao, W.-W. Dong, Y.-Q. Lan, D.-S. Li, C. Sun, X. Bu, *Angew. Chem. Int. Ed.* **2017**, 56, 13001; e) B. Zhu, R. Zou, Q. Xu, *Adv. Energy Mater.* **2018**, 8, 1801193.

[7] a) D. Voiry, R. Fullon, J. Yang, C. de Carvalho Castro e Silva, R. Kappera, I. Bozkurt, D. Kaplan, M. J. Lagos, P. E. Batson, G. Gupta, Aditya D. Mohite, L. Dong, D. Er, V. B. Shenoy, T. Asefa, M. Chhowalla, *Nat. Mater.* **2016**, 15, 1003; b) H. Li, C. Tsai, A. L. Koh, L. Cai, A. W. Contryman, A. H. Fragapane, J. Zhao, H. S. Han, H. C. Manoharan, F. Abild-Pedersen, J. K. Nørskov, X. Zheng, *Nat. Mater.* **2015**, 15, 48; c) M. A. Lukowski, A. S. Daniel, F. Meng, A. Forticaux, L. Li, S. Jin, *J. Am. Chem. Soc.* **2013**, 135, 10274.

[8] M. Chhowalla, H. S. Shin, G. Eda, L.-J. Li, K. P. Loh, H. Zhang, *Nat. Chem.* **2013**, 5, 263.

[9] K. Chang, X. Hai, H. Pang, H. Zhang, L. Shi, G. Liu, H. Liu, G. Zhao, M. Li, J. Ye, *Adv. Mater.* **2016**, 28, 10033.

[10] a) J. D. Benck, T. R. Hellstern, J. Kibsgaard, P. Chakthranont, T. F. Jaramillo, *ACS Catal.* **2014**, 4, 3957; b) D. Kiriya, P. Lobaccaro, H. Y. Y. Nyein, P. Taheri, M. Hettick, H. Shiraki, C. M. Sutter-Fella, P. Zhao, W. Gao, R. Maboudian, J. W. Ager, A. Javey, *Nano Lett.* **2016**, 16, 4047.

[11] M. Acerce, D. Voiry, M. Chhowalla, *Nat. Nanotechnol.* **2015**, 10, 313.

[12] a) Z. Lei, J. Zhan, L. Tang, Y. Zhang, Y. Wang, *Adv. Energy Mater.* **2018**, 8, 1703482; b) D. Voiry, M. Salehi, R. Silva, T. Fujita, M. Chen, T. Asefa, V. B. Shenoy, G. Eda, M. Chhowalla, *Nano Lett.* **2013**, 13, 6222.

[13] M. S. Faber, S. Jin, *Energy Environ. Sci.* **2014**, 7, 3519.

[14] M. A. R. Anjum, H. Y. Jeong, M. H. Lee, H. S. Shin, J. S. Lee, *Adv. Mater.* **2018**, 30, 1707105.

[15] a) J. Wang, F. Xu, H. Jin, Y. Chen, Y. Wang, *Adv. Mater.* **2017**, 29, 1605838; b) N. Mahmood, Y. Yao, J.-W. Zhang, L. Pan, X. Zhang, J.-J. Zou, *Adv. Sci.* **2018**, 5, 1700464.

[16] a) R. Bar-Ziv, O. E. Meiron, M. Bar-Sadan, *Nanoscale* **2018**, 10, 16211; b) C. G. Morales-Guio, L. Liardet, M. T. Mayer, S. D. Tilley, M. Grätzel, X. Hu, *Angew. Chem. Int. Ed.* **2015**, 54, 664.

[17] X. Li, P. F. Liu, L. Zhang, M. Y. Zu, Y. X. Yang, H. G. Yang, *Chem. Commun.* **2016**, 52, 10566.

[18] a) Y. Zheng, Y. Jiao, A. Vasileff, S.-Z. Qiao, *Angew. Chem. Int. Ed.* **2018**, 57, 7568; b) J. Liu, Y. Zheng, D. Zhu, A. Vasileff, T. Ling, S.-Z. Qiao, *Nanoscale* **2017**, 9, 16616.

[19] T. Zhang, K. Yang, C. Wang, S. Li, Q. Zhang, X. Chang, J. Li, S. Li, S. Jia, J. Wang, L. Fu, *Adv. Energy Mater.* **2018**, 8, 1801690.

[20] B. Hinnemann, P. G. Moses, J. Bonde, K. P. Jørgensen, J. H. Nielsen, S. Horch, I. Chorkendorff, J. K. Nørskov, *J. Am. Chem. Soc.* **2005**, 127, 5308.

[21] a) J. Zhang, T. Wang, P. Liu, S. Liu, R. Dong, X. Zhuang, M. Chen, X. Feng, *Energy Environ. Sci.* **2016**, 9, 2789; b) B. Zhang, J. Liu, J. Wang, Y. Ruan, X. Ji, K. Xu, C. Chen, H. Wan, L. Miao, J. Jiang, *Nano Energy* **2017**, 37, 74; c) J. Hu, C. Zhang, L. Jiang, H. Lin, Y. An, D. Zhou, M. K. H. Leung, S. Yang, *Joule* **2017**, 1, 383.

[22] a) R. Subbaraman, D. Tripkovic, D. Strmcnik, K.-C. Chang, M. Uchimura, A. P. Paulikas, V. Stamenkovic, N. M. Markovic, *Science* **2011**, 334, 1256; b) R. Subbaraman, D. Tripkovic, K.-C. Chang, D. Strmcnik, A. P. Paulikas, P. Hirunsit, M. Chan, J. Greeley, V. Stamenkovic, N. M. Markovic, *Nat. Mater.* **2012**, 11, 550; c) V. R. Stamenkovic, D. Strmcnik, P. P. Lopes, N. M. Markovic, *Nat. Mater.* **2016**, 16, 57; d) Z. Zhu, H. Yin, C.-T. He, M. Al-Mamun, P. Liu, L. Jiang, Y. Zhao, Y. Wang, H.-G. Yang, Z. Tang, D. Wang, X.-M. Chen, H. Zhao, *Adv. Mater.* **2018**, 30, 1801171.

[23] a) H. Tang, J. Wang, H. Yin, H. Zhao, D. Wang, Z. Tang, *Adv. Mater.* **2015**, 27, 1117; b) X. Zhang, Z. Lai, C. Tan, H. Zhang, *Angew. Chem. Int. Ed.* **2016**, 55, 8816; c) H. Jin, C. Guo, X. Liu, J. Liu, A. Vasileff, Y. Jiao, Y. Zheng, S.-Z. Qiao, *Chem. Rev.* **2018**, 118, 6337.

[24] X.-Y. Yu, H. Hu, Y. Wang, H. Chen, X. W. Lou, *Angew. Chem. Int. Ed.* **2015**, 54, 7395.

[25] L. Zhao, B. Dong, S. Li, L. Zhou, L. Lai, Z. Wang, S. Zhao, M. Han, K. Gao, M. Lu, X. Xie, B. Chen, Z. Liu, X. Wang, H. Zhang, H. Li, J. Liu, H. Zhang, X. Huang, W. Huang, *ACS Nano* **2017**, 11, 5800.

[26] G. Hai, X. Jia, K. Zhang, X. Liu, Z. Wu, G. Wang, *Nano Energy* **2018**, 44, 345.

[27] J. Xie, J. Zhang, S. Li, F. Grote, X. Zhang, H. Zhang, R. Wang, Y. Lei, B. Pan, Y. Xie, *J. Am. Chem. Soc.* **2013**, 135, 17881.

[28] a) L. Cai, J. He, Q. Liu, T. Yao, L. Chen, W. Yan, F. Hu, Y. Jiang, Y. Zhao, T. Hu, Z. Sun, S. Wei, *J. Am. Chem. Soc.* **2015**, 137, 2622; b) L. Cai, W. Cheng, T. Yao, Y.

Huang, F. Tang, Q. Liu, W. Liu, Z. Sun, F. Hu, Y. Jiang, W. Yan, S. Wei, *J. Phys. Chem. C* **2017**, 121, 15071.

[29] H. Huang, Y. Cui, Q. Li, C. Dun, W. Zhou, W. Huang, L. Chen, C. A. Hewitt, D. L. Carroll, *Nano Energy* **2016**, 26, 172.

[30] a) X. Geng, W. Sun, W. Wu, B. Chen, A. Al-Hilo, M. Benamara, H. Zhu, F. Watanabe, J. Cui, T.-p. Chen, *Nat. Commun.* **2016**, 7, 10672; b) N. H. Attanayake, A. C. Thenuwara, A. Patra, Y. V. Aulin, T. M. Tran, H. Chakraborty, E. Borguet, M. L. Klein, J. P. Perdew, D. R. Strongin, *ACS Energy Lett.* **2018**, 3, 7.

[31] a) Q. Ding, F. Meng, C. R. English, M. Cabán-Acevedo, M. J. Shearer, D. Liang, A. S. Daniel, R. J. Hamers, S. Jin, *J. Am. Chem. Soc.* **2014**, 136, 8504; b) X. Geng, Y. Zhang, Y. Han, J. Li, L. Yang, M. Benamara, L. Chen, H. Zhu, *Nano Lett.* **2017**, 17, 1825; c) A. Ejigu, I. A. Kinloch, E. Prestat, R. A. W. Dryfe, *J. Mater. Chem. A* **2017**, 5, 11316.

[32] X. Fan, P. Xu, D. Zhou, Y. Sun, Y. C. Li, M. A. T. Nguyen, M. Terrones, T. E. Mallouk, *Nano Lett.* **2015**, 15, 5956.

[33] a) Q. Liu, X. Li, Q. He, A. Khalil, D. Liu, T. Xiang, X. Wu, L. Song, *Small* **2015**, 11, 5556; b) X. Zhang, Y. Liang, *Adv. Sci.* **2018**, 5, 1700644.

[34] J. D. Benck, Z. Chen, L. Y. Kuritzky, A. J. Forman, T. F. Jaramillo, *ACS Catal.* **2012**, 2, 1916.

[35] a) Y. Luo, X. Li, X. Cai, X. Zou, F. Kang, H.-M. Cheng, B. Liu, *ACS Nano* **2018**, 12, 4565; b) W. Xiao, P. Liu, J. Zhang, W. Song, Y. P. Feng, D. Gao, J. Ding, *Adv. Energy Mater.* **2017**, 7, 1602086.

[36] J. Zhang, T. Wang, P. Liu, Z. Liao, S. Liu, X. Zhuang, M. Chen, E. Zschech, X. Feng, *Nat. Commun.* **2017**, 8, 15437.

[37] Y. Shi, Y. Zhou, D.-R. Yang, W.-X. Xu, C. Wang, F.-B. Wang, J.-J. Xu, X.-H. Xia, H.-Y. Chen, *J. Am. Chem. Soc.* **2017**, 139, 15479.

[38] Q. Liu, Q. Fang, W. Chu, Y. Wan, X. Li, W. Xu, M. Habib, S. Tao, Y. Zhou, D. Liu, T. Xiang, A. Khalil, X. Wu, M. Chhowalla, P. M. Ajayan, L. Song, *Chem. Mater.* **2017**, 29, 4738.

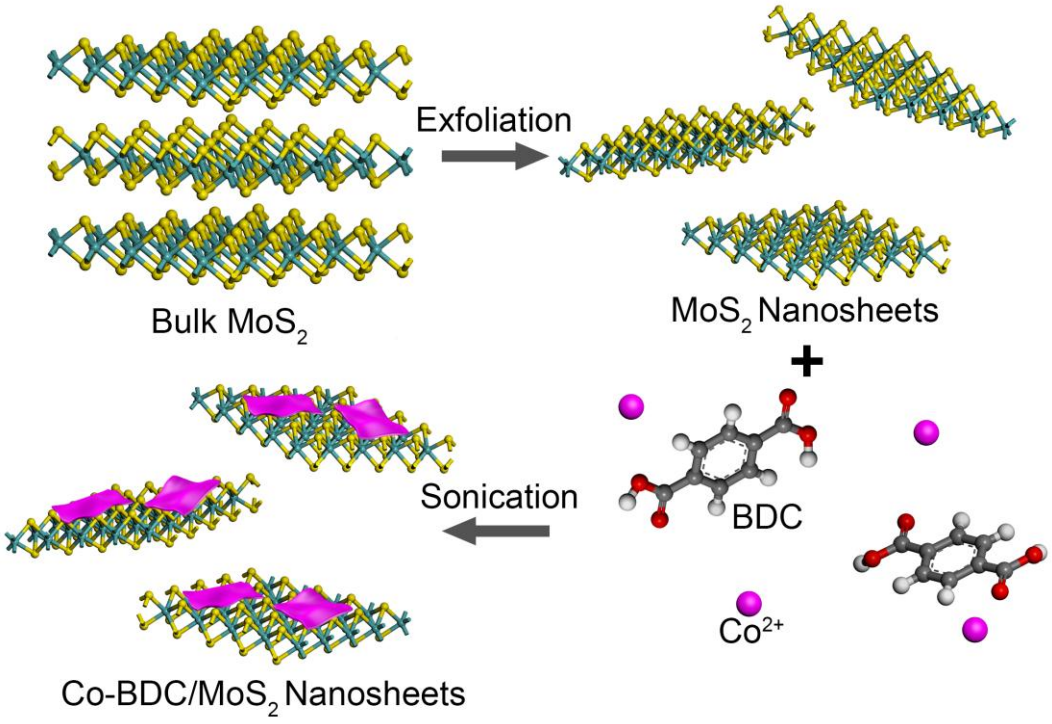

Figure 1. Schematic of the synthesis process for Co-BDC/MoS_2 hybrid nanosheets.

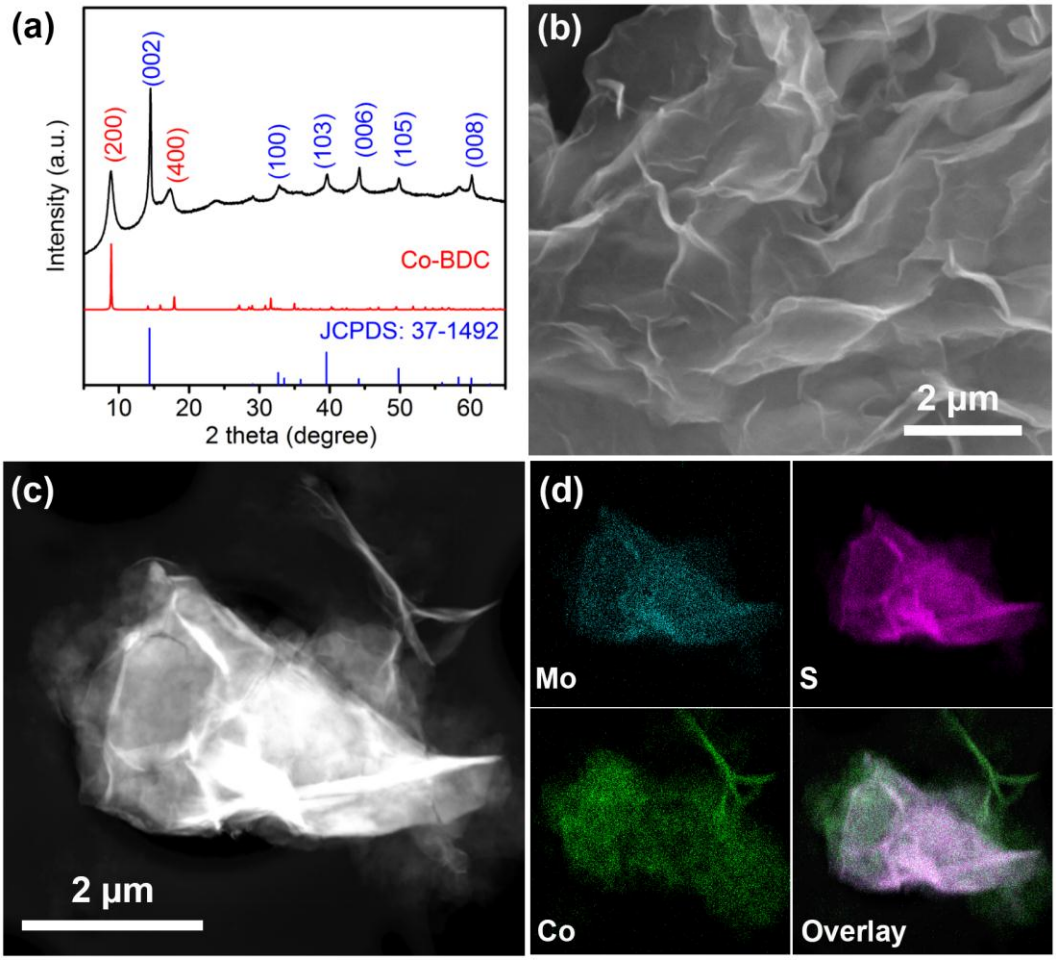

Figure 2. a) XRD pattern of Co-BDC/MoS_2 hybrid nanosheets. b) SEM image of MoS_2 nanosheets. c) HAADF-STEM image and d) corresponding elemental mapping of Co-BDC/MoS_2 hybrid nanosheets.

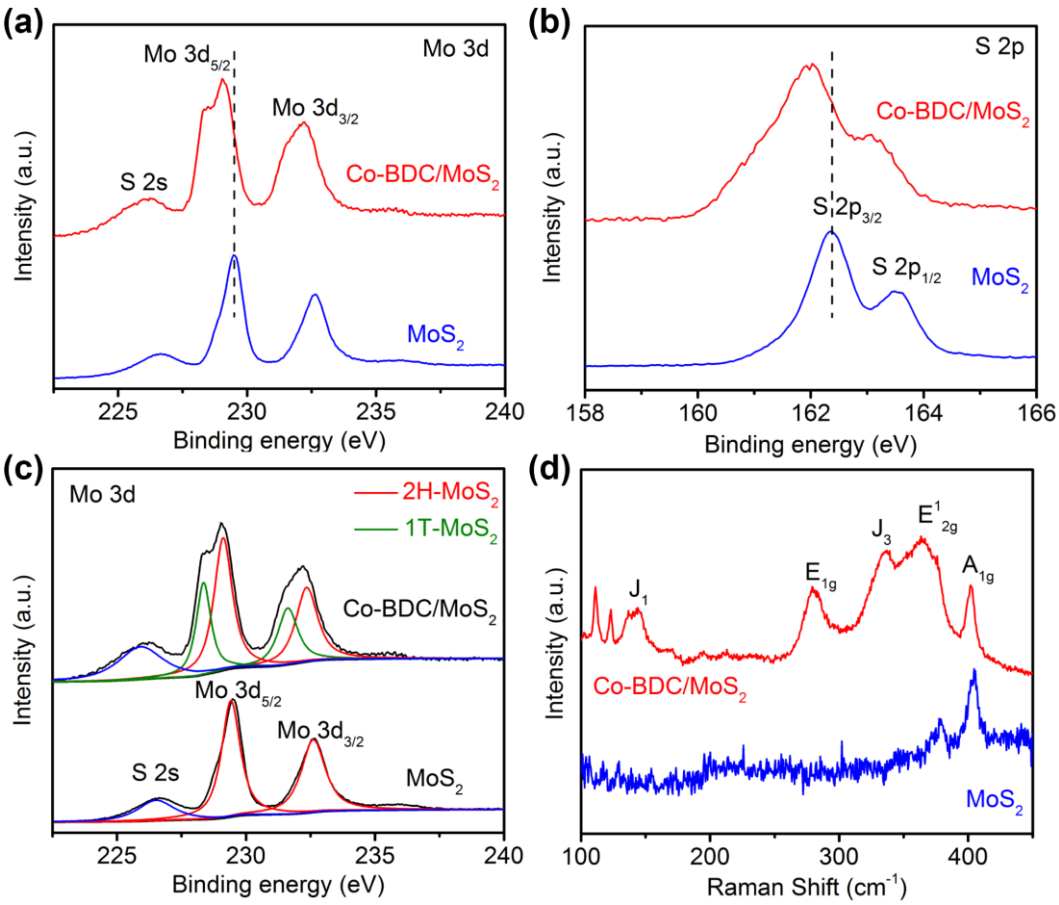

Figure 3. a) High-resolution XPS Mo 3d spectra of MoS_2 and Co-BDC/MoS_2. b) High-resolution XPS S 2p spectra of MoS_2 and Co-BDC/MoS_2. c) The deconvoluted XPS Mo 3d spectra of MoS_2 and Co-BDC/MoS_2. d) Raman spectra of MoS_2 and Co-BDC/MoS_2.

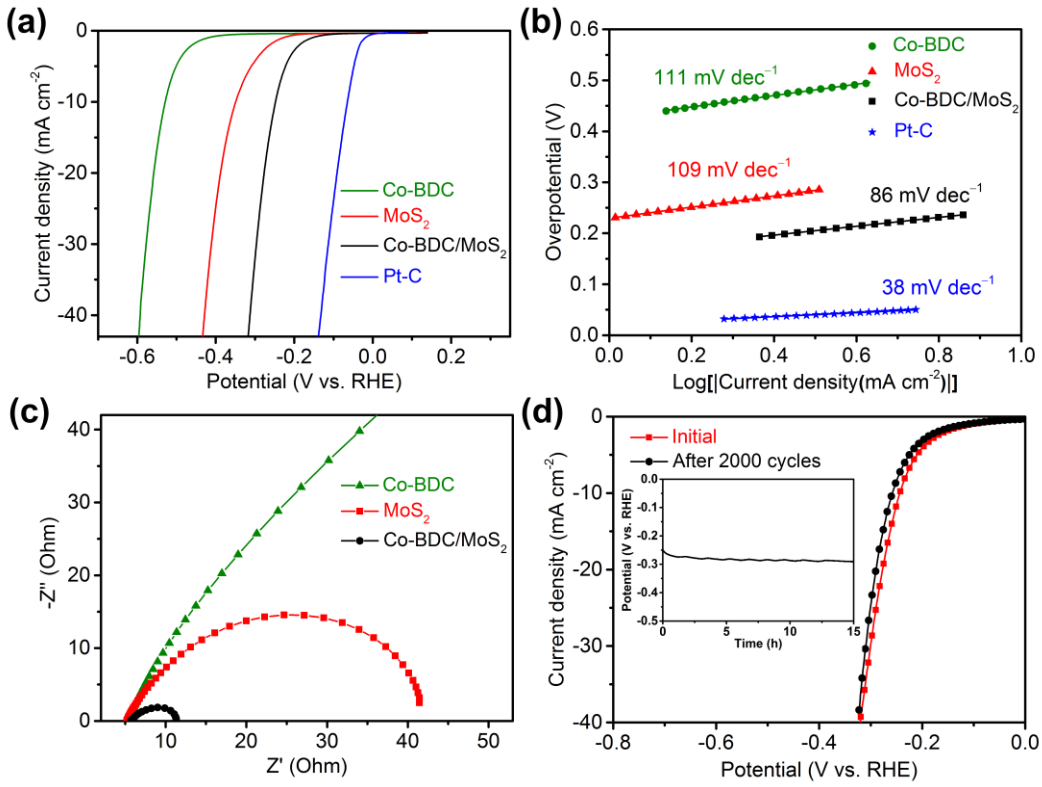

Figure 4. a) LSV curves of Co-BDC, MoS_2, Co-BDC/MoS_2 and Pt-C in 1.0 M KOH at a scan rate of 5 mV s^{-1}. b) Corresponding Tafel plots of Co-BDC, MoS_2, Co-BDC/MoS_2 and Pt-C. c) Nyquist plots of Co-BDC, MoS_2 and Co-BDC/MoS_2 measured at −0.47 V vs. RHE. d) LSV curves of Co-BDC/MoS_2 recorded before and after 2000 CV cycles, and the inset shows the chronopotentiometric response of Co-BDC/MoS_2 at a constant current density of −10 mA cm^{-2} for 15 h.

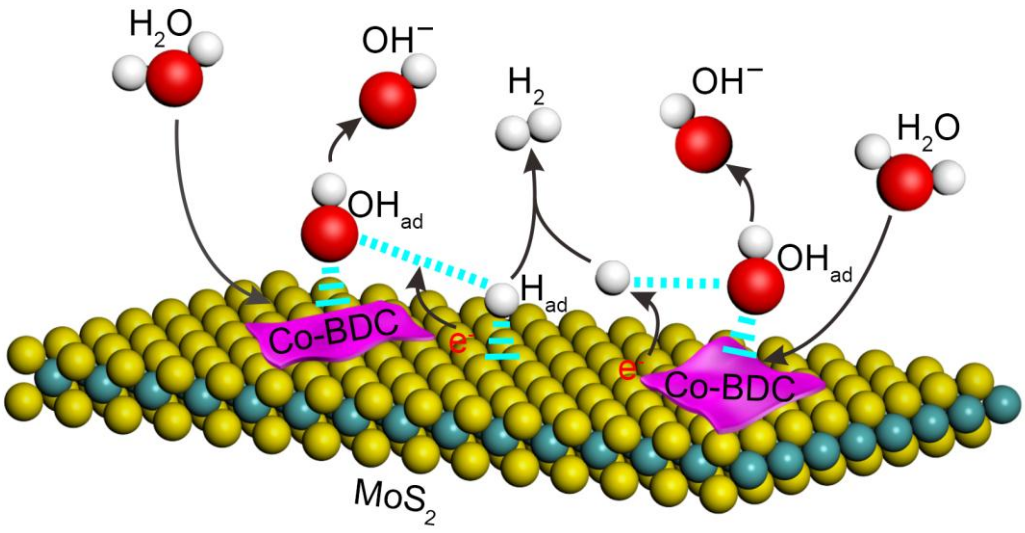

Figure 5. Schematic illustration of catalysis mechanism of alkaline HER on the Co-BDC/MoS_2 hybrid nanosheets.

Supporting Information

Engineering 2D Metal-Organic Frameworks/MoS_2 Interface for Enhanced Alkaline Hydrogen Evolution

*Dongdong Zhu, Jinlong Liu, Yongqiang Zhao, Yao Zheng and Shi-Zhang Qiao**

D. D. Zhu, J. L. Liu, Y. Q. Zhao, Dr. Y. Zheng, Prof. S. Z. Qiao
School of Chemical Engineering, The University of Adelaide, Adelaide, SA 5005, Australia
E-mail: s.qiao@adelaide.edu.au

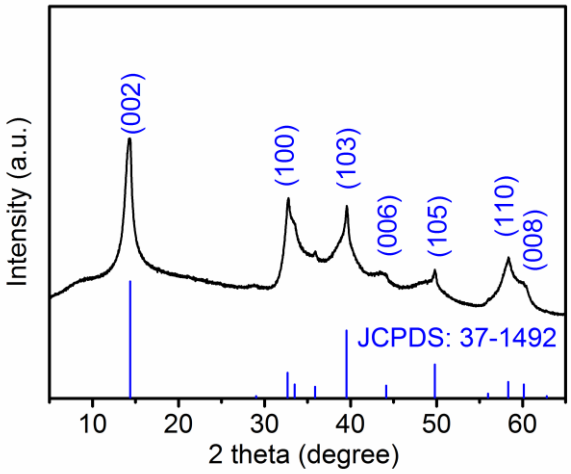

Figure S1. XRD pattern of MoS_2 nanosheets.

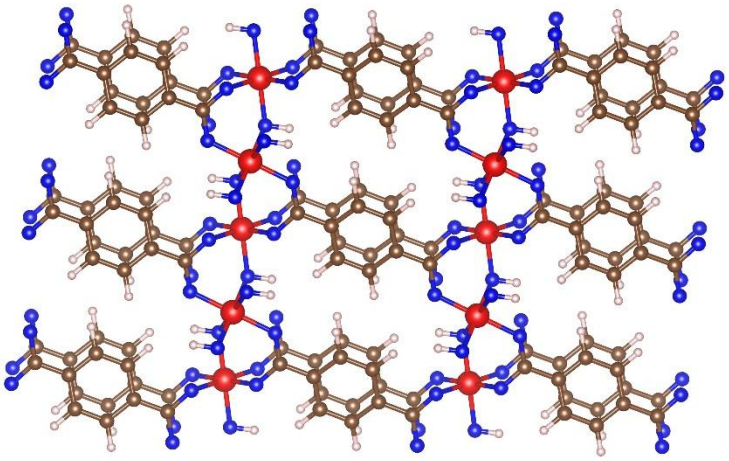

Figure S2. Crystal structure of Co-BDC. Color scheme for atom representation: red for Co, blue for O, grey for C and white for H.

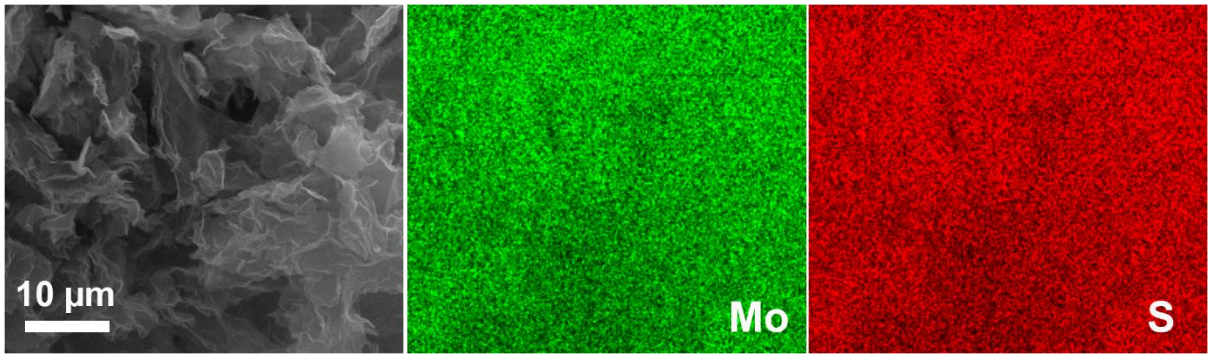

Figure S3. SEM image and corresponding element mapping of MoS_2 nanosheets.

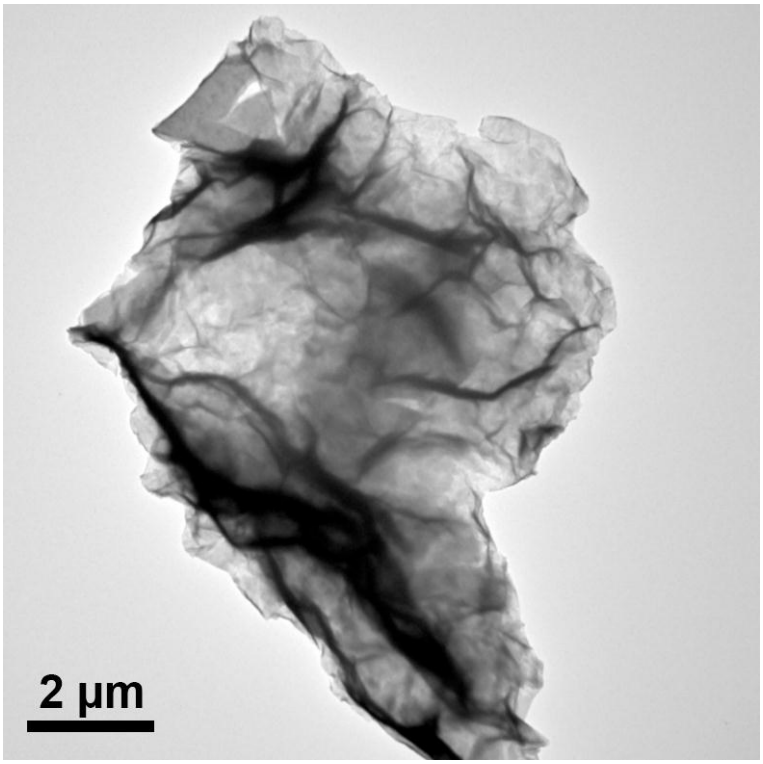

Figure S4. TEM image of MoS_2 nanosheets.

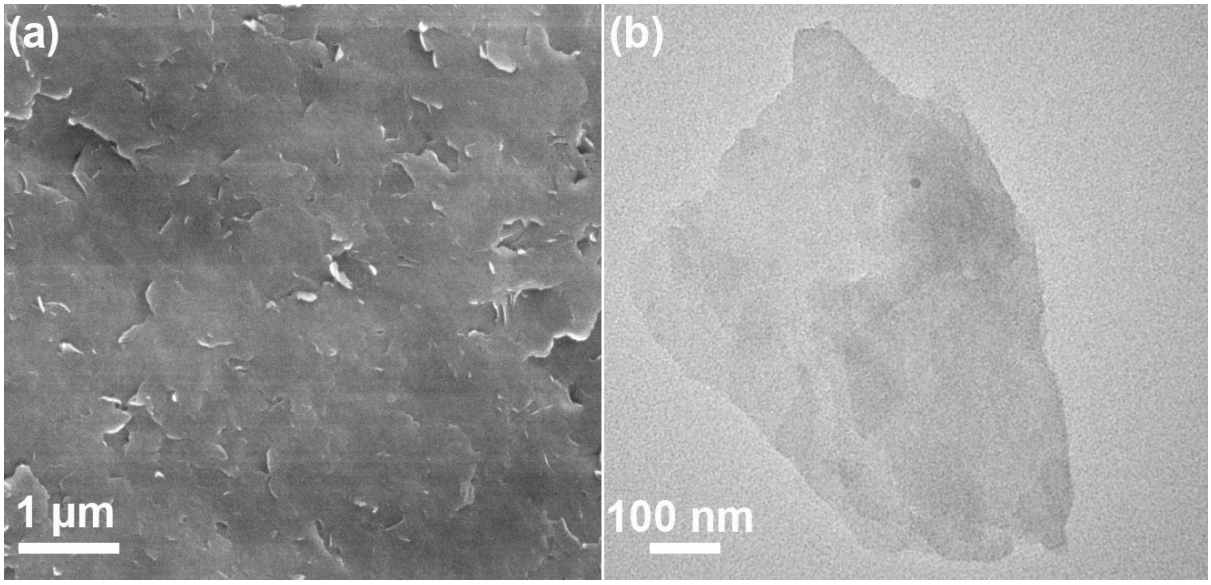

Figure S5. a) SEM image of Co-BDC nanosheets. b) TEM image of Co-BDC nanosheets.

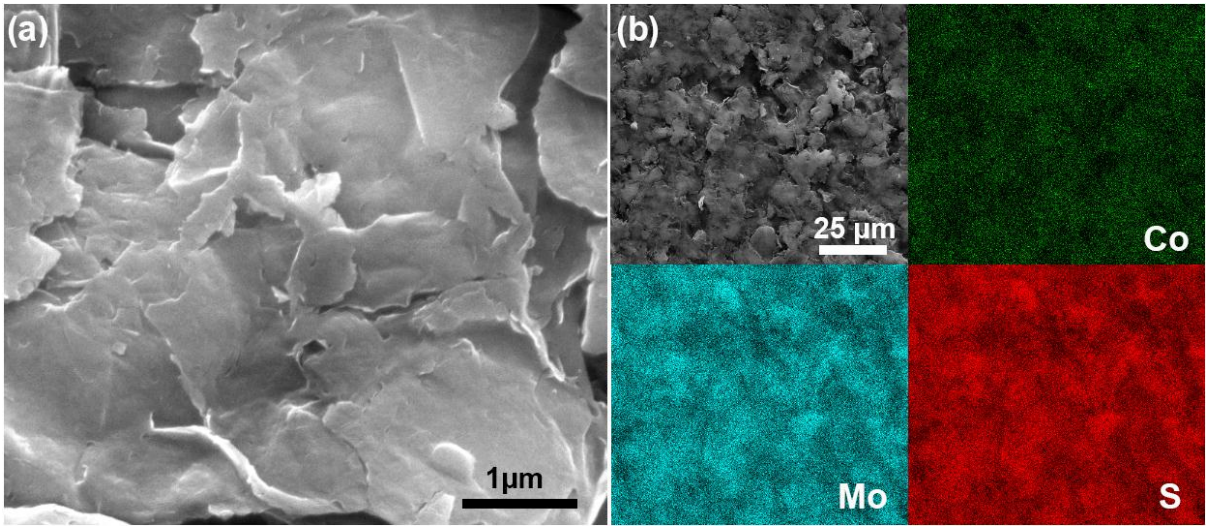

Figure S6. a) SEM image of Co-BDC/MoS_2 nanosheets. b) Element mapping of Co-BDC/ MoS_2 nanosheets for the selected area.

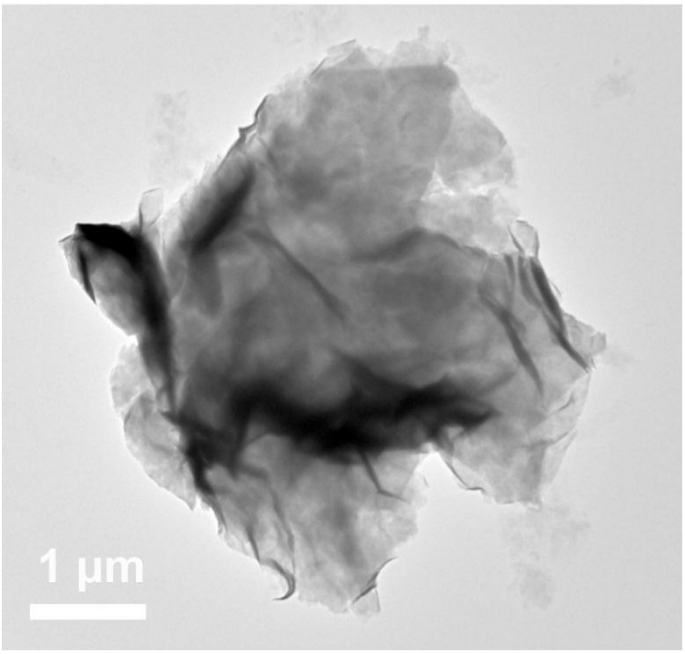

Figure S7. TEM image of Co-BDC/MoS_2 nanosheets.

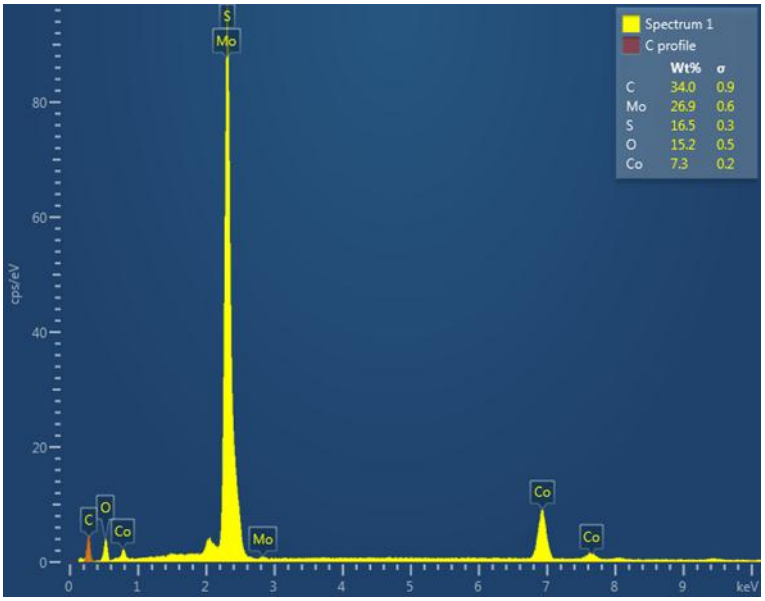

Figure S8. EDX spectrum of Co-BDC/MoS_2 nanosheets.

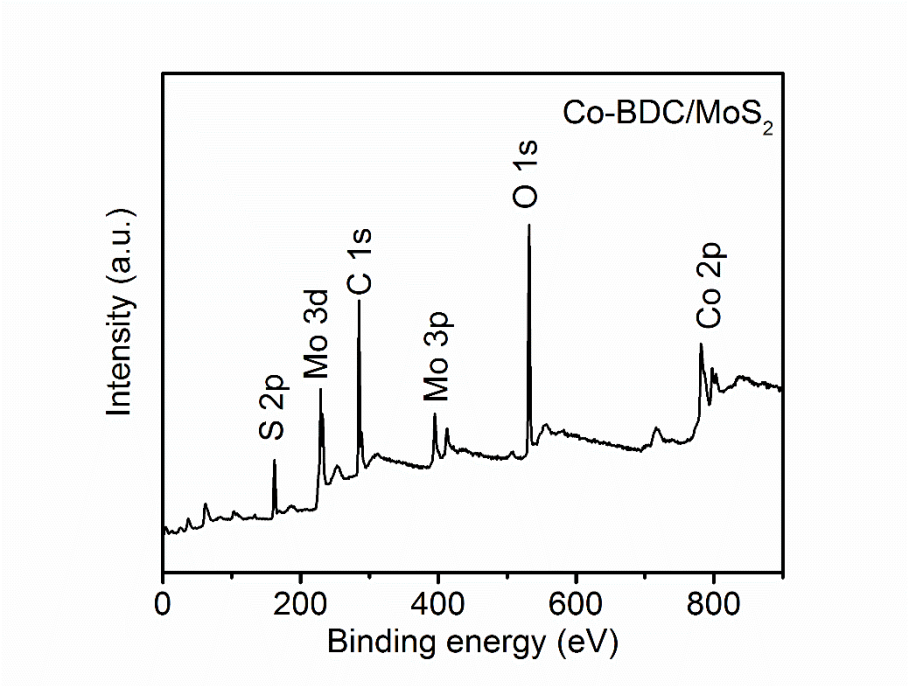

Figure S9. XPS survey spectrum of Co-BDC/MoS_2 nanosheets.

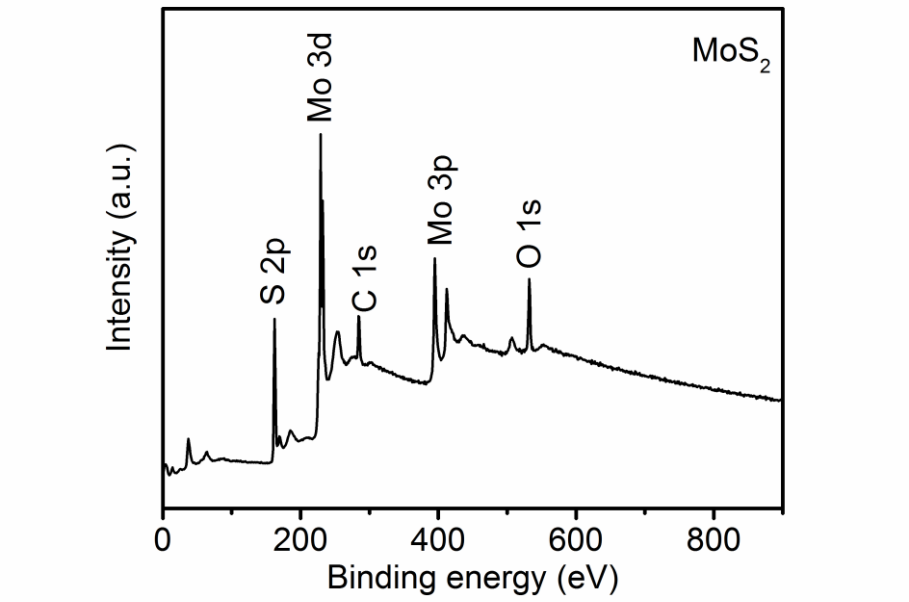

Figure S10. XPS survey spectrum of MoS_2 nanosheets.

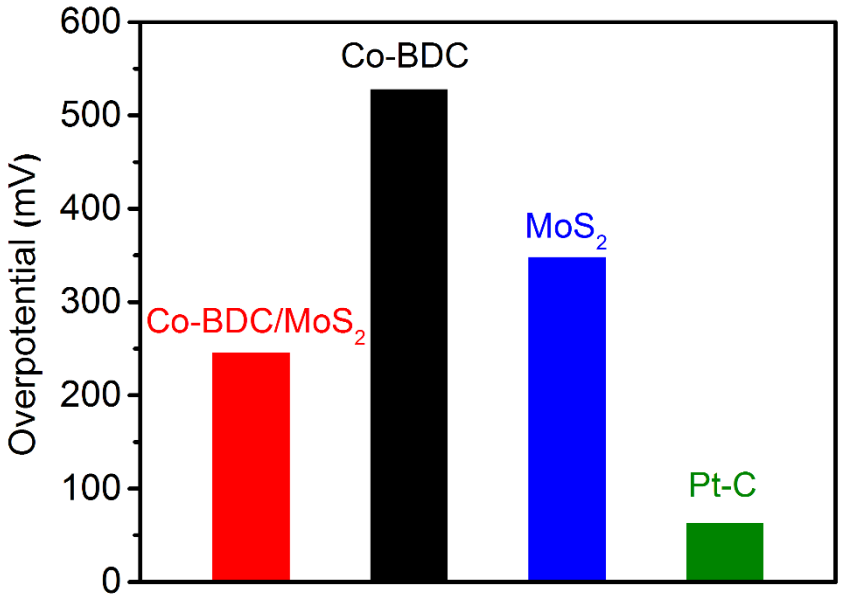

Figure S11. Comaprison of overpotentials required for the samples to reach a HER current density of −10 mA cm^{-2}.

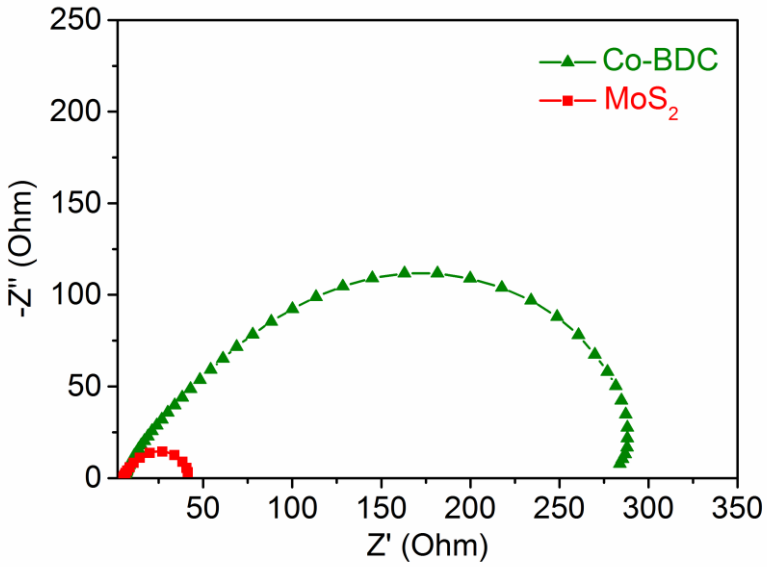

Figure S12. Nyquist plots of Co-BDC and MoS_2 nanosheets measured at −0.47 V vs. RHE.

Table S1. Comparison of HER activity for MOF-based or MoS_2-based catalysts deposited on glassy carbon electrode.

Catalyst	Overpotential @ −10 mA cm^{-2} (mV)	Tafel slop (mV dec^{-1})	Electrolyte	Reference
Co-BDC/MoS_2	248	86	1M KOH	This work
Co-BDC	529	111	1M KOH	This work
MoS_2	349	109	1M KOH	This work
Co-THT	530	NA	0.05M H_2SO_4	[1]
Co-BHT	340	NA	0.05M H_2SO_4	[1]
Ni-THT	333	80.5	0.5M H_2SO_4	[2]
Ni-THT	574	NA	0.05M KOH	[2]
NENU-500	237	96	0.5M H_2SO_4	[3]
NENU-501	392	137	0.5M H_2SO_4	[3]
NENU-499	570	122	0.5M H_2SO_4	[3]
NENU-5	585	94	0.5M H_2SO_4	[3]
HKUST-1	691	127	0.5M H_2SO_4	[3]
Cu-MOF	369	135	0.5M H_2SO_4	[4]
Fe-MOF	576	158	0.5M H_2SO_4	[5]
Cu-BHT	450	95	0.5M H_2SO_4	[6]
Ni-MOF	370	128	0.05M H_2SO_4	[7]
Ru-MOF	337	NA	0.1M H_2SO_4	[8]
Au-MoS_2	280	79	0.5M H_2SO_4	[9]
MoS_x film	520	NA	0.1M KOH	[10]
$CoMoS_x$	210 @ 5 mA cm^{-2}	NA	0.1M KOH	[11]
$NiMo_3S_4$	257	98	0.1M KOH	[12]
MoS_2/C_3N_4	500	43	0.1M KOH	[13]
1T–2H MoS_2	290	65	1M KOH	[14]
MoS_2	308	201	1M KOH	[15]
$Ni(OH)_2/MoS_2$	227	105	1M KOH	[16]

References

[1] A. J. Clough, J. W. Yoo, M. H. Mecklenburg, S. C. Marinescu, *J. Am. Chem. Soc.* **2015**, 137, 118.

[2] R. Dong, M. Pfeffermann, H. Liang, Z. Zheng, X. Zhu, J. Zhang, X. Feng, *Angew. Chem. Int. Ed.* **2015**, 54, 12058.

[3] J.-S. Qin, D.-Y. Du, W. Guan, X.-J. Bo, Y.-F. Li, L.-P. Guo, Z.-M. Su, Y.-Y. Wang, Y.-Q. Lan, H.-C. Zhou, *J. Am. Chem. Soc.* **2015**, 137, 7169.

[4] M. Jahan, Z. Liu, K. P. Loh, *Adv. Funct. Mater.* **2013**, 23, 5363.

[5] L. Wang, D. C. Tranca, J. Zhang, Y. Qi, S. Sfaelou, T. Zhang, R. Dong, X. Zhuang, Z. Zheng, G. Seifert, *Small* **2017**, 13, 1700783.

[6] X. Huang, H. Yao, Y. Cui, W. Hao, J. Zhu, W. Xu, D. Zhu, *ACS Appl. Mater. Interfaces* **2017**, 9, 40752.

[7] X. Sun, K.-H. Wu, R. Sakamoto, T. Kusamoto, H. Maeda, X. Ni, W. Jiang, F. Liu, S. Sasaki, H. Masunaga, H. Nishihara, *Chem. Sci.* **2017**, 8, 8078.

[8] W. Salomon, G. Paille, M. Gomez-Mingot, P. Mialane, J. Marrot, C. Roch-Marchal, G. Nocton, C. Mellot-Draznieks, M. Fontecave, A. Dolbecq, *Cryst. Growth Des.* **2017**, 17, 1600.

[9] S. Zhao, R. Jin, Y. Song, H. Zhang, S. D. House, J. C. Yang, R. Jin, *Small* **2017**, 13, 1701519.

[10] D. Merki, S. Fierro, H. Vrubel, X. Hu, *Chem. Sci.* **2011**, 2, 1262.

[11] J. Staszak-Jirkovský, Christos D. Malliakas, Pietro P. Lopes, N. Danilovic, Subrahmanyam S. Kota, K.-C. Chang, B. Genorio, D. Strmcnik, Vojislav R. Stamenkovic, M. G. Kanatzidis, N. M. Markovic, *Nat. Mater.* **2015**, 15, 197.

[12] J. Jiang, M. Gao, W. Sheng, Y. Yan, *Angew. Chem. Int. Ed.* **2016**, 55, 15240.

[13] X. Qian, J. Ding, J. Zhang, Y. Zhang, Y. Wang, E. Kan, X. Wang, J. Zhu, *Nanoscale* **2018**, 10, 1766.

[14] S. Wang, D. Zhang, B. Li, C. Zhang, Z. Du, H. Yin, X. Bi, S. Yang, *Adv. Energy Mater.* **2018**, 8, 1801345.

[15] J. Zhang, T. Wang, P. Liu, S. Liu, R. Dong, X. Zhuang, M. Chen, X. Feng, *Energy Environ. Sci.* **2016**, 9, 2789.

[16] G. Zhao, Y. Lin, K. Rui, Q. Zhou, Y. Chen, S. X. Dou, W. Sun, *Nanoscale* **2018**, 10, 19074.

Chapter 6: Conclusions and Perspectives

6.1 Conclusions

This thesis is devoted to using pristine MOF nanosheets for electrocatalysis applications and gaining insights into the reaction mechanisms of the electrocatalytic processes. According to the works in this thesis, the following conclusions can be drawn:

1. 2D MOF nanosheets can be directly used for electrochemical oxidation reactions such as OER and UOR without any post-treatments. Compared to bulk MOF, more metal atoms are exposed on the surface of MOF nanosheets as active sites for electrocatalysis. These exposed metal atoms are coordinatively unsaturated, contributing to enhanced catalytic activity. Moreover, the high porosity and specific surface area facilitate the mass transfer of the reactants and the diffusion of generated products. More importantly, by choosing appropriate organic ligands, the electronic structure of metal nodes can be well tailored in MOFs, leading to the formation of metal cations with high oxidation state. For electrochemical oxidation reactions, generally higher oxidation states of metal cations contribute to better catalytic performances. Therefore, the well-designed 2D Ni-MOF nanosheets with high oxidation states exhibit high activity and outstanding stability towards UOR.

2. Despite the advantages of MOF nanosheets, they have an undesirable tendency to aggregate. This is similar to graphene, and the reduced specific surface area of MOF nanosheets is not favourable for electrocatalysis. In order to solve this problem, 2D MOF-based hybrid nanosheets are designed and fabricated through a simple sonication-assisted solution method. After coupling with $Ni(OH)_2$ nanosheets, the large specific surface area of MOFs is well retained. Specifically, the electrochemical surface area of Ni-BDC/$Ni(OH)_2$ nanosheets is about 2.5 times of that of pure Ni-BDC nanosheets. Moreover, the electronic structure of $Ni(OH)_2$ component is well modified to generate Ni cations with higher oxidation states. Thus, significantly enhanced OER performance is achieved on Ni-BDC/$Ni(OH)_2$ nanosheets. Moreover, the facile and general method developed in this thesis can be extended to fabricate other MOF-based hybrid nanosheets such as MOF-metal oxide, MOF-graphene, MOF-MXenes, MOF-metal hydroxide, etc.

3. Though 2D MOF nanosheets are demonstrated as efficient catalysts for electrochemical oxidation reactions, they generally only exhibit very low catalytic activities towards reduction reactions such as HER. Thus, 2D Co-BDC/MoS_2 hybrid nanosheets are fabricated and explored as efficient electrocatalysts for alkaline HER. The well-constructed Co-

BDC/MoS_2 interface is vital for alkaline HER. It is well accepted that water dissociation step cannot be ignored in alkaline HER, and this step very likely is the rate-determining step for alkaline HER. For Co-BDC/MoS_2, Co-BDC promotes the dissociation of water to supply enough protons for the nearby MoS_2, and MoS_2 is responsible for the generation of hydrogen from the protons. More interestingly, partial phase transformation of MoS_2 from 2H-phase to 1T-phase is achieved after the hybridization of Co-BDC and MoS_2. In fact, metallic 1T-MoS_2 is a much better HER catalyst than semiconducting 2H-MoS_2. As expected, the obtained Co-BDC/MoS_2 hybrid nanosheets exhibit greatly enhanced HER performance compared to bare Co-BDC, MoS_2 and previously reported MOF-based catalysts in alkaline solution.

In summary, MOF nanosheets are demonstrated as efficient electrocatalysts for oxidation reactions. By coupling MOFs with other functional materials selectively, the application of MOFs can be extended to more research areas. Moreover, the insightful understanding of the reaction mechanisms of electrocatalysis can lay a solid foundation for designing more efficient MOF-based electrocatalysts

6.2 Perspectives

Though great achievements have been made in the research area of 2D MOFs for electrocatalysis, further work needed to be done to accelerate the development of MOF-based catalysts for clean and renewable technologies.

1. 2D MOFs have been reported as highly efficient catalysts for oxidation reactions. Meanwhile, MOFs suffer from low catalytic activities for reduction reactions such as HER. It is well accepted that the reaction activity and selectivity of a catalyst is determined by the binding energies of reaction intermediates to its surface. Meanwhile, the binding energies of reaction intermediates are governed by the electronic structure of the catalyst itself. Therefore, the electronic structure of MOFs needs to be well tailored by choosing appropriate organic ligands, doping or coupling with other materials to achieve better catalytic performance towards reduction reactions. In fact, besides HER, carbon dioxide reduction and nitrogen reduction are also important and quite challenging, which have drawn increasing attentions from the academia and the industry. Currently, only few MOFs have been reported for these reactions. Therefore, it is urgently needed to explore more 2D MOFs for these emerging electrocatalytic reactions.

2. Low conductivity and unsatisfactory stability are two key factors which hinder the application of pristine MOFs for electrocatalysis. In order to solve the problem of

conductivity, more attention should be paid to electrically conductive MOFs, which is a subclass of MOFs family. Constructing ultrathin 2D bimetallic MOF nanosheets is also an ideal way to improve the conductivity. Moreover, the MOFs can be directly grown on the conductive substrate such as nickel foam, carbon cloth, etc. Besides the enhanced conductivity, this method also avoids the usage of carbon black and Nafion. For the stability, we need to choose appropriate organic ligands and metal nodes in order to guarantee the stability in the specific electrolyte.

3. The mechanisms of 2D MOFs for electrocatalysis need to be further explores. Currently, the ambiguous reaction mechanisms of MOFs for electrocatalysis severely limit insights into the catalyst design. In this regard, combing density functional theory (DFT) calculations with experimental results can provide more insights to understanding the catalytic process. Moreover, advanced characterization techniques, especially in situ characterization techniques, such as in situ Raman spectroscopy, XPS, near edge X-ray absorption fine structure (NEXAFS), surface-enhanced infrared absorption spectroscopy (SEIRAS) are capable of probing the real reaction processes, which are highly significant for ascertaining proposed reaction mechanisms.

4. In order to commercialize MOFs for real applications, mass production of MOFs is crucial. Various strategies including electrochemical deposition, microwave synthesis, ball milling method can be addapted in the future to produce MOFs from laboratory to industrial scale.

We believe that more and more achievements will be made in this exciting research area (2D MOF nanosheets for electrocatalysis) through the combination of material design, computational calculations and advanced characterization techniques.

Appendix: Publications during PhD Candidature

[1] **Dongdong Zhu**, Jinlong Liu, and Shi-Zhang Qiao*, Recent Advances in Inorganic Heterogeneous Electrocatalysts for Reduction of Carbon Dioxide, ***Advanced Materials***, 2016, 28, 3423–3452.

[2] **Dongdong Zhu**, Chunxian Guo, Jinlong Liu, Liang Wang, Yi Du, and Shi-Zhang Qiao*, Two-Dimensional Metal-Organic Frameworks with High Oxidation States for Efficient Electrocatalytic Urea Oxidation, ***Chemical Communications***, 2017, 53, 10906–10909.

[3] **Dongdong Zhu**, Jinlong Liu, Liang Wang, Yi Du, Yao Zheng, Kenneth Davey, and Shi-Zhang Qiao*, 2D Metal-Organic Framework/$Ni(OH)_2$ Heterostructure for Enhanced Oxygen Evolution Reaction, submitted.

[4] **Dongdong Zhu**, Jinlong Liu, Yongqiang Zhao, Yao Zheng and Shi-Zhang Qiao*, Engineering 2D Metal-Organic Frameworks/MoS_2 Interface for Enhanced Alkaline Hydrogen Evolution, submitted.

[5] Jinlong Liu, **Dongdong Zhu**, Chunxian Guo, Anthony Vasileff, and Shi-Zhang Qiao*, Design Strategies toward Advanced MOF-Derived Electrocatalysts for Energy-Conversion Reactions, ***Advanced Energy Materials***, 2017, 7, 1700518.

[6] Jinlong Liu, **Dongdong Zhu**, Tao Ling, Anthony Vasileff, and Shi-Zhang Qiao*, S-$NiFe_2O_4$ Ultra-Small Nanoparticle Built Nanosheets for Efficient Water Splitting in Alkaline and Neutral pH, ***Nano Energy***, 2017, 40, 264–273.

[7] Jinlong Liu, **Dongdong Zhu**, Yao Zheng, Anthony Vasileff, and Shi-Zhang Qiao*, Self-Supported Earth-Abundant Nanoarrays as Efficient and Robust Electrocatalysts for Energy-Related Reactions, ***ACS Catalysis***, 2018, 8, 6707–6732.

[8] Jinlong Liu, Yao Zheng, **Dongdong Zhu**, Anthony Vasileff, Tao Ling, and Shi-Zhang Qiao*, Identification of pH-Dependent Synergy on Ru/MoS_2 Interface: A Comparison of Alkaline and Acidic Hydrogen Evolution, ***Nanoscale***, 2017, 9, 16616–16621.